Technische Universität München
TUM School of Natural Sciences

On lasers and blazars: Evaluation of the LIDAR corrections of MAGIC telescope data and insights into the broadband emission of Markarian 421

Felix Schmuckermaier

Vollständiger Abdruck der von der TUM School of Natural Sciences der Technischen Universität München zur Erlangung eines

Doktors der Naturwissenschaften (Dr. rer. nat.)

genehmigten Dissertation.

Vorsitz:

Prof. Dr. Alejandro Ibarra

Prüfende der Dissertation:

1. Priv.-Doz. Dr. Béla Majorovits
2. Prof. Dr. Elisa Resconi

Die Dissertation wurde am 25.09.2024 bei der Technischen Universität München eingereicht und durch die TUM School of Natural Sciences am 22.10.2024 angenommen.

Abstract

In this thesis, I present new technical results relevant to ground-based gamma-ray astronomy as well as new astrophysical findings on the emission of blazars.

I investigate the impact of non-ideal atmospheric conditions on data taken by the Major Atmospheric Gamma-Ray Imaging Cherenkov (MAGIC) telescopes and the capability of correcting impaired data with a Light Detection and Ranging (LIDAR) system. I have analyzed the data of close to seven years of MAGIC observations of the Crab Nebula, the standard candle in gamma-ray astronomy, which allowed me to characterize the correction method under various observational conditions, as well as to perform a comparison of two different correction algorithms. I demonstrate under which conditions VHE (very-high-energy; >100 GeV) gamma-ray data can still be adequately corrected and where systematic uncertainties increase. The resulting study provides analyzers of MAGIC data with detailed knowledge about the effects of suboptimal atmospheric conditions on real data. An important achievement of my PhD work is that it provides the information and recommendations to recover and reliably use data that would otherwise be discarded, hence extending the duty cycle of the telescopes.

Subsequently, I present two studies I performed on the nearby active galactic nucleus (AGN) Markarian 421 (Mrk 421). It is one of the closest and brightest TeV-emitting AGN, belongs to the subclass of blazars and is an ideal source to study across the entire electromagnetic spectrum with great precision. The first study relies on a data set taken around early 2010, which marks the most active period of the source to date, including the brightest TeV flare ever observed from an AGN. This extensive multi-wavelength (MWL) data set allowed me to characterize the emission during a unique state using various strategies to quantify the multi-band variability and correlations. The source shows a complex correlation behavior with varying trends depending on whether the most extreme flare is included or not. This indicates that different mechanisms are responsible for the emission over the full campaign, which rules out simple explanatory models, such as those based on a single emitting zone. My study shows that these observations can be explained with the existence of two emission zones.

The second study covers a period in 2022 when the Imaging X-ray Polarimetry Explorer (IXPE) satellite observed Mrk 421. This novel instrument, launched in December 2021, provides measurements of the polarization in X-rays for the first time. I analyzed the concurrent MAGIC data to obtain the first combined observations of Mrk 421 with VHE gamma rays and X-ray polarization. During the two-month long campaign, Mrk421 showed a variety of emission states, allowing the investigation of correlations of the different polarization signatures with the spectral and flux evolution in different wavebands. In the second half of the IXPE observations, a rotation of the X-ray polarization angle was observed, during which the source showed strong activity in the X-ray as well as spectral hysteresis patterns. These observations can be indirectly linked to the VHE emission due to a significant correlation with the X-rays and provide information on the mechanism and efficiency of particle acceleration.

Zusammenfassung

In dieser Arbeit präsentiere ich neue technische Ergebnisse für die bodengebundene Gammastrahlenastronomie sowie neue astrophysikalische Erkenntnisse über die Emission von Blazaren.

Ich untersuche die Auswirkungen ungünstiger atmosphärischer Konditionen auf Daten der Major Atmospheric Gamma-Ray Imaging Cherenkov (MAGIC) Teleskope, und den Einfluss von Korrekturen auf beeinträchtigte Daten mit einem Light Detection and Ranging (LIDAR)-System. Ich analysierte Daten von knapp sieben Jahren MAGIC-Beobachtungen des Krebsnebels, einer Standardkerze in der Gammastrahlenastronomie, wodurch eine Charakterisierung der Korrekturmethode unter verschiedenen Beobachtungsbedingungen sowie ein Vergleich von zwei verschiedenen Korrekturalgorithmen erreicht wurde. Ich zeige dadurch, unter welchen Bedingungen VHE (very-high-energy; >100 GeV) Gammastrahlendaten noch adäquat korrigiert werden können und wo systematische Unsicherheiten zunehmen. Die daraus resultierende Studie versorgt zukünftige Analysten von MAGIC-Daten mit detaillierten Kenntnissen über die Auswirkungen suboptimaler atmosphärischer Bedingungen auf reale Daten. Eine wichtige Leistung meiner Doktorarbeit besteht darin, dass sie Informationen und Empfehlungen zur Wiederherstellung und zuverlässigen Nutzung von Daten liefert, die andernfalls verworfen würden, und somit die Betriebszeit der Teleskope verlängert

Anschließend stelle ich zwei Studien über den nahen aktiven Galaxienkern Markarian 421 (Mrk 421) vor. Er ist einer der nächstgelegenen und hellsten aktiven Galaxienkerne, die TeV-Strahlung emittieren. Mrk 421 gehört zur Gruppe der Blazare und ist eine ideale Quelle, um sie entlang des gesamten elektromagnetischen Spektrums mit großer Präzision zu untersuchen. Die erste Studie basiert auf einem Datensatz, der etwa Anfang 2010 aufgenommen wurde. Dies ist der bisher aktivste Zeitraum der Quelle, einschließlich des hellsten TeV-Flusses, der jemals in einem aktiven Galaxienkern beobachtet wurde. Der umfangreiche Multiwellenlängen (MWL)-Datensatz ermöglichte es mir, die Emission während eines einzigartigen Zustands durch Variabilitäts- und Korrelationsstudien zu charakterisieren. Die Quelle zeigt ein unterschiedliches Korrelationsverhalten, je nachdem, ob der größte Strahlungsausbruch einbezogen wird oder nicht. Dies deutet darauf hin, dass verschiedene Mechanismen für die Emission verantwortlich sind, und schließt einfache Erklärungsmodelle, wie z.B. Modelle mit nur einer Emissionsregion, aus. Meine Studie zeigt, dass sich diese Beobachtungen mit mit der Existenz von zwei Emissionszonen erklärt werden können.

Die zweite Studie umfasst einen neueren Zeitraum im Jahr 2022, in dem der Satellit Imaging X-ray Polarimetry Explorer (IXPE) Mrk 421 beobachtete. Mit diesem einzigartigen Instrument, das im Dezember 2021 in Betrieb genommen wurde, können erstmals Messungen der Polarisation von Röntgenstrahlen durchgeführt werden. Ich analysierte die zeitgleich erhobenen MAGIC-Daten, wodurch der erste kombinierte Datensatz von Mrk 421 mit VHE-Gammastrahlung und Röntgenpolarisation erstellt werden konnte. Während der zweimonatigen Kampagne zeigte Mrk421 eine Vielzahl von Emissionszuständen, welche die Untersuchung von Korrelationen

der Polarisationssignaturen mit der Entwicklung des Spektrums und des Flusses in verschiedenen Wellenlängen erlaubte. In der zweiten Hälfte der IXPE-Beobachtungen wurde eine Rotation des Röntgenpolarisationswinkels beobachtet, während derer die Quelle starke Aktivität im Röntgenbereich sowie spektrale Hysteresemuster zeigte. Diese Beobachtungen können aufgrund einer signifikanten Korrelation mit der Röntgenstrahlung indirekt mit der VHE-Emission in Verbindung gebracht werden und geben Aufschluss über den Mechanismus und die Effizienz der Beschleunigung von Teilchen innerhalb des relativistischen Jets.

Contents

Chapter 1

Introduction

Astronomical observations have been carried out for thousands of years. Direct observations by eye were the earliest form of investigating the sky. With the invention of optical telescopes, the accuracy was considerably increased, which triggered the development of more precise instruments for astrophysics. Optical light remained the primary observable until radio waves of cosmic origin were first discovered in the 1930s (Jansky, 1933). In the 1950s, the era of space-based instruments began, opening the electromagnetic window with observations in the infrared, ultraviolet, X-rays, and finally gamma rays. The first significant detection of gamma-ray emission from the Milky Way was performed in 1967 by the OSO-3 satellite (Clark et al., 1968). The field developed further to even higher energies with the launch of the SAS-2 satellite, which detected a diffuse gamma-ray background (Fichtel et al., 1975), and with the discovery of 25 discrete sources by the COS-B satellite (Swanenburg et al., 1981).

The first cosmic messengers besides electromagnetic waves were discovered by Victor Hess in 1912 (Hess, 1912). He performed manned balloon ascents in which he measured the ionization of the atmosphere with increasing altitude and noticed an increase in radiation levels above 1.5 km, indicating that the radiation must be produced by so-called cosmic rays (CRs) originating from the cosmos. Even though the spectrum of CRs can be measured in great detail over many orders of magnitude, revealing a decaying power-law shape with a spectral index between 2.7 and 3.3, the origin is not understood in detail (see, e.g., Spurio, 2018; Gaisser et al., 2016). The spectrum up to the GeV range is dominated by solar activity. Higher-energy particles are believed to be produced within our Galaxy. Particles with energies above $\sim 10^{18}$ eV most likely originate from extragalactic sources because charged particles with higher energies cannot be confined anymore by the galactic magnetic field (Hillas, 1984). These observations suggest the existence of cosmic accelerators that are able to accelerate particles up to immense energies and can produce the observed power-law distributions. Since charged particles are deflected by magnetic fields, when traveling through the cosmos, they do not point back to their origin, which makes the identification of CR sources challenging. Possible galactic example candidates are pulsar wind nebulae and supernova remnants. Possible extragalactic sources responsible for the origin of ultra-high energy CRs with energies above 10^{18} eV are starburst galaxies, gamma-ray bursts, or active galactic nuclei (AGN). As AGN are the sources of relevance for this work, Chapter 2 provides an overview of AGN and the open questions regarding their understanding.

Whatever the sources of CRs might be, the same sites should also produce gamma rays and neutrinos through hadronic interaction and decay channels (Spurio, 2018). Contrary to CRs, magnetic fields do not deflect these, causing gamma rays and neutrinos to point back to their sources. Since neutrinos are exclusively produced via hadronic decay channels, identifying

specific sources of astrophysical neutrinos also leads to identifying sources of CRs. However, gamma rays can also be produced by purely leptonic processes and might be produced without being accompanied by CRs or neutrinos. Therefore, understanding the emission of gamma rays at the highest energies is essential for understanding the mechanism behind their emission and enhancing our knowledge about cosmic accelerators.

Space-based instruments are successful in detecting gamma rays below a few tens of GeV through pair conversion, which produces an electromagnetic shower inside the detector. However, above a few tens of GeV, a large fraction of the electromagnetic shower leaks out the detector and, more importantly, owing to the rapid decrease in the photon fluxes with energy, and due to the small ($< \sim 1\ \mathrm{m}^2$) effective area or any detector put on space, the direct detection of gamma rays becomes very inefficient. On the other hand, one could use the Earth's atmosphere as a large calorimeter and detect gamma rays in an indirect manner. When gamma rays with energies above a few tens of GeV reach the atmosphere, they generate atmospheric air showers, which in turn induce the emission of Cherenkov light in the atmosphere. The observation of gamma rays via the indirect detection of these showers reaches effective areas on the km^2 scale. This so-called Imaging Atmospheric Cherenkov Telescopes (IACT) technique was pioneered by the Whipple Observatory in the late 1980s with the first discovery of VHE gamma rays coming from the Crab Nebula (Weekes et al., 1989) and the following discovery of the first extragalactic source Mrk 421 (Punch et al., 1992a). The HEGRA (High-Energy Gamma-Ray Astronomy) array showed the importance of using a stereoscopic observation mode to improve background rejection and angular resolution (Pühlhofer et al., 2003), which is now applied by the current generation of IACTs, such as the MAGIC telescopes. The IACT technique, in general, as well as the design and data analysis of the MAGIC telescopes, is the subject of Chapter 3 of this thesis.

VHE astronomy faces unique experimental challenges due to its ground-based nature. Using the atmosphere as a calorimeter creates the large effective areas necessary for detecting the very small fluxes of photons at the highest energies. However, this also suffers from the disadvantage of being exposed to atmospheric conditions, which can vary from minute to seasonal fluctuations and represent an uncontrollable external factor for the experiment. Higher aerosol levels, caused by clouds or dust, lead to increased absorption and scattering of Cherenkov light and an impaired reconstruction of the primary gamma-ray properties. The MAGIC telescopes have operated a LIDAR system since 2013 to obtain range-resolved, real-time monitoring of atmospheric conditions to characterize the quality of data, as well as to correct atmospherically degraded MAGIC data. Chapter 4 of this thesis provides a detailed description of the LIDAR system and its data analysis. The following Chapter 5 provides the first systematic evaluation of the quality of the MAGIC data taken under different (non-optimal) atmospheric conditions, after applying the LIDAR corrections. This information is critically important for any analyzer of MAGIC data obtained during non-perfect weather conditions.

So far, over 270 sources emitting VHE gamma-rays have been detected (Wakely and Horan, 2023). These include galactic sources such as pulsar wind nebulae, supernova remnants, or pulsars, as well as extragalactic sources such as gamma-ray bursts and AGN. The overall majority of sources are blazars, which are AGN with their jet pointed close to the line of sight from Earth. Although blazars have been the subject of intensive research for decades, fundamental questions still remain unanswered, such as the acceleration and emission mechanisms within the jet. The

blazar Mrk 421 is one of the most prominent sources in the VHE sky. Due to its proximity and brightness, it can be studied in great detail across the entire electromagnetic spectrum, making it a suitable representative source for the study of all blazars. Chapter 6 presents results from observations of Mrk 421 around early 2010, the most active period of the source so far, and Chapter 7 then focuses on a more recent data set from 2022, which includes the first combined measurements in VHE gamma rays and X-ray polarization.

Chapter 2

Active galactic nuclei

AGN are compact regions in the center of galaxies producing large amounts of non-stellar emission. Accretion by a supermassive black hole (SMBH) is responsible for an enormous power output. They are the most luminous persistent sources in the Universe and can exhibit rapid variability in their emission. The first evidence of galaxies showing additional emission on top of their stellar emission in their center was provided by Carl Seyfert in 1943 (Seyfert, 1943). He found nuclear emission lines with varying Doppler broadening superposed on a typical stellar spectrum. Since then, AGN have been found to emit across the entire electromagnetic spectrum (Padovani et al., 2017).

A subclass of AGN, so-called blazars, comprise the majority of sources in VHE gamma-ray astronomy. The following chapter gives an introduction to the source type. It starts with a description of the elemental composition and subclasses of AGN. The remaining chapter will focus on blazars as the relevant subclass for this thesis and provide a brief overview of acceleration and emission mechanisms. The chapter closes with describing Mrk 421 and its importance to studying blazars.

2.1 Composition

The central engine

AGN can show enormous energy outputs. In the example of 3C 273, this power output lies around a bolometric luminosity of $10^{47}\,\mathrm{erg\ s^{-1}}$ (Paltani and Türler, 2005). On the other hand, the observed flux variability of the source is at a timescale of days, implying a size of the emission region around light days and Dopple factors of 10-100 (Marscher and Gear, 1985). To reach these extreme power densities, AGN are believed to be powered by accretion onto an SMBH in the center of their host galaxy. These SMBHs have masses of $10^6 - 10^9$ solar masses ($M_\odot$). The event horizon of a black hole is used to define its radius, which for non-rotating black holes is given by the Schwarzschild radius (Schwarzschild, 1916):

$$R_S = \frac{2GM}{c^2} \tag{2.1}$$

where M is the mass of the black hole, G the gravitational constant and c the speed of light. Due to causality, variations in the emission of an astrophysical source with size r cannot happen on time scales smaller than r/c, which gives the light crossing time of the source. Using the

Schwarzschild radius, this sets a lower limit on the timescale of variations from any source:

$$T \geq \frac{R_s}{c} \approx 10^{-5} \frac{M}{M_\odot} \text{ s} \tag{2.2}$$

The SMBHs have a hot accretion disk around them, fueling the AGN. Accretion is a highly efficient conversion from kinetic and potential energy to radiation. The maximal thermal luminosity for an accreting black hole is reached once the outward radiation pressure equals the inward gravitational force. The associated luminosity is called Eddington luminosity (Eddington, 1917; Longair, 2011) and is given by:

$$L_{Edd} = 1.3 \cdot 10^{38} \frac{M}{M_\odot} \text{ erg s}^{-1} \tag{2.3}$$

It must be noted that both the observed time scale and the intensity of the emission can be altered by relativistic effects, which will be discussed in more detail later on.

The accretion rate of a black hole can be expressed as the change of mass per time:

$$\dot{M} = \frac{L}{\eta c^2} \tag{2.4}$$

where η parameterized the accretion efficiency. Setting L to the Eddington luminosity and $\eta = 1$, one gets the maximal accretion rate $\dot{M}_{Edd}$. The resulting disk can show different geometrical and optical properties depending on the accretion rate (Longair, 2011).

The vicinity of the black hole

Further outside the central accretion disk, an optically thin torus of dust can be found. The dust absorbs and re-emits radiation coming from the accretion disc, resulting in an emission of infrared radiation (Beckmann and Shrader, 2012). The absorption of the torus also provides a geometric explanation for the existence of several subclasses of AGN, as will be explained in section 2.2.1.

The first notable observational feature of AGN was the discovery of emission lines (Fath, 1909). Some lines can show strong Doppler broadening in the order of $10^3 - 10^4$ km s^{-1} as well as short flux variability, suggesting a location close to the central engine of the AGN with a high gas density. Other lines show a broadening of only a few hundred km s^{-1}. These narrower lines also show a lack of variability and are therefore believed to be emitted in a much larger, less dense, and kinematically separate region. The two regions are called broad-line region (BLR) and narrow-line region (NLR).

Jets

Another important feature of some subclasses of AGN is the formation of extremely energetic and highly collimated outflowing plasma structures, called jets (Beckmann and Shrader, 2012). They appear in pairs flowing outwards roughly orthogonal to the accretion disc and can extend

up to megaparsecs. They can be resolved best with observations in the radio. Using long-baseline interferometry, one can resolve the inner structure of jets, which is not homogeneous but can show individual spots of higher emission, so-called knots. Jets are found in around 10% of AGN, which are then called radio-loud AGN (Padovani, 2011).

The composition of AGN jets is still unclear. Jets certainly consist of relativistic leptons and hadrons, but the extent of their respective contribution remains unclear. Section 2.2.2 will return to this open question in more detail. The exact formation process and geometrical configuration of jets are also still uncertain (see, e.g., Blandford et al., 2019).

2.2 Classification of AGN

2.2.1 The Unified Model of AGN

AGN can differ greatly in their observational properties, such as the mass of the central SMBH, the total luminosity, the flux variability, or the presence of emission lines. This led to the introduction of several subclasses of AGN (see, e.g., Padovani et al., 2017). Below is a short overview of AGN classes, followed by a scheme aiming to unify these observational differences with a simple model.

AGN can be classified into two major groups by their radio emission. The exact criteria on what classifies as radio-loud (RL) or radio-quiet (RQ) has been defined in different ways in the literature. A common definition uses the flux ratio in the radio band versus the optical band (Sramek and Weedman, 1980). Radio loudness R^* can thus be defined as:

$$R^* = \frac{f_{5\,\mathrm{GHz}}}{f_{2500\,\text{Å}}} \tag{2.5}$$

AGN can be considered RL once $R^* \gtrsim 10$ (Kellermann et al., 1989). The exact fraction of RL AGN is still undetermined, but most estimates suggest less than 10% (Beckmann and Shrader, 2012). The main physical difference between the two classes is the existence or nonexistence of jets (Padovani, 2016). RQ AGN are therefore associated with non-jetted AGN, whereas RL AGN with jetted ones.

RL AGN can be subdivided into Fanaroff-Riley I (FR I) galaxies, showing a compact emission arising from close to the core and, with that, an overall low luminosity (Fanaroff and Riley, 1974). Other objects have their dominant emission originating far out from the center at the end of the jets. These are called FR II objects and have large radio lobes far outside of the host galaxy, dominating the radio emission.

Furthermore, the optical spectrum allows for further classification of AGN: So-called Type-1 AGN show broad emission lines and a bright continuum spectrum in the optical. Type-2 AGN show only narrow emission lines, and the emission of the AGN core is less dominant, leading to a weaker continuum. Objects with very unusual emission line features or no strong emission lines at all are referred to as Type-0. In the case of lower luminosity RQ AGN, this creates two subclasses: Seyfert 1 and Seyfert 2 galaxies. Objects with high luminosity are referred to as quasi-stellar objects (QSO) or quasars with their respective type (Padovani et al., 2017).

The Unified Model of AGN aims to explain all observational differences of AGN in terms of three ingredients: The existence or nonexistence of a jet, the overall power of the central

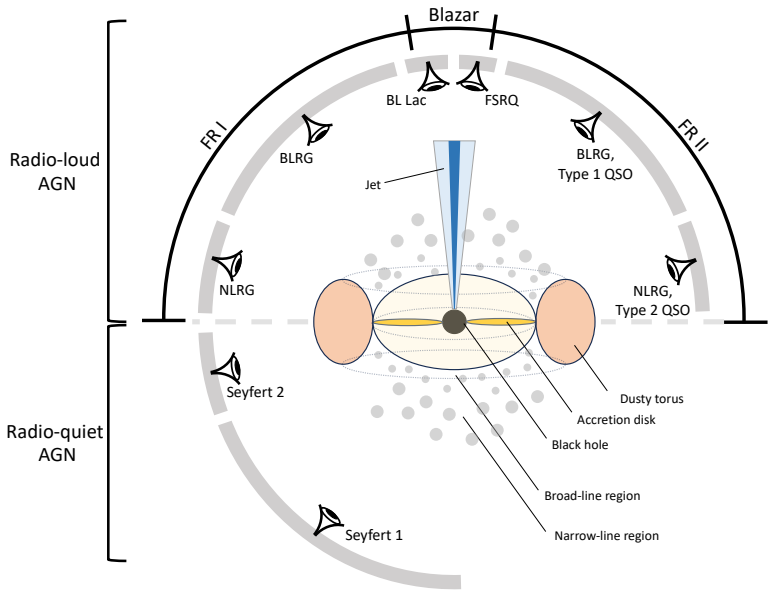

Figure 2.1: Schematic representation of the unification scheme for AGN. Drawing follows the schematic in Beckmann and Shrader (2012)

engine, and the viewing angle at which the object is observed. Figure 2.1 shows a schematic representation of this unified scheme. Seyfert I galaxies are therefore observed when looking at non-jetted, low luminosity objects at a rather larger angle towards the disk. This allows us to observe the BLR and the NLR as well as the accretion disk, leading to broad and narrow lines and a strong thermal continuum emission. Viewing the source at a steeper angle results in the observation of a Seyfert 2 galaxy, where the BLR and accretion disk are obscured by the dusty torus surrounding the core. In the case of RL galaxies, the absorption by the torus divides FR I and FR II galaxies into narrow-line radio galaxies (NLRG) and broad-line radio galaxies (BLRG), depending on the visibility of the BLR. A special subclass is blazars, which are RL AGN viewed at an angle closely aligning with the jet direction ($\theta \lesssim 10°$). The observed emission is dominated by the jet, leading to bright emission across the full electromagnetic spectrum. Relativistic effects additionally enhance the observed luminosity and lead to high variability on short time scales. Some blazars show broad emission lines, so-called flat spectrum radio quasars (FSRQs), whereas others show no or only weak lines, the BL Lac type objects (BL Lacs; named after their prototype source BL Lacertae). A different way of classification of the two source populations moves away from the definition via emission lines (Giommi et al., 2012). The lines of some sources classified as BL Lacs might be heavily diluted by the non-thermal continuum and should be visible via infrared spectroscopy. These sources could then be considered FSRQs in the classical definition. The so-called *simplified blazar view* postulates two main intrinsic blazar types: Low-ionization, mostly beamed FR I sources being classified as BL Lacs, and high-ionization, beamed FR II sources being classified as FSRQs. Another criteria was proposed by Ghisellini et al. (2011). Here, the dividing feature is the luminosity

Table 2.1: The general unification scheme of AGN based on emission lines and radio loudness.

Type	Emission lines	Radio-quiet	Radio-loud
Type 1	Broad and narrow lines	Seyfert 1	BLRG, FSRQ, Type-2 QSO
Type 2	Narrow lines	Seyfert 2	NLRG, Type-1 QSO
Type 0	No lines	-	BL Lac

of the BLR normalised to the Eddington luminosity. In case this ratio is smaller than around $5 \cdot 10^{-4}$, the source is classified as a BL Lac, otherwise as a FSRQ. This criteria also separates low-ionization FR I sources from high-ionization FR II sources, making the two approaches compatible. Blazars, more precisely, BL Lacs are the main sources of interest in this thesis and will therefore be discussed in more detail in the following section.

Table 2.1, gives an overview of all discussed AGN subclasses. Note, that the selection is by no means comprehensive.

2.2.2 Blazars

As mentioned, the spectra of blazars show no or rather weak lines in the case of BL Lacs and broad lines for FRSQs. The separating criterion is given by the equivalent width (EW), which is a measure of the strength of a given emission or absorption line. It gives the line flux in terms of how much continuum one needs to integrate in order to get the same flux value. BL Lacs are defined as having only lines below an EW of 5 Å. Due to the variable emission of blazars and relativistic beaming effects, the flux ratios can get distorted, making this simple criterion not ideal in all cases. Another criterion is based on the luminosity of the BLR compared to the Eddington luminosity (Ghisellini et al., 2011).

The multi-wavelength emission of blazars is usually displayed as the spectral energy distribution (SED), which is the energy flux as a function of energy or frequency. The typical blazar SED consists of two large bumps ranging from radio all the way to VHE gamma rays. Figure 2.2 shows the SED of the BL Lac Mrk 421 taken in 2009 with various instruments. The orange band gives the energy range of the MAGIC telescopes. The low-energy bump is shown in dark blue. Due to spectral and polarization characteristics, it is widely accepted that the first bump originates from leptonic synchrotron emission and is therefore labeled as "Synchrotron bump". Relativistic electrons and positrons are accelerated and emit synchrotron radiation in the jet's magnetic fields ranging from radio to X-rays. The second bump peaks in the gamma-ray range, and its origin is still under debate and will be further discussed in section 2.3.2.

BL Lacs generally tend to have a lower overall luminosity than FSRQs. On the other hand, the SED of BL Lacs is more shifted to high energies. The shift of the SED is also used to further classify blazars by comparing the peak frequency of the synchrotron component ν_S (Abdo et al., 2010a). Objects with a ν_S of less than 10^{15} Hz are called low-synchrotron peak frequency blazars (LSPs). Intermediate synchrotron blazars (ISPs) have peak frequencies of $10^{14}\,\text{Hz} < \nu_S < 10^{15}\,\text{Hz}$. Lastly, blazars with a $\nu_S > 10^{15}$ Hz are called high synchrotron peaked blazars (HSPs). Figure 2.2 shows that during 2009 Mrk 421 had a peak frequency of around 10^{17} Hz, and with that lies in the HSP regime.

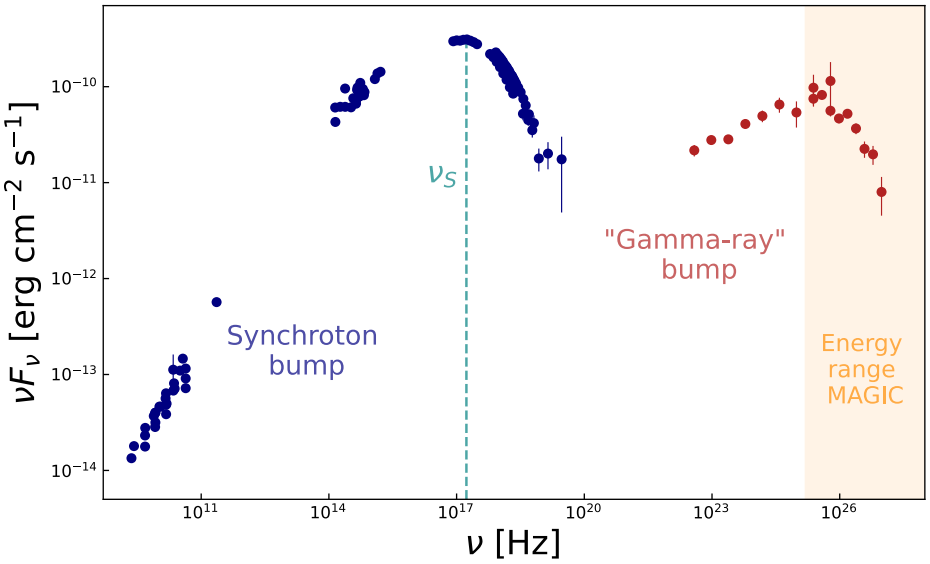

Figure 2.2: Multi-wavelenegth SED from Mrk 421 showing the typical double bump structure for blazars and the energy range covered by the MAGIC telescopes. Data taken from Abdo et al. (2011)

2.3 Blazar emission

2.3.1 Acceleration mechanisms

Several observations require the existence of astrophysical environments capable of accelerating charged particles to high energies.This includes observation of sources producing non-thermal emission (i.e., radiation that cannot be accounted for by the spectrum of thermal bremsstrahlung or black-body radiation) over many orders of magnitude as well as the measurement of cosmic rays reaching energies of $\sim 10^{20}$ eV. The measured energy spectrum of cosmic rays, as well as the required energy spectrum of leptons necessary to reproduce observed non-thermal radiation, follow power-law distributions with spectral indices ranging around 2–3. The exact mechanisms responsible for cosmic accelerators are still under debate, but any proposed mechanism must account for these observations.

The most favored acceleration mechanism in the context of AGN jets is the acceleration by shocks (following the description in Longair, 2011). Shock waves arise when perturbations in a gas travel faster than the speed of sound in that medium. The disturbance then does not behave like a sound wave, and the resulting discontinuity behind and in front of the disturbance is referred to as a shock wave. In the case of AGN, these shock waves may arise in the relativistic outflows of particles in the jets. This scenario is further supported by radio observations revealing substructures within the jet plasma moving at relativistic speeds. The first accelerating mechanism around shock fronts was proposed by Enrico Fermi in 1949 (Fermi, 1949). The original Fermi mechanism describes particles being stochastically reflected by magnetic fields moving at a certain velocity. Every time a particle is reflected back and forth by these so-called

magnetic mirrors, it gains energy by a transfer of momentum. Since that gain in energy scales with the second order of the velocity, it is referred to as second-order Fermi acceleration. The longer the particles stay within the acceleration region, the more energy they can gain. The probability of the particle escaping the region also increases with time, which leads to a power-law-shaped distribution of resulting particle energies.

The most common modern version of Fermi acceleration in the context of shocks is the so-called diffusive shock acceleration (DSA) process. In the DSA scenario, the average energy gain of a particle being reflected back and forth at the shock front is

$$\left\langle \frac{\Delta E}{E} \right\rangle = \frac{4}{3}\frac{V}{c} \quad , \tag{2.6}$$

where V is the speed of the gas downstream of the shock front. Since here the energy gain depends linearly on the velocity, the mechanism is also referred as first-order Fermi acceleration. The energy after one round trip is given by

$$E = \beta E_0 = \left(1 + \frac{4}{3}\frac{V}{c}\right) E_0 \quad . \tag{2.7}$$

Using kinetic theory, one obtains the probability of escape for a particle for each iteration:

$$P_{\mathrm{esc}} = \frac{4}{3}\frac{V}{c} \tag{2.8}$$

The survival probability is then given by $P = 1 - P_{\mathrm{esc}}$. After n collisions, we have $N = N_0 P^n$ particles with energies $E = E_0 \beta^n$. After eliminating n from both equations, one obtains the relation:

$$\frac{N}{N_0} = \left(\frac{E}{E_0}\right)^{\ln P / \ln \beta} \tag{2.9}$$

The resulting energy spectrum is then given by the desired power-law form of the particle energy distribution:

$$N(E)\,\mathrm{d}E = \text{const.} \times E^{-1+\ln P/\ln\beta}\,\mathrm{d}E \tag{2.10}$$

Using the derived values for β and P we get

$$\frac{\ln P}{\ln \beta} = -1 \tag{2.11}$$

and with that a final energy spectrum of the accelerated particles:

$$N(E)\,\mathrm{d}E \propto E^{-2}\,\mathrm{d}E \tag{2.12}$$

This result is close to the observed spectral index of the cosmic-ray spectrum at around 2.7, as well as to the required indices for leptonic particle populations in blazars. The DSA provides a comprehensive explanation of why power-law energy spectra are found in a variety of astrophysical environments, including AGN, where strong shocks are undoubtedly present.

However, the scenario has difficulties explaining the variability on short time scales. Blazars can show variability down to minute time scales (e.g., Albert et al., 2007b), which constrains

the size of the emitting region to be less than what is expected from relativistic shocks in AGN jets. An alternative acceleration mechanism capable of producing variability on short time scales is magnetic reconnection (Longair, 2011; Giannios et al., 2009). It occurs when two magnetic fluxes of opposite polarity encounter each other, causing a release of magnetic energy. Magnetic reconnection allows the possibility of generating ultra-relativistic flows within the reconnection region. These mini-jets can show high Lorentz factors and, with that, short observed variability time scales.

2.3.2 Non-thermal emission mechanisms

The emission of blazars is dominated by non-thermal emission spanning over multiple orders of magnitude in energy. The following section contains a brief description of the types of particles and the associated emission mechanisms that are or could be responsible for the observed radiation.

Synchrotron radiation

Synchrotron radiation (Longair, 2011; Gaisser et al., 2016) is the radiation produced by charged particles that are accelerated along a curved path or orbit, e.g., by the Lorentz force within a magnetic field. The emitted synchrotron radiation is given by the radiative loss rate $-\frac{\mathrm{d}E}{\mathrm{d}t}$. In the case of a relativistic electron in a uniform magnetic field B, spiraling around the magnetic field lines, the loss rate averaged over the electrons directions is:

$$-\frac{\mathrm{d}E}{\mathrm{d}t} = \frac{4}{3}\,\sigma_T\, c\, U_{\mathrm{mag}} \left(\frac{v}{c}\right)^2 \gamma^2 \tag{2.13}$$

where v the velocity of the electron and U_{mag} the energy density of the magnetic field. The Thomson cross section is defined as $\sigma_T = \frac{8\pi e^4}{3 m_e^2 c^4}$. Given a magnetic field, the radiated energy loss is then proportional to:

$$-\frac{\mathrm{d}E}{\mathrm{d}t} \propto \frac{e^4\gamma^2}{m^2} \propto \frac{e^4 E^2}{m^4} \tag{2.14}$$

For a given particle with mass m and unit charge, the radiation will be suppressed by a factor $(m_e/m)^4$ compared to that of an electron. The synchrotron emission from a proton is, therefore, significantly less efficient than that of electrons. It is generally accepted that the previously described first bump of a typical blazar SED is the result of leptonic synchrotron radiation produced by electrons and positrons in the jet. Proton synchrotron radiation might contribute to the second bump under certain jet conditions.

An important observable feature of synchrotron radiation is polarization. The radiation of an electron is circularly polarised when viewed along the direction of the magnetic field lines. From any other angle, the radiation is elliptically polarised. If one considers a distribution of electrons moving at different pitch angles, cancellation effects lead to an overall observed linear polarization. The fractional polarization or polarization degree is defined by the intensities along the polarization axes. It can also be expressed as a function of the spectral index of the electron

spectrum p:

$$\Pi = \frac{I_\perp - I_\parallel}{I_\perp + I_\parallel} = \frac{p+1}{p+\frac{7}{3}} \tag{2.15}$$

Using a typical index of 2.5, the expected polarization degree is around 72%, in the case of a perfectly uniform magnetic field. The more turbulent and less ordered a magnetic field, the lower the resulting polarization degree.

Measuring the polarization of blazar emission can, therefore, provide information about the order of the magnetic fields in the jets. The polarization in the optical in blazars ranges from a few % up to 30% (Abdo et al., 2010c) indicating that the magnetic fields in the optical emission regions must be partially ordered in those sources. New instrumental developments also allow measurements of the polarization in the X-ray emission of blazars for the first time. For HSPs, the X-ray covers the falling edge of the synchrotron bump of the SED. This part is emitted by the most energetic electrons. Measuring the polarization degree allows an estimate of the magnetic field order and, with that, the spatial dependence of turbulence in the jet. In the scenario of particle acceleration at a shock front, simulations predict relatively high polarization degrees, due to the self-generated magnetic field at the shock front reaching a high degree of order (Tavecchio et al., 2018). In the case of magnetic reconnection, the emission most likely originates from turbulent regions with unstructured magnetic fields. High-energy polarization measurements, therefore, might be crucial to differentiate between acceleration scenarios. The first results of X-ray polarization measurements of blazars in a MWL context will be discussed in more detail in chapter 7.

Inverse Compton scattering

As previously mentioned, the origin of the second bump of a typical blazar SED is still a matter of debate. A possible emission mechanism is the inverse Compton (IC) effect. In classical Compton scattering, an electron scatters off a photon and gains energy from the collision. In the IC case, the photons are up-scattered by the electrons and gain energy in the interaction. The synchrotron photons from the first bump can function as the target photons for IC scattering on the same electrons, also producing the synchrotron radiation. This scenario is referred to as the synchrotron self-Compton (SSC) model (Maraschi et al., 1992; Madejski et al., 1999). In some cases, mostly for FSRQs, an additional target photon field, e.g., coming from the accretion disk, is needed to properly explain the SED (e.g., Madejski et al., 1999; Böttcher et al., 2013). One would expect a correlation in the emission of the first and second bump of the SED, since the same underlying particle population of leptons is responsible for the full MWL emission. The correlated behavior of various energy bands is part of the results discussed in the chapters 6 and 7.

The IC effect does not induce polarization by itself. If the target photon field is already polarized, as it is the case for an SSC scenario, part of the polarization is preserved but reduced by at least a factor 1/2 (Bonometto and Saggion, 1973).

Hadronic and Lepto–hadronic scenarios

The leptonic scenario described above explains the entire MWL emission from blazars by electrons and positrons in the jet. Hadrons, i.e., protons, are still present but only make a small contribution to the overall emission since their energies are too low (often called *cold* protons). There is also the possibility of so-called hadronic or lepto-hadronic scenarios in which hadrons contribute to the emission. The low-energy peak of the SED is still attributed to the synchrotron radiation of leptons, but the high-energy peak has a dominant contribution or at least substantial from protons interacting in the jet.

Since protons are charged particles, they can also emit synchrotron radiation. As mentioned previously, the emission is suppressed by a factor of $(m_e/m_p)^4$ compared to electrons. To achieve a high enough emission, different jet environments, e.g., higher magnetic fields or particle densities, are required (Cerruti, 2020). If the high-energy bump is primarily produced by proton synchrotron radiation, the emission would show a potentially high degree of polarization similar to the low-energy bump. For HSPs and most ISPs, the second bump lies in the gamma rays, where sensitive enough polarization measurements are not yet feasible. For ISPs, however, polarization measurements in the X-ray lie within the second bump and might help to disentangle the different possible emission mechanisms. IC emission in an SSC context would still produce some level of polarization but to a lower degree than what is expected from proton synchrotron radiation. Zhang and Böttcher (2013) predicted polarization degrees for different example blazars based on SED modeling. The difference of predicted polarization degree ranges from 15% up to 60% for the considered ISPs. High-energy polarization measurements, therefore, have the potential to differentiate between leptonic and hadronic models. However, even with the launch of new instruments, the experimental challenge of achieving a high enough sensitivity in these energy bands to detect the above-mentioned differences remains high.

The interaction of protons with photons may also provide a contribution. In the so-called lepto-hadronic model, both IC scattering and photon-proton interaction have relevant contributions to the emission (Spurio, 2018). The two primary photo-hadronic processes are photon-meson and Bethe–Heitler pair production of an electron-positron pair:

$$p+\gamma \longrightarrow \begin{cases} p'+\pi^0 \\ n\ +\pi^+ \\ p'+e^-+e^+ \end{cases} \tag{2.16}$$

Depending on the initial energies, more complex processes, producing multiple pions, are possible. The produced pions will undergo further decay:

$$\pi^0 \longrightarrow \gamma+\gamma \tag{2.17}$$

$$\pi^+ \longrightarrow \mu^+ + \nu_\mu \longrightarrow e^+ + \nu_e + \bar{\nu_\mu} + \nu_\mu \tag{2.18}$$

$$\pi^- \longrightarrow \mu^- + \bar{\nu_\mu} \longrightarrow e^- + \bar{\nu_e} + \nu_\mu + \bar{\nu_\mu} \tag{2.19}$$

The decay photons and synchrotron radiation produced by the leptons are energetic enough to cause electromagnetic cascades after interacting with the surrounding photon field. A cascade is formed when particle pairs are created in the interaction, which again causes the emission

of synchrotron radiation. The process is repeated iteratively until the energies are too low for pair production. The resulting emission from the cascades is one of the contributions to the high-energy SED bump. The synchrotron emission from protons and muons can also contribute.

Since the hadronic interactions produce neutrinos as a byproduct, blazars are a possible source of the astrophysical neutrino flux discovered by the IceCube Neutrino Observatory (IceCube Collaboration, 2013). IceCube also found a strong association between the arrival direction of a neutrino coincident with the location of the BL Lac TXS 0506+056, which was in a high flux state (IceCube Collaboration et al., 2018). A recent analysis of the arrival directions of astrophysical neutrinos showed evidence for neutrino emission from NGC 1068, a nearby active galaxy (IceCube Collaboration, 2022). NGC 1068 is a Seyfert Type 2 galaxy and has substantially different characteristics from a blazar such as TXS 0506+056. This suggests that there might be more than one population of sources contributing to the astrophysical neutrino flux. Future results from neutrino observatories might shed more light on the role of blazars as neutrino emitters and help to understand the contribution of hadronic scenarios to the observed MWL SEDs.

2.3.3 Relativstic effects

In blazars, the jet is aimed closely towards the observer's line of sight. If an emission region travels down the jet, relativistic effects such as Doppler boosting greatly alter the observed quantities (see, e.g., Appendix in Urry and Padovani, 1995). The distortion of the intrinsic behavior in the observer's frame is quantified by the Doppler factor δ. It depends on the Lorentz factor, $\Gamma = 1/\sqrt{1-\beta^2}$, which is intrinsic to the region and depends on the speed of the region $\beta = \frac{v}{c}$. The Doppler factor takes into account at which angle, θ, the region is viewed at:

$$\delta = \frac{1}{\Gamma(1-\beta\cos(\theta))} \tag{2.20}$$

The frequency of observed photons then changes linearly with the Doppler factor:

$$\nu = \delta\nu' \tag{2.21}$$

where ν' is the frequency in the source's frame and ν in the observers frame. Similarly, the observed time scale is converted as

$$\Delta t = \delta^{-1}\Delta t' \quad , \tag{2.22}$$

which leads to a shorter observed variability time scale, and can explain the observed minute time scale in some sources.

The observed energy spectrum, or SED, is amplified depending on the spectal index α of the SED ($F_{\nu'} \propto \nu'^{-\alpha}$) of the Doppler factor:

$$\nu F_\nu = \delta^{3+\alpha}\nu' F_{\nu'} \tag{2.23}$$

This can be translated into broadband fluxes by integrating over the frequency, which is boosted by another Doppler factor:

$$\nu F = \delta^4 \nu' F' \tag{2.24}$$

Lastly, one can derive the transformation for the observed variability, which is given by the change of flux in a given time period:

$$\frac{\Delta \nu F}{\Delta t} = \delta^5 \frac{\Delta \nu' F'}{\Delta t'} \tag{2.25}$$

This shows how strongly the observed flux and variability are altered by relativistic Doppler boosting and how sensitively they react to even small changes in the kinematics of the jet.

2.4 Markarian 421 - an archetypical TeV blazar

The aforementioned BL Lac Mrk421 is the main astrophysical source of interest in this thesis. It is one of the brightest and best-studied objects in the VHE sky. The high brightness across the full electromagnetic spectrum is partially due to its proximity with a redshift of $z = 0.031$ (de Vaucouleurs et al., 1991). This allows a study of the source with a variety of instruments with high precision. The source is also visible in states of high and low activity, which enables an unbiased and comprehensive monitoring of the source on short time scales down to below one hour. Most blazars are observable on such short time scales only during flaring states in the VHE. Otherwise, long integration times of several days to several months are required to extract significant signals. This causes an intrinsic bias in the data results and makes studies of the short-time variability impossible. As an archetypical BL Lac, Mrk 421 is an ideal target to study the underlying physics of TeV blazars.

The source was discovered by the astronomer Benjamin Markarian after building a catalog of galaxies with strong excesses in the ultraviolet emission (Markarian and Lipovetskij, 1972). In 1992, the Whipple Observatory detected TeV photons from Mrk 421, making it the first extra-galactic source of that energy range (Punch et al., 1992b). The subsequent Cherenkov telescopes such as the High Energy Gamma Ray Astronomy (HEGRA) telescopes continued to detect and observe the source in the following years (see, e.g. Petry et al., 1996; Aharonian et al., 2002). Since then, numerous detailed studies have been performed to characterize the source's broad-band emission across the full electromagnetic spectrum with a focus on VHE gamma rays and investigate its temporal evolution. Due to its position in the sky, the source is best observed by telescopes located on the northern hemisphere, such as the MAGIC telescopes and the Very Energetic Radiation Imaging Telescope Array System (VERTAS). This generation of telescopes allowed a characterization of the SED at the highest energies with much larger precision (see, e.g., Albert et al., 2007a; Abdo et al., 2011; Acciari et al., 2011; Ahnen et al., 2017b). Additionally, long-term studies spanning over multiple months to years investigated the source's temporal behavior and correlation among the energy bands, such as the well-established correlation between VHE gamma rays and the X-ray (see, e.g., Acciari et al., 2011; Aleksić et al., 2015a; Ahnen et al., 2016; MAGIC Collaboration et al., 2021). Further studies, investigated the behavior in great detail under quiescent states of low activity of Mrk 421 (Baloković et al., 2016; Acciari et al., 2021). On the contrary, the source also shows periods of extreme activity producing strong VHE gamma-ray flares. These observations revealed variability on extremely short time scales and varying correlation behaviors under states of extreme emission (see, e.g., Donnarumma et al., 2009; Acciari et al., 2020). This includes early 2010, which marks the

period in which the source showed its highest activity to date, including the largest flare ever observed (Abeysekara et al., 2020).

Despite these extensive efforts, many fundamental questions remain unanswered. One of them is the origin of the variability of blazars, which shows changes on the annual scale or down to the minute scale. It also remains open whether the blazar emission is primarily produced in a single region or if it occurs in multiple regions simultaneously. As discussed in the last section, the contributions of the different particle populations (leptonic vs. hadronic) to the broadband emission and the way in which these particles are accelerated are also still under debate.

Chapter 3

The MAGIC telescopes

MAGIC telescopes are a pair of IACTs on the Canary Island of La Palma. They are the main instruments used for the studies presented in this thesis. The following chapter will give a general introduction to ground-based gamma-ray observations with the IACT technique. Subsequently, the hardware of the MAGIC telescopes and the various steps of the data analysis will be described. Finally, a brief section discusses the challenges posed by the atmosphere.

3.1 Ground-based gamma-ray astronomy

Observing electromagnetic radiation from Earth entails the inherent difficulty of having the Earth's atmosphere along the line of sight. Figure 3.1 shows the atmospheric absorption of electromagnetic radiation for different wavelengths. In the radio and optical regime, observations from the ground are possible with few limitations. In the infrared and for wavelengths in and below the ultraviolet, direct observations from the ground are impossible because the radiation is absorbed by the atmosphere. This results in two main detection strategies for the observation

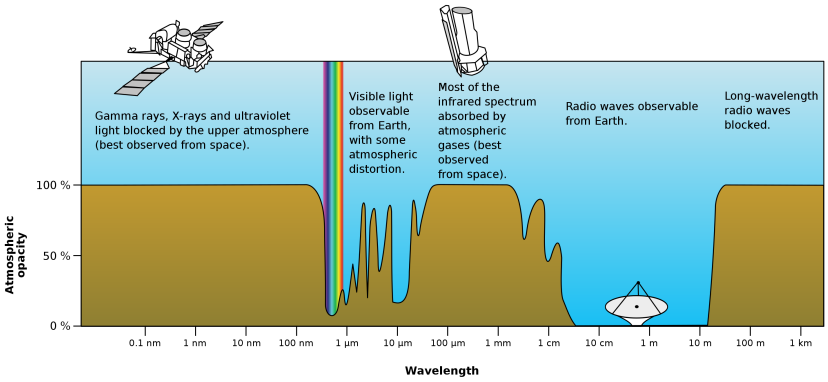

Figure 3.1: Atmospheric absorption of electromagnetic radiation as a function of wavelength (Credit: NASA, public domain).

of gamma rays: First, performing measurements above the atmosphere with space-based instruments mounted on satellites, or second, indirectly measuring incident gamma rays by observing extended air showers from the ground. The former is widely used to observe gamma rays between $\sim$100 keV up to several tens of GeV. At energies above 100 GeV, space-based instruments

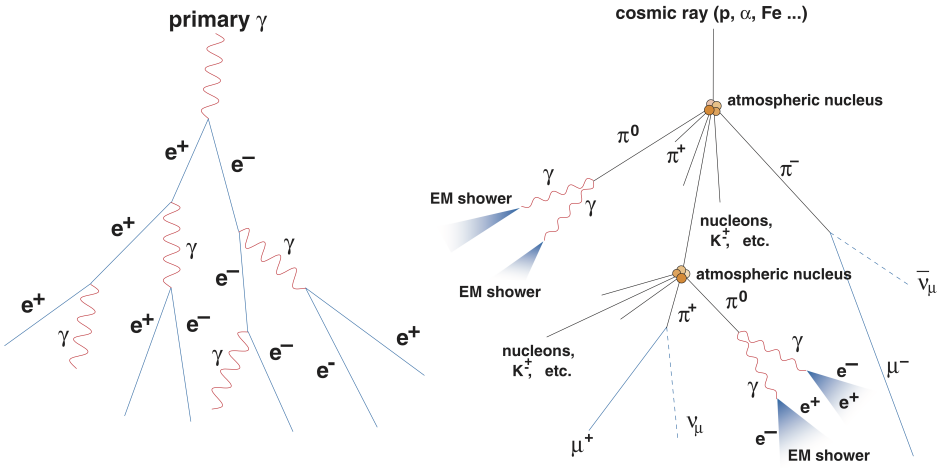

Figure 3.2: Schematic representation of the development of an electromagnetic (left) and hadronic (right) air shower (Otte, 2007).

are increasingly constrained by low event statistics due to the power-law decreasing fluxes with higher energies. The small spatial extent of space-based detectors ($\sim$m^2) results in a limited detection area, making collecting a sufficient number of events difficult or even impossible. For this reason, ground-based methods that use the atmosphere as a calorimeter and achieve effective areas in the order of km^2 are advantageous in detecting gamma rays with energies above 100 GeV, so-called very-high-energy (VHE) gamma rays.

3.1.1 Atmospheric air showers

When gamma or cosmic rays with sufficient energy ($\gtrsim$1 GeV) strike the atmosphere, they initiate a cascade of particles and radiation after their first interaction. High-energy photons will undergo a pair production process upon initial interaction with a nucleus in the atmosphere. The resulting electron and positron radiate photons via Bremsstrahlung, which again initiate pair production. The repetition of this chain of interactions creates a cascade-like electromagnetic air shower. The production of new particles comes to a halt once the energy loss due to ionization of the air is larger than the one due to Bremsstrahlung. The point is reached once the energy of the particles falls below the critical energy of $E_C \approx 85$ MeV. The left image of Figure 3.2 shows a schematic representation of the formation of an electromagnetic air shower.

If the primary particle is of a hadronic nature (protons or heavier nuclei); interactions via the strong force become possible. This leads to the production of mainly neutral and charged pions and other mesons and nucleons in the first interaction. In fact, some mesons were first discovered in hadronic air showers (e.g., the discovery of the kaon (Rochester and Butler, 1947)). The primary decay channel of neutral pions is into a pair of gamma rays, which then trigger electromagnetic subshowers. The charged pions can either trigger another hadronic cascade by interacting with atmospheric nuclei or decay into a muon and a muon neutrino. A schematic illustration of a hadronic air shower is seen in the right image of Figure 3.2.

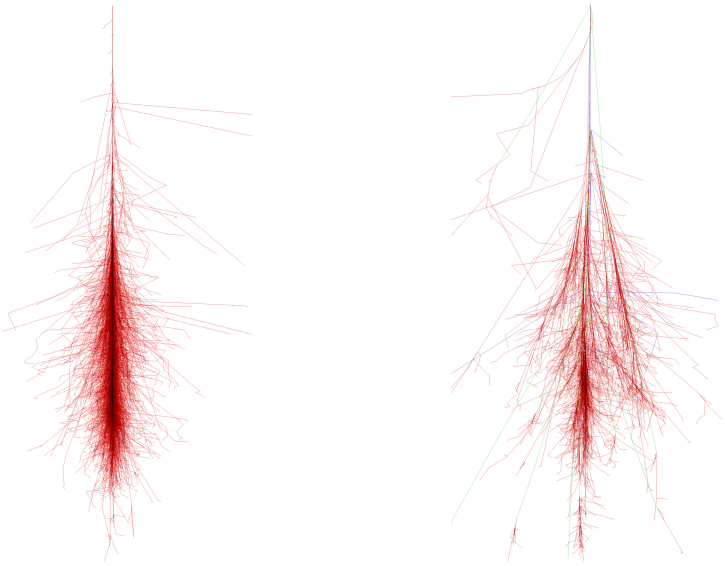

Figure 3.3: Images of simulated air showers using the software CORSIKA. Left: Electromagnetic shower induced by a 100 GeV gamma-ray. Right: hadronic shower induced by a 100 GeV proton (taken from Schmidt (2005)).

Due to the different mechanisms of particle production and shower evolution, electromagnetic and hadronic showers show different morphologies. Electromagnetic showers have a more uniform and tighter structure. Figure 3.3 on the left shows the results of a simulation of an electromagnetic air shower induced by a gamma ray with an energy of 100 GeV. The simulation is performed by the widely used software package CORSIKA (Heck et al., 1998). The shower shows a dense structure around the center line, with few particles scattering far from the ellipse around the center. Due to the possible formation of electromagnetic subshowers in hadronic showers, the overall structure is much more scattered and fragmented (see right image in Figure 3.3). This different morphology can be used to distinguish between primary gamma rays and cosmic rays initiating the shower.

3.1.2 Imaging Atmospheric Cherenkov Telescope technique

Two main strategies are used to detect atmospheric air showers: First, one can directly detect the charged particles produced in the shower. So-called extensive air shower arrays exploit this technique by placing particle detectors over a wide area at high altitudes. This allows the detection of gamma rays with energies well above 1 TeV, but at the cost of a poorer angular resolution and lower signal-background seperation. Second, the charged particles can also be detected via the subsequent production of Cherenkov radiation.

Cherenkov radiation was first discovered by P. Cherenkov and S. Vavilov in 1934 (Cherenkov, 1934). I. Frank and I. Tamm provided an explanation of the effect in 1937 (Frank and Tamm, 1937). Cherenkov light is emitted when a charged particle travels through a medium faster than the speed of light in that medium. A slow-moving charged particle will cause a fully isotropic polarization of the surrounding medium. Once the particle exceeds the medium's light speed,

Figure 3.4: The MAGIC telescopes at sunset (Credit: Giovanni Ceribella, 2019)

the surrounding dipoles will polarize asymmetrically, causing a constructive interference of the varying dipole moments. As a result, a conical wavefront with an opening angle θ forms, given by:

$$\cos\theta = \frac{1}{n\beta} \quad , \tag{3.1}$$

where n is the refractive index depending on the altitude and $\beta \approx 1$ for highly relativistic particles.

All newly produced particles in atmospheric air showers have energies above the previously mentioned critical energy of 85 MeV. This lies well above the lower limit required for producing Cherenkov light; therefore, every particle emits Cherenkov radiation. The superposition of all individual emitting particles forms a circular-shaped light pool where the overall majority of light is cast within a radius of 120 m given vertical incidence. Since every particle contributes to the general light pool, the total amount of Cherenkov light emitted is proportional to the number of particles produced, which is proportional to the primary particle's energy. Air showers are rather faint, and the emission of Cherenkov light happens on the scale of nanoseconds. To successfully detect these showers, IACTs employ large segmented optical mirrors providing a large light collection area to image the air showers onto a camera. The camera must have a high light sensitivity and a time resolution down to nanoseconds. These are the basic requirements for IACTs, and the technical implementation in the case of the MAGIC telescopes is presented in more detail in the following sections.

3.2 The hardware of the MAGIC telescopes

The MAGIC telescopes are composed of two IACTs (MAGIC I and MAGIC II) located at an altitude of around 2200 m above sea level at the Observatorio Astrofisico del Roque de los Mucha-

chos (ORM) on the Canary island of La Palma (see Figure 3.4). They started scientific operations in 2004 and 2009, respectively.

3.2.1 Structure

The telescopes are placed at a distance of around 85 m from each other. The underlying structure consists of a base fork made from steel tubes mounted on a circular rail, allowing rotation in the azimuth direction. The fork holds the optical dish made from carbon fiber tubes to minimize the overall weight. The optical dish can be rotated in a zenith direction. Due to the choice of carbon-fiber-reinforced polymers as the primary material for the tubes of the telescope dish, the weight of the total telescope only amounts to around 65 t. This enables repositioning of the telescope to any location in the sky in around 30 s. This is especially important for the follow-up observation of short transient events like gamma-ray bursts. The optical dish holds 247 mirrors with a reflective area of 1 m^2 each. Individual mirrors have spherical surfaces of varying radii to approximate an overall parabolic shape of the mirror dish. Since the telescope structure bends slightly under its gravitational load, depending on the altitude angle of the telescope dish, an active mirror control adjusts the individual mirrors and compensates for this effect (Biland et al., 2008). This way, the focal point of the parabolic mirror dish on the camera surface can be minimized.

3.2.2 Camera

Both telescope cameras are mounted on an aluminum arch supported by steel ropes. The cameras consist of 1039 1-inch photo-multiplier tubes (PMTs) (Aleksić et al., 2016b). Each PMT has a hexagonal Winston cone to close gaps between the circular PMTs and guide the light toward the photosensitive area. Each pixel has a field of view (FoV) of 0.1°, resulting in an overall FoV of the camera of 3.5°.

3.2.3 Data taking

The electrical signal from the PMTs is converted to an optical signal and gets transferred via optical fiber cables to the Counting House, where the data is processed, and the telescopes are also controlled. The optical signal is converted back into an electrical signal by receiver boards. The subsequent readout (Aleksić et al., 2016b) is based on Domino Ring Sampler version 4 (DRS4) analog memories. The DRS4 comprises an array of 1024 switching capacitors for each channel, sampling the analog signals coming from the receiver boards. The sampling rate is set to 1.64 GHz. In the event of a trigger, the analog signal sampling stops, and the capacitors' charges are read out with an analog-to-digital converter on a region-of-interest of 50 capacitors, i.e., time samples. This corresponds to a time window of around 30 ns and a resulting dead time of 26 μs.

For an event to trigger the readout, several criteria need to be met in the form of trigger levels. The L0 trigger gives the first trigger level. It is triggered once individual pixels in the inner part of the camera reach a given Discriminator Threshold (DT). The DT depends on the night-sky background level as well as the individual sensitivity of the pixel. Afterward, the L1 trigger looks

for neighboring pixels passing the L0 trigger. Under regular observations, a three-next-neighbor (3NN) logic is applied. If necessary, a 2NN or 4NN trigger can also be used. The successful L1 trigger, done independently by the two telescopes, is then fed into the L3 trigger, which checks for coincident events. The L1 signal of each telescope is stretched by 100 ns and is adjusted for different arrival times between the telescopes before checking for the time coincidence, which would fire the L3 trigger. If the event passes the L3 trigger, the readout finally writes the digitized event to the disk.

Observations by MAGIC are performed in so-called wobble mode (Fomin et al., 1994). The telescopes do not point directly at the observed source but with a slight angular offset. Under regular operation, that offset is 0.4°. The off-center observation allows the simultaneous extraction of an ON region and a symmetric OFF region in the camera FoV, which will be important later for signal detection. Every 20 min, the pointing rotates around the source in a fixed pattern of four points 90° apart. This also averages out potential instrumental inhomogeneities of the camera acceptance.

3.3 Analysis of MAGIC data

In the following sections, the analysis is described starting from triggered events. It is performed using the MAGIC Analysis and Reconstruction Software (MARS) (Zanin et al., 2013a).

3.3.1 Extraction, cleaning and characterization of events

Before writing the capacitor charges, the pedestal (i.e., signal baseline taken at the beginning of each night) is subtracted. The charge is read out within a sliding window, covering five continuous time samples. The window with the largest charge is saved with the arrival time given by a count-weighted average over the time samples (Albert et al., 2008). The counts are then converted to photoelectron units (phe). Specific events are created by illuminating the camera with short laser pulses from the center of the mirror dish to obtain the conversion factors. The final camera images are then defined by the charge and arrival time of all individual pixels.

Once the signal is extracted in terms of charge and time, the image is cleaned to remove pixels from the image that are not associated with the event but contain charge originating from the background of the night sky. This ensures that the parametrization of the image is not influenced by strong outliers of the image. The image from a gamma-ray-induced air shower is expected to show a compact elliptical shape. A multi-step process determines first the core part of the ellipse. The algorithm looks for groups of neighboring pixels reaching a certain cleaning level in the form of a charge threshold. Pixels neighboring the core pixels are included as boundary pixels if their charge also matches a certain cleaning level that is lower than that of the core pixels. Not-associated pixels are removed based on proximity, charge, and time information. The background of an image can vary significantly depending on the night-sky conditions, i.e., the moon's brightness. The appropriate charge thresholds, therefore, depend on the moon's brightness, and analyzing affected data requires increased cleaning levels. Since all data analyzed for this work were taken under *dark* conditions, further peculiarities of the analysis of data taken under bright moonlight will not be discussed. For more information see (Ahnen

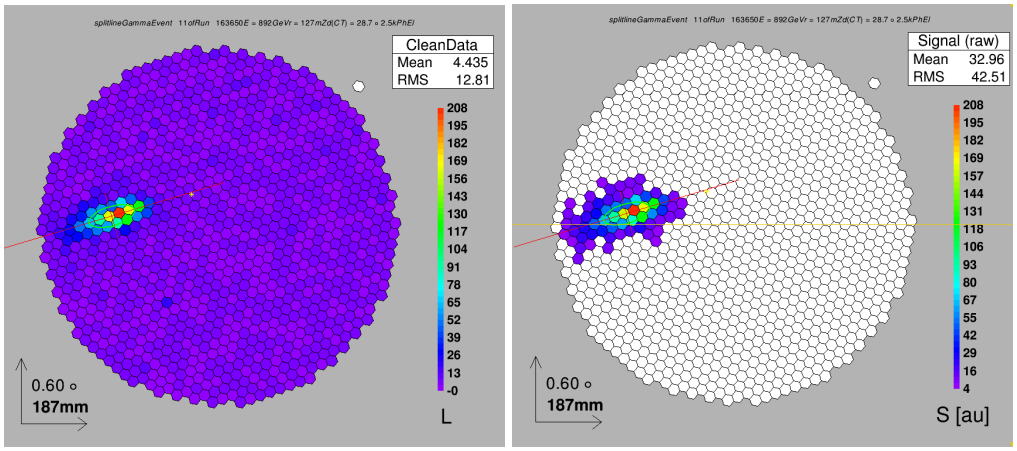

Figure 3.5: Example of a gamma-ray event before cleaning (left) and after cleaning (right).

et al., 2017c). An example of a gamma-ray event taken under dark conditions before and after the image cleaning can be seen in Figure 3.5.

To extract the physical information from an event later, given the energy, direction, and gamma/hadron separation, the images are parameterized by a list of features. These parameters are called "Hillas parameters" and were first introduced by Michael Hillas in 1985 (Hillas, 1985a). In the analysis of MAGIC data, the original list of parameters was expanded to include a more comprehensive list of features (the list is taken from internal documentation):

- *Size*: Overall number of photoelectrons in the image.
- *CoG*: The Center of Gravity (CoG) is the position of the weighted mean signal in the camera.
- *length*: Root Mean Square (RMS) spread along the shower axis.
- *width*: RMS spread perpendicular to the shower axis.
- *Conc-n*: The fraction of photoelectrons in the n brightest pixels of the image.
- *Leakage 1/2*: Fraction of signal distributed in the outermost camera ring/two outermost camera rings with respect to the total image size
- *M3long*: Third longitudinal momentum of the image along the major shower axis of the ellipse.
- *Asym*: Difference between the pixel with the highest charge and the CoG.
- *Number of islands*: Number of distinct groups of pixels in the image.

Some of the Hillas parameters are visualized in Figure 3.6. Additionally, there are parameters depending on the position of the observed source:

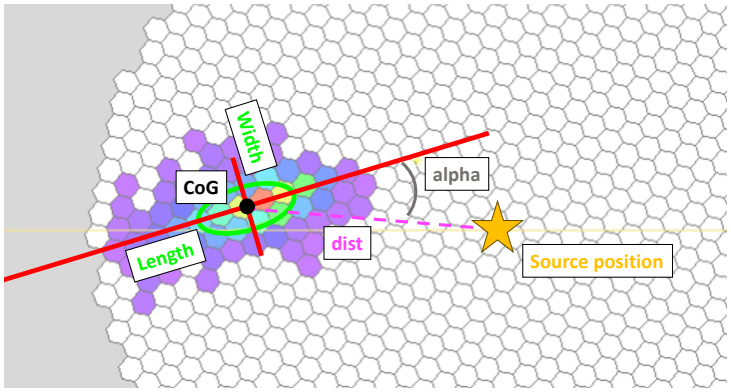

Figure 3.6: Sketch of a few selected Hillas parameters used to characterize events.

- *alpha*: The angle between the major axis and the line between the CoG and the source position.
- *Dist*: The distance of the image CoG to the source position.

Lastly, two parameters take into account the arrival time of the photoelectrons:

- *Time-Gradient*: The slope of the arrival times of all pixels projected on the major axis.
- *Time-RMS*: The RMS of the arrival times of all pixels.

These parameters are extracted from the images of the two individual telescopes. To exploit the stereoscopic observation of two telescopes, additional parameters are defined, which are especially relevant for the later reconstruction of the direction of the gamma ray:

- *Shower axis direction*: Crossing point of the major axes of both telescope images after laying them on each other.
- *Impact point*: The reconstructed point of the shower impact can be calculated by taking the crossing point of both major axes after prolongation.
- *Impact parameters*: The distance between the shower axis and the telescope positions.
- *Height of the shower max*: The reconstructed altitude where the shower reaches the highest number of particles. It is derived from the shower axis and the CoG.
- *Cherenkov radius*: The radius at the ground level of the Cherenkov ring produced by a 86 MeV electron emitted at the shower max.
- *Cherenkov density*: The photon density at the ground produced by the same electron.

The geometric reconstruction of the shower axis direction and the impact point is shown in Figure 3.7.

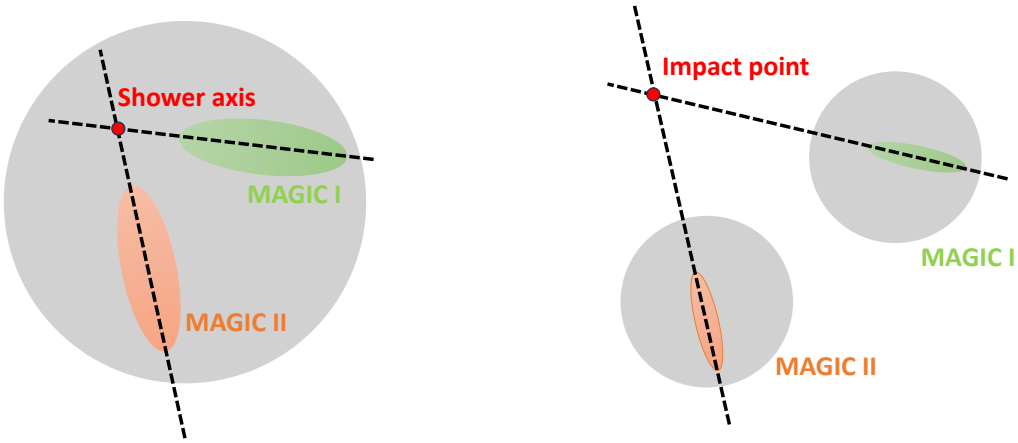

Figure 3.7: Sketch of the stereoscopic parameter reconstruction. The reconstruction of the shower axis after superimposing both camera images can be seen in the left image. On the right, the reconstruction of the impact point by crossing the prolonged major axes of both camera images separately is shown.

3.3.2 Event reconstruction

The full list of features is then reduced to only three properties characterizing the event:

- The type of event (gamma ray or hadronic background)
- The energy of the primary particle
- The direction of the primary particle

All relevant high-level results can be obtained with estimations of these three properties.

Gamma-hadron separation

To construct high-level results, the signal events originating from gamma rays must be separated from the background events of hadronic origin. Even when observing bright gamma-ray sources, the vast majority of events detected by IACTs are hadronic background events. This means that less than 1 out of 1000 events originates from a primary gamma ray for most sources. The machine learning technique Random Forest (RF) is used to estimate the type of event (Aleksić et al., 2016c). The RF builds a collection of binary decision trees and takes the previously presented list of image parameters as input. As with any machine learning algorithm training, a training set must be created first. For the signal events, dedicated Monte-Carlo (MC) simulations produce images solely originating from gamma rays (Majumdar et al., 2005). The MC simulations replicate the entire observation process. First, atmospheric air showers and the emission of Cherenkov light are generated with the CORSIKA software package (Heck et al.,

1998). Subsequently, the reflection of the Cherenkov photons on the mirror surface is simulated to determine their resulting position on the camera. Finally, the camera's response and data acquisition are simulated to obtain images as close to reality as possible. This way, a data set of only gamma-ray-like events is created. Real observations containing as few gamma rays as possible are used for the hadronic background events. This can be observations of spots in the sky with no known gamma-ray sources or very faint sources. The RF is then trained to estimate the so-called *hadroness*, that is a parameter between 0 and 1, indicating the confidence that an event is of hadronic origin. A hadroness cut is applied to separate gamma-like from hadron-like events in the final analysis.

Energy reconstruction

Next, the energy of the primary particle is reconstructed. In the first order, the energy is proportional to the number of particles created in an air shower and, with that, to the number of Cherenkov photons. Hence, the *size* parameter is the most influential parameter, but other geometric parameters such as the impact point or Cherenkov radius and density are also taken into account. The energy estimation can be performed in two ways: The traditional well-established method uses Look-Up Tables (LUTs) (Aleksić et al., 2012). An individual LUT is created from the MC simulations for each telescope by binning the events in a multi-dimensional table based on the relevant parameters. The average between both telescopes is taken for the final estimate of the energy. The second and newer method uses an RF (Ishio and Paneque, 2024), resulting in a slightly more accurate energy reconstruction. Both methods were utilized for this work. Results shown in chapter 5 were obtained using the LUT method, whereas all other results rely on the RF method.

Direction reconstruction

Lastly, the direction of the event is reconstructed. Naively, one can reconstruct the original direction by taking the crossing point of the two major axes. The crossing point can, however, fluctuate strongly in the case of a small angle between the two axes, which makes the reconstruction very sensitive to small uncertainties. The favored method is, therefore, the *DISP*-method, which also takes into account the timing and shape information of the image (Aleksić et al., 2016c). The DISP parameter describes the distance between the CoG and an assumed source position along the major axis. Two RFs estimate the DISP for real data after being trained on MC data with a known DISP parameter. Since the source position is assumed to be on the line of the major axis, two possible positions are reconstructed. To resolve the ambiguity, the images from both telescopes are again superimposed, and the distances between all possible source positions are computed. The two points with the shortest distance between them are selected. A sketch of the stereoscopic DISP method is shown in Figure 3.8. 1A and 1B show the two possible source positions after the RF estimates the DISP for MAGIC I. 2A and 2B show the corresponding positions from MAGIC II. Since the distance between 1B and 2B is the smallest, those points are selected. The final estimate of the source position is then given by the average between the two points, 1B and 2B, in the given example.

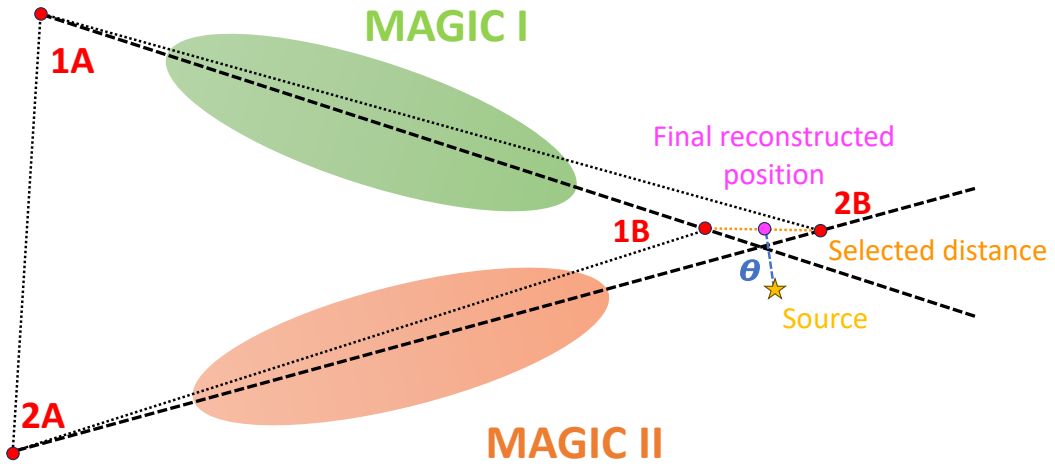

Figure 3.8: Sketch of the stereoscopic DISP-method. The reconstructed positions by the DISP RFs (1A, 1B, 2A, 2B) are shown as red circles. The dotted lines show the distances between all four positions, with the shortest one marked in orange. The final reconstructed position is shown in pink as the average of 1B and 2B. The true source position is marked with a star and enables the computation of the angular distance θ shown in blue.

After estimating the source position, a new parameter θ can be constructed. It is the angular distance between the reconstructed position and the nominal assumed position of the gamma-ray source. Later on, it will be used to further discriminate between signal and background events.

3.3.3 High-level analysis

After the reconstruction of each event for a particular observation, high-level observational results can finally be obtained.

Signal detection

As a first step, it is evaluated if the data sample contains a significant signal. To assess whether a source emits a significant number of signal events against the strong background, the number of excess photons from the source region must be calculated. The source region is defined by using the previously introduced θ-parameter. The events are binned in one dimension in θ^2, and only events below a certain θ^2-cut are considered close enough to the assumed source position to be included. As mentioned in a previous section, the MAGIC telescopes observe in wobble mode, where several OFF regions are observed simultaneously. The center of another OFF region can now be treated as a reference point, and again, events are selected with the same θ^2-cut. Integrating the surviving number of events for both regions gives the number of events in the signal region N_{ON} and the number of events in the OFF region N_{OFF}. The number of excess photons is then given by:

$$N_{\mathrm{exc}} = N_{\mathrm{ON}} - \alpha N_{\mathrm{OFF}} \tag{3.2}$$

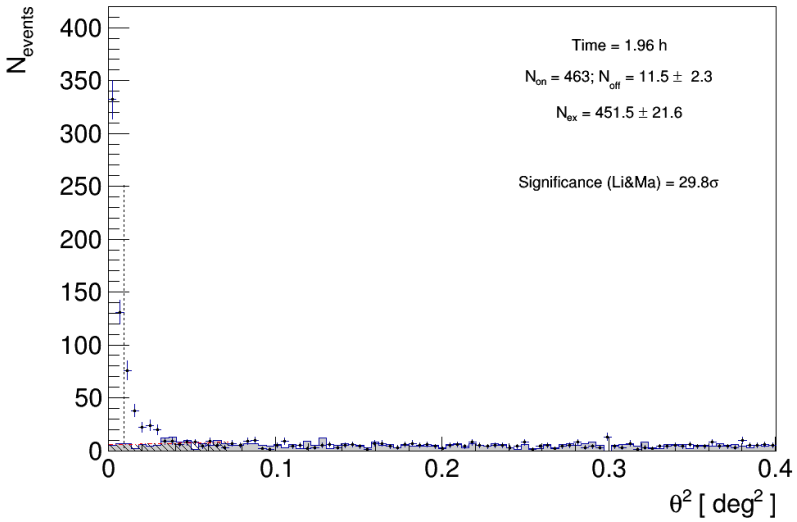

Figure 3.9: Example of a θ^2-histogram. The data set was obtained from observations of the Crab Nebula in January 2022. The histogram shows a strongly rising excess of events at low values of θ^2.

To account for the number of simultaneous OFF regions, α is defined as 1/(number of OFF regions). Finally, one can compute the significance of the signal using the expression defined by formula 17 of Li and Ma (1983):

$$\sigma = \sqrt{2\left(N_{\mathrm{ON}} \ln\left[\frac{1+\alpha}{\alpha}\left(\frac{N_{\mathrm{ON}}}{N_{\mathrm{ON}}-N_{\mathrm{OFF}}}\right)\right] + N_{\mathrm{OFF}} \ln\left[(1+\alpha)\left(\frac{N_{\mathrm{OFF}}}{N_{\mathrm{ON}}-N_{\mathrm{OFF}}}\right)\right]\right)} \tag{3.3}$$

An example of an θ^2 histogram is shown in Figure 3.9. In the example, the Crab Nebula is detected with a significance of almost $30\,\sigma$.

Spectrum and light curve

In this work, only point sources are analyzed, i.e., the gamma-ray sources have such a small spatial extent that the structure cannot be resolved with the angular resolution of MAGIC. Thus, only the energy and timing of events are the relevant parameters for obtaining results. The most crucial high-level result for this work is the differential spectrum. It is given by the number of photons per unit of energy, time, and area:

$$\frac{\mathrm{d}\phi}{\mathrm{d}E} = \frac{\mathrm{d}N(E)}{\mathrm{d}E\,\mathrm{d}A_{eff}(E)\,\mathrm{d}t} \quad [\mathrm{cm}^{-2}\,\mathrm{s}^{-1}\,\mathrm{TeV}^{-1}] \tag{3.4}$$

The number of photons $N(E)$ is given by the excess events N_{exc} within the energy range E. The *effective area* $A_{eff}(E)$ combines the geometric area covered by the telescopes with the detection probability. It is the equivalent area of a detector with an assumed detection probability of 100%.

It is calculated by simulating MC events and comparing the number of detected events N_{det} with the number of simulated ones N_{sim} within the simulated area on the ground A_{sim}:

$$A_{eff}(E) = A_{sim}(E)\,\frac{N_{det}(E)}{N_{sim}(E)} \tag{3.5}$$

The effective area depends on the event's energy since the detection probability decreases with lower energies due to the lower number of Cherenkov photons. It also depends on the observational zenith angle. Due to a larger angle, the Cherenkov light from the shower particles transverses more atmosphere, enlarging the Cherenkov light pool at the ground. However, the longer path in the atmosphere also leads to a stronger absorption of the photons. The result is a decreasing effective area for low energies up to around 300 GeV, but an increasing one at larger energies for higher zeniths.

The time interval in the differential spectrum is given by a source's *effective observation time*. This is the overall observation time, but it accounts for gaps in the observation and the dead time after recording an event. It is determined by sampling the distributions of arrival times to obtain the event rate. The total number of events divided by the event rate yields the effective time.

The differential spectrum is often converted into a spectral energy distribution (SED). It is obtained by multiplying the energy of the corresponding bin squared with the spectrum: $E^2\,\frac{d\phi}{dE}$. This corresponds to the energy flux of the source in units of $\mathrm{TeV\,cm^{-2}\,s^{-1}}$. It shows each waveband's relative contribution to the source's total energy output.

Once the differential spectrum is estimated, the integral flux in a given energy range can be easily obtained:

$$\phi = \int_{E_1}^{E_2} \frac{\mathrm{d}\phi}{\mathrm{d}E} \tag{3.6}$$

The time evolution of the integral flux ϕ over time is referred to as a light curve.

Up to this point, the used energy E refers to the estimated energy from the LUT or RF. Because the detector is non-ideal, this initial energy estimation has a limited resolution in the order of 15%-25% (Aleksić et al., 2016c) depending on the energy. This leads to events ending up in bins of estimated energy, which do not match their true energy. The resulting migration of events leads to an overall distortion of the spectrum, which has to be corrected by performing a so-called unfolding procedure.

There are two main unfolding methods: In the first method, a migration matrix $M_{i,j}$ is obtained from MC events. It describes the probability of events from true energy bin j migrating to an estimated energy bin i. Ideally, one can now invert the matrix and apply it to observational data. Since the inversion of the matrix is not always possible, it is obtained by a Chi-square minimization. To stabilize the minimization, a regularization term is introduced. There are several options to regularize the expression. More details on the different regularization methods and the unfolding procedure can be found in Albert et al. (2007c).

The second method is the so-called *forward unfolding*. An assumed spectral shape is multiplied by the effective area and time. A further convolution with the migration matrix predicts the number of events in bins of estimated energy. Using a maximum likelihood approach, the difference between the predicted and real number of events per bin is minimized regarding the parameters of the assumed spectral shape. This results in a model-based fit of the spectrum, but no set of uncorrelated spectral points can be obtained.

Spectral points in this work were obtained using the first method (with Tikhonov regularization as described in Albert et al. (2007c)), whereas spectral fits were obtained with a forward unfolding approach.

3.4 The influence of the atmosphere

As previously noted, MAGIC is located at the ORM on the island of La Palma. The ORM is one of the best astronomical sites in the Northern Hemisphere. The primary reasons are the weather conditions at the Canary Islands, which give rise to exceptional dust-free and dry air and provide good sky transparency throughout the year (Puerto-Giménez et al., 2013). Nevertheless, the site can exhibit certain weather phenomena that negatively affect the atmospheric quality. With a latitude of around 28°, the island is located between two large atmospheric cells, the Hadley cell in the southern direction and the Mid-altitude cell or Ferrel cell in the northern direction. The rotation of these cells gives rise to the prevailing wind direction. Until a latitude of 30°, trade winds from the eastern direction dominate, which are stronger during summer and can further extend North. Between around 30° and 60°, the Westerlies dominate, which are strongest during the winter. La Palma is located at the border of both phenomena and is seasonally influenced by both. Another consequence of the atmospheric circulation is a temperature inversion layer at an altitude of around 1300 m (Puerto-Giménez et al., 2013), where a wide sea of stratocumulus clouds can appear. Below this layer is moist maritime air, whereas above it, the air is dry and free of clouds. During winter, the Westerlies can cause higher clouds at all altitudes. During summer, the trade winds tend to bring large amounts of Saharan dust to the island, giving rise to a higher aerosol concentration in the sky at lower altitudes. This is referred to as calima.

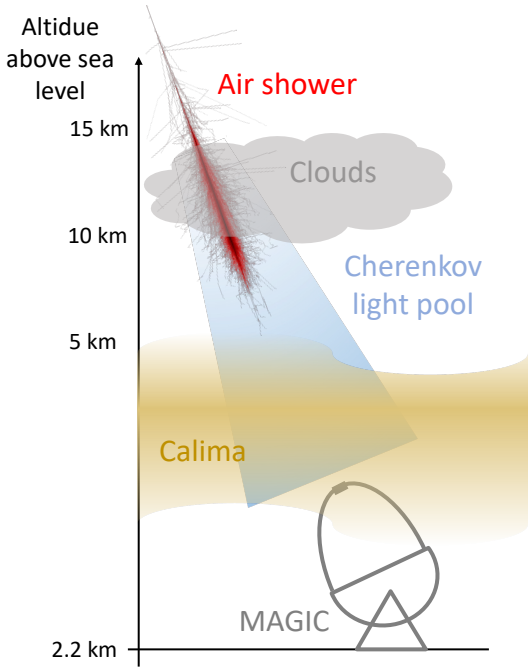

Figure 3.10: Sketch of the influence of aerosols on the IACT method.

The atmospheric composition up to an altitude of around 20 km, where the density is largest, has the highest influence on the observation of gamma-ray showers with IACTs. Both described phenomena, clouds and calima, increase the aerosol content in the atmosphere and, with that, the absorption of Cherenkov light. Figure 3.10 shows a sketch of the absorption of Cherenkov light by clouds and calima. A resulting loss of photons can significantly impair the accuracy of the event reconstructing of the primary gamma rays. The reduced number of Cherenkov pho-

tons emitted by a given air shower makes the shower appear less luminous compared to perfect atmospheric conditions. As already noted, the total light yield of a shower is proportional to the energy of the primary particle. A smaller number of detected photons leads to an underestimation of the reconstructed energy of the primary gamma ray. Additionally, the impaired transmission can affect the trigger efficiency of the telescopes since the lower light yield leads to a less luminous image on the camera, which might prevent a telescope from triggering an event it would have triggered under clear atmospheric conditions. This modifies the detection probability and, with that, reduces the effective area. In addition, partial sky coverage by clouds can also lead to a distortion of the projected image of the air shower. The gamma-hadron separation can then be impaired, which leads to a worse overall event reconstruction. For all the above reasons, IACTs need to implement methods of atmospheric monitoring.

Chapter 4

The MAGIC LIDAR

During the operation of the MAGIC telescopes, various instruments are used to monitor the atmosphere. These include instruments to measure basic weather parameters, such as temperature, wind speed, or humidity. They are mandatory to determine if the weather conditions still allow the safe operation of the telescopes. Additionally, a pyrometer measures the temperature of the sky, which can be used to determine the presence of clouds. This allows a later quality selection of the data during the analysis but does not provide sufficient information to correct atmospherically impaired data. To enable an accurate correction of IACT data, it is imperative to have range-resolved information on atmospheric transmission. For that reason, the MAGIC collaboration is operating a LIDAR system (see Figure 4.1), allowing a precise characterization of the atmospheric transmission and, with that, the correction of impaired IACT data.

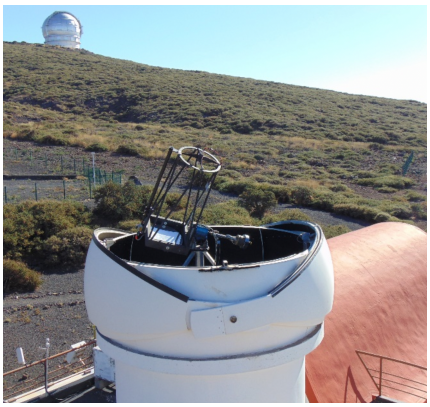

Figure 4.1: The MAGIC LIDAR.

This chapter describes the hardware of the MAGIC LIDAR, followed by an outline of the analysis of its data and a correction method for IACT data. Parts of the method description and images were previously published in Schmuckermaier et al. (2023). The text and structure of this chapter closely follow Schmuckermaier et al. (2023) in parts. Parts of the methods have been developed and shown in previous work (Fruck, 2015; Fruck et al., 2022a, 2013) and were developed further in Schmuckermaier et al. (2023).

4.1 The hardware of the LIDAR

The core principle of a LIDAR is the same as that of a RADAR but in the optical wavelength range. A laser shoots close to the observation direction of MAGIC. The light from the laser scatters across its path with molecules and aerosols in the atmosphere. The scattering occurs isotropically, and part of the light will be backscattered at 180°. A mirror collects the backscattered light and focuses it into a photodetector. Arrival time information and intensity of the backscattered light are then used to extract an atmospheric profile of the transmission.

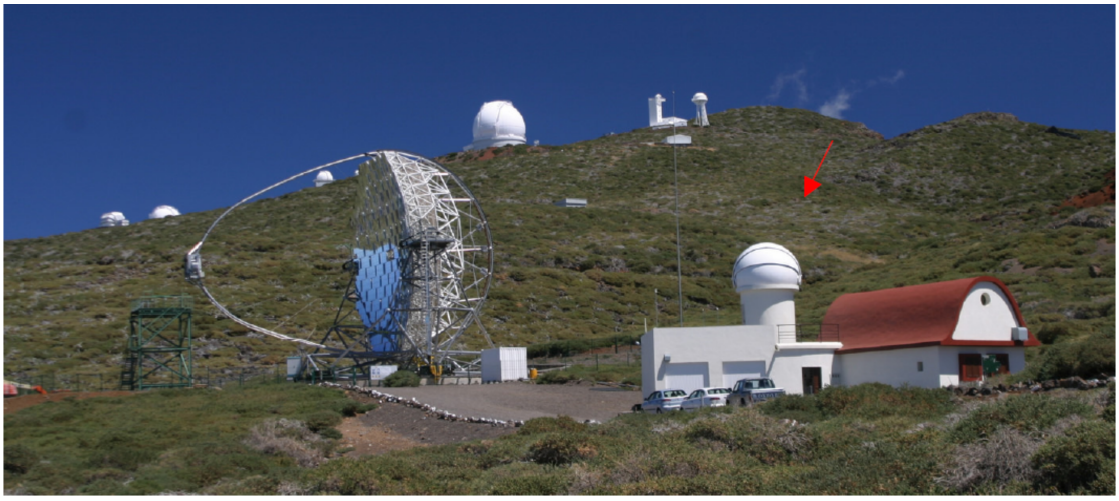

Figure 4.2: The LIDAR tower with the protective dome on top of the MAGIC counting house.

4.1.1 Structure

The LIDAR sits inside an elevated, protective dome next to the MAGIC telescopes (see Figure 4.2). The tower under the dome houses the power supplies and control for the systems located inside the dome. This includes the control of the laser, the control of the telescope mount, the supply voltage of the photodetector, and the PC coordinating all subsystems and reading out the data. A CAD image showing all components in the dome is shown in Figure 4.3. The telescope frame sits on a commercially available equatorial mount, the *ASTELCO NTM 500*. It is elevated by 33 cm by solid steel beams. The telescope frame is a custom-made welded aluminum frame with a matt black coating to minimize light reflectance. The frame has a length of around 160 cm and a width at the squared bottom of about 72 cm. The laser mount is attached to the outside of the frame. Since the renewal of the mirror and the laser mount are part of the hardware upgrades I performed, a detailed description of these components is given in the appendix in section A.1 and A.2.

4.1.2 Light emission and data acquisition

The laser mount carries a passively Q-switched Nd:YAG laser firing pulses of 25 μJ energy. The laser is operated at a repetition rate of 250 Hz. The intrinsic wavelength of a Nd:YAG of 1064 nm is halved using a non-linear optical material. The resulting wavelength of 532 nm is much closer to the peak wavelength of the Cherenkov spectrum produced by atmospheric air showers. Optimally, the wavelength of the laser is identical to the Cherenkov peak wavelength to allow characterization of the atmosphere at the same wavelength. Since this peak is in the UV range, it is not visible to the human eye, which poses some safety and practicality issues. The laser beam then enters a beam expander, which widens the beam width by a factor of 20. This reduces the beam divergence to around 0.6 mrad (full angle). A guidance tube with baffle rings inside directly screwed onto the beam expander minimizes any remaining stray light. A borosilicate glass mirror collects the backscattered part of the light with a diameter of 61 cm and

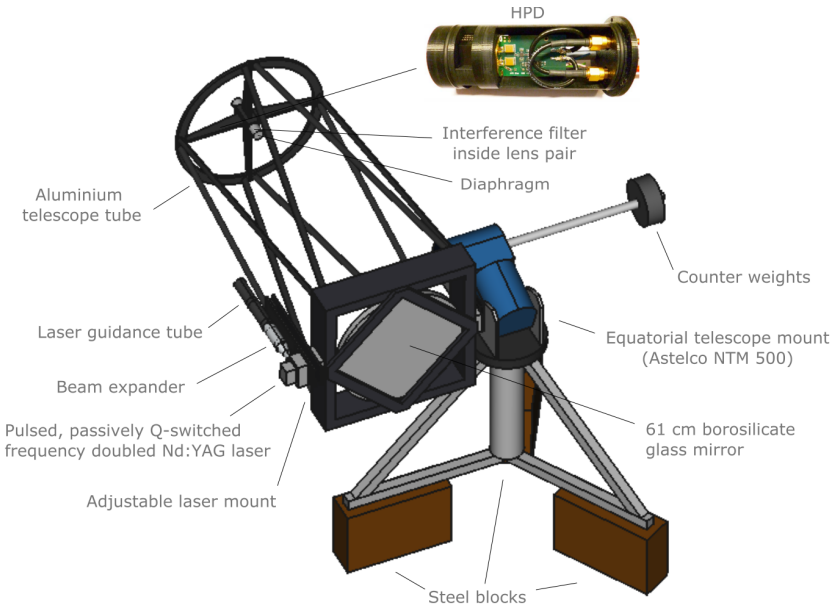

Figure 4.3: CAD image of the LIDAR hardware.

a focal length of 150 cm. The detector element sits in the focal points. A diaphragm with an aperture of around 6 mm at the entrance of the detector reduces any background light from the night sky. Before the photodetector itself, a lens parallelizes the light. A subsequent interference filter around 532 nm further reduces the night sky background's light by over a factor of 100. A second lens focuses the light again and enters a hybrid photodetector (HPD). A Hamamatsu R9792U-40 HPD is used, which has a quantum efficiency of around 50% at 532 nm (Orito et al., 2009). The HPD requires a bias voltage of 400 V supplying the incorporated avalanche diode and a high voltage of 8 kV to accelerate electrons from the photocathode to the diode. The detector element pre-amplifies the signal before transmitting it to the PC. In the PC, an FADC card registers the signal. Two algorithms then analyze the digital signal to count detected photoelectrons. For photons registered at long distances above around 4.5 km above the LIDAR, the first algorithm looks for individual peaks caused by single photoelectrons. For closer distances, photoelectron events overlap, and a second algorithm integrates the waveform and divides it by the charge of a single photoelectron to determine the count number.

4.1.3 Operations

A LabVIEW program controls all components of the LIDAR and the data collection. A user interface (see Figure 4.4) allows the shifters of the MAGIC telescope to access all relevant functions. During regular observations of the MAGIC telescopes, the LIDAR follows the observation coordinates with an offset of $\sim 5°$. This ensures that the laser beam does not cross the FoV of MAGIC. To obtain a single profile, the LIDAR fires 25000 shots. At 250 Hz, this takes 100 s followed by some computing time used for the profile extraction. This way, a profile can be ob-

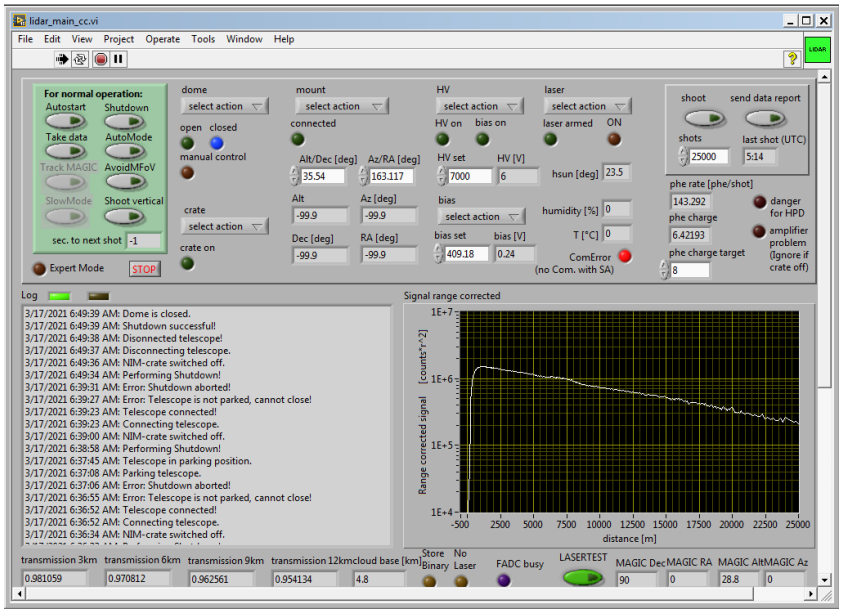

Figure 4.4: A screenshot of the LabVIEW program to control all components of the LIDAR.

tained every 4 min, allowing quasi-continuous monitoring of the atmosphere in the observation direction of MAGIC.

4.2 Analysis of LIDAR data

4.2.1 The LIDAR equation

The data obtained by the LIDAR is given as the number of backscattered photons per time interval. Due to the constant and known speed of light in the atmosphere, this can be converted into the number of photons per distance $\frac{\mathrm{d}N}{\mathrm{d}r}$. A parameterized expression for this term is given by the *LIDAR equation* (description and explanation taken from Fruck et al. (2022a) and Fruck (2015)):

$$\frac{\mathrm{d}N}{\mathrm{d}r} = N_0 C_F G(r) \frac{A}{r^2} \beta(r) \exp\left(-2 \int_0^r \alpha(r') \mathrm{d}r'\right) \tag{4.1}$$

The initial number of emitted photons is given by N_0, and C_F is a general calibration factor. It incorporates several parameters like the mirror reflectivity and the detection efficiency of the photodetector. $G(r)$ is the geometric factor parameterizing the overlap between the FoV of the telescope and the laser beam. $G(r)$ is small at short distances but rises to 1 quickly for larger distances when full overlap is reached (usually at around 500 m). $\frac{A}{r^2}$ describes the covered solid angle by the system. $\alpha(r)$ describes the extinction coefficient in the atmosphere, whereas $\beta(r)$ is the backscatter coefficient. Both parameters have a molecular and an aerosol component that is $\alpha(r) = \alpha_{\mathrm{mol}}(r) + \alpha_{\mathrm{aer}}(r)$ and $\beta(r) = \beta_{\mathrm{mol}}(r) + \beta_{\mathrm{aer}}(r)$.

The LIDAR equation can be integrated over a short digitization length l since the laser pulses are extremely short with an FWHM of around 1 ns. Additionally, the LIDAR equation is

weighted with r^2 since the geometric decrease of the signal with $1/r^2$ has the biggest impact on the signal, and features in the atmospheric profile get lost. This then becomes:

$$\Sigma(r) = \ln(N(r) \cdot r^2) \approx \ln(N_0 C_F A l) + \ln(\beta(r)) - 2\int_0^r \alpha(r')\,\mathrm{d}r' \tag{4.2}$$

In the differential form, this turns into a differential equation with two further parameters (α and β), which cannot be solved without further information:

$$\frac{\mathrm{d}\Sigma(r)}{\mathrm{d}r} = \frac{1}{\beta}\frac{\mathrm{d}\beta}{\mathrm{d}r} - 2\alpha \tag{4.3}$$

Several ways of inverting the signal, meaning to extract $\alpha(r)$ and $\beta(r)$ from $\Sigma(r)$ are discussed in Fruck (2015). The inversion is possible whenever the two variables have a known relation. Example cases would be assuming a homogenous atmosphere without backscattering or cases where aerosol scattering is the dominant mechanism. In the case of the MAGIC LIDAR shooting at 532 nm, both effects, scattering on aerosols and Rayleigh scattering on molecules, are equally influential. The LIDAR operates as an elastic LIDAR, simultaneously measuring the backscatter signal of both types of scattering. Other forms of LIDAR, e.g., the Raman LIDAR, operate at multiple wavelengths and can separate molecular from aerosol scattering with less assumption but require higher laser powers due to more inefficient forms of scattering. This makes them unsuitable for constant use during data taking, as it would disturb gamma-ray observations.

4.2.2 Extraction of the aerosol extinction profiles

For the extraction of the aerosol extinction, a special algorithm was developed. The following description follows the representation in (Fruck, 2015).

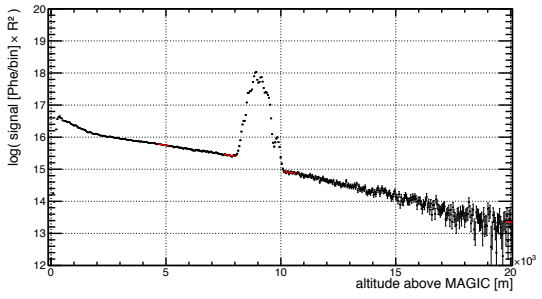

Figure 4.5: LIDAR backscatter profile showing the presence of excess scattering due to the ground layer and some clouds at around 9 km altitude. Image taken from (Fruck, 2015).

The density profiles of molecules in the atmosphere follows an exponential function as a function of height:

$$\rho(h) \approx \rho_0 \frac{h - h_0}{h_S} \tag{4.4}$$

where ρ_0 and h_0 is the density and height at some reference altitude and h_S the scale height of the atmosphere. h_S depends on the temperature and the mass of the molecules with a typical value of around 8 km. The exponential decrease of molecule density also causes an exponential decrease in backscattered photons. A backscatter profile caused purely by Rayleigh scattering of molecules, $S_{\mathrm{mol}}(h)$, can therefore be described with an exponential function:

$$S_{\mathrm{mol}}(h) = C \cdot \exp\frac{h}{h_s} \tag{4.5}$$

The profile is parameterized with the amplitude C incorporating all effects scaling the absolute amplitude of the LIDAR profile. This profile can be fitted within a sliding window along the profile. By evaluating the resulting goodness of fit, regions of pure molecular scattering can be identified. A sudden worsening of the fit indicates the presence of excess aerosols.

There are two main regions where excess aerosols appear in the atmosphere above La Palma: directly above the ground in the atmospheric boundary layer and in clouds at higher altitudes. As previously mentioned, the effect of Calima can cause a strong excess of aerosols in the atmosphere. The heavier aerosols in the form of Sahara dust and sand lie closer to the ground up until 3-4 km, whereas clouds are typically found between 8-12 km (Fruck et al., 2022a). Figure 4.5 shows a LIDAR profile with a clear excess of aerosols at an altitude of around 9 km, indicating the presence of clouds. At very low altitudes from 0-2 km, a small excess of aerosols can also be identified. In between, the profile matches a straight line in the logarithmic representation of the plot. The exponential profile is a good description, which suggests a pure molecular atmosphere in between.

Two different techniques are utilized to extract the aerosol extinction of a cloud layer. In cases where the cloud layer attenuates more than 10% of light, the so-called *extinction method* is applied. The atmosphere below and above the cloud is parameterized with the molecular fit and the two resulting amplitudes C_1 and C_2. The transmission of a cloud layer is then computed by comparing the amplitudes of the molecular fits before and after the cloud. The square of the ratio yields the transmission since the light is attenuated two times:

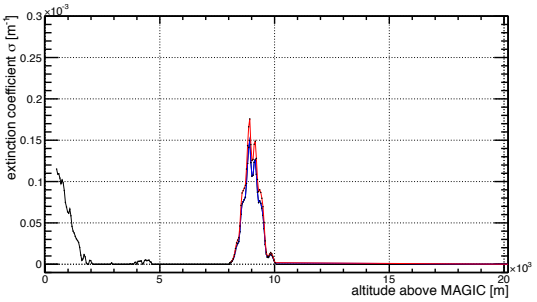

Figure 4.6: Aerosol extinction profile obtained with the LIDAR ratio method (red) and the extinction method (blue). Image taken from Fruck (2015).

$$\tau_{\text{aer}} = \sqrt{\frac{C_2}{C_1}} \tag{4.6}$$

For the molecular component of the signal inside the cloud layer, the average of both amplitudes is used:

$$\bar{S}_{\text{mol}}(h) = \frac{C_1 + C_2}{2} \cdot \exp\frac{h}{h_s} \tag{4.7}$$

The signal excess caused by aerosols, $S_{\text{aer}} = S(h) - \bar{S}_{\text{mol}}(h)$, is then used to extract the aerosol extinction:

$$\alpha_{\text{aer}}(h) = \sqrt{\frac{C_2}{C_1}} \frac{S(h) - \bar{S}_{\text{mol}}(h)}{\int_{h_1}^{h_2} (S(h) - \bar{S}_{\text{mol}}(h))\,\mathrm{d}h} \tag{4.8}$$

In the case of optically thinner clouds with transmission below 10%, a second method is applied. In the *LIDAR ratio method*, a constant relation, the LIDAR ratio K_{aer}, between α and β is assumed within the cloud layer. This allows a direct computation of the extinction coefficients from the signal excess:

$$\alpha_{\text{aer}}(h) = K_{\text{aer}}\,\beta_{\text{mol}}(h)\,\frac{S(h) - \bar{S}_{\text{mol}}(h)}{\bar{S}_{\text{mol}}(h)} \tag{4.9}$$

Using both methods, Figure 4.6 shows the extracted extinction profile from the backscatter profile shown in Figure 4.5. The methods, shown in red and blue, produce comparable results.

Both algorithms only work on clouds since either the Rayleigh fit before and after the cloud layer or the LIDAR ratio needs to be known. A different approach needs to be used to extract the extinction and resulting transmission of the ground layer. Here, the reference amplitude is given by measurements taken under clear sky conditions on earlier nights. The system is then considered to be stable enough to estimate the ground layer transmission by comparing the amplitudes of the reference amplitude with the amplitude of the first sliding window, where a Rayleigh fit describes the profile well:

$$\tau_{g.l.} = \sqrt{\frac{C_0}{C_{\text{ref}}}} \tag{4.10}$$

The system's stability is monitored, and regular re-calibrations minimize the systematic error. A detailed discussion of the systematic uncertainties of the profile extraction will be later given in the discussion in section 5.5.

4.2.3 Correction of aerosol extinction due to the LIDAR wavelength

The resulting extinction profiles correspond to the extinction at 532 nm. The Cherenkov light detected by MAGIC has a much higher contribution of shorter wavelengths reaching into the UV. Figure 4.7 shows the average detected wavelength of Cherenkov light from atmospheric air showers. The obtained values incorporate losses due to the mirror reflectivity and photon detection efficiency of the PMTs (Borla Tridon et al., 2009). LIDAR-based data corrections are applied until a zenith angle of 62°, after which sampling the atmosphere with sufficient depths becomes exceedingly challenging. The average Cherenkov wavelength $\bar{\lambda}_{\text{Cher}}$ lies at around 400 nm until 62°, which is considerably shorter than $\lambda_{\text{LIDAR}} = 532\,\text{nm}$ used by the laser of the LIDAR. Aerosol extinction is significantly higher for UV compared to the optical, which leads to an underestimation of the extinction by the LIDAR. To mitigate this problem, a new correction of the aerosol extinction was introduced in 2022.

The Ångström exponent, Å, relates the ratio of aerosol extinctions at two wavelengths with the ratio of the wavelengths (Ångström, 1929):

$$\frac{\alpha_{\bar{\lambda}_{\text{Cher}}}}{\alpha_{\text{LIDAR}}} = \left(\frac{\bar{\lambda}_{\text{Cher}}}{\lambda_{\text{LIDAR}}} \right)^{-\text{Å}} \tag{4.11}$$

The Ångström exponent can be extracted from the Aerosol Robotic Network project (AERONET, http://aeronet.gsfc.nasa.gov/) Sun photometer data. The network has a location on the ORM around 400 m away from the LIDAR. The data contains Ångström exponents measured for the wavelength ranges 380–500 nm and 340–440 nm. Figure 4.8 shows the histograms of the obtained values for both wavelength ranges and the combined histograms. The data shows a bimodal distribution, where the first peak corresponds to periods with higher dust concentrations, especially Calima. Both peaks of the combined histograms are fitted with a Gaussian distribution to obtain mean values. This allows us to provide aerosol extinction corrections for two different

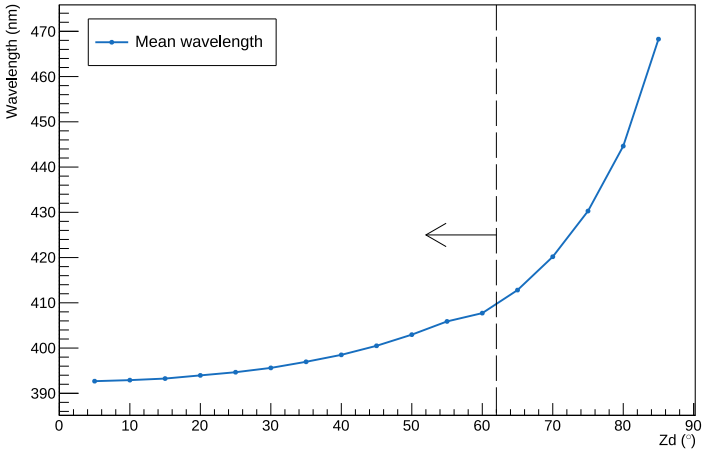

Figure 4.7: Average detected wavelength of Cherenkov light from air showers as a function of zenith angle after being reflected by the telescope mirrors and detected by the PMTs. The dashed line marks 62°, the highest zenith angle where LIDAR corrections are still applied within the MAGIC data analysis.

conditions. In periods with high dust concentrations, a value of Å$\approx 0.32 \pm 0.21$ was obtained, leading to a correction of:

$$\alpha_{\bar{\lambda}_{\text{Cher}},\text{calima}} = \alpha_{\text{LIDAR}} \cdot \left(\frac{400\ \text{nm}}{532\ \text{nm}}\right)^{-(0.32\pm0.21)} = \alpha_{\text{LIDAR}} \cdot (1.10 \pm 0.07) \tag{4.12}$$

For non-dusty periods, the mean value of the peak lies a bit higher at Å$\approx 0.45 \pm 0.46$ due to a higher UV dependence:

$$\alpha_{\bar{\lambda}_{\text{Cher}},\text{non-dusty}} = \alpha_{\text{LIDAR}} \cdot \left(\frac{400\ \text{nm}}{532\ \text{nm}}\right)^{-(1.45\pm0.46)} = \alpha_{\text{LIDAR}} \cdot (1.51 \pm 0.20) \tag{4.13}$$

The method of Fruck et al. (2022a) is used to differentiate between Calima and non-dusty periods. Transmission of the ground layer above 0.93 counts as non-dusty, whereas less transmission is classified as Calima.

4.2.4 Extraction of the transmission profiles

Finally, the integral aerosol transmission profile can be obtained from the aerosol extinction profile via integration:

$$\begin{aligned} T_{\text{aer}}(r) &= \exp\left(-\int_0^r \alpha_{\bar{\lambda}_{\text{Cher}}}(r')\,\mathrm{d}r'\right) \equiv T_{\text{aer}}(h,\theta) \\ &= \exp\left(-\int_0^{h/\cos\theta} \alpha_{\bar{\lambda}_{\text{Cher}}}(h')/\cos\theta\,\mathrm{d}h'\right) \end{aligned} \tag{4.14}$$

The distance r was converted into heights h with the zenith angle θ. Figure 4.9 shows the final integral aerosol transmission profile obtained from the aerosol extinction profiles of Figure 4.6. One can see how the presence of excess aerosols causes a drop in transmission due to clouds

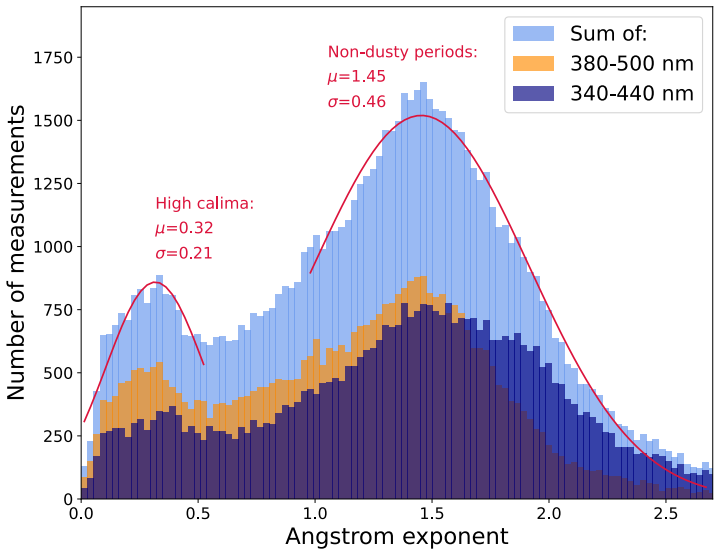

Figure 4.8: Ångström exponents provided by the AERONET station at the ORM for two wavelength regions. The combined histogram is fitted with a Gaussian distribution. The data cover the period between November 2019 and July 2022.

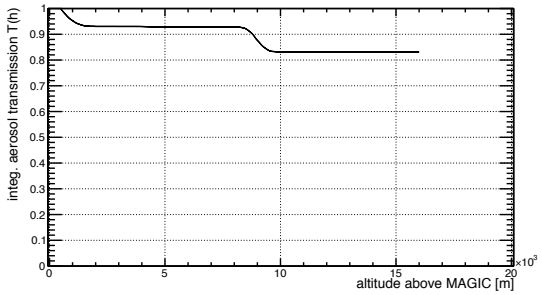

Figure 4.9: Example integral aerosol transmission profile. Image taken from Fruck (2015).

and dust at the ground layer. At low zenith angle (below $\sim 30°$), the LIDAR can obtain profiles up to an altitude of around 20 km with a range resolution of ~ 50 m at lower altitudes increasing up to ~ 100 m at higher altitudes. The majority of Cherenkov photons are emitted well below 15 km. Since the profiles are obtained every 4 min, they get interpolated in time to continuously sample the atmosphere. The binning is done in height bins of 250 m. For MAGIC data outside of the time range covered by the LIDAR, the profiles can be extrapolated up to 15 min. The resulting profiles provide the relevant range of resolved information about the transmission, which is later used to correct MAGIC telescope data.

4.3 Correction of MAGIC telescope data using the LIDAR

4.3.1 Correction of the energy

The largest effect on the image reconstruction caused by higher atmospheric aerosol concentrations is the overall reduction of Cherenkov light arriving in the MAGIC cameras. This primarily distorts the energy reconstruction of gamma-ray events since the energy scales roughly linearly with the amount of Cherenkov light (Hillas, 1985b). Since the Cherenkov light is emitted over a

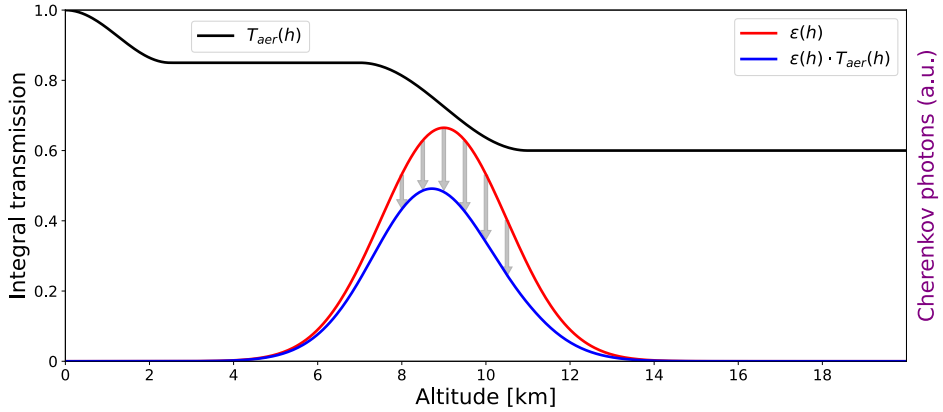

Figure 4.10: Sketch of the correction of the shower energy. An assumed emission profile, shown in red, is downscaled by an example transmission profile in black, resulting in a decreased emission, shown in blue.

wide range of altitudes depending on the energy and zenith of the incoming gamma ray range-resolved, knowledge of the transmission is imperative. In the case of excess aerosols close to the ground, most Cherenkov light is produced above the aerosols, and the height profile becomes less relevant. Previous work on data corrections has exploited this advantage (Garrido et al., 2013; Doro et al., 2014). In the case of aerosols at higher altitudes, especially clouds, an assumption about the normalized emission profile $\varepsilon(r)$ needs to be made. As an approximation, the emission profile of atmospheric showers follows a Gaussian profile in the longitudinal direction. The emission of Cherenkov light increases with the creation of new particles in the shower. It starts to decrease once ionization losses of the particles become the dominant form of energy loss, and new pair creation of particles starts to halt. The mean of the Gaussian corresponds to the reconstructed shower maximum, which is part of the stereo reconstruction of the MAGIC data analysis (Fegan, 1997; Aleksić et al., 2016c). The width is obtained from toy MC simulations (Fruck, 2015):

$$\sigma = 3.6 - 0.4 \log_{10}\left(E_{\text{est}}[\text{GeV}]\right) \cdot (\cos\theta)^{0.15} \text{ km} \tag{4.15}$$

Figure 4.10 illustrates the effect of an example transmission profile shown in black on a typical air shower profile. The transmission profile indicates transmission loss due to a cloud at around 9 km, and the ground layer. The red curve displays a normalized Gaussian profile approximating the emission profile of an air shower with a maximum emission at a similar height as the center of the cloud. A more realistic emission profile is obtained by folding the transmission profile over the emission profile. Integrating over the new emission profile results in the average optical depth seen by the shower:

$$\overline{T}_{\text{aer}} = \int_0^\infty \varepsilon(h) \cdot T_{\text{aer}}(h)\, \mathrm{d}h \tag{4.16}$$

The inverse of the optical depth corresponds to the atmosphere-induced light yield bias and can now be used to correct the initial estimated energy:

$$E_{\text{corr}} = \frac{E_{\text{est}}}{\overline{T}_{\text{aer}}} \tag{4.17}$$

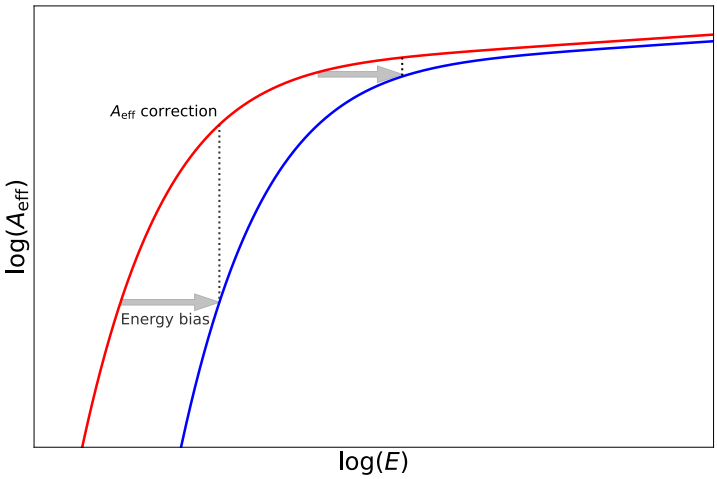

Figure 4.11: Sketch of the effective area shift caused by excess aerosols as a function of energy. The red curve represents the effective area under clear conditions. The blue curve demonstrates the resulting shift caused by an impaired atmospheric transmission.

As shown in equation 4.15, the width of the shower profile depends on the energy itself. Therefore, the correction and new calculation of the energy bias are repeated iteratively until sufficient convergence is achieved.

It is not enough to scale up the energy of individual gamma-ray events to obtain correct high-level results, e.g., flux estimates or energy spectra. The instrument response functions (IRFs) also depend on the reconstructed energy.

4.3.2 Correction of the effective area

The dominant energy-dependent factor of the IRFs is the effective collection area. It is given by the equivalent geometric area of the detector, assuming a detection probability of 100%. It shows a strong dependence of the energy below 100 GeV, which decreases for higher energies (Aleksić et al., 2016c). As mentioned in the previous section, the dominant effect of an impaired atmosphere is the lower Cherenkov light yield of the air shower. A lower effective area must be attributed to the event to account for this effect. The assumption is that air showers under suboptimal aerosol conditions produce comparable images to showers with smaller energy under clear conditions. Therefore, the effective area is evaluated at the energy $E \cdot \overline{T}_{\text{aer}}$, which is the event energy before the energy correction is applied. This results in a shift of the effective area as a function of energy, as it is displayed in Figure 4.11. The gray arrows represent the energy shift. It is important to note that the shift is not the same across the curve and is itself slightly energy dependent since also the factor T_{aer} depends on the energy-dependent maximum shower height. This way, each event is assigned an individual effective area. When computing fluxes of gamma-ray sources, the number of gamma-ray events per time and area are computed. Different assumptions can be valid when averaging the effective area for a given exposure under suboptimal conditions. In the following, two different methods are presented and later compared in the next chapter.

4.3.3 Averaging the effective area: Method I

In the first method, the assumption is made that the effective area of a given energy bin scales roughly with the event rate observed in that bin. Even though the observed rate is usually background dominated, i.e., not gamma-ray dominated, the assumption can be considered valid for this purpose (Hahn et al., 2014; Stefanik et al., 2019). To calculate the average effective area over a time T, one must translate the integral over time into a discrete sum over individual events by using the assumed relation $A \propto \mathrm{d}N_i/\mathrm{d}t$:

$$\bar{A}(E_i) = \frac{\int_0^T A(E_i,t)\mathrm{d}t}{\int_0^T \mathrm{d}t} = \frac{\int_0^T A(E_i,t)\mathrm{d}t}{\int_0^T A(E_i,t)/A(E_i,t)\mathrm{d}t} \xrightarrow{A\propto \mathrm{d}N_i/\mathrm{d}t} = \frac{\int_0^T \frac{\mathrm{d}N_i}{\mathrm{d}t}\mathrm{d}t}{\int_0^T \frac{\mathrm{d}N_i}{\mathrm{d}t}/A(E_i,t)\mathrm{d}t} = \frac{N_i}{\sum_{j=0}^{N_i}\frac{1}{A_j(E_i)}}$$

The index i refers to the energy bin, whereas j refers to individual events. N_i is the total number of events in a given bin, and A_j is the effective area assigned to an individual event. As previously outlined, the effective area is evaluated at the energy before the energy correction:

$$A_j(E_i) = A\left(E_{\mathrm{corr,i}} \cdot \overline{T}_{\mathrm{aer},j}\right) \tag{4.18}$$

The procedure is followed by unfolding the measured energy spectrum, resulting in another migration of energy events. A detailed description can be found in the Appendix of Schmuckermaier et al. (2023).

Method I was the standard method of averaging the effective area in the context of LIDAR-based data corrections of the MAGIC collaboration. In 2018, the support of this method was terminated, and Method II became the preferred approach.

4.3.4 Averaging the effective area: Method II

For Method II, a histogram with the event-wise correction factors $T_{\mathrm{aer},j}$ is created with bins k and weighted with the elapsed time spent under each condition. The histogram shows how long the atmosphere was under a similar condition; with that, the energy correction factor was at a similar value. Events were additionally classified by their zenith angle leading to a binning in $T_{\mathrm{aer,k}}$ and θ. The average effective area is then given by the energy-shifted effective areas weighted by the time spent under all observation conditions:

$$\langle A_{\mathrm{eff}}(E_i,\theta)\rangle = \frac{\sum_k A_{\mathrm{eff}}(E_i \cdot \overline{T}_{\mathrm{aer},k},\theta)\cdot t_{\mathrm{elapsed},k}(\theta)}{\sum_k t_{\mathrm{elapsed},k}(\theta)} \tag{4.19}$$

A critical remark is that the same shift in evaluating the effective area is applied to Method II. As previously noted, the correction factor is energy-dependent. A high cloud at around 10 km will not significantly impact a gamma-ray shower of high energy, e.g., 5 TeV, since its shower maximum will be well below that altitude. Clouds at lower altitudes will affect showers of all energies more equally. Assuming the same shift for all energies will introduce a systematic error, particularly in fast-changing clouds. The neglected energy dependence of the shift makes the method work better if the aerosols get closer to the telescope; then, showers of all energies are affected equally. Since Method II is the currently used and supported approach in the MAGIC collaboration, all corrections shown in section 5.3 were done using Method II. Section 5.4 will then compare both methods.

Chapter 5

First detailed evaluation of the LIDAR-based corrections

This chapter contains a detailed investigation of the performance of the LIDAR-based corrections using an almost seven-year data set of the MAGIC telescopes. The subsequent study was published in Schmuckermaier et al. (2023). As the leading author of the publication, I conducted the analysis of the MAGIC data, produced all the high-level results, and wrote most of the manuscript. Markus Gaug contributed, in particular, to the introduction and discussion of systematic uncertainties and writing parts of the text. The other authors contributed small segments to the draft, assisted with proofreading, or contributed to the development of the LIDAR and its data analysis. The text and structure of this chapter closely follow Schmuckermaier et al. (2023), and parts of the text have been adopted verbatim. Earlier preliminary results of this work have been presented by myself at the *AtmoHEAD* conference in 2022 and have been published as a conference proceeding (Schmuckermaier et al., 2022). A very early and outdated stage of this study is the subject of my master's thesis (Schmuckermaier, 2021)

5.1 Data set

The following section will evaluate and compare the LIDAR-based data corrections using a data set collected by the MAGIC telescopes over almost seven years. To isolate the effect of the corrections, the data sets need to be from a constant source without a significant intrinsic variability, i.e., a standard candle. In VHE gamma-ray astronomy, the Crab Nebula functions as a standard candle. Its flux is very bright and stable over multiple years (Abdo et al., 2010d; Aleksić et al., 2015c; Jourdain and Roques, 2020). Flaring periods in gamma-rays of lower energies (above 100 MeV) have been detected in the past (Tavani et al., 2011; Rudy et al., 2015; Arakawa et al., 2020), but were not detectable in the VHE regime (H. E. S. S. Collaboration, 2014; van Scherpenberg et al., 2019). The source, therefore, only varies within the instrument's intrinsic systematic uncertainties and is considered stable in the context of this study.

Due to its stability, the Crab Nebula is regularly observed by MAGIC for calibration purposes. I used data from mid-2013 until early 2020, covering a period of almost seven years in the following study. The data were taken within a zenith of 5–62°. Under higher zenith angles, sampling the atmosphere at sufficient depth becomes infeasible with the laser power used. Additionally, I only used data taken under dark conditions, referring to a low level of light from the night sky background. The analysis under stronger moonlight is possible but comes with

Table 5.1: Available data (in hours) for all included analysis periods and transmission bins.

Period tag	Time period	$T_{9\,\mathrm{km}}$ >0.95	>0.9	0.9 - 0.82	0.82 - 0.65	0.65 - 0.5
ST.03.03	27.07.2013 – 05.08.2014	39.1	42.4	1.6	0.7	1.1
ST.03.05	31.08.2014 – 22.11.2014	5.7	10.1	1.8	0.3	0.5
ST.03.06	24.11.2014 – 28.04.2016	58.6	70.1	7.6	5.6	5.4
ST.03.07	29.04.2016 – 02.08.2017	21.3	31.5	3.8	2.4	1.2
ST.03.09	10.11.2017 – 29.06.2018	9.3	14.3	2.6	0.2	0
ST.03.10	30.06.2018 – 30.10.2018	6.3	7.4	0	0.1	0
ST.03.11	01.11.2018 – 15.09.2019	19.2	20.6	1.2	1.8	1.2
ST.03.12	16.09.2019 – 22.02.2020	13.4	28.6	7.7	5.2	0.9
Total	27.07.2013 – 22.02.2020	176.2	221.6	26.3	16.1	10.4

higher complexity and systematic uncertainties (Ahnen et al., 2017c). Only data with favorable conditions in terms of background light are used to isolate the effect of the atmosphere.

Aerosol transmission from 9 km above the ground of MAGIC, $T_{9\,\mathrm{km}}$, is used as the criterion for classifying the data according to their atmospheric quality. Since aerosol transmission is a continuous function of height, putting it into a single number allows for easier comparison. 9 km roughly corresponds to the typical maximum emission of Cherenkov light by an atmospheric shower with 100 GeV (Bernlöhr, 2000). Given that MAGIC lies at an altitude of around 2.2 km, most Cherenkov light will be produced below 9 km above the ground and is therefore unaffected by even higher aerosols. By evaluating $T_{9\,\mathrm{km}}$, I divided the data into five groups (the internal label is given in parentheses):

- Very good quality data with $T_{9\,\mathrm{km}} > 0.95$ for the construction of the reference spectra (see section 5.2)
- Data with $T_{9\,\mathrm{km}} > 0.9$ (*highest transmission*)
- Data with $0.82 < T_{9\,\mathrm{km}} < 0.9$ (*high transmission*)
- Data with $0.65 < T_{9\,\mathrm{km}} < 0.82$ (*medium transmission*)
- Data with $0.5 < T_{9\,\mathrm{km}} < 0.65$ (*low transmission*)

Table 5.1 gives the available data under each condition in hours. The data are broken down by their date range and assigned to MAGIC analysis periods, which define periods of consistent hardware status and data analysis. The first period, ST.03.03, is interrupted by ST.03.04, which has been excluded from the data sample. It only contains three days of stereo data and adds no meaningful statistics to the sample. The same reasoning applies for period ST.03.08, which covers three months only.

5.2 Construction of the reference spectra

To evaluate the effect of the corrections, a standard of reference for the emission of the Crab Nebula must be defined. The differential flux, i.e., flux as a function of energy, provides a com-

prehensive emission characterization and can be accurately measured from bright sources like the Crab Nebula. The most straightforward approach now would be to set a single spectrum of the Crab Nebula, which has already been measured and published by MAGIC, as the reference. However, this brings a disadvantage. Even though the Crab Nebula is a non-varying source in VHE gamma rays, MAGIC still detects slightly different spectra in different periods due to either hardware upgrades, e.g., camera upgrades, or environmental influence, e.g., dust deposition on the mirrors, the instrument response function of MAGIC changes. If changes become influential enough, a new analysis period with corresponding MC simulations is introduced. The accuracy of the new set of MCs can vary from period to period, and the reconstruction of spectra can differ slightly. This variation is within the systematic uncertainty of MAGIC, which is estimated at a maximum of 15% for the absolute energy scale and 11% for the flux normalization (at 300 GeV) (Aleksić et al., 2016c). To achieve a comparison with minimal systematic bias, I define a reference spectra for each analysis period. The reference spectra are reconstructed using only the data with $T_{9\,\mathrm{km}} > 0.95$.

I then combined the data within a period with the appropriate transmission into a single spectrum and is characterized by fitting a log-parabola function with the shape:

$$\frac{\mathrm{d}\phi}{\mathrm{d}E} = f \cdot \left(\frac{E}{275\,\mathrm{GeV}}\right)^{a - b^2 \cdot \log_{10}\left(\frac{E}{275\,\mathrm{GeV}}\right)} \tag{5.1}$$

The energy is normalized at 275 GeV. This is equivalent to the mean de-correlation energy of all spectra. At the de-correlation energy, the correlation of the flux normalization parameter f, the index parameter a, and the shape parameter b is minimal.

This way, a reference spectrum for each analysis period is determined. Figure 5.1 shows all obtained spectra in the form of SEDs and, for comparison, two published Crab Nebula SEDs taken from Aleksić et al. (2015c) and Aleksić et al. (2016c). At the bottom of the figure, the ratio of the reference spectra to the SED from Aleksić et al. (2016c) is taken to allow a better visual comparison. The shaded bands give the one-sigma uncertainty bands of the SEDs. Table 5.2 contains the fitted parameters for all analysis periods. The flux normalization parameters show an excess fluctuation of 3.5%, which is within the night-wise fluctuations of 5% found in Aleksić et al. (2016c). The spectral index parameter a shows about 0.03 excess fluctuation, and the curvature parameter b is about 0.02.

In the following sections, data taken under suboptimal conditions are analyzed with and without corrections and then compared to the corresponding reference spectrum of the same period.

5.3 Evaluation of the LIDAR performance on a nightly basis

I processed the data into single-night spectra as an initial way of evaluating the effects of the LIDAR-based corrections. Four examples of individual nights are given in the Figures 5.2 and 5.3. Each column depicts the range-corrected photo-electron counts, the resulting aerosol transmission, and the reconstructed spectrum with and without data correction taken in one specific night. The first column of Figure 5.2 shows the night of November 13, 2015. The backscatter profile reveals a high excess of aerosols in the ground layer up to ∼1.5 km and a layer of clouds between ∼8.5 km and ∼11 km. The resulting aerosol transmission profile shows two substantial

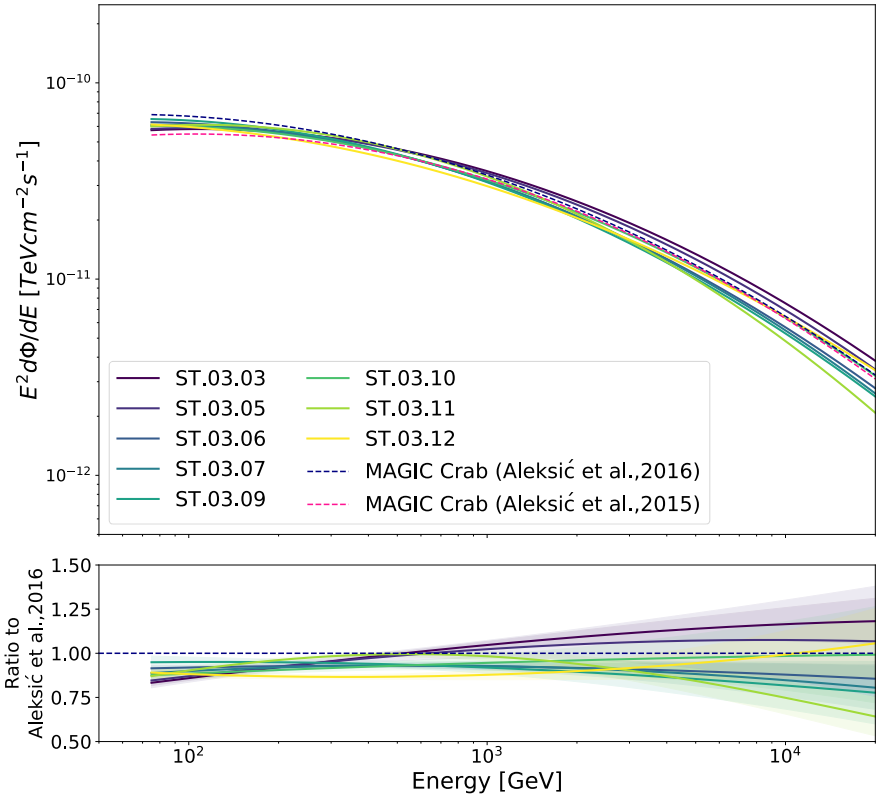

Figure 5.1: Reference spectra of all included analysis periods. Top: All spectral fits and, for comparison, spectra published by MAGIC in Aleksić et al. (2016c) and Aleksić et al. (2015c). Bottom: Ratio between the spectrum of a given analysis period and the published spectrum of Aleksić et al. (2016c). The shaded bands show the one-sigma uncertainty band of the spectral fits.

Table 5.2: Fitted spectral parameters of the reference spectra of all periods.

Period tag	f ($\times 10^{-10}$TeV cm^{-2} s^{-1})	a	b
ST.03.03	7.05 ± 0.06	-2.19 ± 0.01	0.48 ± 0.01
ST.03.05	7.04 ± 0.16	-2.20 ± 0.03	0.48 ± 0.03
ST.03.06	6.90 ± 0.05	-2.27 ± 0.01	0.47 ± 0.01
ST.03.07	6.89 ± 0.08	-2.26 ± 0.01	0.49 ± 0.02
ST.03.09	7.04 ± 0.13	-2.29 ± 0.01	0.48 ± 0.02
ST.03.10	6.80 ± 0.13	-2.25 ± 0.03	0.46 ± 0.03
ST.03.11	7.29 ± 0.08	-2.23 ± 0.02	0.54 ± 0.02
ST.03.12	6.45 ± 0.09	-2.28 ± 0.02	0.43 ± 0.02
Weighted means	6.94 ± 0.22	-2.24 ± 0.04	0.48 ± 0.03

drops resulting from both regions of aerosol excess. At 9 km, the transmission is roughly 0.7. The reconstructed SED is shown in the top right corner. A clear bias from the corresponding reference spectrum can be seen without corrections (in red), which can be successfully eliminated after corrections (in blue). The second column shows the same type of plots but for March 4, 2016. One can see some strong calima above the ground and very thin clouds. The SED taken that night can also be adequately recovered. In the left column of Figure 5.3, data from November 29, 2016, is shown. A ∼2 km thick layer of fast varying clouds makes the correction difficult and results in a slight over-correction of the spectrum. It is worth noting that the data covers only a period of around 15 min. The particular example is, therefore, also limited by statistics. The last column, showing results from December 1, 2016, displays a thick layer of clouds from 5 km up to almost 11 km altitude. The whole layer of clouds reduces the transmission by 40-50%, resulting in $T_{9\,\mathrm{km}} < 0.6$ for all profiles. The corrections improve the SED compared to the reference, but a fully adequate reconstruction is not reached.

The LIDAR-based corrections work well in cases where calima is the dominant atmospheric effect. In the two cloud-dominated cases, the reconstruction is more limited. A detailed description of the various challenges and systematic uncertainties associated with clouds and calima can be found in section 5.5.

I extracted two high-level results to quantitatively compare the corrected and uncorrected data: Spectral parameters and integral fluxes. Analogous to the reference spectra, the bad-weather data is fitted first with a log-parabola function to extract the spectral parameters characterizing the spectrum's shape. The unfavorable atmospheric conditions and sometimes low observation times of individual nights can lead to relatively low statistics. To assist the convergence of the spectral fit, the curvature parameter, b, in the log-parabola function was fixed to the value from the corresponding reference spectrum. The amplitude, f, which parameterizes the overall scale of the spectrum, and the index parameter, a, which parameterizes the spectral tilt, are fitted freely. This is because the curvature is strongly affected by the high end of the spectrum, where the statistics become scarce, and the potential for the curvature to take on very different values is more significant for short data sets. The amplitude and the index are dominated mainly by the low energy end of the spectrum, where statistics is good, making the latter two the most important parameters for quantification of the spectrum under suboptimal conditions.

The second way of characterizing the emission is to take the integral flux over a wider energy range. It is equivalent to the number of photons within the given energy range per area and time. In this study, three energy ranges were considered: 200 GeV – 400 GeV (low energy), from 400 GeV – 1 TeV (medium energy), and above 1 TeV (high energy).

The resulting parameters and fluxes, using q as a substitute variable for both, are then compared to the reference spectrum in two ways. At first, the percental deviation from the reference value was determined to get the relative deviation:

$$D_{\%} = \left(\frac{q_i}{q_{\mathrm{ref}}} - 1 \right) \cdot 100. \tag{5.2}$$

Second, the statistical significance of a given deviation is estimated by expressing the deviation in units of standard deviations:

$$D_{\sigma} = \frac{q_i - q_{\mathrm{ref}}}{\Delta q}. \tag{5.3}$$

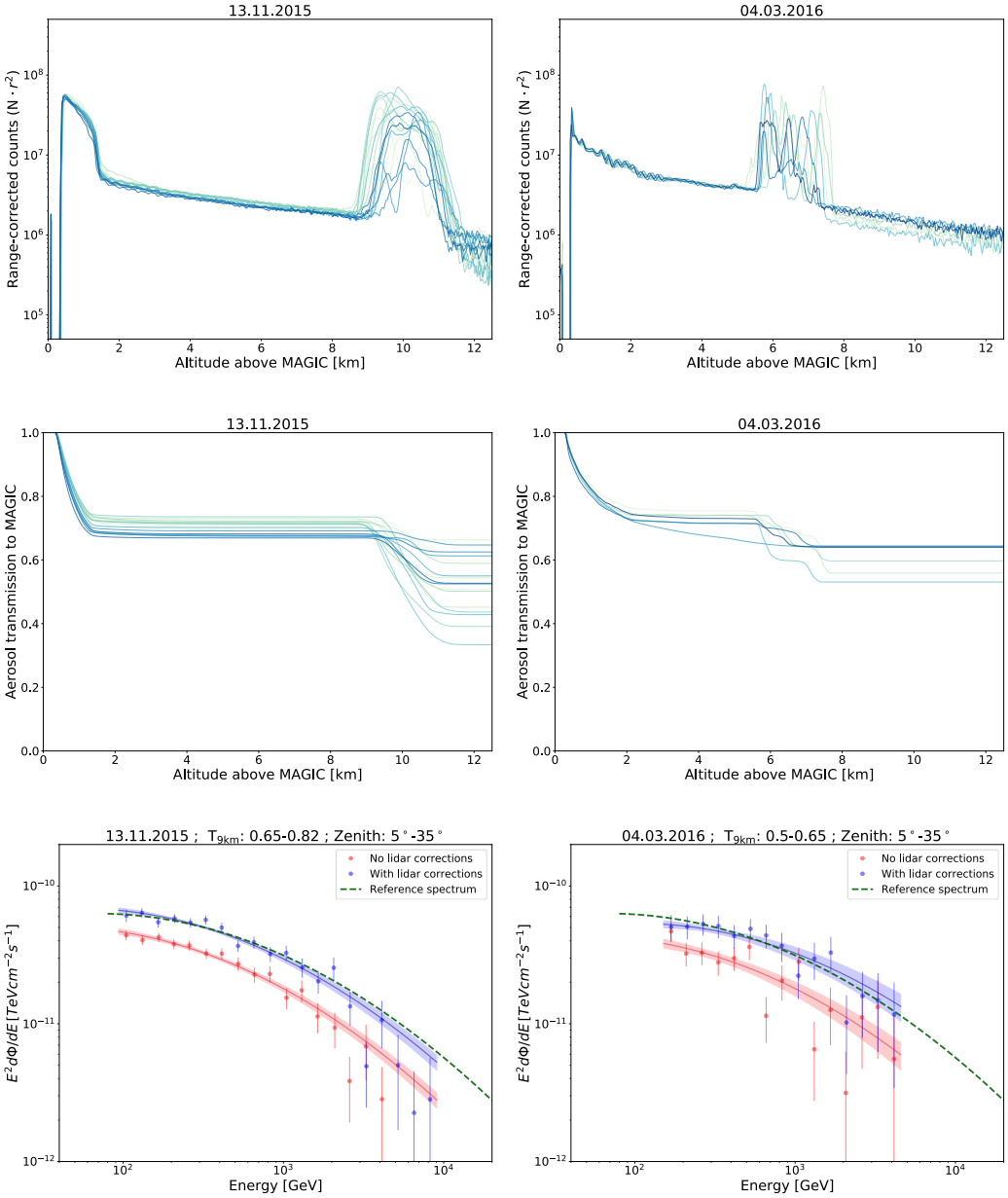

Figure 5.2: Two example nights that show the effect of the LIDAR corrections. Top row: LIDAR profiles in the form of range-corrected photo-electron counts for two example nights. Different color shadings mark the consecutive profiles and provide a sample every 4 minutes. Middle row: Resulting integral aerosol transmission curves, $T_{\mathrm{aer}}(h)$. Bottom row: SEDs of concurrent observations of the Crab Nebula shown without (red) and with (blue) LIDAR correction. For comparison, the reference spectrum of the corresponding period is shown as a dashed green line.

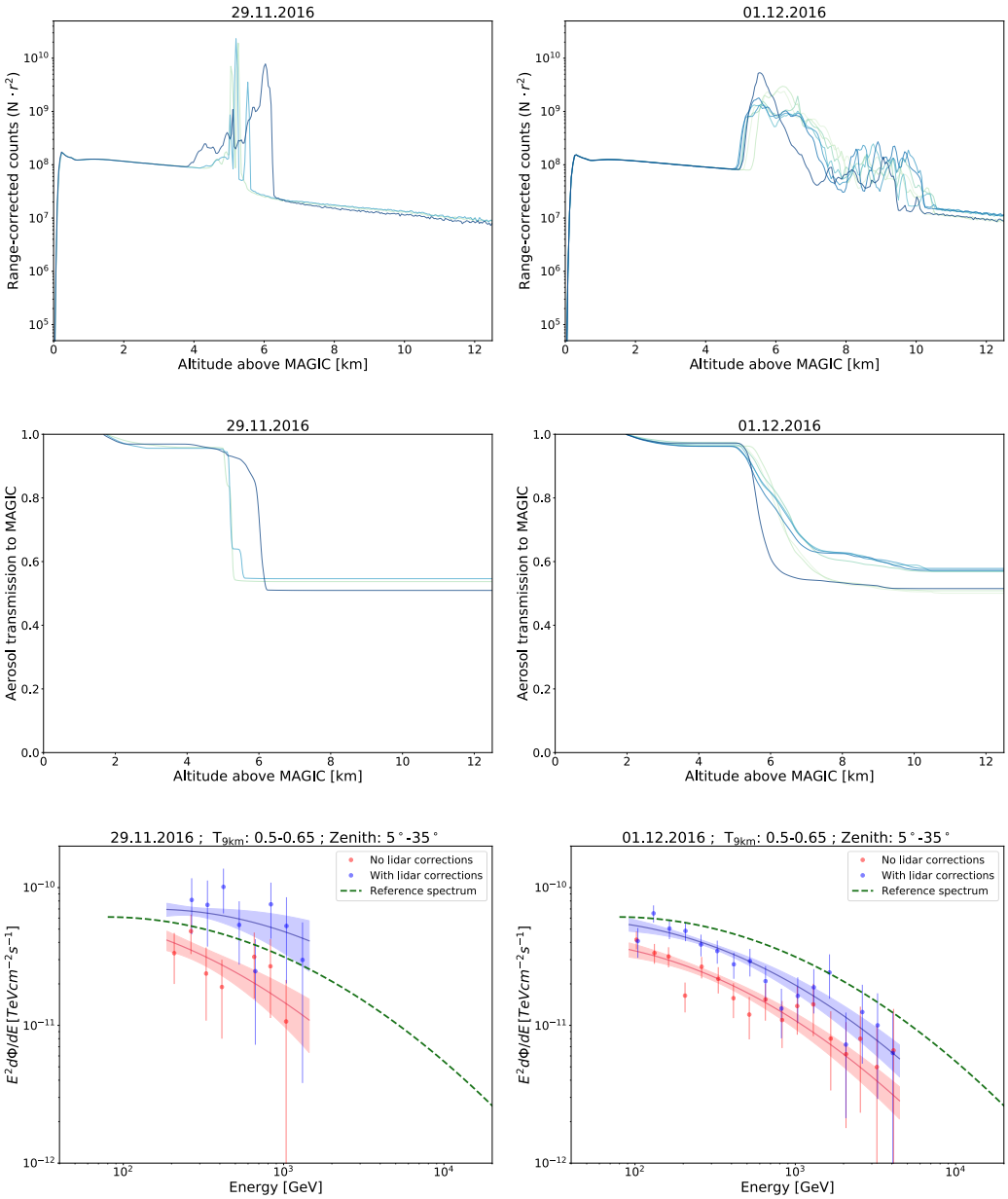

Figure 5.3: Same as Figure 5.2, but for two more nights.

Δq contains the resulting statistical uncertainty obtained from both the individual spectrum and the reference spectrum:

$$\Delta q = \sqrt{\Delta q_i^2 + \Delta q_{\text{ref}}^2}. \tag{5.4}$$

The two deviations comprehensively quantify how substantially a given quantity deviates from the expected value. A large percental deviation combined with a small statistical deviation can be attributed to low statistics, while a large statistical deviation together with a low percental deviation can be caused by the intrinsic systematic uncertainties of the spectral analysis of the MAGIC data.

5.3.1 Influence of the LIDAR corrections on the parameter reconstruction

First, I evaluated the LIDAR corrections by their influence on the spectral shape. Since the energy threshold of MAGIC rises with the zenith angle, the energy threshold of the spectral fits was set to 100 GeV for low zenith data taken between 5° and 35°, 200 GeV for medium zenith between 35° and 50° and 400 GeV for high zenith data between 50° and 62°. This ensures that only data above the applicable threshold is included. The results of both types of previously discussed deviations are portrayed as scatter plots. The images show the deviation of the parameters obtained from a single night as a scatter point and the overall distribution of nights as projected histograms. Over-estimations of the parameters result in positive values, whereas under-estimations are negative.

The upper plot of Figure 5.4 shows the results for the flux normalization, f. The plot shows data from the three transmission bins taken under suboptimal conditions with $T_{9\,\text{km}}$ between 0.5 and 0.9, and all zenith ranges together. The histograms of both deviations show substantial improvement due to the LIDAR corrections. The error-weighted mean of the percental deviations moves from $-24.2 \pm 0.3\%$ to $-4.3 \pm 0.5\%$. The mean of the deviation significances from $-2.7\,\sigma$ to $-0.3\,\sigma$. The number of nights with statistical deviation greater than $3\,\sigma$ has been considerably reduced from 48 (out of 137 tested samples) down to 7 due to the impact of the LIDAR corrections.

In the lower plot of Figure 5.4, the deviations of the spectral index parameter a are shown. Instead of the percental deviation, as defined in equation 5.2, the difference $a_i - a_{ref}$ is portrayed on the horizontal axis. Here, the difference between the corrected and uncorrected distributions is marginal. The weighted mean of the differences shifts from a slight negative bias of -0.05 ± 0.01 to 0.00 ± 0.01 after applying corrections. The clear-night case, taken from Table 5.2, already shows an error of 0.04 on the mean. Both deviations are compatible with this, and no significant biases can be claimed. Overall, suboptimal atmospheric conditions do not seem to strongly influence the spectral tilt.

The data are now separated by their transmission and zenith angle. Also, data of the high transmission bin with $T_{9\,\text{km}}$>0.9 is now included. In terms of zenith angle, the same binning as in the MC data of MAGIC is used: a low zenith bin from 5° to 35°, a mid zenith bin from 35° to 50° and a high zenith bin from 50° to 62°. The number of nights in a given region has further decreased due to the separation of the data, and the available statistics is reduced. The information is therefore condensed in the following manner: For the percental deviation, an error-weighted

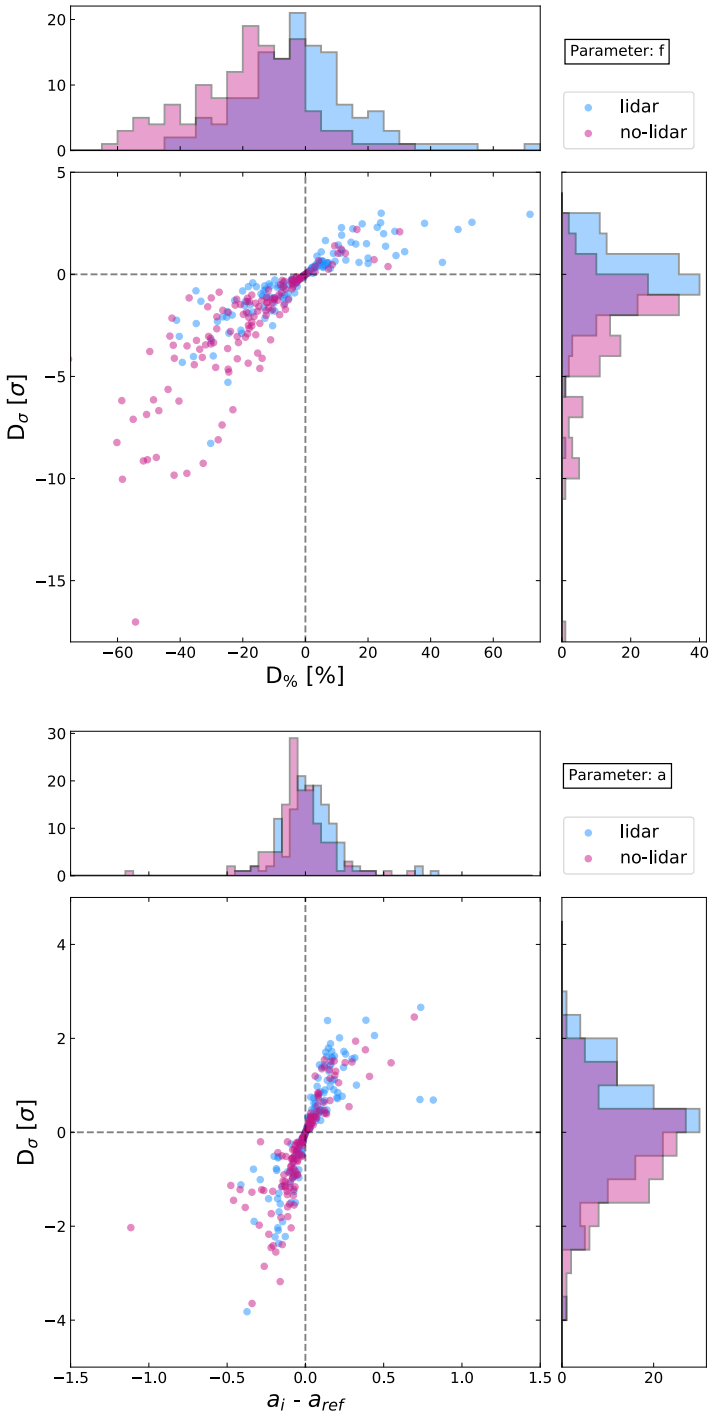

Figure 5.4: Scatter plots with projected histograms, showing deviations of the spectral parameters of individual nights. Top: Distribution of the percental and statistical deviation of the reconstructed flux normalization obtained from nights with an aerosol transmission between 0.5 and 0.9 from the reference spectrum for individual nights with projected histograms. Bottom: Same for the index parameter but using the difference instead of the percental deviation in the x-axis.

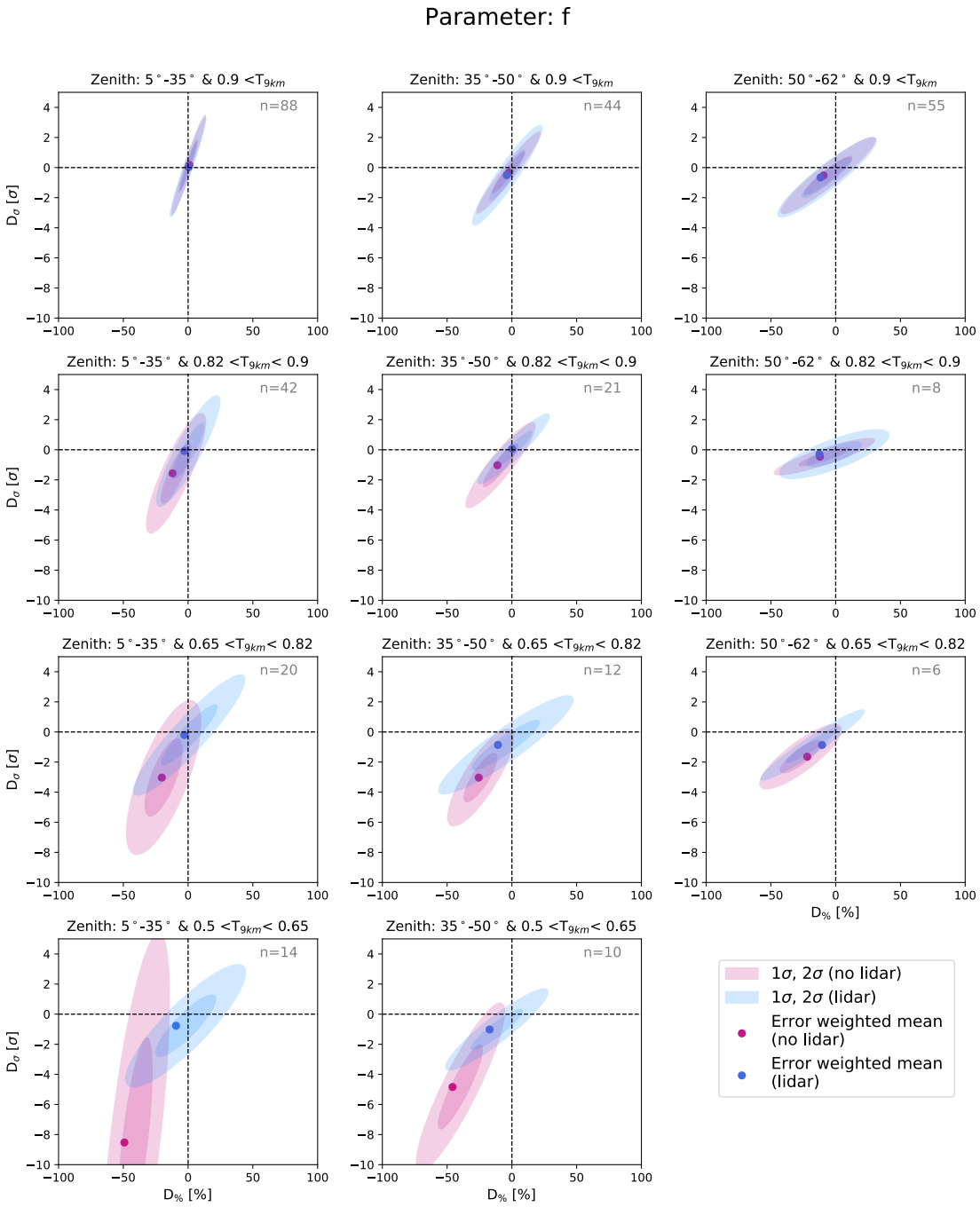

Figure 5.5: Error-weighted mean percental and mean statistical deviation of the flux normalization parameter, f, without (red dot) and with (blue dot) LIDAR corrections for eight zenith and aerosol transmission $T_{9\,\mathrm{km}}$ bin combinations. The shaded areas give the error ellipses at 1σ and 2σ. Note that, by construction, the uncertainty ellipses may not pass through the coordinate system origin, reflecting reconstruction biases. The number of averaged nights, n, is provided in the top-right corner of each plot. Sufficient data are unavailable in the low aerosol transmission and high zenith bin.

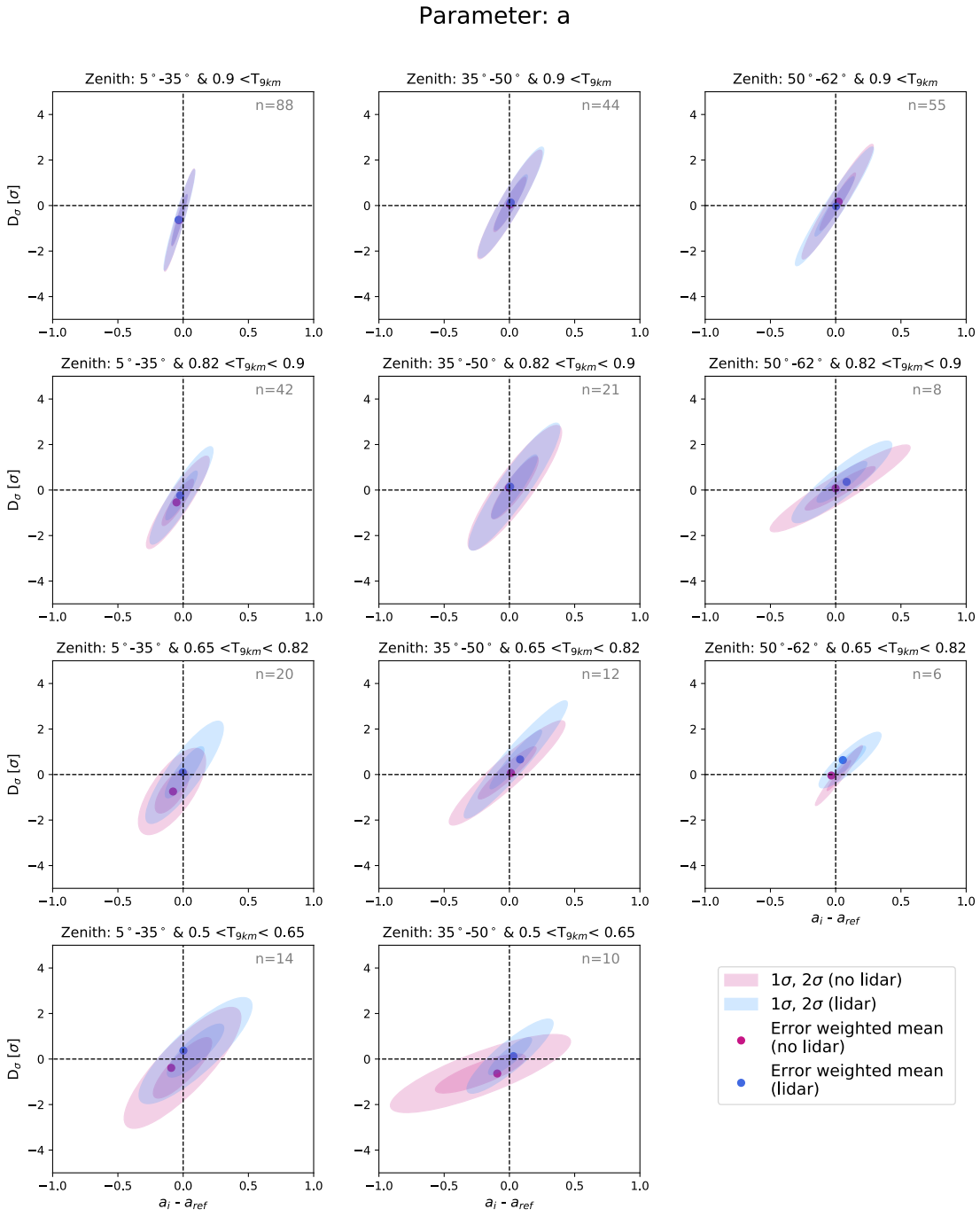

Figure 5.6: Same as Figure 5.5, but for the index parameter, *a*. Sufficient data are unavailable in the low aerosol transmission and high zenith bin.

mean is calculated from individual nights. A standard mean over individual nights is taken for the statistical deviation since the parameter estimate's error is already considered. Covariance error ellipses are constructed to visualize the underlying data distribution over which the means were taken. The ellipses were derived from the standard mean, standard deviation, and the Pearson correlation coefficient. For normally distributed data, the $1\,\sigma$ ellipse is expected to enclose roughly 68% of the data, whereas the $2\,\sigma$ encompasses around 95%.

The results for the flux normalization parameter are given in Figure 5.5. Eight combinations of zenith and $T_{9\,\mathrm{km}}$ cover a wide range of observation conditions. An individual panel shows results obtained before (red) and after (blue) applying the LIDAR corrections. The covariance ellipses indicate the $1\,\sigma$ and $2\,\sigma$ within the shaded area. It is important to note that the ellipses have been constructed using the geometric mean. The error-weighted means, therefore, do not lie precisely on the center of the ellipses in the horizontal axis.

Looking at the first column, the results at low zeniths are displayed. The flux normalization is reconstructed without bias in almost all cases, as indicated by the good agreement of the means with the origin. In the lowest $T_{9\,\mathrm{km}}$ bin, the error-weighted mean shows a remaining bias of $(-9 \pm 2)\%$ after using corrections. Under medium zenith angles, shown in the middle column, the corrections produce bias-free reconstructions in the two higher transmission bins. Below $T_{9\,\mathrm{km}} < 0.82$, a residual bias of $(-11 \pm 3)\%$ is found. The deviation in the lowest transmission bin worsens to $(-17 \pm 4)\%$ and -1.0$\,\sigma$. The high zenith bin is shown in the right column. In the highest $T_{9\,\mathrm{km}}$ bin, LIDAR corrections produce a marginal worsening indicated by the slightly wider ellipse and the mean value moving away from the origin. A downward flux correction is possible if the LIDAR reconstructs better aerosol conditions than those employed for the standard Elterman model used in the MC simulations (Garrido et al., 2013). In the transmission bin $0.82 < T_{9\,\mathrm{km}} < 0.9$, the corrected weighted mean barely shows an improvement toward the origin. The error ellipse widens slightly after applying corrections. Both distributions are still compatible with the origin, and with only eight nights, the statistics is very limited. Below $T_{9\,\mathrm{km}} \approx 0.82$, the corrected mean shows an offset of $-10 \pm 6\%$. The spectral amplitude is normalized at the overall sample-wide de-correlation energy of 275 GeV. This is already rather close to the energy threshold under clear conditions. Under suboptimal conditions, the threshold can rise higher, requiring an extrapolation of the spectrum to lower energies to determine the flux normalization. This effect might cause an additional impairment of the amplitude reconstruction in the high zenith region. In the lowest $T_{9\,\mathrm{km}}$ bin, insufficient data is available.

An analogous representation of the results for the index parameter, a, is shown in Figure 5.6. In most cases, the distributions of the index parameter a do not change significantly before and after applying LIDAR corrections, as noted in the scatter plots. At $T_{9\,\mathrm{km}} > 0.82$, uncorrected and corrected data produce almost identical results, except for the largest zenith angles, where a reduction of the spread of the data can be observed. In the medium transmission range, $0.65 < T_{9\,\mathrm{km}} < 0.82$, improvements for low zenith angles can be observed, but also slight worsening in the form of over-corrections at larger zeniths. Under low aerosol transmissions, $0.5 < T_{9\,\mathrm{km}} < 0.65$, significant improvement is achieved for the shape parameter, indicated by the narrower distributions and mean values close to the origin.

5.3.2 Influence of the LIDAR corrections on the integral flux reconstruction

As the second way of characterizing the emission, I computed the influence of corrections on the integrated flux. The three energy bands considered are 200–400 GeV, 400–1000 GeV, and >1000 GeV. Analogous to before, the error-weighted means and distributions of both types of deviations were computed for different zenith and $T_{9\,\mathrm{km}}$ ranges.

The results for the lowest energy range are shown in Figure 5.7. A four-by-two arrangement covers all relevant combinations of zenith angle and aerosol transmission bins. The highest zenith bin is excluded, since the energy threshold, for optimal atmospheric conditions, lies at ∼200 GeV at 50° zenith and at ∼420 GeV at 62° (Aleksić et al., 2016c). A lower aerosol transmission will further increase the energy threshold. Threshold effects might strongly distort the results in this energy range. The results confirm the previously discussed improvements for the spectral parameters: In the highest transmission bin, close to no difference can be observed between uncorrected and corrected data. The uncorrected and corrected data show similar distributions in the two zenith regions. Both averages are close to the origin, indicating no significant offset of the reconstructed fluxes from the reference on average. In the range $0.82 < T_{9\,\mathrm{km}} < 0.9$, further improvements can be achieved by applying corrections. Both corrected distributions move closer to the origin. The data taken under $0.65 < T_{9\,\mathrm{km}} < 0.82$ are corrected satisfactorily for low zeniths. A small bias of $(-10 \pm 4)\%$ remains at medium zeniths. For the lowest aerosol transmission case, an improvement of the means of the distribution from $(-50 \pm 3)\%$ to $(-15 \pm 4)\%$ and from $-4.0\,\sigma$ to $-0.6\,\sigma$, respectively, can be observed at low zenith angles. The LIDAR corrections achieve an almost full recovery of the flux on average. For medium zenith ranges, improvements from $(-44 \pm 3)\%$ to $(-26 \pm 5)\%$ and from $-3.8\,\sigma$ to $-1.4\,\sigma$ are observed. The rather low transmission under an increased zenith angle might make threshold effects start to influence the data here.

The results for the medium energy range 400-1000 GeV are shown in Figure 5.8. Now, the high zenith bin is included. For low and medium zenith angles and aerosol transmission $T_{9\,\mathrm{km}} > 0.9$, the data show an almost identical distribution before and after correction. At higher zeniths, differences become apparent. Mean values of both uncorrected and corrected data show a small offset from the origin. Data taken close to the highest zenith angles of 62° may still suffer from threshold effects here, which leads to a slight under-reconstruction of the flux. The LIDAR corrections worsen the flux reconstruction even further: the standard deviation increases from 12% to 15% and $1.2\,\sigma$ to $1.6\,\sigma$. As previously observed, the LIDAR corrections can cause a downward flux correction in some cases. The results without corrections in the transmission bin $0.82 < T_{9\,\mathrm{km}} < 0.9$ show offsets of up to around -18% for all three zenith ranges. After corrections, the distributions become well-centered, except in one case, where -10% remains. For $0.65 < T_{9\,\mathrm{km}} < 0.82$, the corrections reach a similar improvements. In the lowest transmission region, $0.5 < T_{9\,\mathrm{km}} < 0.65$, an improvement from $(-52 \pm 3)\%$ to $(-22 \pm 4)\%$ and from $-3.5\,\sigma$ to $-0.7\,\sigma$, respectively, can be observed at low zeniths. A deviation of the mean from the origin remains after correction, but the distribution of individual nights is close to the origin. A few nights with better statistics show some strong remaining offset. The general wider spread of percental deviations can be attributed to the worse statistics in this low aerosol transmission

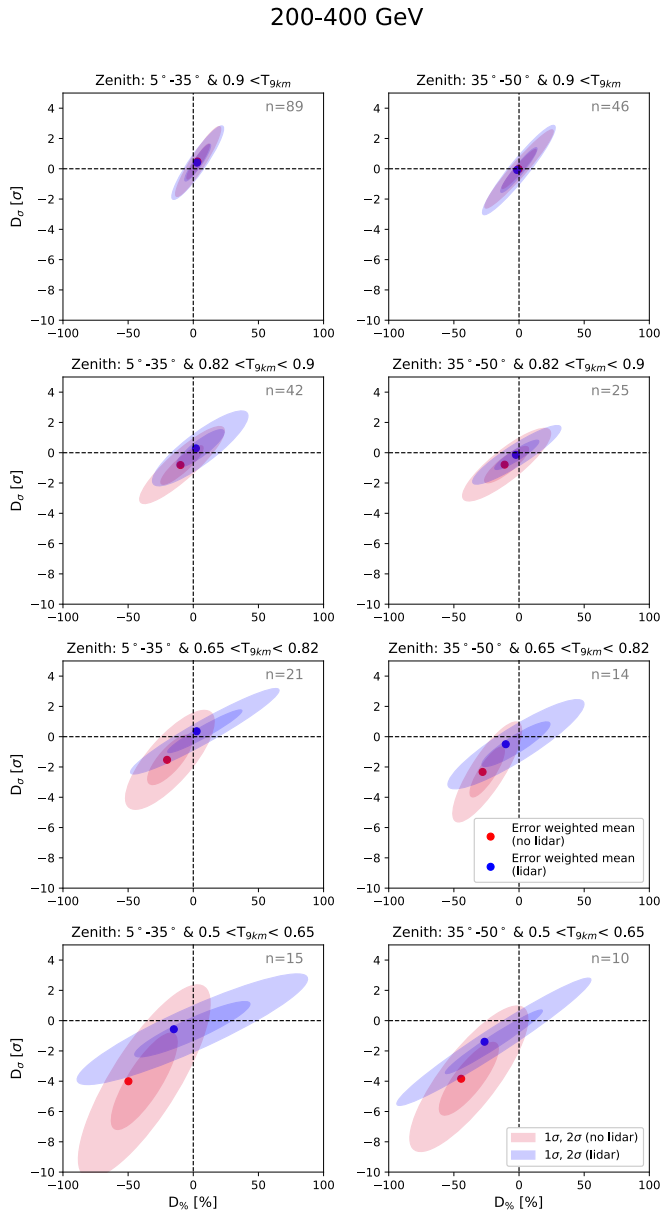

Figure 5.7: Error-weighted mean percental and mean statistical deviation of the flux between 200 GeV and 400 GeV from the reference spectrum shown without (red dot) and with (blue dot) LIDAR corrections for six zenith and aerosol transmission $T_{9\,\mathrm{km}}$ bin combinations. The shaded areas give the error ellipses at 1σ and 2σ. The number of averaged nights, n, is provided in the top-right corner of each plot.

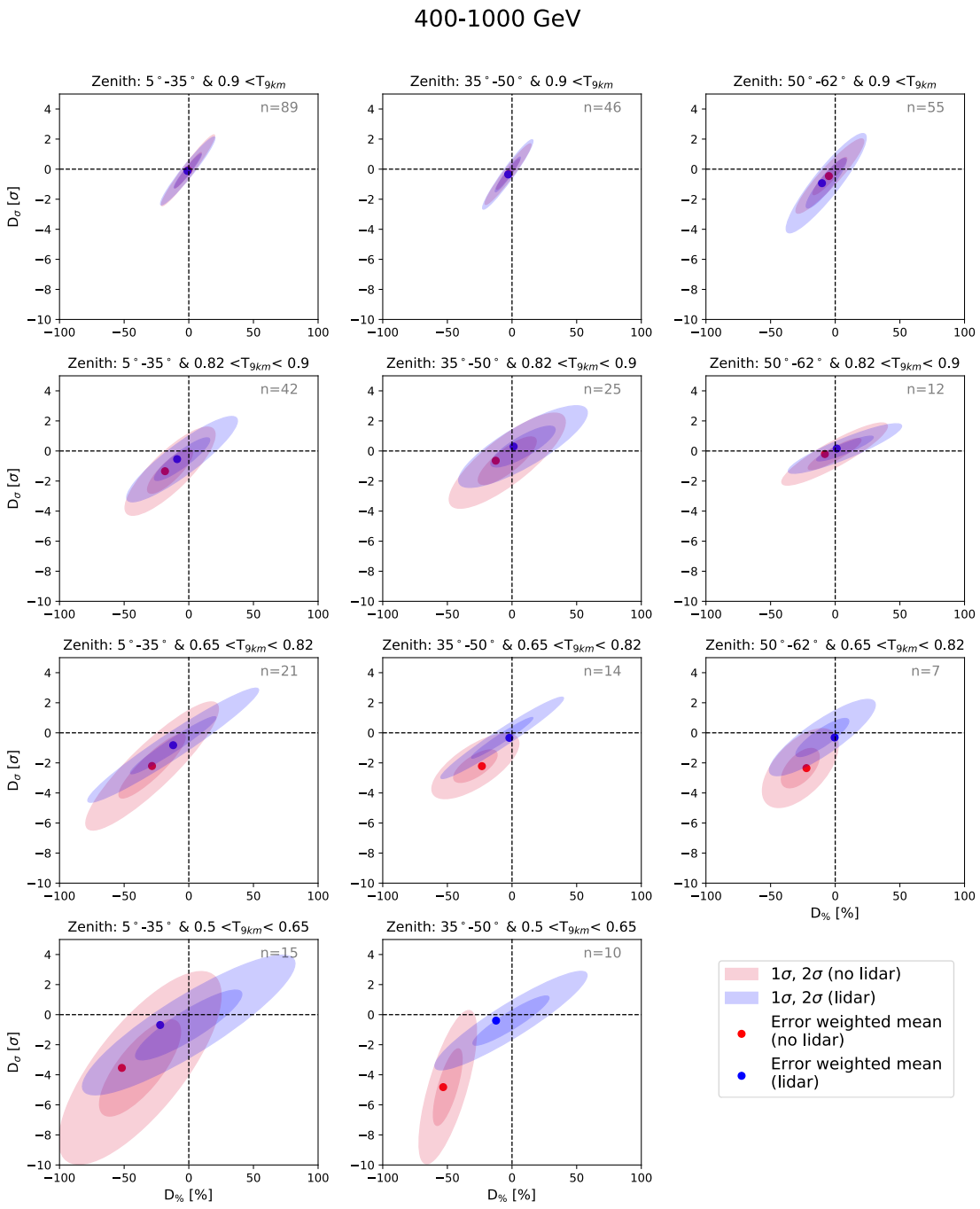

Figure 5.8: Same as Figure 5.7, but for the energy region between 400 GeV and 1 TeV. Sufficient data are unavailable in the low aerosol transmission under a high zenith bin.

bin. A strong improvement is achieved at medium zeniths, with a remaining systematic offset of $(-12 \pm 5)\%$ from the origin. In the zenith angle region above 50°, there is again not sufficient data available to conclude.

Lastly, Figure 5.9 shows the results obtained for the energy region above 1 TeV. No difference between uncorrected and corrected data for low and medium zenith angles can be recognized in the top row. At high zeniths, the LIDAR corrections lead again to a broader distribution of deviations and slightly less centered mean values. For high aerosol transmission, $0.82 < T_{9\,\mathrm{km}} < 0.9$, the results are also comparable to the previous energy ranges. Low offsets from zero without corrections are significantly reduced to below -15% on average after corrections. In the medium aerosol transmission bin, $0.65 < T_{9\,\mathrm{km}} < 0.82$, the corrections work well for the two higher zenith bins. At low zeniths, an offset of $(-16 \pm 4)\%$ persists after corrections. The surprisingly worse performance in this realm might be due to a few outliers resulting from the limited event statistics at such high energies. At lowest aerosol transmissions, $0.5 < T_{9\,\mathrm{km}} < 0.65$, conclusions are also comparable to those obtained from previous energy ranges: at lowest zeniths, data are strongly corrected but still show a bias of around $(-15 \pm 6)\%$ from the origin after correction. At medium zeniths, a high discrepancy of about $(-36 \pm 6)\%$ remains. Again, insufficient data are available in the zenith angle region above 50°. Generally, the offsets observed for all uncorrected data are larger than those obtained at lower energies, reaching $\lesssim -60\%$ in the lowest transmission bin. This can be interpreted as a result of the spectral softening at higher energies: the steeper the spectrum, the larger the effect of a wrongly reconstructed energy on the resulting flux. Additionally, the ellipses are much wider along the horizontal axes. This results from the lower event statistics above 1 TeV. The width of the distributions in terms of statistical significance remains very similar to the previous energy ranges.

5.4 Comparison of the two methods of LIDAR corrections with period-averaged data

All reported results so far have been obtained from averaging over multiple single-night spectra. In this section, I have combined data spanning over the entire period of the data set and across different analysis periods into single spectra, only separated by zenith angle and aerosol transmission. This leads to the smallest statistical uncertainties for a given aerosol parameter region. Figure 5.10 shows the estimated SEDs without applying LIDAR corrections (red) and those obtained after applying both types of correction algorithms, described in the sections 4.3.3 for Method I and 4.3.4 for Method II. The blue SEDs correspond to the second method used to obtain all previous results. SEDs obtained with the first method are shown in purple. The observation time corresponding to the used data is provided in the top-right corner of each panel. The displayed reference spectrum (green) has been obtained by combining all data (used for the respective period-wise references) into a single spectrum, which was subsequently fitted to a log-parabola (resulting fit: f=(6.96±0.03)·10^{-10} TeV $\mathrm{cm}^{-2}\mathrm{s}^{-1}$, a=-2.238±0.006, b=0.485±0.007). This period-averaged reference spectrum provides the shape parameter b, which had been fixed for all individual spectral fits of the previous sections analogous to before. To make uncertainties better comparable, the reference spectrum of Figure 5.10 and 5.11 was then fitted with the shape parameter fixed, yielding the shown statistical uncertainty band. For a more detailed representa-

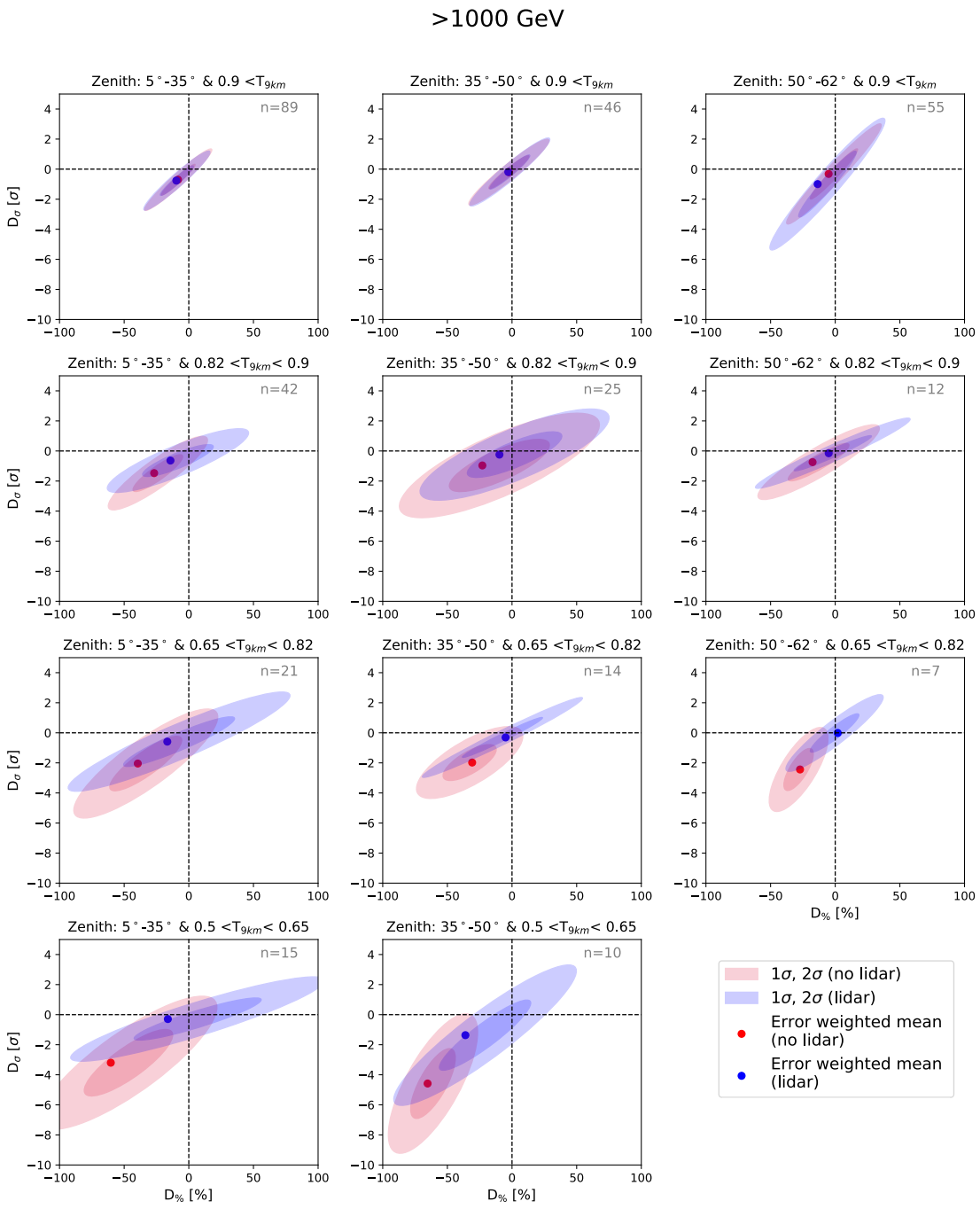

Figure 5.9: Same as Figure 5.7, but for the energy region above 1 TeV. Sufficient data are unavailable in the low aerosol transmission under a high zenith bin.

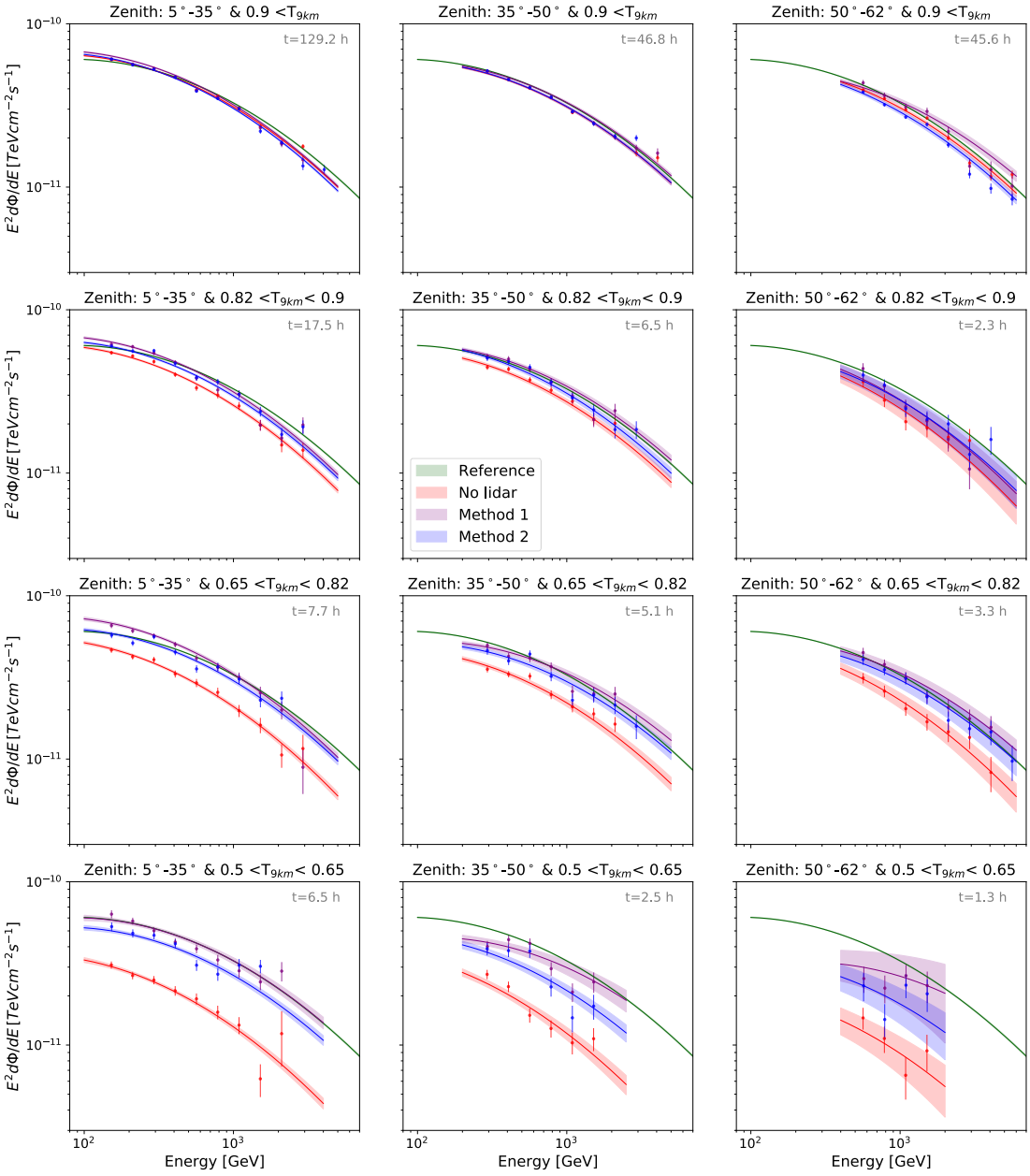

Figure 5.10: Period-averaged SEDs and corresponding flux points for nine different zenith angle and atmospheric transmission bins without (red) and with either type (purple and blue) of LIDAR corrections. The reference spectrum is given in green. The shaded areas correspond to the 1σ contours. The effective time of the data used for the individual spectra is displayed in the top-right corner of each subplot.

tion, Figure 5.11 shows the residuals regarding the relative difference concerning the reference SED.

The results from this combined spectral analysis support previously drawn conclusions: the spectra taken under good aerosol conditions, $T_{9\,\mathrm{km}} > 0.9$, and low zeniths show that the flux normalization is fitted correctly with both methods with a slight observable divergence for the spectral tilt. A similar behavior already became apparent in the top-left part of Figure 5.6. At medium zeniths, all three spectra show deviations below 10%, with the corrections barely altering the spectra. In the high zenith bin, Method I corrects the spectrum slightly harder than the reference. Method II causes a marginal downward flux correction and, with that, does not improve the uncorrected SED.

In the second row, the results for high aerosol transmissions ($0.82 < T_{9\,\mathrm{km}} < 0.9$) are displayed. The spectrum without corrections at zeniths below 35° is reconstructed to be too soft, which leads to a discrepancy from the reference of up to 30% at a few TeV. Both correction methods upscale the flux but fail to recover the correct spectral tilt accurately. On the other hand, Method I corrects the flux normalization stronger than Method II and crosses the reference spectrum at around 500 GeV. The normalization for Method II coincides with the reference at 200 GeV. In the medium zenith range, Method I reconstructs compatibility with the reference, whereas Method II produces a spectrum that is too soft. Both LIDAR correction methods have similar results at high zenith angles, achieving corrections very close to the reference spectrum, with a slight under-reconstruction.

In the aerosol transmission bin ($0.65 < T_{9\,\mathrm{km}} < 0.82$), the LIDAR corrections can substantially improve the distorted spectra. Before corrections, deviations range from 20% for low energies upwards to 50% for high energies. All three spectra show a stronger spectral tilt compared to the reference. At low zeniths, the flux normalization of the corrected spectrum of Method I crosses the reference spectrum at about 1 TeV, leading to an over-correction for lower energies. Method II normalizes the flux correctly at around 150 GeV, resulting in a good overall agreement but a slight under-correction at higher energies. In the medium zenith bin, both methods slightly overestimate the spectral tilt (i.e., too steep spectra), with flux crossings at 700 GeV (Method I) and 7 TeV (Method II). At the highest zeniths, the uncorrected spectra again show a steep spectral tilt, which is correctly reconstructed by both methods. The statistics, however, become relatively low here.

For the lowest aerosol transmission bin ($0.5 < T_{9\,\mathrm{km}} < 0.65$) and at low zeniths, Method I is able to fully correct the original deviations from 40% up to 70%. Method II shows a relatively constant remaining deviation of ∼15%, after correction, across the entire energy range. At medium zeniths from 35° to 50°, the deviations without LIDAR lie between 50% and 75%. Method I reconstructs a slightly too flat spectrum crossing the reference at 2.5 TeV. Method II underestimates the spectrum by 25-35%. For the highest zenith bin, only 1.3 h of data are available in total, which results in poorly constrained spectra. Method I reconstructs the spectrum compatible with the reference. Method II results in too low reconstructed fluxes.

Altogether, both LIDAR data methods to correct spectra obtained with IACTs work well in most domains. Method I almost always produces corrected spectra compatible with the reference, whereas Method II seems to insufficiently correct throughout.

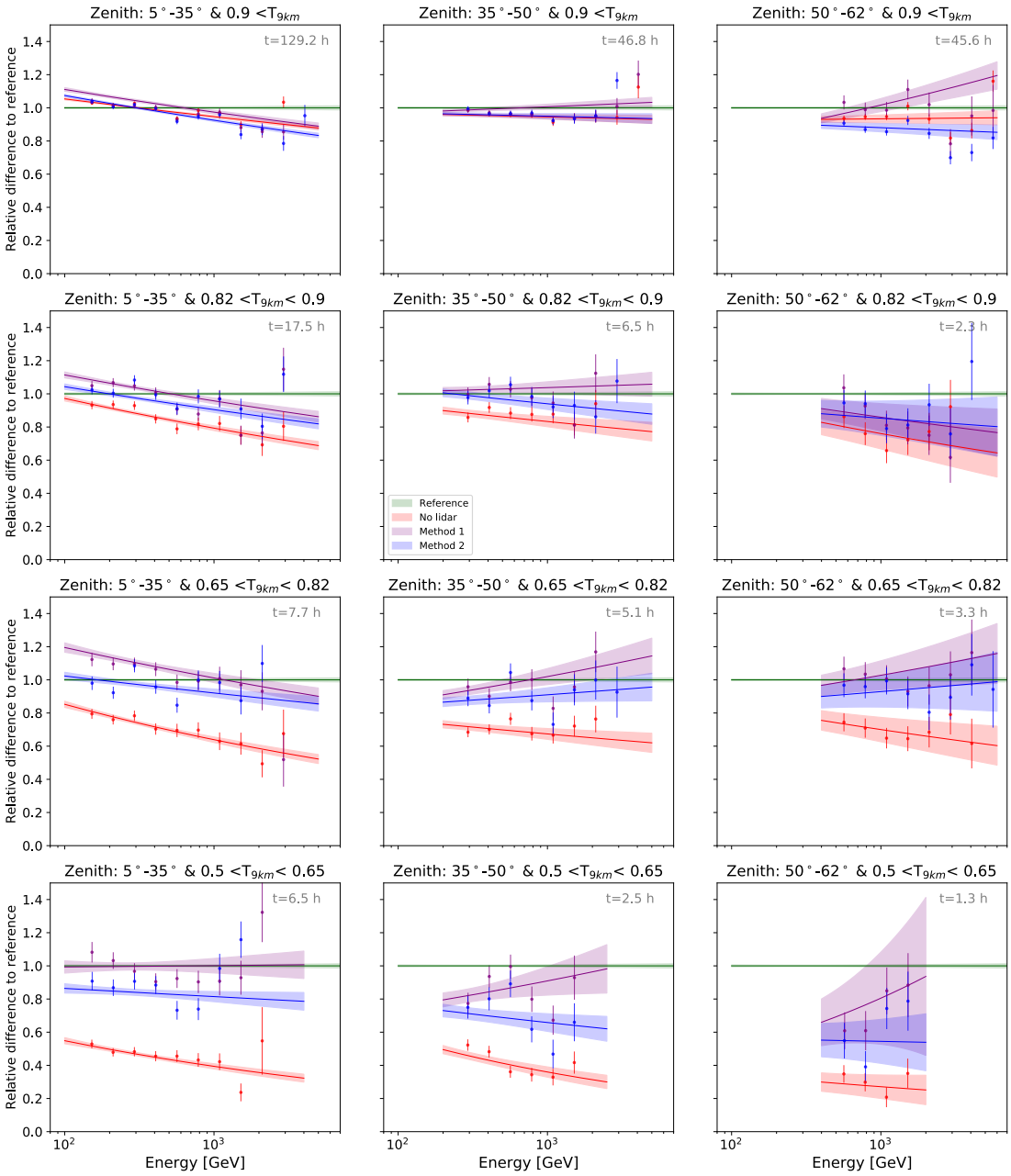

Figure 5.11: Relative difference between the period-averaged spectral fits and flux points to the reference spectrum for nine different zenith angle and atmospheric transmission bins without (red) and with either type (purple and blue) of LIDAR corrections. The reference spectrum is given in green. The shaded areas correspond to the 1σ contours. The effective time of the data used for the individual spectra is given in the top-right corner of each subplot.

5.5 Discussion

5.5.1 Systematic uncertainties

In the following, a detailed discussion of the systematic uncertainties of the LIDAR corrections is given. The uncertainties can be classified into three major categories: uncertainties originating from the LIDAR hardware and its data analysis, those related to the combined LIDAR and IACT observation modes, and lastly, those arising from the IACT data correction.

LIDAR hardware and transmission profile extraction

The first primary source of uncertainties originates from the LIDAR and the aerosol transmission profile extraction. The LIDAR hardware, the aerosol extinction profile reconstruction method, and associated systematic uncertainties are extensively described in Fruck et al. (2022b). The absolute calibration of the LIDAR leads to an accuracy of $\lesssim$2%. For unfavorable Cherenkov light emission heights, like those located inside an extended aerosol or cloud layer, assumptions on the LIDAR ratio do affect the accuracy of reconstructing the aerosol transmission from that point to its base height. In that case, the accuracy is estimated to be about 0.1 times the optical depth of that layer.

The wavelength correction of the aerosol extinction coefficients, described in section 4.2.3, introduces a systematic uncertainty of 0.5% for the ground layer transmission during clear nights and up to 5% for the case of nights affected by strong calima. A neglected but most likely small bias is introduced due to the use of diurnal Ångström coefficients for nocturnal observations.

In order to investigate the influence of cloud movements, the difference of subsequent LIDAR shots affected by clouds is sampled. Figure 5.12 (top row) shows histograms of the differences in cloud transmissions for subsequent LIDAR shots every 3-4 min. The three columns show different seasons. All data have been selected such that at least one of the two data sets separated by the given time span contains at least one cloud, and both belong to the same tracked sky coordinates. The distributions are normalized, meaning no information about the relative occurrence frequency of clouds between seasons can be read from the plots. All distributions show a double-Gaussian (shown in a logarithmic scale) structure that suggests two types of cases: case 1 represents both LIDAR profiles seeing the same cloud and produces the narrow part of the distribution, whereas case 2 shows the wider distribution and corresponds to cases, where only one out of the two subsequent LIDAR shots observes the cloud. When different parts of a cloud move through the FoV of the LIDAR during its data taking or when the LIDAR FoV covers several substructures of a cloud at the same time, uncertainties $\lesssim$2% are obtained (as can be seen by the values obtained for σ_1 and $Prob_1$ in Figure 5.12, top, representing width and relative area of the thinner of the two Gaussians fitted). This affects about 55%-80% of the cloud data. Additionally, it may be possible that the cloud moves through the LIDAR FoV during its exposure, and parts of the laser returns are already characterized by the absence of clouds. This scenario is sketched in the upper part of Figure 5.13. It is estimated that $<$44% of cloud observations during winter, $<$22% during spring, and $<$31% during summer are impaired by rapid cloud movement (see the values obtained for σ_2 and $Prob_2$ in Figure 5.12, top) with associated uncertainties ranging from 8% to 12%. It must be emphasized that the analyzed Crab Nebula

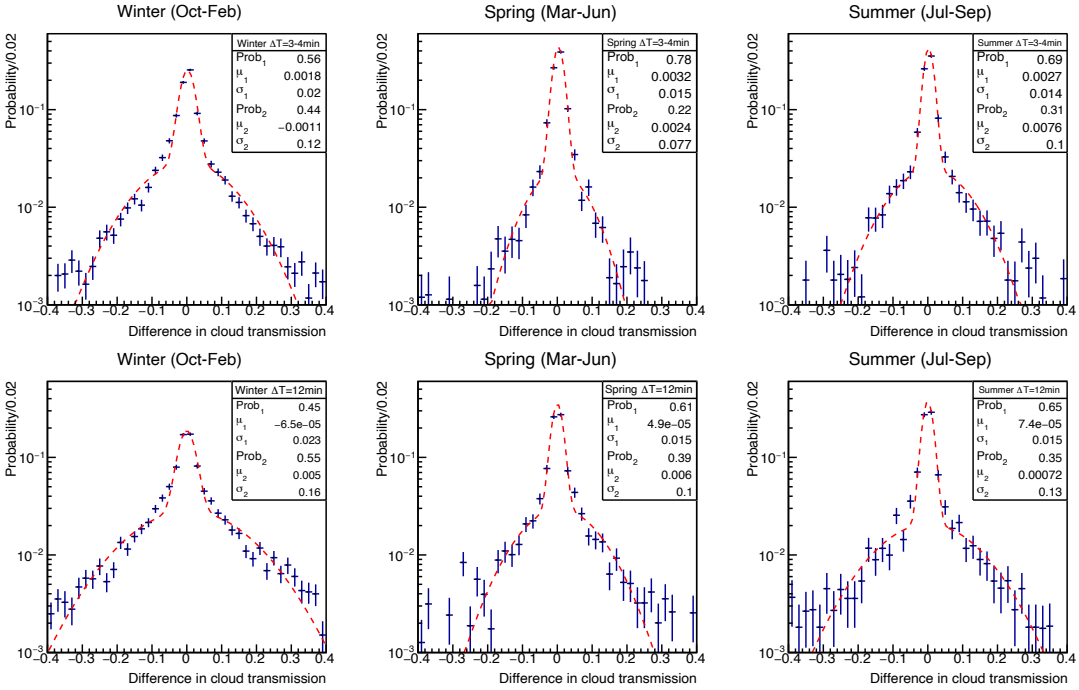

Figure 5.12: Differences in cloud transmission for LIDAR data sets separated by three or four minutes (top, according to the LIDAR operation schemes before or after 2016; see Fruck et al. (2022b)), or by 12 minutes (bottom). The columns show the separation by seasons: the winter months, where the highest cloud fractions are observed (left); the spring months, with the lowest cloud fraction (center); and the summer months (right). The bin width of the difference in transmission is 0.02. [Plot produced by M. Gaug and taken from Schmuckermaier et al. (2023)]

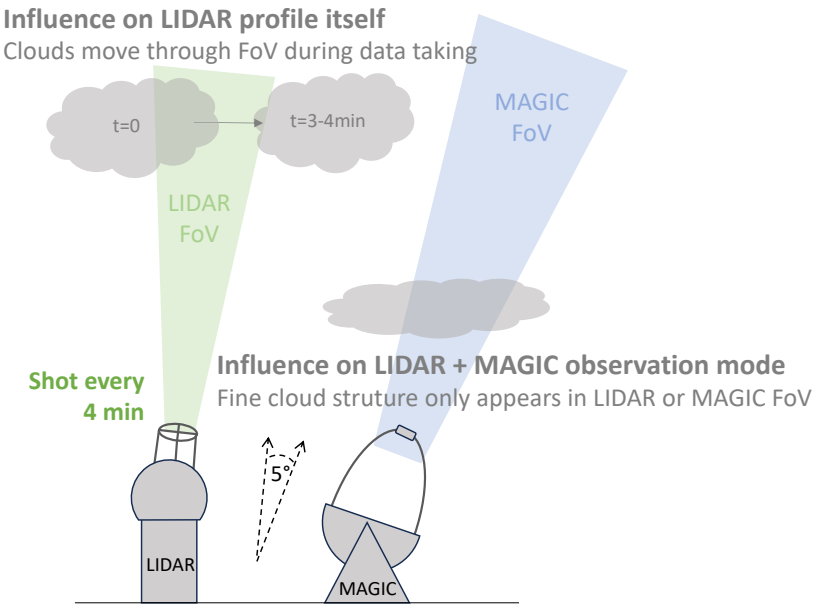

Figure 5.13: Sketch of two example scenarios, in which the movement and structure of clouds influence the uncertainties of the correction method. Top left part: cloud movement during data taking influences the extraction of the transmission profile. Bottom right part: A localized cloud only visible in the FoV of MAGIC, which leads to an under-correction of the data.

test sample in this thesis shows a high prevalence of winter data. The Crab Nebula can only be observed with MAGIC from September to April. Hence, most of the data were taken during the colder winter months, when the influence of clouds above the MAGIC site is more substantial. The phenomenon of calima usually, but not exclusively, occurs from July until September and is therefore under-represented in my data set. Thus, the previously described uncertainty may overly affect the tested data sample. Uncertainties of such type can only be reduced through faster sampling LIDARs, which operate with shorter exposure times and higher sampling rates.

Combined LIDAR and IACT observation modes

To avoid shooting the laser into the FoV of the MAGIC telescopes, the LIDAR tracks the telescopes with an offset of 5°. In the case of extended aerosol layers, e.g., calima or extended clouds, the mismatch between observed and characterized FoVs produces a negligible error. But in the case of very localized layers, e.g., fine cirrus clouds, this can lead to a stronger discrepancy between the estimated transmission profile and the real aerosol transmission that has affected the Cherenkov light detected by the IACT. In the worst case, science data affected by such a thin cloud may remain completely uncorrected. This scenario is sketched in the bottom part of Figure 5.13, where a cloud is in the FoV of MAGIC but is not registered by the LIDAR. In contrast, other data in temporal proximity become over-corrected because the cloud has moved out of the FoV of the IACT but into the one of the LIDAR. Typical cloud base heights that cause such

effect lie above 8 km above sea level at La Palma (Gaug et al., 2022), which affects particularly low-energy gamma-ray events by this effect. Cherenkov light of showers with higher energy gets emitted largely below such clouds. Figure 5.12 (bottom row) shows differences in cloud transmission for LIDAR profiles separated by 12 min, which is the typical time that the FoV of the MAGIC telescopes will enter the line of sight characterized by the LIDAR during regular tracking. Analogous to before, all distributions show a double-Gaussian structure on a logarithmic scale, again suggesting two types of cases: a cloud observed in both data sets or a cloud observed in only one. From the fits of these distributions, it can estimated that up to 55% of the data (particularly during winter) affected by cirrus suffer from such a FoV mismatch, which leads to an uncertainty of the estimate of the aerosol transmission proportional to about half the clouds optical depth at low energies (i.e., up to 8% in transmission correction; see values for $Prob_2$ and σ_2 shown in Figure 5.12, bottom), and about 20% to 30% of it for the higher energies, resulting in an estimated $\sim$6% error on the transmission correction.

Gamma-ray data correction method

The previous correction of the gamma-ray event energy requires an estimated emission profile of the Cherenkov light. Monte Carlo simulations imply that a Gaussian profile can describe the longitudinal shower evolution well, while the shower maximum has to be determined from stereo reconstruction.

A detailed discussion of the reconstruction accuracy of the shower maximum is given in Schmuckermaier et al. (2023), where the bias, μ_{max}, and the fluctuations around it, i.e. the uncertainty σ_{max}, of the maximum are shown separately for low and high zeniths derived from extensive simulations. The bias increases the systematic uncertainty of the full-spectrum reconstruction, whereas the uncertainty of the reconstruction mainly affects the energy resolution. Figure 5.14 shows a sketch of the relevant parameters and their uncertainties for the correction method, which will be discussed in the following.

From the simulations, an average reconstruction bias of $\mu_{\text{max}} \lesssim 0.8$ km in the dominant range (e.g., from 9 km to 12 km above sea level of shower maxima at vertical incidence) can be estimated. For a typical width of cirrus clouds of $\bar{w}_{\text{cloud}} \sim$2.5 km (Fruck et al., 2022b), the effect roughly scales with the ratio of $\mu_{\text{max}}/\bar{w}_{\text{cloud}} \approx 0.3$ times the aerosol transmission of cirrus. In my Crab Nebula test sample, about half the data are affected by cirrus clouds, reducing the overall influence of this effect on the data set by around half.

As previously stated, the uncertainty on the shower maximum height adds to the energy resolution for data affected by clouds. An average uncertainty of $\sigma_{\text{max}} \sim$1.5 km is derived from simulations. Since $\Delta E_{\text{corr}}/E_{\text{corr}} = \Delta T/T$, and $\Delta T/T$ is proportional to $\sigma_{\text{max}}/\bar{w}_{\text{cloud}}$, this leads to a resolution of the correction of about $0.6 \cdot (1 - \overline{T}_{\text{aer}})$. This needs to be added quadratically to the energy resolution of $\sim$16% (Aleksić et al., 2016c).

The width of the longitudinal emission profile is also dependent on the energy. It fluctuates around the most probable value for a given energy with a standard deviation of $\sigma_{\text{width}} \sim 10-15\%$ (Fruck, 2015). Fluctuations of the shower width, in combination with a cloud layer crossing the atmospheric air shower, primarily lead to an impairment of the energy resolution, similar to the case of the air shower maximum reconstruction. Assuming a linear growth of extinction

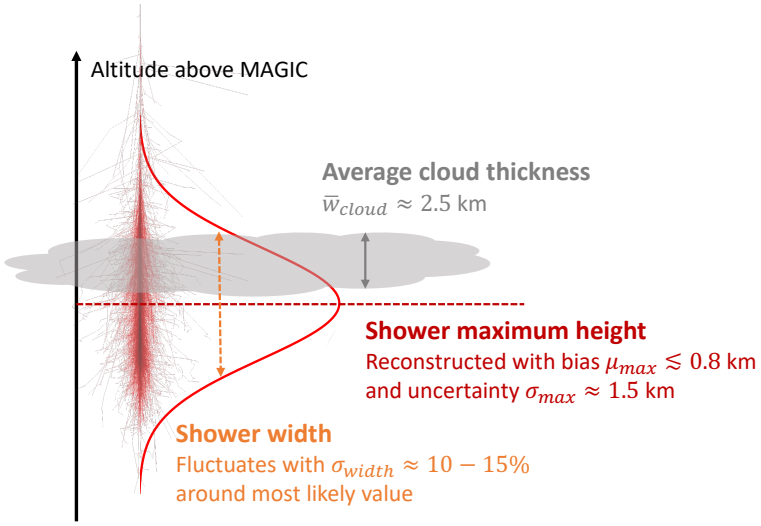

Figure 5.14: Sketch of the shower and cloud parameters and their corresponding uncertainties. The red distribution shows the Gaussian approximation of the Cherenkov light emission of a shower used for the energy correction. Values in orange and dark red denote the width and maximum emission height derived from the Gaussian model as well as the stereo reconstruction.

across the cloud layer, this leads to a small bias of 0.05 influencing the correction on the energy and an estimated contribution of $0.3 \cdot \overline{T}_{\text{aer}}$ to the energy resolution itself.

Table 5.3 summarizes the systematic uncertainties described so far relative to $\overline{T}_{\text{aer}}$. It must be noted that many of the listed uncertainties may be correlated.

Lastly, the underlying assumptions and approximations made in Method I and II lead to intrinsic systematic uncertainties. The observed fluctuations in this study, which are beyond what is expected from statistical fluctuation, can be used to characterize the overall systematic uncertainties. One can then compare these fluctuations with the sum of the previously estimated uncertainties. The remainder can then be attributed to the methodological assumptions.

Comparison with excess fluctuations

It has been shown in Garrido et al. (2013) that the relative energy reconstruction bias $(E_{\text{corr}} - E_{\text{est}})/E$ scales roughly as $1/\overline{T}_{\text{aer}}$, and therefore additional systematic uncertainties on the energy scale are expected to roughly scale $\propto \Delta\overline{T}_{\text{aer}}/\overline{T}_{\text{aer}}$. Similarly, the flux reconstruction biases $(F_{\text{corr}} - F_{\text{est}})/F$ at a given energy scale as $\overline{T}_{\text{aer}}$ in first order Garrido et al. (2013). The LIDAR correction-induced systematic uncertainty on a SED normalization is expected to scale roughly as $\propto \Delta\overline{T}_{\text{aer}}/\overline{T}_{\text{aer}}$.

These relations can be used to derive predictions for the systematic uncertainties, which can be compared to the corrected and uncorrected data set. The systematic uncertainties of the data set are estimated by calculating so-called excess fluctuations. These are given by the square root

Table 5.3: Systematic uncertainties for the aerosol optical depths that affect the correction of MAGIC data. Top part: Uncertainties originating from LIDAR hardware and profile extraction. Middle part: Uncertainties influencing the correction method. Bottom part: Uncertainties influencing the primary energy estimation in the case of clouds.

Type	clouds (%)	calima (%)	this sample (%)
Uncertainties on optical depth of layer - LIDAR only			
Absolute calibration of LIDAR	–	2	1
Light emission inside layer / assumptions LR	10	$\ll 10$	$\lesssim 6$
Color correction	< 1	< 5	$\lesssim 1$
Larger LIDAR FoV than cloud substructures	2	–	1.5
Rapid cloud movement during LIDAR exposure	12	–	6
Quadratic sum for optical depth	16	< 8	$\lesssim 9$
Systematic errors on $\overline{T}_{\text{aer}}$ - data correction			
Rapid cloud movement / mismatch obs. vs. char. FoVs	8	–	4
Air shower maximum reconstruction	$\lesssim 30$	–	$\lesssim 15$
Assumptions mean width air shower long. profile	$\lesssim 5$	–	$\lesssim 2.5$
Quadratic sum for $1-\overline{T}_{\text{aer}}$	$\lesssim 31$	–	$\lesssim 16$
Resolution on $\overline{T}_{\text{aer}}$ - energy resolution			
Air shower maximum reconstruction	$\lesssim 60$	–	$\lesssim 33$
Assumptions mean width air shower long. profile	$\lesssim 30$	–	$\lesssim 17$
Quadratic sum for resolution of $1-\overline{T}_{\text{aer}}$	$\lesssim 70$	–	$\lesssim 37$

Table 5.4: Comparison of estimated vs. observed systematic uncertainties after the LIDAR correction Method II. Predictions have been calculated from the total displayed in Table 5.3. Observed quantities refer to the average of the observations from three zenith-angle bins (e.g., displayed in Figure 5.5). Reduced quantities have been obtained from "observed," after quadratic subtraction of the excess uncertainty observed with the clear-nights reference spectrum.

$T_{9\,\text{km}}$ bin	Prediction uncertainty $\Delta\overline{T}_{\text{aer}}/\overline{T}_{\text{aer}}$	Observed bias for f	Observed excess fluct. for f	Reduced atm. excess fluct. for f
0.9 - 1.0	1%	$(0\pm2)\%$	$(6\pm3)\%$	$(4\pm5)\%$
0.82 - 0.9	3%	$(-2\pm2)\%$	$(8\pm1)\%$	$(7\pm2)\%$
0.65 - 0.82	7%	$(-5\pm4)\%$	$(18\pm4)\%$	$(18\pm5)\%$
0.5 - 0.65	15%	$(-11\pm4)\%$	$(16\pm8)\%$	$(16\pm9)\%$

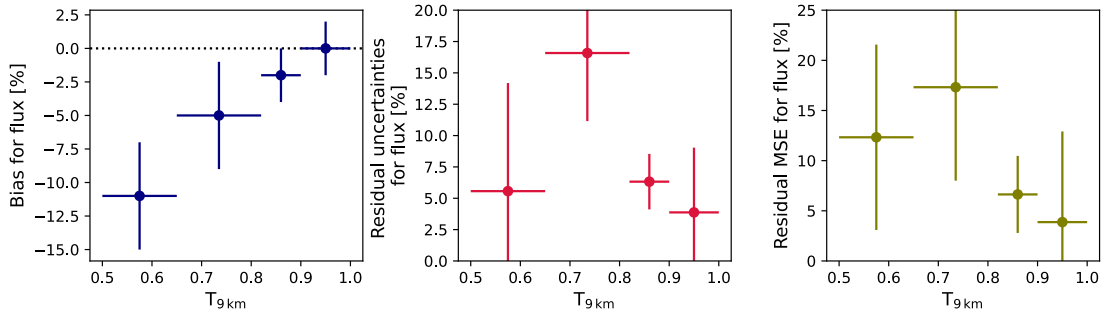

Figure 5.15: Residual flux reconstruction bias after corrections with Method II (left). Excess uncertainties are attributed to the method (i.e., after quadratically subtracting the second from the fifth column in Table 5.4) (middle). The mean squared error, as a function of aerosol transmission at 9 km above ground computed by quadratically adding the bias and method uncertainty (right).

of variances in excess of expected purely statistical fluctuations,

$$\sqrt{\mathrm{Var}(D_{\%}) - 100/(N-1)\sum_{i=1}^{N}(\Delta q_i)^2/q_{\mathrm{ref}}^2}, \tag{5.5}$$

using the data shown in figures 5.5 and 5.6. Given no systematic uncertainties, the observed variance of the data should match the predicted one by purely statistical fluctuations. Additionally, the 4% period-wise excess fluctuations on the flux observed in the absence of aerosol-induced atmospheric changes with data taken under perfect conditions (obtained in section 5.2) is quadratically subtracted from these to get purely the systematics attributed to the atmospheric conditions and corrections.

The results, together with residual biases for Method II, are presented in Table 5.4. No residual biases can be found within the available precision after correction, except for the flux reconstruction in the lowest $T_{9\,\mathrm{km}}$ bin from 0.5 to 0.65. The second column of Table 5.4 shows the predictions for the uncertainty of $\Delta\overline{T}_{\mathrm{aer}}/\overline{T}_{\mathrm{aer}}$ (obtained from the estimated systematics shown in Table 5.3). These can be compared to the excess fluctuations in the fourth column, observed for the flux reconstruction. These numbers have also been processed into Figure 5.15. The left plot shows the residual bias of the corrected flux normalization parameters of Method II. In the middle, the excess uncertainties attributed to the method are shown. These can be obtained by quadratically subtracting the predictions for the uncertainty on the transmission (second column in Table 5.4) from the observed and reduced excess fluctuations (fifth column in the same table). Lastly, the mean square error of Method II is shown in the right plot, which is computed by quadratically adding the bias and method uncertainty.

Within the available precision, $\lesssim$17% residual mean squared error must be attributed to the methodical assumptions made in Method II (see left image in Figure 5.15). For Method I, about $\lesssim$15% can be assumed since the bias is much smaller here. As previously stated, the MAGIC collaboration decided to move from Method I to Method II as the officially supported LIDAR correction method in 2018.

The residual uncertainties on the flux reconstruction could be attributed to changes in the Hillas parameters of events taken under suboptimal conditions. These do not necessarily resemble parameters of events of accordingly down-scaled energy and influence effective areas differently than the assumed scaling of energy at which the effective area is evaluated. Sobczyńska and Bednarek (2014) found that the shapes of the width and length parameter distributions are only slightly distorted by clouds at different altitudes, even if these are opaque. These findings support the assumptions of effective areas as a function of energy from cloud-affected data resembling those from clear nights after rescaling the energy. Should one go below the energy threshold of an IACT, this assumption breaks down (Garrido et al., 2013). At a higher zenith angle, where the energy threshold moves up, the effect is expected to be stronger on the spectral index. For Method I, this can be seen in Figure 5.11, where increasing observation zenith angles seem to "flip" the relative difference of the reconstructed spectral index from positive to negative values. Method II appears primarily unaffected by this effect but shows much larger discrepancies in the reconstructed flux.

The assumptions made for each method, i.e., the scaling of energy with inverse average transmission of emitted Cherenkov light (for both methods) and the scaling of event rate with effective area in Method I and the typical shift of effective area for all events ending up in the same $\overline{T}_{\mathrm{aer}}$ bin in Method II, may have introduced parts of the additional systematics. The assumption of energy scaling seems to be well supported by simulations (Doro et al., 2014). Simulations have not tested the other assumptions inherent to the two methods to a comparable extent. This implies that any future improvement of the atmospheric correction method must pay particular attention to improving the model for the effective area above all (Gaug, 2017).

5.5.2 Application to sources with different spectra or varying fluxes

The presented study has been carried out uniquely with Crab Nebula data, and one could ask to what extent the obtained results on correction accuracy apply to less hard spectra or varying sources, e.g., gamma-ray bursts (MAGIC Collaboration, 2019).

The key factor is the nature of the atmospheric phenomena that affect the IACT data: in the case of ground-layer aerosol, e.g., calima, systematic uncertainties can be considered independent of the respective spectral shape parameters in first order since for low zenith angle observations, the aerosol scattering layer is found well below the entire emission region of Cherenkov light. In that case, aerosol scattering is equal for all Cherenkov light irrespective of the shower height, and $\overline{T}_{\mathrm{aer}}$ becomes a constant independent of the shower energy (Holch et al., 2022). At large zenith angle observation and aerosol optical depths $\gtrsim 0.3$, the TeV gamma-ray energy range can be affected differently from the GeV range (Holch et al., 2022). Hard sources are then affected differently by corrections than soft ones. Nevertheless, $\overline{T}_{\mathrm{aer}}$ should correct for this dependence with the corresponding systematic uncertainties described in Table 5.3. In this scenario, no difference is expected in systematic uncertainties between stable and fast-varying sources since the aerosol conditions are themselves stable.

The situation changes for the case of cirrus clouds, typically at higher altitudes: the dominating systematics (i.e., mismatches between characterized and affected FoVs, rapid cloud movement during the exposure) can strongly affect varying sources if the timescale of the variability of the gamma-ray flux is comparable or longer than the variability timescale of the cloud layer.

In this case, it becomes impossible to disentangle atmospheric effects from intrinsic emission fluctuations from the source and residual systematics. The effect on reconstructed light curves and spectra can only be studied on a case-by-case basis involving detailed simulations. Suppose the gamma-ray sources are stable in emission. In that case, it can be assumed that the reconstruction of the low energy part of the spectrum gets corrected through larger values of $\overline{T}_{\mathrm{aer}}$ and consequently affected by larger systematics in the case of cirrus clouds. Such a scenario will lead to more considerable systematic uncertainties on the reconstructed spectral index of soft sources compared to hard ones. A quantitative estimate cannot be given here if the exact height of the cloud layer is variable or unknown.

5.5.3 Possible improvements of the method

The initial extraction of the transmission profile may be improved by substantial hardware upgrades or changes. In the following, a non-exhaustive list of example improvements is given.

Uncertainties stemming from rapid cloud movement within a single LIDAR shot can only be reduced through faster sampling LIDARs, which operate with shorter exposure times and higher sampling rates. Closely related, the uncertainties from the FoV mismatch of the LIDAR and MAGIC during rapid cloud mismatch could be decreased with a passive device following the exact FoV of an IACT (e.g. Ebr et al., 2021). Uncertainties of the assumptions about the LIDAR ratio inside cloud layers may be reduced in the future by using Raman LIDARs operating at multiple wavelengths (Gaug et al., 2019). As previously mentioned, Raman LIDARs operate at higher powers and can, therefore, only be used sporadically during observations, if at all. In addition, if used during twilight before operations, Raman LIDARs can provide precise estimates of the molecular profile of the atmosphere. Lastly, the uncertainty introduced by the mismatch of the average wavelength of Cherenkov light detected by MAGIC and the wavelength used by the LIDAR could be remedied through the use of a laser operating closer to the average Cherenkov wavelength or a system adding an additional UV line to the currently used green one (Gaug et al., 2019). Depending on the chosen power, this might cause more interference with regular observations, and the feasibility must be carefully reviewed.

However, it became apparent that the largest part of the uncertainty comes from the data correction method, namely the air-shower maximum reconstruction and the correction model used for rescaling energy and effective area. A possible method of improvement would be time-interval-wise simulations matching the observed aerosol extinction profile with that encountered by the LIDAR and simulating the full interaction of all gamma-ray showers with the observed clouds. This would significantly increase the complexity of the analysis and require a large amount of computational resources.

Chapter 6

The blazar Mrk 421 during its most violent year

At this point, the topic of the results presented in this thesis changes as the next two chapters focus on new astrophysical findings about the blazar Mrk 421. The first study, described in this chapter, is based on a data set taken around early 2010, which is the most active period of the source to date. At the time of writing this thesis, the study has been submitted as a publication and is under review by *Astronomy & Astrophysics*. It will be referenced as Abe et al. (2024) in the following. I am the lead author of the publication, as I analyzed the MAGIC and *Fermi*-LAT data, produced all the results, and wrote the manuscript. Axel Arbet-Engels contributed to the discussion of the results, by proofreading the draft, and providing a code base used for the variability and correlation analysis. David Paneque organized and coordinated the campaign, gathered much of the MWL data, and assisted with writing the discussion and proofreading. All other co-authors were involved in the low-level analysis of the remaining MWL data or are part of the MAGIC collaboration. The text and structure of the following chapter closely follow Abe et al. (2024), and parts of the text have been adopted verbatim.

6.1 Observations of Mrk 421 from 2009 to 2010

Since the beginning of VHE observations, Mrk 421 has been one of the most observed sources due to its brightness and proximity. Nevertheless, observations primarily focused on phases of high activity, such as the flare in 2008 (Donnarumma et al., 2009). In order to obtain a broader and deeper understanding of the source, observations of a variety of emission states, including low states, were required. This motivated the start of an extensive monitoring campaign in 2009, which continues to this day. New instruments, such as the *Fermi* Gamma-ray Space Telescope, launched in June 2008, allowed full coverage of the electromagnetic spectrum from radio to VHE for the first time. The 4.5 month-long campaign in 2009 found Mrk 421 in a typical, non-flaring state of activity and could show that certain behaviors, such as the correlation between X-rays and VHE gamma rays, are also found during states of average activity (Aleksić et al., 2015a). The unprecedented MWL coverage also enabled a view at the full SED, which could be modeled by both a leptonic as well as a hadronic model (Abdo et al., 2011).

As a continuation, a dense monitoring campaign was performed from November 2009 to June 2010. During this period, Mrk 421 showed much stronger activity, even compared to all previous

campaigns. In the beginning of 2010, around mid-January, the source started to produce a flare lasting multiple days and reaching almost 3 Crab Units (C.U., the flux emitted by the Crab Nebula in the same energy range) above 200 GeV. The flare was the subject of a PhD thesis focusing on the low-level MAGIC analysis and SED modelling (Steinke, 2012), but no further publication followed. In February 2010, the Very Energetic Radiation Imaging Telescope Array System (VERITAS) observed the highest VHE flux ever recorded from Mrk 421 (Abeysekara et al., 2020). Due to adverse weather conditions, the MAGIC telescopes could not observe during the same days. The highest flux measurement reached a level of ∼27 C.U. above 1 TeV, making it the largest VHE gamma-ray flux ever recorded for an AGN. The resulting high photon statistic during such a flaring activity allowed for a binning of the flux in 2-minute intervals. A cross-correlation study with the optical band revealed a significant positive correlation with a time lag of ∼25-55 minutes. Additional correlation studies between the VHE and X-ray bands showed a complex and fast-varying correlation from linear to quadratic behavior down to no correlation at times. Shortly after, in March 2010, a decaying flare was detected by the MAGIC and VERITAS telescopes (Aleksić et al., 2015b). A detailed and broad MWL coverage enabled the construction of 13 consecutive daily SEDs, which could be described by the emission of a one-zone SSC model. The variation of only a few model parameters successfully describes the SED variation and makes the underlying particle population a very plausible cause of the variable emission. However, the manuscript also mentioned that a leptonic scenario with two zones (an extended and a compact one) would be a more natural way of explaining the broadband SED variations during this flaring activity.

As the final step, I now exploit the campaign's full potential by combining the complete data set from November 2009 to June 2010. This wealth of data allows for a detailed study of the variability and correlation behavior of Mrk 421 during its most violent recorded year.

6.2 MWL observations and data analysis

MAGIC

I selected the MAGIC data for the time period from November 11, 2009, (MJD 55149) until June 16, 2010, (MJD 55363). The MAGIC telescopes observed Mrk 421 for a total of 62.4 h during 94 nights in the zenith angle range from 5° to 50°. I performed the analysis using the MAGIC Analysis and Reconstruction Software (MARS; Zanin et al., 2013b; Aleksić et al., 2016a). The final data are selected based on quality criteria to exclude periods with unfavorable weather conditions or too bright moon.

Since the campaign took place long before the LIDAR was installed, alternative methods must be used to estimate the atmospheric quality. For once, I applied a cut on the so-called cloudiness. Cloudiness is a parameter ranging from 0 to 100 derived from sky temperature measurements by a pyrometer. The cloudiness only provides a coarse estimate of the atmospheric conditions, and its correlation to the actual atmospheric transmission is broadly dispersed. Figure 6.2 shows the correlation of LIDAR and pyrometer measurements over 2 years, excluding cases of calima. An overall trend is visible, but the spread is rather large. In my analysis, I chose an upper cloudiness value of 40. This excludes periods of very strong cloud coverage that otherwise

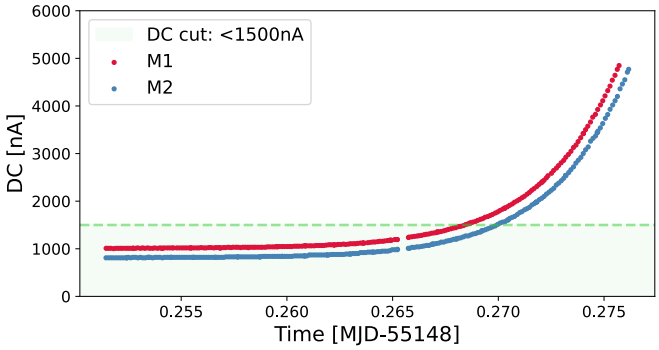

Figure 6.1: Median PMT anode currents (DC) in both MAGIC cameras (M1 and M2) on November 13, 2009.

affect the accuracy of the flux reconstructions. On the other hand, I still keep the majority of data with an estimated transmission of above 0.8.

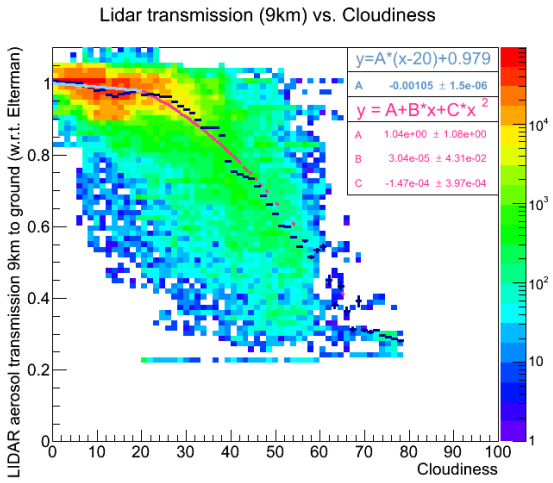

Figure 6.2: Correlation of 2 years of LIDAR transmission from 9 km to ground (without calima) and simultaneous cloudiness data from the pyrometer (plot taken from Betorz (2015)).

In addition, I apply a cut on the rates of events seen by the telescope. To only consider the rates of events relevant to my analysis, I look at the rates of events that have a size of 50 or above (see section 3.3 for an explanation). Too low rates indicate poor atmospheric quality, which reduces the number of events seen by the telescopes due to the higher aerosol content. Excessively high rates are caused by a sudden increase in the light that triggers the telescope. This can be caused by a car driving past the telescopes with its headlights on, or by excessive background light from the moon. I tried to compromise between the two limits by setting a lower threshold of 50 Hz and an upper limit of 150 Hz.

The data were also selected for low moonlight conditions in order to limit contamination from too high night sky background light (Ahnen et al., 2017c). I used a median DC limit of

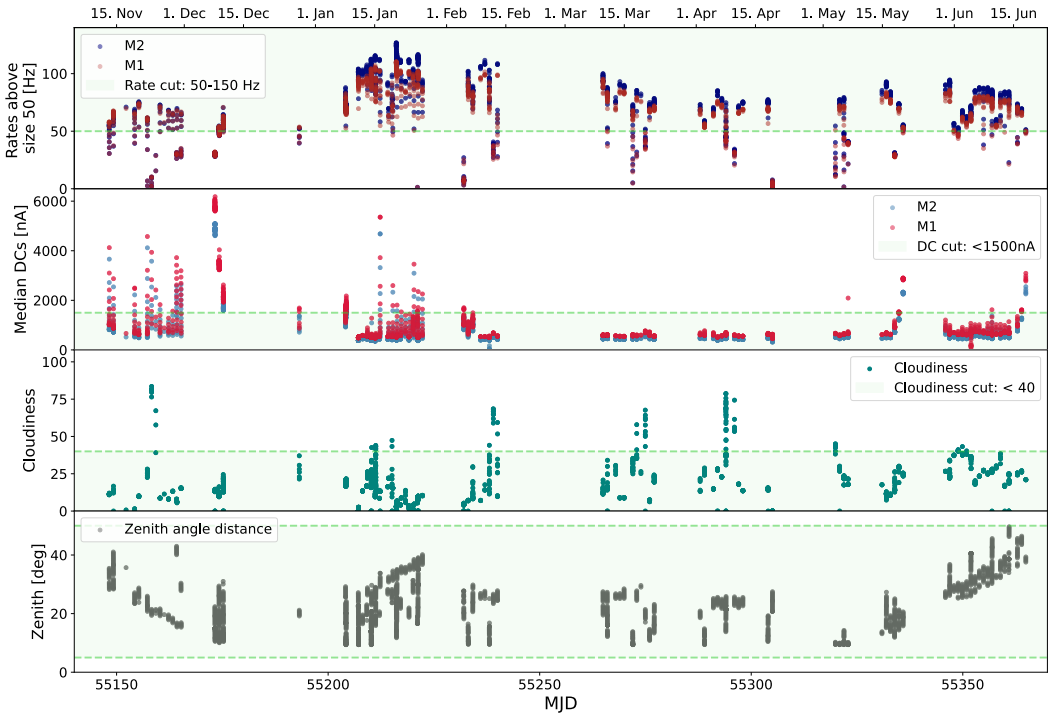

Figure 6.3: Quality selection for the MAGIC data between November 2009 to June 2010. The upper panel shows the rates of events with size above 50; the second panel shows the PMT anode currents to reduce excess background light; the third panel shows the cloudiness and the fourth panel shows the distribution of zenith angle distances.

1500 nA in both cameras. As an example, Figure 6.1 shows the course of the median PMT anode currents, usually abbreviated as DC, during the moon's rise on November 13, 2009. As the moonlight increases, the DC goes up rapidly. The data with a DC above 1500 nA is excluded on such a night.

Figure 6.3 shows a summary of the quality parameters of the data and all applied quality cuts as light green bands. Each dot represents a sub-run of MAGIC data covering only a few minutes of data. The first row shows the rate cuts above size 50. The second row shows the median DCs, where one can clearly see phases where the moon influences the data the most, such as the first two months of data. The third row shows the distribution of cloudiness. The last row displays the zenith angle distances. No data is rejected by this cut since I include the range from 5° to 50°. After applying these quality cuts and excluding nights with technical problems, 50.1 h of data remained. From the initial 94 nights, 74 remained.

In the following study, I focus on the variability and correlations of different energy bands. Therefore, I only use light curves that report the integrated VHE gamma-ray emission of Mrk 421 as a function of time, as described in section 3.3. Due to the high gamma-ray brightness of Mrk 421, two separate light curves can be constructed in the VHE band covering two energy ranges: 0.2-1 TeV and >1 TeV. As will be shown later, there is additional VHE data taken by VERITAS as part of the MWL campaign, which has been published. It covers some days in February and March at a flux of above 0.2 TeV. In order to create a joint light curve, I also constructed a third light curve from the MAGIC data for this open energy range.

Fermi-LAT

The *Fermi* satellite carries the LAT detector on board. It is a pair-conversion telescope surveying the gamma-ray sky in the 20 MeV to $>$ 300 GeV energy range (Atwood et al., 2009; Ackermann et al., 2012). I performed a binned-likelihood analysis for the construction of light curves using tools from the `FERMITOOLS` software[1] v2.2.0. I used the instrument response function `P8R3_SOURCE_V3` and the diffuse background models `gll_iem_v07` and `iso_P8R3_SOURCE_V3_v1`[2].

To better investigate the nuanced emission for the HE gamma rays, I created two light curves in the range from 0.3 GeV to 3 GeV and 3 GeV and 300 GeV by selecting `Source` class events in a circular region of interest (ROI) with a radius of 20° around Mrk 421 in the respective energy band. I chose an energy threshold of 0.3 GeV over the more usual 0.1 GeV in order to make use of the improved angular resolution of *Fermi*-LAT at higher energies. In addition, a higher energy threshold reduces background contamination, which leads to an overall improvement of the signal-to-noise ratio for hard sources such has Mrk 421 (photon index < 2). For the source model, I include all sources from the fourth Fermi-LAT source catalog Data Release 3 (4FGL-DR3; Abdollahi et al., 2020; Ajello et al., 2022) that are found within the ROI plus an additional 5°. The obtained model is fit to the data covering the time period from MJD 55141 to MJD 55379. The initial fit results are used to remove weak components from the model (defined by counts < 1 or TS < 3). The test statistic TS is defined as $-2\log(\mathscr{L}_{\mathrm{max},0}/\mathscr{L}_{\mathrm{max},1})$, where $\mathscr{L}_{\mathrm{max},0}$ is the maximum likelihood value for a model without an additional source, the null

[1] `https://fermi.gsfc.nasa.gov/ssc/data/analysis/`
[2] `http://fermi.gsfc.nasa.gov/ssc/data/access/lat///BackgroundModels.html`

hypothesis, and $\mathscr{L}_{\max,1}$ is the maximum likelihood value for a model with the additional source at a specified location. After this first optimization, each time bin is fit with the model. During the fitting procedure, the normalization of bright sources (TS $>$ 10), sources close to the ROI center ($< 3^\circ$), the diffuse background, and the spectral parameters of Mrk 421 itself are all kept free to vary. I produce the light curves with a 3-day binning. This is a good compromise between a small enough temporal resolution without reducing the signal in each bin too much to obtain strong fluctuations of the points. In all time bins, the source is detected with TS $>$ 25 (i.e., $> 5\sigma$).

X-ray data

Observations in the X-ray by the X-Ray Telescope (XRT; Burrows et al., 2005) on board the *Neil Gehrels Swift Observatory (Swift)* were scheduled throughout the full campaign to achieve the best possible coincidence with the observations by MAGIC. The exact details of the analysis can be found in Abe et al. (2024). The data from XRT were used to extract fluxes in the 0.3-2 keV, and 2-10 keV energy bands.

On board *Swift*, there is also the Burst Alert Telescope (BAT). It is an all-sky monitor that provides alerts for transient events such as GRBs. Since it is not a pointing telescope such as XRT, the sensitivity for an individual source such as Mrk 421 is much lower than that of XRT. However, its temporal coverage is excellent since it monitors the full sky continuously. Its data is publicly accessible online[3]. I used the daily light curve.

I also include data from the Rossi X-ray Timing Explorer (RXTE; Bradt et al., 1993) satellite. As part of the organized MWL campaign, RXTE performed almost daily pointing observations of Mrk 421 during the time period from MJD 55177 to MJD 55315. For more details on the analysis settings see the instrument description given in Aleksić et al. (2015b). RXTE also has an all-sky monitor on board, the ASM. The data is also publicly accessible online[4]. In this work, the one-day average light curve is used.

UV data

The *Swift* satellite also provides coverage in the UV with its UV/Optical Telescope (UVOT; Roming et al., 2005). Observations were performed in the W1, M2, and W2 filters by applying standard quality checks to all observations in the chosen time interval. Those with unstable attitudes or affected by contamination from nearby starlight (primarily 51 UMa) are excluded. For each individual observation, photometry over the total exposures in each filter is performed to extract flux values.

Optical data

I use the data already published in Carnerero et al. (2017) to cover the R-band. These observations were performed within the GLAST-AGILE Support Program (GASP) of the Whole

[3] https://swift.gsfc.nasa.gov/results/transients/
[4] http://xte.mit.edu/asmlc/ASM.html

Earth Blazar Telescope (WEBT; e.g., Villata et al., 2008, 2009). It includes multiple optical telescopes around the globe.

Optical polarization measurements can also be taken from Carnerero et al. (2017). They were performed by the Lowell (Perkins), Crimean, Calar Alto, and Steward observatories.

Radio data

The radio data were provided by the 14 m Metsähovi Radio Observatory at 37 GHz, the 40 m Owens Valley Radio Observatory (OVRO) telescope at 15 GHz, and the 26 m University of Michigan Radio Astronomy Observatory (UMRAO) at 14.5 GHz. Observations at 225 GHz (1.3 mm) were performed by the Submillimeter Array (SMA) near the summit of Mauna Kea (Hawaii). For more details on the instruments and observations, see the descriptions given in Aleksić et al. (2015b).

In addition, the Very Long Baseline Array (VLBA) performed observations at 43 GHz (Napier et al., 1994). The data were provided by the Boston University blazar group[5] and are part of their continuous monitoring program of gamma-ray blazars. VLBA is an array of ten radio telescopes all around the USA. It makes use of the Very Long Baseline Interferometry (VLBI) technique, for which the signals from each antenna are digitized locally and recorded. In contrast to conventional interferometry, where the data is correlated in real-time on-site, the data from VLBA is correlated offline at a later instance. This enables the usage of telescopes at different locations, increasing the baselines substantially. The result is an angular resolution of up to 0.1 milliarcsecond (mas) (Weaver et al., 2022). At the distance of Mrk 421, this corresponds to a resolution in the order of ~ 0.05 pc.

This extremely high resolution enables the imaging of the jet in blazars. In all other wavebands, these sources appear as point sources. The VLBI technique can be used to detect substructures within the jet, such as the central core and radially moving components (Jorstad et al., 2017).

6.3 Characterization of the emission throughout the campaign

6.3.1 MWL light curves

Figure 6.4 shows the light curves, i.e., fluxes over time, obtained from all previously described instruments and energy bands in the time period from MJD 55140 until MJD 55380.

The first row shows the light curves provided by the MAGIC telescopes in the 0.2-1 TeV and >1 TeV band. For reference, multiples of the flux of the Crab Nebula[6] are given with dashed or dotted lines. At the start of the campaign in November 2009, Mrk 421 was already in an elevated state of activity with an emission of around 1 C.U. in both bands. The average emission state of the source is around 0.45 C.U., as was estimated by Whipple over a time span of 14 years (Acciari et al., 2014). After that, there is a small observation gap caused by the data being

[5] https://www.bu.edu/blazars/VLBAproject.html

[6] The flux of the Crab Nebula is taken from Aleksić et al. (2016a)

influenced by too much moonlight. In January 2010, Mrk 421 showed a strong flaring activity reaching over 3 C.U. above 1 TeV. The fluxes show strong variability by up to a factor of almost three on a daily timescale. I also found significant intranight variability on some of the days (see the later section 6.5). After a short phase where the flux is again at around 1 C.U., another observational gap due to adverse weather conditions is present in the MAGIC telescope data. In March, a decaying flare starting at around 2 C.U. could be observed, which is discussed in great detail in Aleksić et al. (2015b). The source showed average emission for the following two months around 0.5 C.U. until it entered an especially low emission state around June going even below 0.25 C.U.. Since the fluxes above 1 TeV were compatible with zero emission, I additionally derived upper limits, which can be seen in the zoomed-in figure in the top right.

In addition to the data from MAGIC, I also include the VERITAS light curves with VHE gamma-ray fluxes above 0.2 TeV published in Aleksić et al. (2015b) and Abeysekara et al. (2020). The second row shows the combined VHE light curve provided by MAGIC and VERITAS on a logarithmic scale since the large flare in February would otherwise cause a strong visual downscaling of the rest of the period. The majority of data is provided by MAGIC, and the fluxes above 0.2 TeV are very similar to the 0.2-1 TeV band. However, the gap in February 2010 is now covered due to the additional VERITAS data. These observations resulted in the observation of the largest VHE flux ever observed in an AGN, reaching almost 10 C.U. for the daily average. Using a shorter binning, the peak flux values reached $\sim$15 C.U. above 0.2 TeV (Abeysekara et al., 2020). During the following decaying flare in March, VERITAS provided a comparable coverage as MAGIC.

The third row displays the emission in HE gamma rays obtained by *Fermi*-LAT using a three-day binning in the 0.3 GeV to 3 GeV and 3 GeV and 300 GeV bands. During the large VHE flare in February, both bands also showed increased emission and reached their highest flux coincident with the highest VHE flux point. The other two VHE flares during January and March do not show increased activity in HE gamma rays. I additionally checked, without success, if a daily binning reveals any activity on a shorter scale during these two flares that might be hidden with a 3-day binning.

In the fourth row, results from the all-sky monitors in the X-ray are shown. Both instruments, *Swift*-BAT and RXTE-ASM, detected a short flaring outburst in the X-ray in November 2009, around MJD 55145, shortly before VHE data was available. The flare quickly drops off, and the source remains at a comparably lower activity level without any noticeable outbursts. Coinciding with the February flare, both instruments show a steep increase in emission, which slowly decreases during the following month. At the end of the campaign, the X-ray emission also enters a remarkably low emission state.

In the following row, the fluxes from the pointing instruments in the X-ray, namely *Swift*-XRT and RXTE-PCA, are reported. *Swift*-XRT still detects the decaying part of the short X-ray outburst at the beginning of the campaign. All energy bands reach their maximum flux levels coincident with the February flare. After a slow and quite variable decay, they also end in the same low-emission state.

Hardness ratios (HRs) can be obtained using the two separate VHE and X-ray light curves. The HR is given by the ratio of the flux in the higher-energy band to the flux in the lower-energy band. This can be done for the pairs of energy bands given in VHE gamma rays and X-rays, which are shown in row six. Overall, the source showed a harder-when-brighter trend in VHE

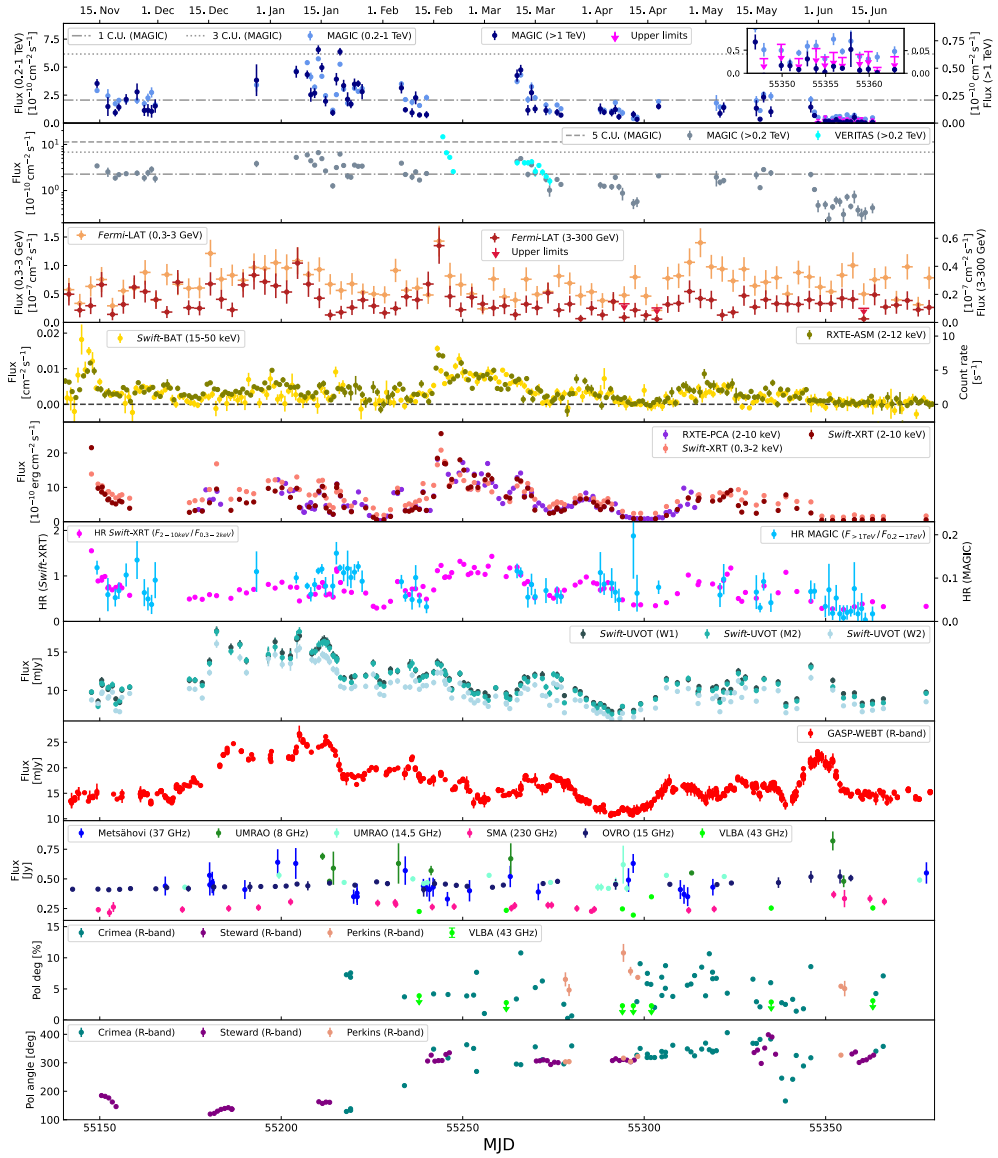

Figure 6.4: MWL light curves covering the time period from the 5th of November 2009 (MJD 55140) to the 3rd of July 2010 (MJD 55380). Top to bottom: MAGIC fluxes in daily bins for two energy bands (note the two different y-axes); VHE fluxes obtained from MAGIC and VERITAS above 0.2 TeV (in log scale); *Fermi*-LAT fluxes in 3-day bins in two energy bands; X-ray fluxes in 1-day bins from the all-sky monitors *Swift*-BAT and RXTE-ASM; X-ray fluxes from the pointing instruments *Swift*-XRT and RXTE-PCA; hardness ratio between the high and low-energy fluxes of *Swift*-XRT and between the two VHE bands of MAGIC (note the two different y-axes); optical R-band data from GASP-WEBT; radio data from Metsähovi, UMRAO, SMA, OVRO and VLBA; polarization degree and polarization angle observations in the optical from the Steward and Perkins observatories and in radio from VLBA.

and X-ray, which has been observed frequently in the past (see, e.g., Acciari et al., 2021; MAGIC Collaboration et al., 2021). More details on this trend are described in the following section 6.3.2

Data obtained for the three different UV filters are shown in row seven. The light curve indicates a rather low activity in the UV at the beginning of the campaign. The UV reached its highest emission during the January flare seen in VHE. When the subsequent February flare starts, there is no clear visible increase in activity in the UV. During the decaying VHE flare in March, a broad rising and falling peak is visible.

The optical data in the R-band, in row number eight, shows similar behavior to that of the UV throughout the whole period due to the closeness of the two energy bands. Some small differences, nevertheless, are noticeable, such as the little outburst at the end of the campaign in June, around MJD 55350. The same outburst is barely visible in the UV, which can also be due to the sparser coverage.

The ninth row shows the fluxes obtained from various radio instruments. The instruments cover a variety of frequencies, which makes flux comparisons difficult. The source showed low activity and low variability in all radio bands. Since variability in radio is normally observed on long-time scales, the short duration of the campaign is partly responsible for this.

The second to last row displays the polarization degree in the R-band and upper limits in radio, derived with VLBA data at 43 GHz. The polarization degree shows strong fluctuations throughout the campaign, going from values as low as 0.3% up to $\sim$11% around a mean of $\sim$5%. In radio, the upper limits are much lower on average at around 2.8%. The electric vector polarization angles (EVPA) in the optical are shown in the row below. The data were adjusted for the intrinsic 180° ambiguity. The EVPA shows a constant behavior at the beginning at around $\sim$150° followed by a wide rotation happening around MJD 55230. The remaining campaign fluctuates around $\sim$350°. Since the EVPA rotates by around 200° during a time interval with very limited coverage by only one measurement, one cannot completely exclude that this rotation arises from an improper correction of the 180° ambiguity.

6.3.2 Hardness ratios of VHE gamma rays and X-rays

As mentioned in the previous section, the HRs in VHE and X-rays indicate a harder-when-brighter trend. For better visualization, I also plot the HRs as a function of the fluxes. Figure 6.5 shows the HRs of all MAGIC observations as a function of the flux between 0.2-1 TeV in the left plot and above 1 TeV in the right one. Both plots show a clear harder-when-brighter trend. The rise of the HR with the flux is steep at low fluxes but flattens out at higher flux levels. In the right plot, the HR seems to remain constant with a rising flux above $\sim 3 \times 10^{-11}\,\mathrm{cm}^{-2}\mathrm{s}^{-1}$. The graph on the left shows similar behavior, but the overall scatter of the data is slightly higher due to the worsening statistics at higher energies. This flattening harder-when brighter-trend at VHE gamma rays is consistent with previous reports (e.g. Acciari et al., 2021).

Figure 6.6 shows the HRs of the *Swift*-XRT observations as a function of the fluxes between 0.3-2 keV in the left and 2-10 keV in the right plot. When the source is in a low activity state at the end of the campaign, the HR goes as low as $\sim$0.26. Similar to the VHE, a strong harder-when-brighter trend is visible. On the contrary, the HR does not show a clear flattening but a rather linear behavior over the full flux range. This is especially pronounced in the left plot. The highest HR of $\sim$1.55, directly at the start of the campaign, still seems to follow an almost

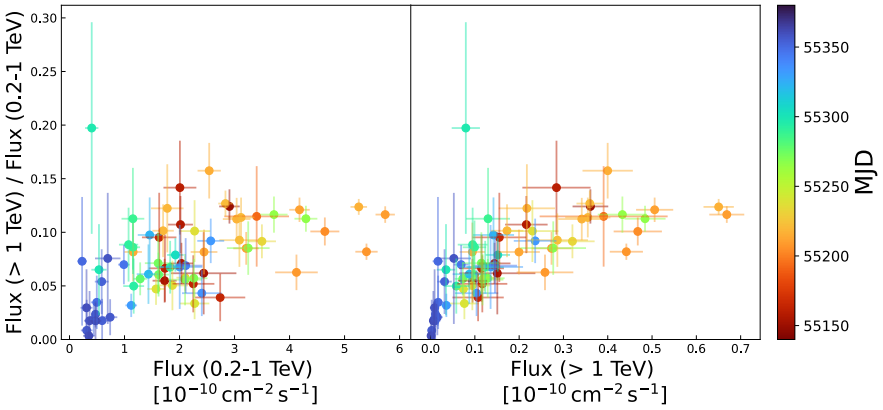

Figure 6.5: Hardness ratios as a function of the flux 0.2-1 TeV (left) and above 1 TeV(right) obtained by MAGIC. The color indicates the time of the observation in MJD.

linear trend. However, the HR ratio corresponding to the highest flux values is more compatible with a flattening of the trend. Overall, the flattening of the HR is much less pronounced than in previous works, such as Acciari et al. (2021).

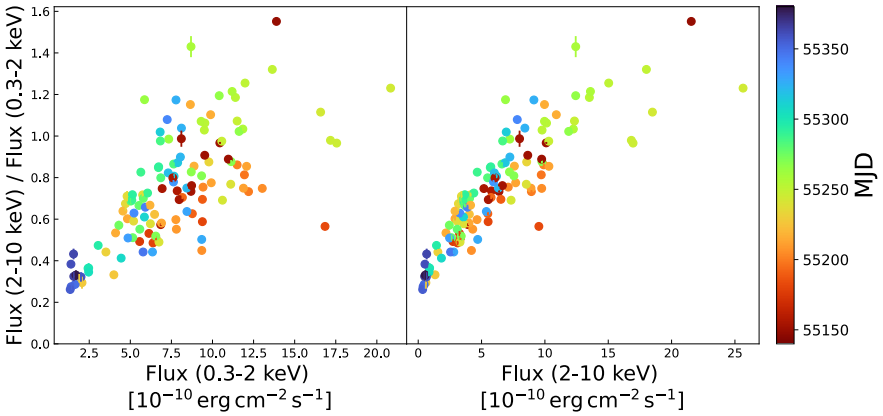

Figure 6.6: Hardness ratios as a function of the flux between 0.3-2 keV (left) and 2-10 keV (right) obtained by *Swift*-XRT. The color indicates the time of the observation in MJD.

6.4 VLBA observations of the jet evolution

Figure 6.7 shows the images of Mrk 421 from May 2010 to August 2011 taken by VLBA. The images are shown from May onwards. The plot shows the total intensity profile of each image. The structure is modeled using a number of emission components (knots) with circular Gaussian brightness distributions. Based on their parameters, knots can be identified across the epochs. The brightest knot at the jet's southern end is the VLBI core at 43 GHz, which is placed at zero distance. The VLBI core, named A0, is assumed to be a stationary physical structure of

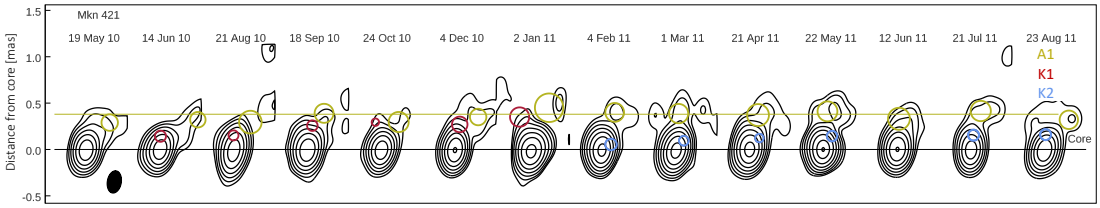

Figure 6.7: Total intensity VLBA images of Mrk 421 from May 2010 to August 2011. The black and yellow lines show the average positions of the stationary features A0 and A1. The yellow, red, and blue circles show the fitted positions of A1, K1, and K2, respectively. [Plot produced by S. Jorstad]

the jet. Another (quasi-)stationary feature, A1, is located at 0.38 ± 0.06 mas from the core. Interestingly, two new components emerged from the core, K1, and K2, during the observations. The components were already mentioned in Jorstad et al. (2017). As explained in the reference, the existence of B1 (named K1 in this work) as a real knot is not absolutely certain due to the larger measurement uncertainties. The average parameters of the components, i.e., name of the knot, number of epochs at which the knot is detected, the flux density, distance from the core, position angle with respect to the core, and the size of the knot, are listed in Table 6.1. For the two moving components, kinematic properties can also be extracted. They are listed in Table 6.2, in which *Phi* refers to the speed direction. The newly emerging component K1 moves at a speed of 0.78 mas/yr, which corresponds to an apparent speed of 1.56 ± 0.45 c, making it just about a superluminal knot (note the large uncertainty). The component K2 moves much slower with a speed of 0.16 mas/yr corresponding to 0.32 ± 0.07 c.

For better visualization, Figure 6.8 shows the angular distance from the core of the components A1, K1, and K2, as a function of time. Since A1 is identified as a stationary feature, the distance versus time of A1 with respect to A0 is assumed to be constant and fit with a horizontal line. The separations of the two new components from the core are approximated by linear fits. Extrapolating the linear fits back to the core position allows for the determination of the ejection times, i.e., the time of passage of K1 and K2 through the center of the VLBI core. K1 is ejected at MJD 55112 ± 88 and K2 at MJD 55400 ± 157. Both ejection times fall well within the main period of this study, which is shown in light grey, from MJD 55140 to 55380 within their one-sigma band. However, because of the large uncertainties of the extrapolation, it is impossible to claim a connection with a particular event, such as one of the three VHE flares (in January, February, and March) marked with solid grey lines.

Nevertheless, it is remarkable that in the period where Mrk 421 exhibited the most violent behavior with three large VHE flares, including the brightest flare ever, an ejection of two new components is observed. Radio components have been identified for a few TeV-emitting blazars (mostly FSRQs), but a potential association of gamma-ray flares with the ejection and propagation of knots is rarely observed in HSPs such as Mrk 421 (Weaver et al., 2022). This is the only time the ejection of new components in the jet of Mrk 421 was observed. Previous works only found stationary or already present subluminal knots (e.g. Piner and Edwards, 2005; Lico et al., 2012; Richards et al., 2013; Blasi et al., 2013).

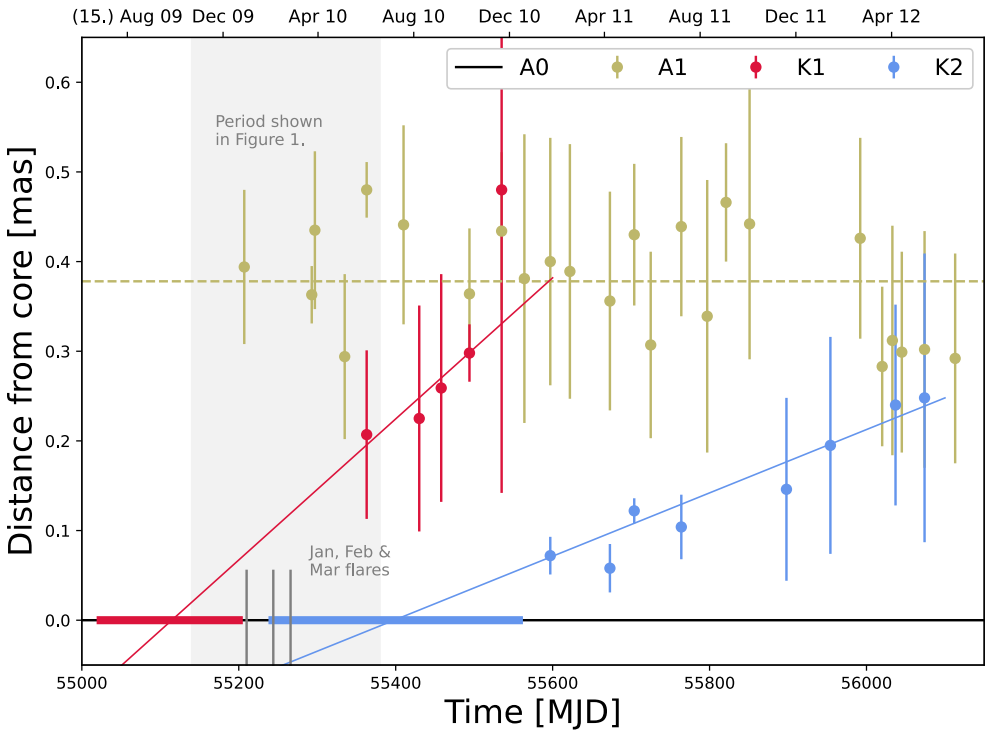

Figure 6.8: Distance of A1 (yellow), K1 (red), and K2 (blue) from the jet core (black). The dotted yellow line indicates a constant fit of the quasi-stationary component. The red and blue lines show linear fits to determine the components' ejection time. The uncertainties on the ejection times are given by the red and blue bands. The campaign of this work is given by the light grey band with the three flares marked with grey lines.

Table 6.1: Average parameters of the features shown in Fig. 6.7

Component	Number of epochs	Flux (Jy)	Distance (mas)	Theta (deg)	Size (FWHM,mas)
A0	31	0.210 ± 0.048	0.0	...	0.072 ± 0.030
A1	24	0.025 ± 0.012	0.378 ± 0.062	-28.9 ± 14.3	0.267 ± 0.117
K1	5	0.011 ± 0.008	0.29 ± 0.18	-34.2 ± 27.2	0.146 ± 0.131
K2	8	0.060 ± 0.005	0.20 ± 0.12	-37.3 ± 7.6	0.145 ± 0.036

Table 6.2: Kinematic properties of the knots K1 and K2.

Knot	Proper motion (mas/yr)	Phi (deg)	Apparent speed (c)	Ejection time (yr)	Ejection time (MJD)
K1	0.775 ± 0.225	49.5 ± 15.2	1.56 ± 0.45	2009.77 ± 0.24	55112 ± 88
K2	0.157 ± 0.033	-21.8 ± 20	0.32 ± 0.07	2010.56 ± 0.43	55400 ± 157

6.5 Variability of the emission

6.5.1 Intranight VHE variability

As chapter 2 explains, blazars can show variability on timescales as short as minutes. I checked for whether there was significant intranight variability in the MAGIC data for each night. Figure 6.9 shows the intranight light curves in the 0.2-1 TeV band of four selected nights. The nights were selected because they either show significant variability, or they have excellent intranight coverage during the flare in January 2010. The upper panel shows the January 14, 2010, (MJD 55210), where the highest fluxes are recorded by MAGIC during the flare in January. I fit the data with a constant model using a χ^2-minimization in order to test the hypothesis of a non-variable emission. Despite the high emission activity, the source shows no significant variability but a stable and high emission throughout the full exposure of around 3 hours.

The second panel shows the following night of the January 15 (MJD 55211). Using a χ^2-test, the hypothesis of a constant emission is rejected at 3.7 σ, indicating a significant variability on an hour time-scale in VHE gamma rays.

During the flare in January, the VHE flux increases again around January 20 (MJD 55216). No significant variability is seen, but a strong but constant emission throughout the exposure.

Lastly, the lowest panel shows April 18 (MJD 55304). The flux shows a quick decay and small rise, which corresponds to significant variability at 4.5 σ, again indicating hour time-scale variability.

In total, only two nights showed significant variability despite the high overall activity. During the flare in February 2010, VERITAS found strong variability within one night. The large number of events allowed a 2 min binning of the light curve, which revealed two bursts with a flux rise and fall on a 20 min time scale (Abeysekara et al., 2020).

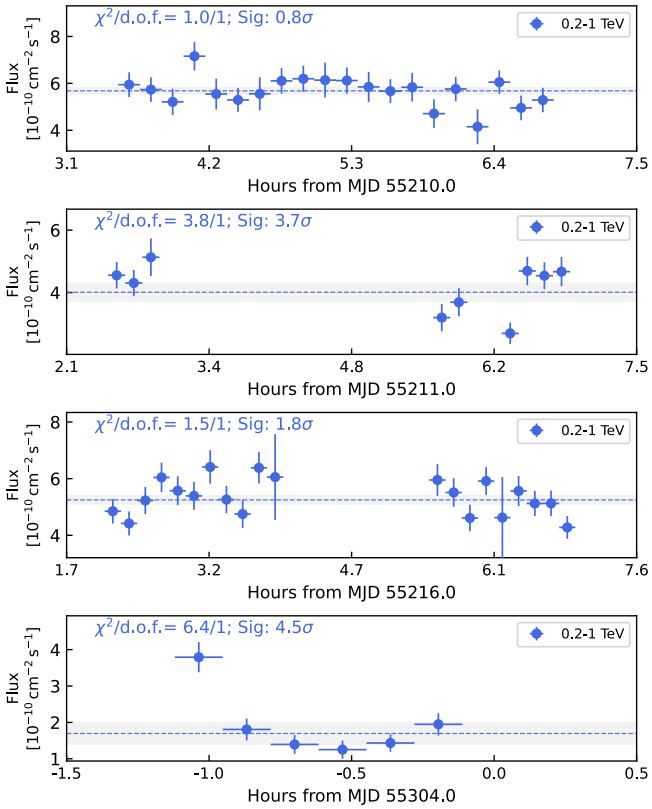

Figure 6.9: Intranight VHE variability detected by MAGIC in the 0.2-1 TeV energy band. The data are binned in 10 minutes. The dotted line shows the constant fits for the 0.2-1 TeV band.

6.5.2 Fractional variability

In order to estimate the degree of variability in each energy band over the entire campaign, I use the fractional variability (F_{var}; Vaughan et al., 2003). F_{var} provides a measure for the excess variability of a series of fluxes x_i by taking into account their measurement uncertainties $\sigma_{err,i}$. It is given by:

$$F_{var} = \sqrt{\frac{S^2 - \bar{\sigma}_{err}^2}{\bar{x}^2}} \quad , \tag{6.1}$$

where S^2 gives the variance of the fluxes, $\bar{\sigma}_{err}^2$ the mean square error of the uncertainties and $\bar{x}$ the mean flux. I use the prescription given in Poutanen et al. (2008) to estimate the corresponding uncertainties. Figure 6.10 shows the resulting fractional variability using the full light curves in open markers. The full markers show the results for quasi-simultaneous data with VHE coverage. I defined quasi-simultaneity as the temporal agreement with VHE data within 6 h for X-ray and UV data, within 1 day for optical data, and within 3 days for radio and *Fermi*-LAT data. The varying intervals are a result of the different binning and variability time scales of the data, which can be taken from Figure 6.4.

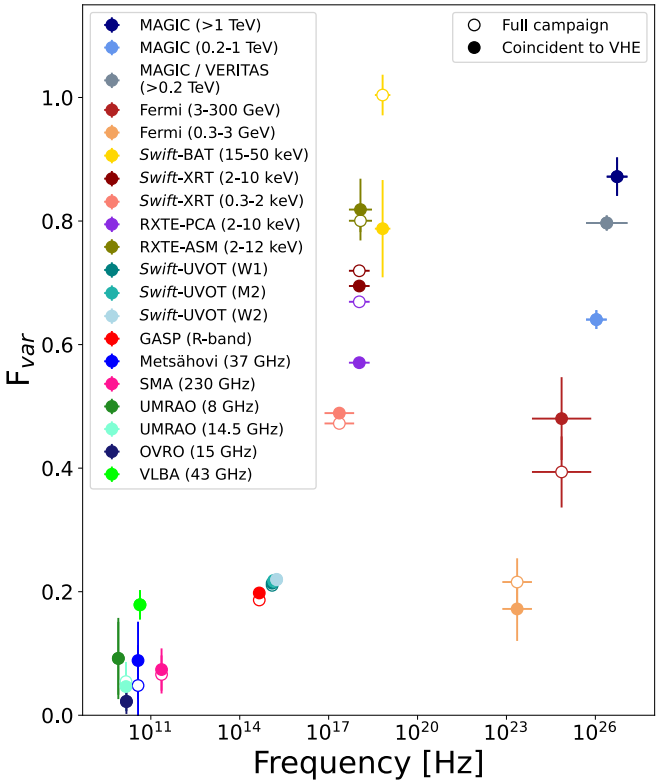

Figure 6.10: Fractional variability F_{var} as a function of the frequency for the light curves shown in Figure 6.4. Open markers show the results using the whole campaign for each light curve. Full markers only include quasi-simultaneous data to the VHE data (quasi-simultaneity is defined as temporal agreement with VHE data within 6 h for X-ray and UV data, within 1 day for optical data, and within 3 days for radio and *Fermi*-LAT data.)

For both markers, a pronounced and almost identical two-peak structure is visible. The first peak rises from radio up to X-ray. The maximum of the F_{var} is reached in the hard X-rays by *Swift*-BAT at about 0.8 for the quasi-simultaneous data and around 1.0 for the full period. The second peak includes the gamma rays up to TeV energies, where it reaches its maximum at about 0.9. A similar behavior have been observed multiple times for Mrk 421 (see, e.g., Aleksić et al., 2015a; Baloković et al., 2016; MAGIC Collaboration et al., 2021). The typical SED from a blazar such as Mrk 421 shows a double bump structure (see Figure 2.2 in section 2.2.2), where the first bump is caused by leptonic synchrotron emission. The most freshly accelerated and energetic electrons emit that bump's falling edge. These electrons also have the shortest cooling times, which results in a high degree of variability. The corresponding region is covered by the X-rays, where the first peak reaches its maximum. At energies below the X-rays, the electrons responsible for the synchrotron emission have lower energies and, with that, longer cooling times, resulting in a strong decrease in variability. In the context of an SSC model, the same electrons produce the second bump of the SED in the gamma rays via inverse Compton emission (more on that in section 6.7). Therefore, a similar variability pattern is also expected in

the variability of the gamma-ray peak. Figure 6.10 shows the same degree of variability at TeV energies as in keV energies. This result already suggests the existence of a correlation between the two wavebands, which is investigated in more detail in section 6.6.

6.5.3 Power spectral density

Additionally, I investigate the variability of Mrk 421 in more detail with the use of the power spectral density (PSD). The PSD results from the Fourier spectrum of the fluxes over time. It quantifies the power of the variability as a function of the timescale of the variations. The actual underlying PSD shape could theoretically be obtained by the Fourier spectrum of the true and continuous underlying flux variations. In the case of real observations with discrete sampling, the variability power, $P(\nu_k)$, is computed from the modulus square of the complex Fourier spectrum for a discrete and finite time series (following the description in Arbet Engels, 2021):

$$P(\nu_k) = \left(\sum_{i=0}^{N} f_i \cos(2\pi\nu_k t_i)\right)^2 + \left(\sum_{i=0}^{N} f_i \sin(2\pi\nu_k t_i)\right)^2, \tag{6.2}$$

where f_i is the flux observed at a time t_i and ν_k is the frequency, which relates to the timescale being evaluated, and it is defined as k/T, where k ranges from 1 to $N/2$ and T is given by $\frac{N}{(t_N - t_1)(N-1)^2}$.

The typical shape of the PSD for blazars follows a simple power law $P_\nu \propto \nu^{-a}$ with the spectral index a ranging between 1 and 2 (e.g. Uttley et al., 2002; Chatterjee et al., 2008; Abdo et al., 2010b). A decreasing power law indicates a large variability at long timescales / small frequencies and a decreasing variability power as one goes to shorter timescales / higher frequencies. This pattern is referred to as red noise when the power-law index is 2, while it is called pink noise when the index is 1.

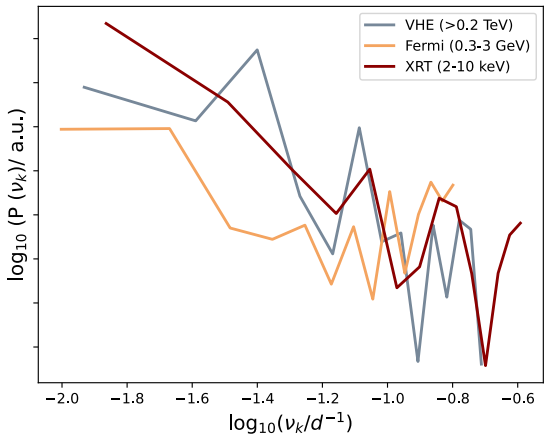

Figure 6.11: Example PSDs shown in log-scale for three different energy bands. >0.2 TeV in gray, 0.3-3 GeV in yellow and 0.2-10 keV in dark red.

Figure 6.11 shows the results of applying equation 6.2 for three selected light curves (>0.2 TeV, 0.3-3 GeV, and 0.2-10 keV). All three curves fluctuate around a decreasing power law (note the log scale of the y-axis) .

The true underlying PSD shape cannot be estimated reliably by directly fitting the resulting curve with a power law since a discrete sampling modifies the Fourier spectrum. Real observations suffer from unevenly sampled data with large gaps in their coverage. The limited time coverage and the specific temporal binning of the data can cause a transfer of variability power from higher to lower frequencies and vice versa. These distortions must be accounted for to accurately estimate the true PSD.

I estimate the true PSD index using a simulation-based forward-folding procedure. I used and further developed the code base described in Arbet Engels (2021); MAGIC Collaboration et al. (2021), which my colleague Axel Arbet-Engels developed. The procedure works as follows: In the first step, I simulate light curves using the same binning and sampling as a given real light curve. There are two main ingredients for the simulation of light curves: A probability density function (PDF) of the underlying flux distributions and the underlying PSD index of the power law defining the amplitude and time-scale of variability. The PDFs are obtained by fitting the real data with a tailed Gaussian profile as described in Emmanoulopoulos et al. (2013). Since the PSD is the unknown parameter that I want to extract, simulations are performed for a variety of PSDs. I run simulations with PSD indices ranging from 0.3 to 2.5 using steps of 0.1. For each assumed spectral index, I simulate a set of 3000 light curves using the assumption of the given power-law-shaped PSD. The simulated light curves are 10 times longer than the real light curves and are then cut to the desired length by having the same temporal binning applied to account for the previously mentioned leakage effects. The result is a set of 3000 simulated light curves for each assumed PSD shape. These simulations can then be compared to the real data.

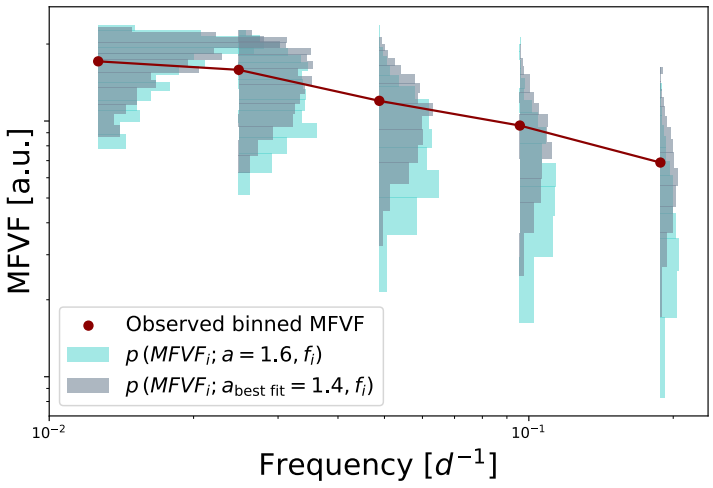

Figure 6.12: MFVF as a function of frequency for two different sets of simulations resembling the sampling of the 2-10 keV light curve from *Swift*-XRT. The two sets of MFVF histograms were obtained for a PSD index of 1.4 and 1.6 for five frequency bins. The real data is shown in dark red.

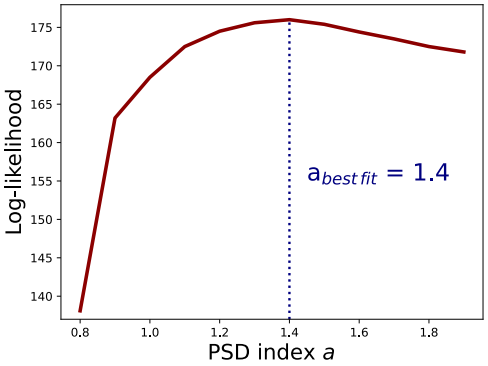

Figure 6.13: Likelihood profile $\mathscr{L}(a)$ (see Eq. 6.3) for the 2-10 keV band with its best-fit value of 1.4 denoted by a vertical blue dotted line.

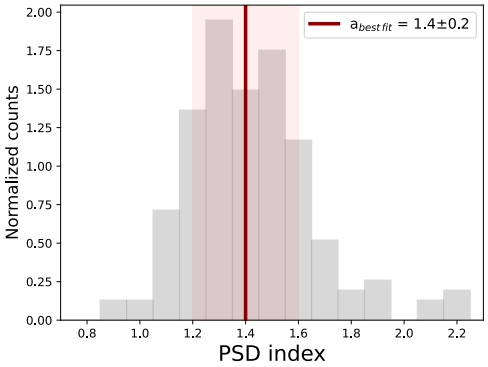

Figure 6.14: Histogram of the best-fit indices derived from simulations using as input a simulated light curve that has a known PSD index $a = 1.4$, in agreement with the real data for the 2-10 keV band.

For the comparison, I use the multiple fractions variance function (MFVF) as a proxy for the PSD (Kastendieck et al., 2011). The MFVF does not require interpolation of the data and is a simple method to obtain the variance of the fluxes as a function of time scale. This makes it an alternative representation of the PSD. The MFVF is computed by splitting a given light curve in the temporal middle and taking the flux variance of both halves. The two halves are then split again into two halves, and the variances are again estimated. This is repeated until a minimum time scale of one day is reached. The result is a set of variances as a function of time scale, which resembles a robust alternative representation of the PSD. The MFVF is computed for all simulated light curves. For a given PSD index, the 3000 light curves then produce a histogram of MFVF values at each frequency bin f_i. In this work, five frequency bins are used. The histogram resembles a probability density function $p(a, f_i)$ for each out of N frequency bins. It gives the probability of measuring an MFVF value in the frequency bin f_i, assuming the underlying PSD with the index a.

Now, the MFVF is also computed for the real data. Figure 6.12 shows two example sets of histograms of MFVF values for each frequency bin obtained from simulations resembling the sampling of the 2-10 keV light curve from *Swift*-XRT. The image has two sets of histograms corresponding to different example PSD indices (1.4 and 1.6). The real data is shown in dark red. The best-fit value for the spectral index of the real light curve can then be estimated with a maximum likelihood estimation by finding the index a out of all simulations maximizing:

$$\mathscr{L}(a) = \sum_{i=0}^{N} \ln(p(a, f_i)) \tag{6.3}$$

Figure 6.13 shows the resulting likelihood profile for the 2-10 keV band for a range of indices from 0.8 to 2.0. The best-fit value can be found at the maximum of the profile, which is 1.4 in this case.

Table 6.3: PSD index best fit a for each energy band.

Energy band (instrument)	Best fit a
> 1 TeV (MAGIC)	$1.4^{+0.4}_{-0.3}$
0.2-1 TeV (MAGIC)	$1.5^{+0.5}_{-0.3}$
> 0.2 TeV (MAGIC/VERITAS)	$1.5^{+0.5}_{-0.2}$
3-300 GeV (*Fermi*-LAT)	$0.8^{+1.0}_{-0.6}$
0.3-3 GeV (*Fermi*-LAT)	$0.4^{+0.8}_{-0.3}$
15-50 keV (*Swift*-BAT)	$1.3^{+0.2}_{-0.2}$
2-10 keV (*Swift*-XRT)	$1.4^{+0.2}_{-0.2}$
0.3-2 keV (*Swift*-XRT)	$1.4^{+0.2}_{-0.2}$
W1 (*Swift*-UVOT)	$1.6^{+0.3}_{-0.3}$
R-band (GASP-WEBT)	$1.9^{+0.3}_{-0.2}$

I continued to follow the procedure from Arbet Engels (2021); MAGIC Collaboration et al. (2021) to estimate the uncertainties of the indices. For this, I simulate 100 light curves, assuming the best-fit index for the underlying PSD of each simulated light curve. I then refit each simulated light curve using the same method as before for the initial fit of the real data. This creates a histogram of the resulting indices. The more narrow the resulting histogram is, the better constrained the PSD index fit for that light curve. The uncertainties for a given energy band are then given by the 68% (1 σ) containment region. As an example, Figure 6.14 shows the resulting histogram for the 2-10 keV band. Since the histograms can show a slightly skewed distribution, I provide upper and lower uncertainties separately.

The resulting best-fit values of this procedure for all light curves are given in Table 6.3. The values derived for *Fermi*-LAT are noticeably lower but also have large uncertainties. This is a result of the large uncertainty on the flux values of the light curve, which causes the derived PSD index to be poorly constrained. Overall, the values are well compatible with the ones derived in previous works (see, e.g., Aleksić et al., 2015a).

I did not find evidence of a spectral break of the PSD index in any energy band. In addition, I used the Lomb-Scargle method (Lomb, 1976; Scargle, 1982) to search for signs of periodicity but found no periodicity in my data set.

6.6 Correlation studies

6.6.1 VHE gamma rays vs X-rays

Figure 6.10 shows that the VHE gamma rays and the X-rays are the two energy bands in which Mrk 421 has the greatest flux variations. These can occur on timescales as short as hours, as shown in section 6.5.1. Due to the short time scale, the observing campaign was organized with a special focus on maximizing the simultaneity between the VHE gamma rays and X-ray measurements. The collected dataset allows us to investigate the correlations with a large number of VHE gamma rays and X-ray measurements taken within a time window of only a few hours. Previous work investigated the behavior of the source either during a low activity state (Baloković et al., 2016), a typical activity state (MAGIC Collaboration et al., 2021) or during a flaring activity (Acciari et al., 2020). The uniquely large variety of states shown by Mrk 421 during the MWL campaign in 2010 allows us to probe the correlation behavior across all states of emission within a single campaign lasting about half a year. The referenced previous works also showed that there is no expected time delay between the two bands. Therefore, I will evaluate the data in a straightforward way with a flux-flux plot. The quasi-simultaneous measurements allow us to plot fluxes in the VHE gamma-ray and X-ray bands within a time window of only 6 hours.

Figure 6.15 shows the decimal logarithm of the fluxes of all three VHE bands vs the fluxes of the two *Swift*-XRT bands and the one provided by *Swift*-BAT. I build pairs of fluxes by matching X-ray observations within 6 hours of a VHE observation and if more than one *Swift* observation fall within that window, the weighted mean is computed. The color of each point displays the time of the observation in MJD.

In order to evaluate the degree of correlation, I use the Pearson coefficient (Pearson, 1895). I compute the statistic using the regular flux data without applying the decimal logarithm shown in Figure 6.15. For each computed Pearson coefficient, I perform a test of significance by testing the null hypothesis that the probability distributions underlying the flux samples are uncorrelated. I simulate a set of 100.000 uncorrelated pairs of light curves for each combination, following the previous prescription in 6.5.3. To get the same degree of variability at different frequencies as the real data, I now use the PSD indices obtained in section 6.5.3 as the input for the simulations. The simulated light curves are binned with the same temporal sampling as the real data. I then compute the Pearson coefficient for each of the 100.000 pairs. The resulting distributions are fitted with a Gaussian Kernel model to resemble the probability density function (PDF). Integration of the PDF above the Pearson coefficient given by the real dataset results in a p-value. It indicates the probability of finding an uncorrelated dataset that has a Pearson coefficient at least as extreme as the one computed from the real dataset. I then translate the p-value into a significance expressed in levels of $1\,\sigma$. It must be emphasized that the standard approach for assessing the significance of the Pearson coefficient uses the assumption of two Gaussian-distributed data sets and is not applicable here because the given datasets show flux distributions with strong tails towards higher fluxes. Additionally, measurement uncertainties are not taken into account in the standard method. I, therefore, rely on simulations to estimate the significance, which gives a robust and more conservative estimate.

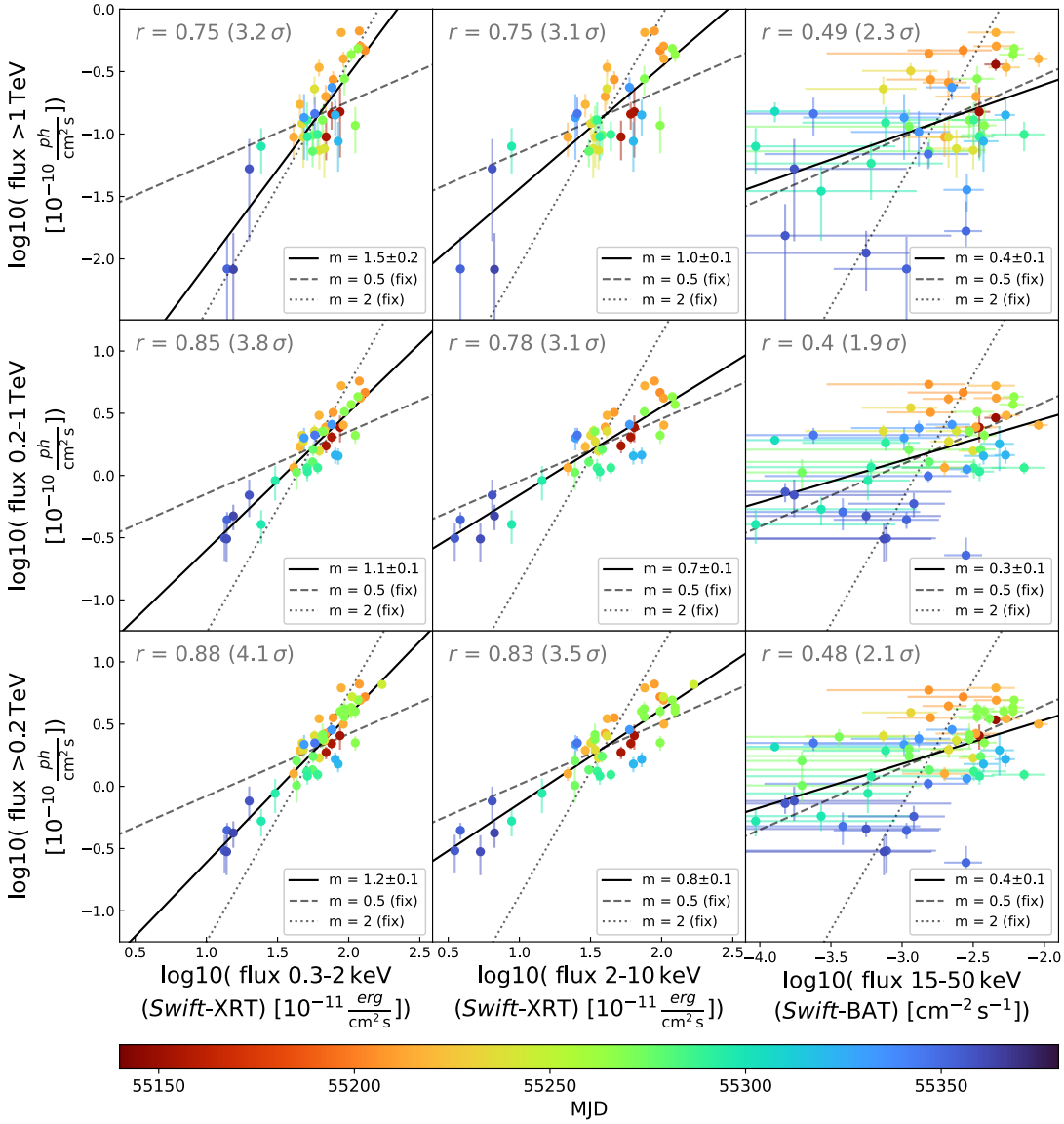

Figure 6.15: VHE flux versus X-ray flux obtained by MAGIC/VERITAS and *Swift*-XRT/BAT. Only pairs of observations within 6 hours are considered. VHE fluxes are in the >1 TeV band (top panels), in the 0.2-1 TeV band (middle panels) and in the >0.2 TeV band (bottom panels). *Swift*-XRT fluxes are computed in the 0.3-2 keV (left panels) and 2-10 keV bands (middle panels). *Swift*-BAT provides the flux in the 15-50 keV band (right panels). The top left corner of each panel shows the Pearson coefficient of the flux pairs, with the significance of the correlation given in parentheses. The gray dashed and dotted lines depict a fit with slope fixed to 0.5 and 2, respectively, and the black line is the best-fit line to the data, with the slope quoted in the legend at the bottom right of each panel.

I find strong correlations between all VHE and *Swift*-XRT energy bands. In all six panels, the Pearson coefficients are above 0.75 with significances ranging from slightly above 3 up to 4 σ. The correlation between the VHE and the *Swift*-BAT band is much weaker, reaching coefficients around 0.4-0.5 and significances of around 2 σ. This lower significance is most likely caused by the large flux uncertainties of the BAT measurements in comparison to the small uncertainties in the flux measurements from XRT.

I investigate the correlation slopes by fitting lines to the decimal logarithm of the data shown in the scatter plots. Since there is no significant change in the correlation slope over time by fitting individual ∼1 month periods, a single line fit is fitted for the whole campaign. The distribution of observations can be scattered, with some points lying far outside the average fitting line. The linear fits must be, therefore, viewed as an overall trend and not a precise model of the data. It is noteworthy that in the subplots between the >0.2 TeV flux with both X-ray bands, the observations of the highest and lowest X-ray flux lie well on the linear fit, indicating a linear trend reaching over a full order of magnitude of emission and on the timescale of multiple months. Line fits with fixed slopes at m=0.5 and m=2 are displayed for reference. The steepest slope is 1.5 ± 0.2, obtained for the fluxes above 1 TeV vs 0.3-2 keV (i.e., the highest VHE gamma-ray band vs the lowest X-ray band), while the flattest slope is 0.3 ± 0.1, obtained for the 0.2-1 TeV vs 15-50 keV (i.e., the lowest VHE gamma-ray band vs highest X-ray band).

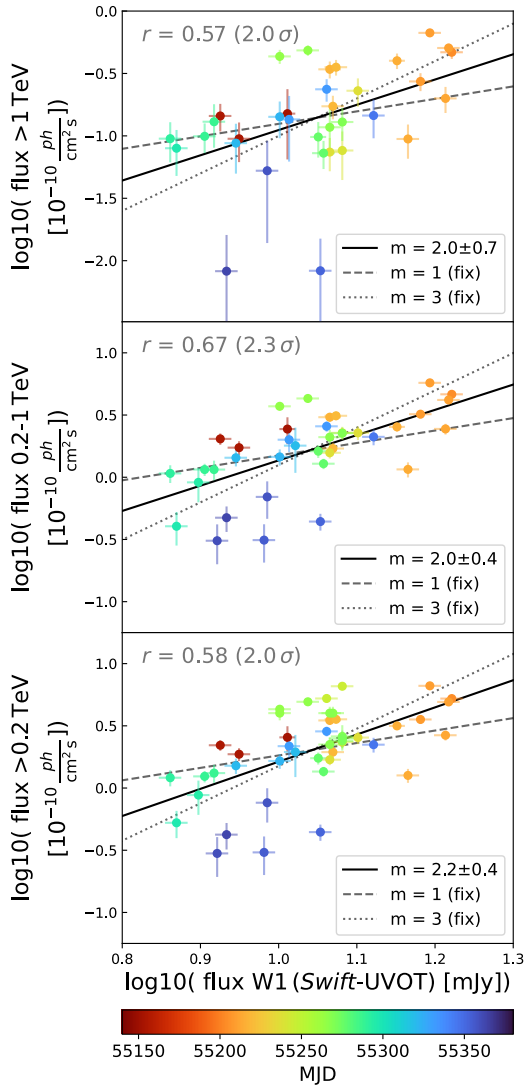

Figure 6.16: Same as Figure 6.15 but for the VHE fluxes versus the UV W1 flux obtained *Swift*-UVOT.

Overall, the slope is increasing with rising VHE energy, showing a greater scaling of the >1 TeV flux with rising X-ray fluxes. In addition, the slope decreases with rising X-ray energy. The same trends have also been found in MAGIC Collaboration et al. (2021), but the absolute slope values were found to be greater, reaching a cubic relation in some cases.

6.6.2 VHE gamma rays vs UV

The *Swift*-UVOT instrument has the same data coverage in the UV as *Swift*-XRT in X-rays. This suggests following the same approach as in the previous section and investi-

gating a possible correlation between the VHE and UV band pairs at zero time lag within 6 h. Figure 6.16 displays the decimal logarithm of the fluxes of all three VHE bands vs the flux of the W1 filter. All three UV filters show almost identical results, and I selected W1 simply as a representative for the UV. Again, the correlation is evaluated with the Pearson coefficient analogously. The former shows values around 0.6 for all three panels, indicating a positive correlation. However, the corresponding significances of these correlations are all around $2\,\sigma$, and hence, this result can only be considered as a hint of correlation. If the correlation were real, this would be the first time, that a positive correlation between VHE gamma rays and the UV band is found.

Again, line fits are performed to estimate the correlation slope. In all panels, the slope is around m=2. Due to the higher dispersion of the data, the uncertainties of the fit become rather large. The higher slope indicates a steeper correlation between the VHE and UV compared to X-rays. Since the degree of variability is much higher in the VHE than the UV (as can be seen in Fig. 6.10), the flux varies substantially more in the y-direction, and a steeper slope is expected in the case of a correlation.

6.6.3 VHE gamma rays vs HE gamma rays

Next, I investigate the correlation between the two energy bands in gamma rays. The highest temporal coverage in VHE gamma rays is achieved with the combined light curve above 0.2 TeV from MAGIC and VERITAS. From now on, I will move away from using scatter plots since, due to the limited sensitivity of *Fermi*-LAT, the data has a 3-day binning. Any effects on shorter time scales are already lost by the binning and correlations might also happen at a time lag. The temporal coincidence of the two light curves is, therefore, not as strict as in the previous two cases. I now correlate the bands using the discrete correlation function (DCF; Edelson and Krolik, 1988). The DCF provides an assumption-free estimation of the correlation at a time lag τ between two given discrete and possibly unevenly sampled time series, a and b. This makes it suitable for the usage of astronomical light curves. It is given by:

$$\mathrm{DCF}(\tau) = \frac{1}{N} \sum_{i,j} \frac{(a_i - \bar{a})(b_j - \bar{b})}{\sqrt{(\sigma_a^2 - e_a^2)(\sigma_b^2 - e_b^2)}} \tag{6.4}$$

The DCF considers pairs of flux points, a_i, b_j, at times t_i and t_j, if the time difference of the data pair, $\Delta t_{i,j} = t_j - t_i$, matches the time delay, τ, within a given time bin width, $\Delta\tau$, i.e. $\tau - \Delta\tau/2 \leq \Delta t_{i,j} \leq \tau + \Delta\tau/2$ is fulfilled. σ_a and σ_b are the standard deviations of the light curves and $\bar{a}$ and $\bar{b}$ are their mean values. e_a and e_b give the measurement errors of the flux pair. The error on the DCF is computed using the description in Edelson and Krolik (1988). It must be noted, that the analytical formula for the standard error of the DCF is not a great estimate of the significance of the correlation, since it assumes uncorrelated measurements within a time bin. Assessing the significance with a simulations-based approach as before, is the most robust and reliable way and is therefore also done here.

I use a 3-day binned time lag in the range of -40 to +40 days to check for any delay in the correlation. A peak in the DCF scan signals a potential correlation between the two bands with a time delay to the position of the peak. The significance of the corresponding DCF value is

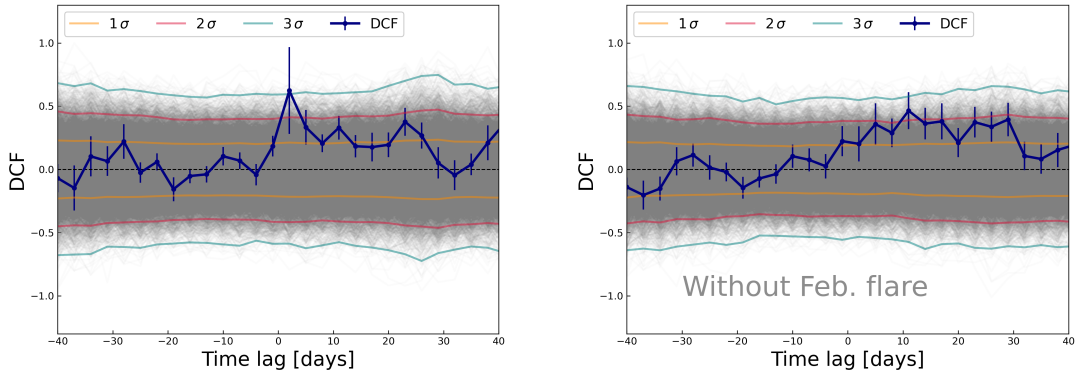

(a) >0.2 TeV vs 3-300 GeV

(b) >0.2 TeV vs 3-300 GeV without the flare in February 2010

Figure 6.17: Discrete correlation function computed between the VHE gamma-ray fluxes above 0.2 TeV, as measured by MAGIC and VERITAS, and the HE gamma-ray fluxes in the 3-300 GeV energy range measured by *Fermi*-LAT. The left panel shows the results for the full dataset, and the right panel those obtained when excluding the large flare in February 2010 (see text for details). The DCF is computed using a time bin of 3-days for a range of time lags between -40 to +40 days. The 1 σ, 2 σ, and 3 σ confidence levels obtained by simulations are shown by the yellow, red, and green lines, respectively.

estimated with Monte Carlo simulations similar to the approach in MAGIC Collaboration et al. (2021): I first simulate a set of 10000 uncorrelated light curves for a pair of energy bands similar as before. I then compute the DCF of the 10000 simulated light curve pairs. The 1 σ, 2 σ and 3 σ confidence bands are derived from the distribution of the simulated DCF values in each time lag bin.

The result for the DCFs between the >0.2 TeV band with the 3-300 GeV band is shown in Figure 6.17a. The figure shows the DCF scan obtained from the data in dark blue. It shows the DCF values for various time lags in three-day bins. One can see a big pronounced peak in the center. All 10000 DCF curves from the simulated light curves are shown in light gray, and the confidence intervals constructed from them in yellow, red and green. The DCF peaks at a time lag of 2 ± 2 days and crosses the 3 σ line. This can be seen as a marginally significant correlation.

To estimate the uncertainty of the time lag, I follow the method outlined in Peterson et al. (1998), for which 10000 new pairs of light curves for both energy bands considered are created. The new light curves are generated via flux randomization and random subset selection to account for statistical fluctuations as well as sampling effects. For each light curve pair, I again compute the DCF, and the centroid of the lags above 80% of the maximum DCF value is calculated. Finally, the 1 σ band for the lag is estimated from the 68% containment of the centroid distribution.

It is important to note that the marginally significant (a little over 3 σ) peak at zero time lag is primarily driven by the big flare in February 2010. The highest flux points in the VHE and HE light curves both occur during this flare. If the highest flux in the HE light curve (covering

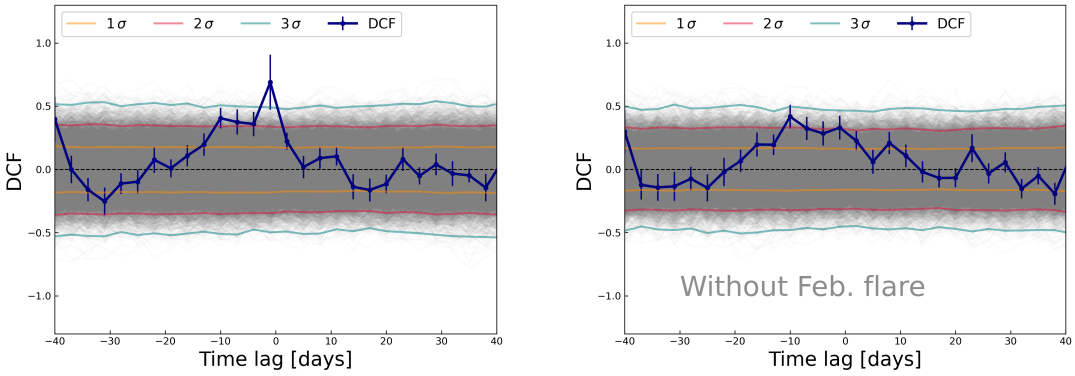

(a) 3-300 GeV vs 0.3-2 keV

(b) 3-300 GeV vs 0.3-2 keV without the flare in February 2010

Figure 6.18: Same as in Fig. 6.17, but this time using the 3-300 GeV range provided by *Fermi*-LAT, and the fluxes in the 0.3-2 keV band, as measured by *Swift*-XRT.

the period from MJD 55242 to MJD 55245), together with the corresponding VHE fluxes in this time interval, are removed from the DCF study, the correlation at zero time lag vanishes. The resulting plot is shown in Figure 6.17b. A similar behavior is also seen in the correlation between the >0.2 TeV band and the 0.3-3 GeV band. The results are shown in the Appendix B.1 in Figure B.1. But this time, the significance of the peak at zero time lag is just over the 2 σ line.

6.6.4 HE gamma rays vs X-rays

For the correlation between HE gamma rays from *Fermi*-LAT and X-rays from *Swift*-XRT, again the DCF at different time lags with a 3-day binning is applied. I correlate each of the two HE gamma-ray bands with each of the X-ray bands from XRT. In this section, I only display the strongest correlation as an example, which is found between the 3-300 GeV and the 0.3-2 keV band. The DCF is shown in Figure 6.18a. The central peak lies well above the 3 σ line and is located at a time lag of -1 ± 2 days. Similar to the VHE vs HE gamma-ray case, the sharp peak at zero time lag is caused by the outstanding flaring activity on February 17. Figure 6.18b shows the same DCF analysis but with the flare removed from both the light curves taken by *Fermi*-LAT, as well as the simultaneous flux in the X-ray light curve as before. The high peak at zero time lag completely vanishes, but only a broad peak closely reaching $\sim$2.5 σ remains. The peak has its highest values at a time lag of -10 $\pm$ 4 days.

The other three combinations of energy bands can be found in Appendix B.1 in Figure B.2 for completeness. In all three combinations, one can see a marginally significant peak at a time lag of about zero that disappears when removing the 3-day LAT flux bin and corresponding X-ray fluxes from the outstanding flaring activity around February 17, 2010. This period in early 2010, including the flare, marks the first time such a correlation was observed, as was previously reported in Abeysekara et al. (2020).

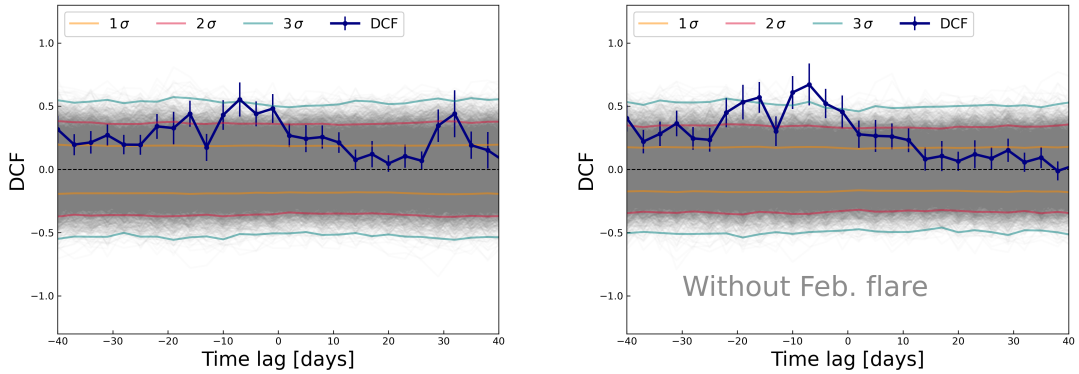

(a) 3-300 GeV vs UV-W1

(b) 3-300 GeV vs UV-W1 without the flare in February 2010

Figure 6.19: Same as in Fig. 6.17, but this time using the 3-300 GeV range provided by *Fermi*-LAT, and the UV-W1 fluxes measured by *Swift*-UVOT.

6.6.5 HE gamma rays vs UV

Next up, the correlation between HE gamma rays and the UV band is investigated. Figure 6.19a contains the DCF between the 3-300 GeV band and the UV W1 filter. The image shows a broad peak, which reaches its highest value at a time lag of -7 ± 6 days. At the peak, the DCF of the data crosses the $3\,\sigma$ line. A negative time lag indicates that the correlated HE gamma-ray emission arrives 7 days before the UV emission. The time lag is, however, still compatible with zero within just a little over $1\,\sigma$.

Between the 0.3-3 GeV band and the UV, the highest value is reached at -1 ± 6 days, which is well compatible with zero. The peak also reaches a significance level of above $3\,\sigma$. The corresponding plot is shown in B.3 in the Appendix.

The positive correlation between both HE gamma-ray regions and the UV band is a novel behavior with no previous reports. Acciari et al. (2021) found a positive correlation between the 0.3-300 GeV band, and the R-band, which is close to the UV in energy. The correlation was found by investigating the time period of 2007-2016 with a 15-day binning resulting in a low temporal resolution but huge overall time coverage.

Contrary to the previous cases, the correlation between HE gamma rays and the UV increases if the flare in February is excluded. Figure 6.19b shows the result of correlating the 3-300 GeV light curve with the W1 light curve without the flare. The peak is clearly enlarged, going well above $3\,\sigma$ for multiple bins, indicating a stronger correlation than previously. The improvement is only marginal for 0.3-3 GeV (Figure B.3 in the Appendix).

6.6.6 HE gamma rays vs R-band

Lastly, I test if the correlation between the HE gamma rays and the optical as previously reported in Acciari et al. (2021) is also present in our data set. Figure 6.20a shows the DCF for 3-300 GeV vs the R-band. The results do not reveal any significantly correlated behavior. Similar for the

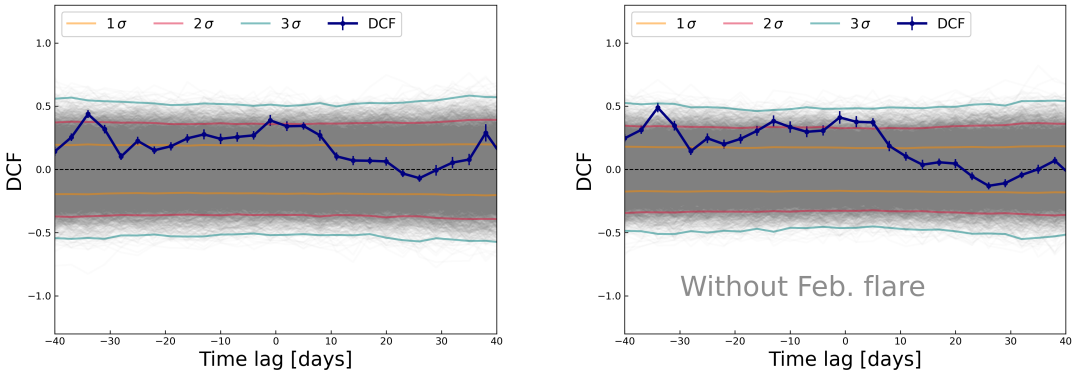

(a) 3-300 GeV vs R-band

(b) 3-300 GeV vs R-band (GASP-WEBT) without the flare in February 2010

Figure 6.20: Same as in Fig. 6.17, but this time using the 3-300 GeV range provided by *Fermi*-LAT, and the R-band fluxes provided by GASP-WEBT.

0.3-3 Gev band shown in the Appendix in Figure B.4a. The latter has a marginally significant ($\sim 3\sigma$) feature at about -35 days, which is most likely an artifact of the binning/sampling, since the feature is very difficult to explain by a physical meachnism.

Removing the 3-day interval that contains the large VHE and X-ray flare in February 2010 does not substantially change the shape and the significance of the DCF results for these two bands (see images 6.20b and B.4b). Only a slight increase to $2.5\,\sigma$ is seen for the former 3-300 GeV case.

6.6.7 Other energy bands

I also investigated the correlation behavior between all other wavebands not discussed in the previous sections. No correlations (positive or negative) were found between any bands in the X-ray and the UV or the optical. Previous works have found anti-correlated behavior at times (e.g. MAGIC Collaboration et al., 2021; Di Gesu et al., 2022), which was not observed in this data set. Naturally, there is a strong correlation between the UV and optical since both bands are very close to each other in energy. Since there is a hint of a correlation between VHE and UV, I also checked if the correlation is still present between the VHE and the optical. Applying the same method yields no correlations at all between VHE and optical. I also found no correlation of any sort between radio and other energy bands. Due to the limited duration of the campaign, the overall number of radio observations is also very limited. Correlations with the radio tend to reveal themselves over much longer time scales (see, e.g., the 8-year data set in Acciari et al., 2021).

6.7 Discussion

6.7.1 Ejection of radio knots

Observations by VLBA revealed the ejection of two features in the jet. The emission times are close to the observed VHE gamma-ray flares. The ejection and propagation of bright knots in the jet has been associated with gamma-ray flares repeatedly in blazars, but the vast majority of these detections were reported in FSRQs (like PKS 1510-089) or LSP/ISP BL Lacertae (see Jorstad et al., 2001; Marscher et al., 2008; MAGIC Collaboration et al., 2018). Such an association has rarely been observed in HSPs, and this is the first time for Mrk 421 (see, e.g., the sample in Weaver et al., 2022), hence making the dataset presented in this work unique on its own. The large uncertainties of the ejection time, however, prevent me from significantly correlating the appearance of the radio features with a specific VHE gamma-ray flare. There are previous works on Mrk 421 reporting a possible connection between GeV gamma-ray and radio flares detected with single-dish telescopes (Hovatta et al., 2015). This large GeV flaring activity, which was measured with *Fermi*-LAT in the year 2012, and the exceptionally large radio flare, which was primarily measured with OVRO also in 2012, was not associated with the ejection of features in the VLBA images (Richards et al., 2013).

In the following, I make the assumption that the strongest flare in the 2010 campaign, the one in February, is indeed correlated with the ejection of the radio features, and estimate if the derived Doppler factors allow for a connection. The flare showed an intranight variability in the VHE band detected on a time scale of less than 1 h, which implies a small, compact zone responsible for the emission based on causality arguments. Abeysekara et al. (2020) observed intranight variability down to 22 min at VHE in February 2010, which was used to derive a lower limit on the Doppler factor of the emission region of $\delta_{\mathrm{min}} \gtrsim 33$ based on opacity arguments. From VLBA observations, Jorstad et al. (2017) estimate the average Doppler factor to be around 24, well below the lower limit mentioned above using the VHE observations. This often appearing discrepancy between the observed jet kinematics in the radio and the Doppler factors derived from the fast variability at high energies is called the *Doppler crisis*. The discrepancy could potentially be resolved in several ways. One option is the presence of structured jets, in which different regions show different Lorentz factors, such as a fast spine responsible for the gamma-ray emission and a slower sheath layer responsible for the radio emission (Ghisellini et al., 2005). Recent works also suggested a scenario in which the discrepancy is reconciled by assuming, a large viewing angle relative to the jet explaining the slow-moving and lower Doppler factor of the knot in radio, while on the other hand, the gamma-ray flare originates from a magnetic reconnection scenario within a misaligned layer that effectively generates larger Doppler factors (Jormanainen et al., 2023). Additionally, a decelaration of the jet occurring between the time of the gamma-ray flare and the detection of the radio feature may partly also solve this crisis (Georganopoulos and Kazanas, 2003).

6.7.2 VHE vs X-ray correlation

I found a close correlation at zero time lag between the emission in the VHE gamma rays with the X-rays over an order of magnitude in flux. In addition, a comparable level of variability

was observed in both energy bands, similar to the results in MAGIC Collaboration et al. (2021) and Acciari et al. (2021). The fractional variability shows a pronounced double-peak structure, with the two peaks reaching values around ∼0.8-1 in X-rays and VHE gamma rays. This tight correlation and similar variability behavior suggest a cospatial origin, meaning both types of radiation are produced in the same emission region. A natural explanation for this is given by the SSC scenario described in section 2.3.2, where the same electron population is responsible for the emission of X-ray photons via synchrotron emission and the VHE gamma-rays by upscattering the synchrotron photons via IC process.

I find the strongest correlation between the 0.3-2 keV and >200 GeV bands reaching a level of 4 σ. The energy in the X-rays can now be used to estimate the energies of the electrons responsible of the synchrotron emission. Assuming standard values for the jet parameters ($B =$ 0.1 G and $\delta = 35$, see, e.g., Aleksić et al. (2015b)), electrons with a Lorentz factor of around 10^5 (source reference frame) are required to emit ∼ keV photons (in observer's frame). Now, using Equation 14 of Tavecchio et al. (1998), which takes into account the Klein-Nishina effects, one expects that electrons with such an energy emit ∼0.5 TeV photons via IC scattering of ∼ keV photons. Those estimates show a good agreement with the observed correlation trends and with a SSC scneario.

The slope in the correlation between different energy bands shows a different pattern depending on the combination. The slope increases for a fixed X-ray band as one increases the energy of VHE band. On the other hand, if one fixes the VHE band, the slope decreases as one increases the energy of the X-ray band. A similar trend has been reported in previous studies (e.g., Acciari et al., 2020, 2021; MAGIC Collaboration et al., 2021). This work confirms this behavior over a full order of magnitude in VHE gamma-ray and X-ray fluxes, ranging from low-emission to extremely large flaring states. In the majority of cases, the slopes are compatible with a linear relationship. The only correlation slope greater than one is found when considering the $>$ 1 TeV, and the 0.3-2 keV bands ($m = 1.5 \pm 0.2$). This is in line with the behavior for flux-flux correlations of an SSC model as described in Katarzyński et al. (2005). The correlation slope is expected to be linear in most cases, but can show an above linear relation for certain energy bands closely situated at the synchrotron peak, which is the case for the 0.3-2 keV band in Mrk 421.

6.7.3 Possible UV vs HE gamma-ray correlation

I found for the first time in Mrk 421 a marginally significant correlation between the UV and HE gamma radiation at a level very slightly above 3 σ. Such a trend would also be well in line with the previously proposed SSC model. The UV photons are emitted by electrons with lower energies compared to the previous case for the X-ray. The same electrons are then responsible for the emission of HE gamma-ray photons at the rising edge of the gamma-ray bump via IC scattering. Both bands also show a similar level of variability, as shown by the fractional variability (see Figure 6.10), which further supports a common spatial origin. The overall lower observed variability and the broad DCF peaks suggest a longer variability time scale, which points towards a larger emitting zone.

Analogous to the estimates performed in the previous section, once can derive estimates of the necessary electron energies / Lorentz factors. Synchrotron photons in the UV W1 band

are produced by electrons with a Lorentz factor of $\sim 10^4$ (assuming the same jet parameters as before). These electrons then produce IC emission at a few tens of GeV, falling well within the 3-300 GeV band, for which the highest correlation is observed. These estimates provide a consistent picture of the observed correlation trends and give additional support for the SSC scenario, with a cospatial emission for the UV and HE bands.

The correlation strength and and its significance decrease to a non-significant level (i.e., well below 3σ) when going from the UV to the optical band. The UV and R-band are close together in frequency, but these results imply that the underlying particle population responsible for the HE gamma rays is dominantly radiating in the UV rather than in the R-band. Carnerero et al. (2017) and Acciari et al. (2021) reported significant positive correlations between the HE gamma rays and the R-band. These two studies considered much longer periods ($\sim$8 years) in which Mrk 421 showed an overall lower activity. The slightly different correlation behavior could be explained by the different overall magnitude and timescales of the flux variability considered, as well as the underlying mechanisms driving the variability, such as e.g. evolution of the emitting region environment, change in the acceleration/cooling efficiencies etc...

It is important to point out that the correlation strength increases when the 3-day time interval corresponding to the large VHE flare in February 2010 is excluded. This behavior can be explained if the HE gamma-ray emission during the large flare in February 2010 does not primarily originate from the same, possibly large, region that dominates the HE and UV/optical emission throughout the campaign, but from a separate smaller emission region.

6.7.4 Evidence of multiple emission zones

The above-mentioned correlations, as well as the lack of correlations (e.g. I did not find any correlation between the X-ray and the UV), can be explained by assuming two separate particle populations, of which a *compact zone* with higher particle energies is responsible for the keV (and TeV) emission, and a larger and more *extended zone* dominates the emission in the eV (and possibly GeV) band. As an alternative, fine-tuning of the parameters may still be able to explain this lack of correlation between the UV and X-rays using a single zone if one assumes that the flux variability is dominated by changes in the particle population at the highest energies, that are not propagated to the lower energy particles, bit is less natural.

I also investigated a possible correlation between VHE gamma rays and the UV. I find a positive trend, but only at a significance level of $\sim 2.0 - 2.3\,\sigma$, which cannot be considered a robust result. If one views this trend as a hint, it could point towards a weak, barely detectable behavior that is difficult to explain by a single particle population. The two-zone explanation can provide a fully consistent picture: the compact zone is embedded within the extended zone, and both are responsible for the dominant synchrotron emission in the UV and X-ray, respectively. In case the UV emission increases due to a change in the underlying particle population, synchrotron photons from the extended zone can enter the compact zone and provide additional seed photons for IC scattering. This *interaction* can then increase the observed VHE gamma-ray flux. Figure 6.21 shows a sketch of the scenario and the resulting SED. On the left, a simplified sketch of the two-zone scenario is displayed. In the case of shock acceleration as the method of particle acceleration (see Section 2.3.1), the compact zone is located close to the shock front, where particles still have the highest energies after being freshly accelerated. As particles spread and

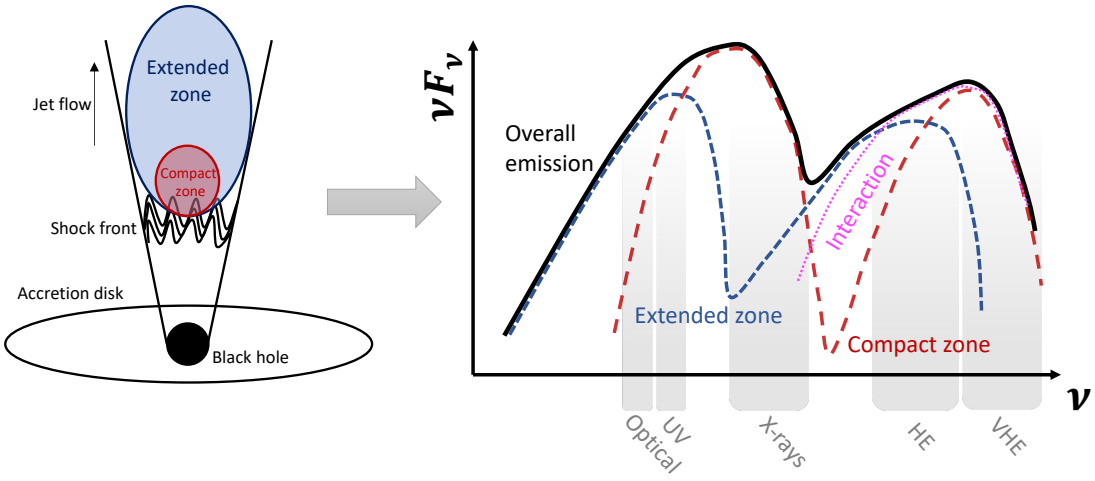

Figure 6.21: Left part: Sketch of the proposed two-zone scenario, showing the compact zone close to the shock front in red and the extended zone in blue. Right part: Resulting SED emission components of the two zones, including the contribution of the interaction between the two zones. Image is based on the sketch and SED modeling presented in MAGIC Collaboration et al. (2024)

cool down, they emit synchrotron radiation at lower energies over a wider region forming the extended zone. This multiple-zone scenario as a result of shock acceleration is also motivated by new findings of the Imaging X-ray Polarimetry Explorer (*IXPE*), which suggest an energy dependency of the polarization degree from radio to the X-ray[7]. The energy dependency points towards an energy-stratified jet creating emission zones of different extent as a result of shock acceleration (Di Gesu et al., 2022, 2023; Abe et al., 2024). The proposed scenario of two separate emission zones is a simplified implementation of an energy-stratified jet. Similar findings have also been reported for the HSP Mrk 501 (Liodakis et al., 2022a), for which the outlined two-zone leptonic model with interaction between the zones has been successfully used to fit the SEDs during the *IXPE* observations (MAGIC Collaboration et al., 2024). The right part of Figure 6.21 sketches the resulting SED from such a scenario based on the modelling in MAGIC Collaboration et al. (2024). The extended zone reaches its first peak in the UV and dominate the second peak up to GeV energies. The compact zone dominates the emission in X-ray and VHE gamma-rays. The described interaction effect will contribute in addition over the gamma-ray peak. The figure shown is not a result of quantitative modeling but should only demonstrate qualitatively the contributions to different energy bands.

The idea of multiple emission zones contributing to the overall SED is also supported by a long-term flux trend between January 15, 2010, and March 1, 2010. Fluxes are decreasing in both the UV and R-band, whereas the simultaneous X-ray (and VHE) emission show an uncorrelated very strong variability. Strong fine tuning between the parameters would be required within a one-zone SSC scenario, to obtain a slowly and mildly decreasing UV/optical flux simultane-

[7] More details can be found in Chapter 7, where the results of *IXPE* on Mrk 421 in the context of MWL observations are discussed extensively.

ous to strong X-ray variability. The observed UV/optical trend could rather be explained by a long-term evolution of the environment of the region, such as the Doppler factor or the magnetic field strength, and be unrelated to the emitting region producing the short timescale X-ray/VHE flares.

Previous works on the large flare in February in 2010 find a correlation between the VHE gamma rays and optical band during the night of the big flare on February 17 (Abeysekara et al., 2020). The correlation was determined with 2 min binned light curves and showed a time lag of 25-55 min. The authors argue that the pattern can appear within a small region under a localized leptonic single-zone SSC scenario. This correlation is not present in the dataset of this work, where the results are dominated by a much larger time binning (usually daily), and, therefore, not sensitive to effects on sub-hour timescales. In addition, the minimum electron energies of the particle population that dominates the emission at VHE gamma rays is very large, at $\gamma_{min} \sim 10000$ and, for typical magnetic fields and Doppler factors, B$\sim$0.1G and $\delta \sim 20$, would produce only a subdominant contribution to the emission in the R-band. In this case, a positive optical correlation should only be detected during very strong flaring events as the one in February 2010, but not over extended periods, which explains the non-detection in my dataset.

6.7.5 Peculiarities of the flare in February 2010

In February 2010, Mrk 421 showed the most violent X-ray and VHE flare to date: TeV fluxes going beyond 25 times the TeV flux of the Crab Nebula were measured, and X-ray fluxes increased by a factor of 70 within the campaign (for the 2-10 keV band). The MWL coverage during this activity was limited but sufficient for several noteable observations, as reported and discussed in Abeysekara et al. (2020). In this thesis, I consider the MWL data from the entire campaign in 2010, which extends over 8 months, from November 5, 2009, until July 3, 2010, and naturally contains the data related to the February 2010 flare. The exceptional nature of the event influenced some of the results I obtained with the entire 2010 data set, which are discussed below.

I found a positive correlation between the VHE and HE gamma rays. A correlation between these two energy bands (to be exact > 2 GeV and >0.7 TeV) was reported for the first time for the campaign covering 2015-2016 (Acciari et al., 2021). During that period, Mrk 421 was in a historically low-activity state, which is very different from the activity that Mrk 421 showed during the 2010 campaign. However, in my dataset the VHE vs HE correlation is non-significant when removing the 3-day interval related to the large February 2010 flare, and hence these two bands were directly connected only during this exceptional flaring event. Put differently, the VHE vs HE correlation is not representative of the behavior of Mrk 421 during the 8-month long 2010 campaign, which covers many different activity levels.

A similar trend is seen when considering the correlation between the HE gamma rays and X-rays. The correlation is estimated for the entire 2010 dataset using two bands for HE gamma rays and two bands for X-rays, and is marginally significant ($\sim 3\sigma$) for all given combinations. A positive correlation between the two energy regions was previously reported in Abeysekara et al. (2020) using the light curves around the February flare provided by *Fermi*-LAT at 0.1-100 GeV and MAXI at 2-20 keV. My results confirm this correlation using slightly different energy bands. However, this correlation becomes non-significant when the 3-day time interval of the February

2010 flare is removed from the dataset. The direct relation between these two bands appears only during the large February 2010 flare. If the flare is included, the strongest correlation occurs for the highest-energy band of *Fermi*-LAT (3-300 GeV) and the lowest-energy band of *Swift*-XRT (0.3-2 keV). The discussion given so far unveils that the X-rays are tightly related to the VHE gamma rays, indicating a co-spatial emission, while the UV and HE bands may come from a different region. The flare might be driven by a single compact zone, whose activity becomes high enough such that it not only dominates at VHE but also contributes significantly to the emission at lower energies in the HE gamma rays. The two bands might then lie near the peaks of the SED bumps caused by synchrotron and IC emission of the same particles. Consistent with this scenario, the 0.3-3 GeV band, which lies at the rising edge of the second bump, and the 2-10 keV band, which lies at the falling edge of the synchrotron bump, show the weakest correlation.

Chapter 7

Results from the first combined VHE and X-ray polarization measurements of Mrk 421

The following chapter presents new findings on the emission of Mrk 421 based on new instrumental developments using a recent data set from 2022. It contains the first characterization of the emission behavior of Mrk 421 with VHE gamma rays and simultaneous X-ray polarization measurements in addition to various other MWL data. The subsequent study was published in Abe et al. (2024), of which I am one of the three corresponding authors. I contributed by analyzing the MAGIC data, processing and plotting MWL data, performing the intra-night correlation studies, interpreting results, and producing the text. Axel Arbet-Engels was involved with analyzing the Fermi-LAT data and parts of the X-ray data, processing and plotting MWL data, performing the long-term correlation studies, and producing the text. David Paneque organized and coordinated the observations of the MWL campaign and assisted with editing of the text. All other co-authors were involved in the low-level analysis of the remaining MWL data or are part of the MAGIC collaboration. The text and structure of the following chapter closely follow Abe et al. (2024), and parts of the text have been adopted verbatim.

7.1 Blazar observations with IXPE

Until recently, polarization measurements of blazars were only feasible in the optical and longer wavelengths such as radio and infrared. In the case of HSPs, these measurements do not reach the peak frequencies of the synchrotron component of the SED. The peak region is emitted by the most energetic electrons, which are freshly accelerated and closest to the acceleration site in the jet. As described in section 2.3.2, polarization measurements of the synchrotron radiation give potential insight into the emission mechanisms.

On December 9, 2021, IXPE was launched into orbit (Weisskopf, 2022). IXPE is able to perform measurements of the linear polarization between 2 and 8 keV. Since the measurement of X-ray polarization is a rather inefficient process, observations focus on the brightest sources. The two HSPs, Mrk 421, and the similar source, Mrk 501, were observed as one of the first blazars. Shortly after, within the year 2022, the first detection of X-ray polarization of a blazar in Mrk 501 by IXPE was reported in Liodakis et al. (2022b). A high degree of linear polariza-

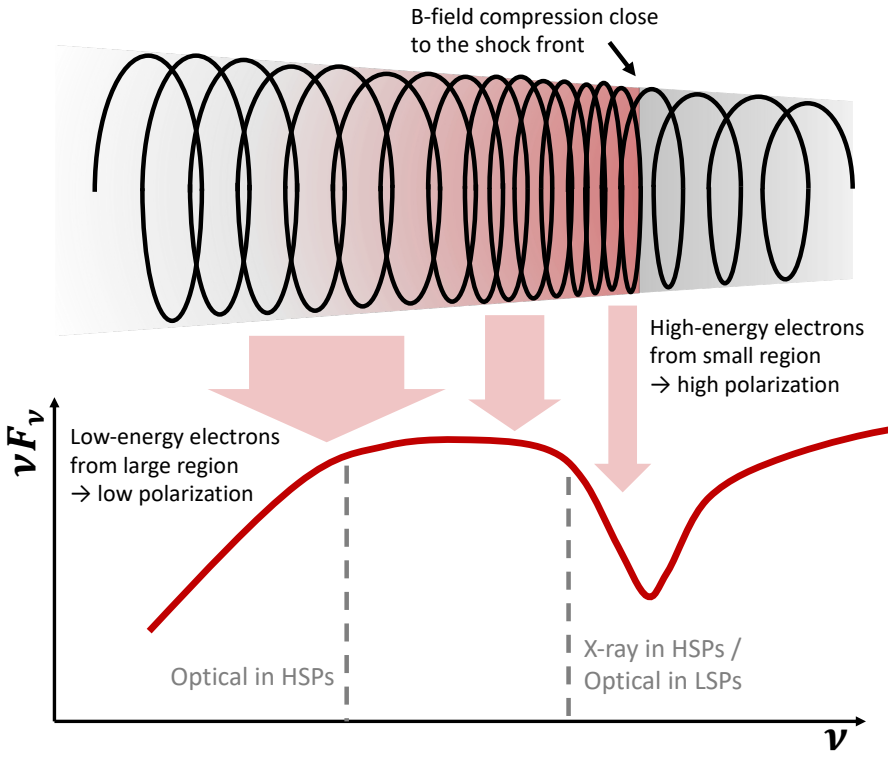

Figure 7.1: Sketch of the shock-in-jet scenario, where the emission of the falling edge of the synchrotron bump is caused by the electrons with the highest energy over a small region. For HSPs this region lies in the X-rays, whereas for LSPs it is in the optical. The downstream direction of the jet is towards the left. Drawing follows the schematic in Angelakis et al. (2016)

tion, at the level of 10%, was detected without significant polarization variability. The X-ray polarization was, in fact, found to be significantly higher than in the optical and radio bands. This energy-dependent polarization behavior suggests the existence of an energy-stratified jet, in which radiation at different energies is emitted from separate regions. The most energetic particles are emitted from a smaller, magnetically more ordered region, which leads to a higher polarization degree (Liodakis et al., 2022b; Angelakis et al., 2016). Larger regions allow for less magnetic order and produce an overall lower polarization degree. Those properties favor shocks as the prime acceleration mechanism. The most energetic particles are then emitted close to the shock front, which leads to a small spatial extent and increased magnetic order. These energetic particles subsequently cool, stream away from the shock to populate broader regions, and then emit synchrotron radiation at lower energies under less ordered magnetic fields. Figure 7.1 shows a sketch of this scenario, where the the region closest to the shock front is responsible for the falling edge of the synchrotron bump. Larger regions downstream the jet are then responsible for the emission at lower energies. For HSPs, this falling edge lies in the X-rays, where polarization measurements were not feasible until IXPE started to operate in the year 2022.

IXPE observed Mrk 421 in the same year in May and June. The first observation spanned from May 4, 2022, 10:00 UTC (MJD 59703) until May 6, 2022, 11:10 UTC (MJD 59705), for a total

exposure of 97 ks. The two additional observations took place in June 2022: from June 4, 2022 10:56 UTC until June 6, 2022, 11:08 UTC (MJD 59734 to MJD 59736; 96 ksec exposure time), and from June 7, 2022, 08:49 UTC until June 9, 2022, 09:51 UTC (MJD 59737 to MJD 59739; 86 ksec exposure time). Similarly to Mrk 501, a high degree of linear polarization was detected in the X-ray compared to the optical and radio. During the first IXPE observation, in May 2022, no variability of the polarization degree and angle is measured (Di Gesu et al., 2022), and the values averaged over the full exposure are considered. Regarding the two observations in June 2022, the polarization angle exhibits a large rotation (Di Gesu et al., 2023) at a speed of $80 \pm 9\,^{\circ}$/day (June 4-6, 2022; MJD 59734 to MJD 59736) and $91 \pm 8\,^{\circ}$/day (June 7-9, 2022; MJD 59737 to MJD 59739). The rotation is evident when considering the data binned in 3 hour intervals. Based on simulations, Di Gesu et al. (2023) estimated that the probability of detecting these rotations due to random walks is about 2%, and thus, it is highly unlikely to have occurred by chance. As described in Di Gesu et al. (2023), the polarization degree remains consistent with a constant behavior hypothesis. These results of the polarization measurement will be put into context and further discussed in section 7.3.

7.2 MWL observations and data analysis

MAGIC

As outlined in the previous chapter, the blazar Mrk 421 has been the focus of a multi-year program consisting of dedicated half-year observations with a number of instruments covering the broadband emission from the radio to VHE gamma rays since 2009. Triggered by the planned observations of Mrk 421 by IXPE, the multi-instrument observations related to the extensive campaign on Mrk 421 were intensified during (as well as before and after) the times when IXPE observed Mrk 421. This intensified monitoring was particularly important for the MAGIC telescopes. MAGIC performed daily observations around and during the first IXPE observation of Mrk 421 in early May, followed by several observations throughout May to monitor the source's behavior in between the IXPE pointings. Since the brightness of the moon increased strongly during early June 2022, MAGIC could only observe for the beginning of the second IXPE observation. After the full moon phase, the visibility of Mrk 421 on the night sky deteriorated so that no further observations were possible at this time of year.

During the full period covered by this study, MAGIC observed Mrk 421 for 20.2 h in total. I only considered data taken under a zenith angle range between 5° and 62°. At even higher zenith angles, the energy threshold of MAGIC increases rapidly beyond ~ 400 GeV (Aleksić et al., 2016a) to an unsatisfactory level. I selected the data according to their quality since clouds were present on some nights. The LIDAR was used to check the atmospheric quality for the nights taken in June.

In May, the LIDAR was not operational due to a technical upgrade. I traveled to the MAGIC site and led this technical maintenance and upgrade, which consisted, among other things, of the exchange of the reflecting mirror and proper alignment (see Appendix A.1 for further details). As a side note, I was also among the telescope operators taking the data of Mrk 421 during those nights. The quality of the May data was ensured by checking the background rates and sky

temperature measurements with a pyrometer, which indicates the presence of clouds. After applying quality cuts to remove data taken at too high of a zenith angle and during adverse weather conditions, 17.3 h of data remained. The data were taken under low moonlight conditions, thus limiting contamination from night sky background light (Ahnen et al., 2017c). Thanks to the brightness and proximity of Mrk 421, two separate light curves can be obtained in the VHE regime covering an energy range from 0.2-1 TeV and above 1 TeV. The former light curve only contains data taken with a zenith angle of up to 50°, while the latter includes the entire zenith range until 62°. The cut on the zenith angle is applied because the energy threshold increases to above 0.2 TeV for zenith angles greater than 50°, and it would introduce artificial downward fluctuations in the reported fluxes (e.g., by producing a light curve above 0.2 TeV when using data with an energy threshold well above this energy).

The spectral analysis of the MAGIC data was performed by fitting the data with a log-parabolic model defined as follows:

$$\frac{\mathrm{d}N}{\mathrm{d}E} = f_0 \left(\frac{E}{E_0}\right)^{\alpha - \beta \log_{10}(E/E_0)} . \tag{7.1}$$

The normalization constant is given by f_0, α is the photon index at a normalization energy E_0, and β is the curvature parameter. For the normalization energy, E_0, a fixed value of 300 GeV was chosen. Flux points were obtained by performing the Tikhonov unfolding procedure as described in Albert et al. (2007c). All obtained parameters and flux points were corrected for the extragalactic background light absorption following the model of Domínguez et al. (2011).

Fermi-LAT

The HE gamma rays are again covered by the *Fermi*-LAT instrument. This time, a light curve is extracted for the 0.3-300 GeV band using 3-day time bins. In all time bins, the source is detected with TS > 25 (i.e., $> 5\sigma$). Finally, a SED is computed around each IXPE observation by averaging the data over 7 days. This time bin choice is a good compromise solution, given the flux variability observed in the light curves and the limited sensitivity of LAT to measure gamma-ray spectra over short time intervals.

X-ray data

In addition to IXPE, observations from three other X-ray satellites are used in this study. Several X-ray pointings from the *Swift* X-ray Telescope (XRT; Burrows et al., 2005) were coordinated. A special effort was put into scheduling the observations simultaneously with the MAGIC exposures. This allows extraction of source spectra between $0.3 - 10$ keV, as well as two light curves covering the 0.3-2 keV, and 2-10 keV energy bands, with the best possible coincidence to the VHE data.

Additionally, there are two multi-hour exposures from the Nuclear Spectroscopic Telescope Array (*NuSTAR;* Harrison et al., 2013), which consists of two co-aligned X-ray telescopes focusing on two independent focal plane modules, FPMA and FPMB. The instrument provides unprecedented sensitivity in the 3-79 keV band. The observations took place June 4-5, 2022

(MJD 59734 to MJD 59735) and June 7-8, 2022 (MJD 59737 to MJD 59738; observation ID 60702061002 and 60702061004, respectively), with a total exposure time of 21 ks and 23 ks, respectively. For both exposures, the source spectra dominate over the background up to roughly ≈ 30 keV. Hence, in this work, fluxes are quoted only up to 30 keV, and in two separate energy bands: 3-7 keV and 7-30 keV.

As a third instrument, the *XMM-Newton* observatory carries on board several co-aligned X-ray instruments: the European Photon Imaging Camera (EPIC) and two reflection grating spectrometers (RGS1 and RGS2; Jansen et al., 2001). The EPIC cameras consist of two metal oxide semiconductors (EPIC-MOS1 and MOS2; Turner et al., 2001) and one pn junction (EPIC-pn, Strüder et al., 2001) CCD arrays operating in the 0.2–10 keV energy band. Source spectra were extracted in the full energy range (0.2–10 keV) with an energy resolution of 5 eV. The spectra were re-binned to avoid oversampling the intrinsic energy resolution of the EPIC cameras by a factor larger than 3 while making sure that each spectral channel contains at least 25 background-subtracted counts. For every observation, spectral fits were performed, and spectral parameters were derived from the combined EPIC instruments available (i.e., EPIC-pn and EPIC-MOS2). All spectra were fitted using a log-parabola model (with a pivot energy set at 1 keV).

UV, optical and radio data

In the UV band, again the *Swift* UV/Optical Telescope (UVOT; Roming et al., 2005) provides coverage. Observations between April 26, 2022 (MJD 59695) and June 27, 2022 (MJD 59757) with the W1, M2, and W2 filters are considered. This results in a sample of 43 observations of Mrk 421 from the official data archive after applying standard quality checks to all observations in the chosen time interval, excluding those with unstable attitude or affected by contamination from a nearby starlight (51 UMa).

In the optical, R-band photometric and polarimetric observations from the RoboPol (Skinakas Observatory, Greece; King et al., 2014; Ramaprakash et al., 2019), Nordic Optical Telescope (NOT; ORM, Spain), and KANATA (Higashi-Hiroshima observatory, Japan) telescopes are used. In addition, the H-band (infrared; IR) data from the Perkins telescope (Perkins Telescope Observatory, Flagstaff, AZ) is included. All these data were published in Di Gesu et al. (2022) and Di Gesu et al. (2023), where more details on the analysis procedures can be found. Additional polarimetric and photometric observations of the source in the Johnson Cousins R band were performed at Sierra Nevada Observatory, Granada, Spain, with a four-unit polarized filter-wheel mounted at the 0.9 m telescope (hereafter dubbed T90). Unpolarized standard stars were also observed to compute the instrumental polarization that was subtracted from the actual data. Standard pre-reduction and analysis steps were performed. All the polarization and photometric data were corrected for the contribution of the host galaxy using the host fluxes reported in Nilsson et al. (2007). The intrinsic polarization degree was obtained using the following formula: $P_{deg,intr} = P_{deg,obs} \cdot I/(I - I_{host})$, where $P_{deg,obs}$ the observed polarization degree, I the observed flux and I_{host} the host flux. Finally, the flux densities were also corrected for a galactic extinction of 0.033 mag.

Data in the microwave band at 3.5 mm (86.24 GHz) and 1.3 mm (230 GHz) wavelengths were collected with the 30 m telescope of the Institut de Radioastronomie Millimetrique (IRAM) that

is located at the Pico Veleta Observatory (Sierra Nevada, Granada, Spain). Additional radio observations were performed by the Metsähovi telescope. Finally, millimeter radio polarimetric measurements were collected at 1.3 mm (approximately 230 GHz) with the Submillimeter Array (SMA; Ho et al., 2004).

For more information on any of the above-mentioned instruments and their low-level data analysis, the reader is referred to Abe et al. (2024) and its further references.

7.3 Characterization of the MWL emission during the IXPE observations

Figure 7.2 shows the MWL light curves from MJD 59695 (April 26, 2022) to MJD 59760 (June 30, 2022), which includes all IXPE observing periods. The VHE energy bands (0.2-1 TeV and >1 TeV) are shown in the top row. As previously mentioned, data observed at a zenith above 50° are excluded from the 0.2-1 TeV energy band, while for the >1 TeV fluxes, no cut on the zenith angle was used. This cut only removed a small fraction of the data from the 0.2-1 TeV light curve (it affects only three nights, removing a total of ≈ 2 hrs), and no intra-night variability was found in any of the two bands. The slightly different underlying data selection does not affect the hardness ratio in any significant manner. Measurements from *Fermi*-LAT in the 0.3-300 GeV band are shown in the second panel from the top. The *Fermi*-LAT fluxes are computed in 3-day bins, providing a good trade-off between statistical flux uncertainty and temporal resolution. In X-rays, shown in the third panel, a dense temporal coverage is given by *Swift*-XRT in two energy bands (0.3-2 keV and 2-10 keV). Additional data by *NuSTAR* and *XMM-Newton* are available on selected days during the IXPE observations. The corresponding spectral evolution is quantified using the hardness ratio in X-rays, which is defined as the ratio of the $2-10$ keV flux to the $0.3-2$ keV flux in the fourth panel. The hardness ratio of the VHE data (defined as the ratio of the >1 TeV flux to the $0.2-1$ TeV flux) is also shown. UV observations from *Swift*-UVOT in the W1, M2, and W2 filters are portrayed in the fifth panel from the top. The MWL light curves are complemented with data in the optical/IR and radio plotted in the sixth and seventh panels, respectively. The last two panels at the bottom of Figure 7.2 display the polarization degree and angle evolution in the radio, optical, IR, and X-ray.

7.3.1 IXPE observation in May 2022

The first observation of Mrk 421 by IXPE occurred between 4 May and 6 May 2022 (MJD 59703.42 - MJD 59705.47) and is shown as the first vertical gray band in Figure 7.2. Here and in the following, this time period will be referred to as IXPE 1.

The MAGIC telescopes achieved continuous daily coverage over the entire first IXPE exposure. The flux exhibits a constant behavior throughout the specified time period in both VHE energy bands, showing a flux slightly below 10% of the emission of the Crab Nebula[1] in the range above 1 TeV, and around 25% for the 0.2-1 TeV range. There is no significant flux or spectral variability on daily and intra-night timescales. The simultaneous X-ray characterization is obtained thanks to *Swift*-XRT as well as a long exposure from *XMM-Newton* on MJD 59704

[1] The flux of the Crab Nebula is taken from Aleksić et al. (2016a)

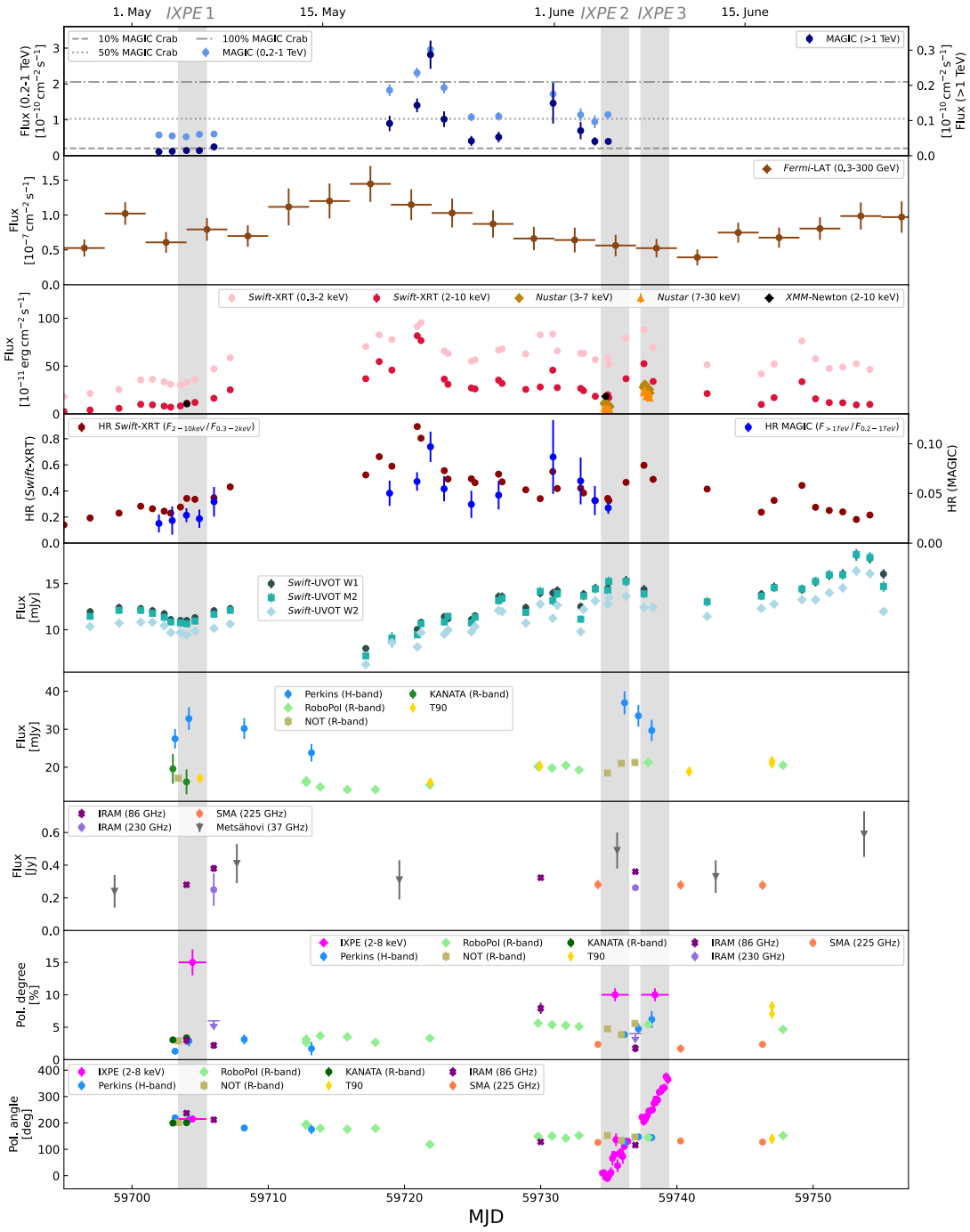

Figure 7.2: MWL light curve for Mrk 421 covering the whole campaign from MJD 59695 (April 26, 2022) to MJD 59757 (June 27, 2022). The gray bands correspond to the three IXPE observations. Top to bottom: MAGIC fluxes in daily bins for two energy bands (note the two different y-axes); *Fermi*-LAT fluxes in 3 day bins; X-ray fluxes in daily bins including *Swift*-XRT, *NuSTAR* and IXPE; hardness ratio between the high- and low-energy fluxes of *Swift*-XRT and between the two VHE bands of MAGIC (note the two different y-axes); optical R-band data from NOT, RoboPol KANATA; IR H-band data from Perkins; radio data from IRAM and; polarization degree and polarization angle observations in the optical to radio from NOT, RoboPol, KANATA, Perkins, IRAM, SMA and in X-rays from IXPE.

(May 5, 2022). The flux in both energy bands of the *Swift*-XRT instrument shows moderate daily variability. A flux increase at the level of 20% is observed in the 0.3-2 keV band, while it is 40% in the 2-10 keV band. The hardness ratio rises from 0.23 ± 0.01 up to almost 0.35 ± 0.01, which indicates a harder-when-brighter trend in agreement with previous observations of Mrk 421 (see for instance Aleksić et al., 2015a; Acciari et al., 2021; MAGIC Collaboration et al., 2021). Regarding the multi-hour *XMM-Newton* exposure, the average 2-10 keV flux (black marker in Figure 7.2) is consistent with *Swift*-XRT results. Little variability was observed during the observation. A more detailed 500 s binned *XMM-Newton* light curve can be found in the Appendix of Abe et al. (2024). The simultaneous optical/IR (R band and H band) and radio flux data in Figure 7.2 around IXPE 1 show small variability, although the limited temporal coverage prevents a detailed variability characterization.

The polarization degree from radio to optical shows fluctuating values around 3%. The results of the IXPE observation (taken from Di Gesu et al. (2022)) show a much higher constant degree of polarization of 15 ± 2 % in the X-ray band at 2-8 keV. The polarization angle determined by IXPE is $215 \pm 4^\circ$ (or $35 \pm 4^\circ$, if one considers the 180° ambiguity in polarization angle measurements). This is in agreement with the angles measured in radio to optical, which range from around 200° up to 230° and remains constant throughout the observation period.

7.3.2 IXPE observation in June 2022

The second and third IXPE observations of Mrk 421 were performed between June 4 and 6, 2022 (MJD 59734.46 - MJD 59736.46) and between 7 and 9 June, 2022 (MJD 59737.36 - MJD 59739.41). In the following, these two observing epochs are called IXPE 2 and IXPE 3, respectively. They are highlighted with the other two gray bands in Figure 7.2.

Because of the bright moon period starting, MAGIC only managed to observe during the first day of the IXPE 2 period as well as two days before, for a total of 3.3 h. Over the course of three days, the flux in the 0.2-1 TeV band is close to ≈50% of the Crab Nebula and ≈20% above 1 TeV, showing a flux about twice as high as during IXPE 1.

In X-rays, significantly higher activity is observed throughout the entire IXPE 2 and IXPE 3 windows with respect to IXPE 1. The source shows clear variability of the spectral shape and the flux. Between the IXPE 2 epoch and the start of the IXPE 3 epoch, the 2-10 keV flux shows an increase by a factor of ≈ 2.6, together with a clear hardening of the emission that is highlighted by the hardness ratio evolution (a more detailed spectral analysis is presented in section 7.3.3). The peak activity in the 2-10 keV band is about five times as high as the average flux level observed during IXPE 1. Although this flux state is still below previous large X-ray outbursts of Mrk 421 (see Chapter 6), this activity is among the highest states recorded during 2022. The flux decreases during the last *Swift*-XRT observation during IXPE 3. The *XMM-Newton* data confirms the higher X-ray activity compared to IXPE 1. The observation took place at the beginning of IXPE 2, slightly before the flux increase witnessed by *Swift*-XRT. In addition to *Swift*-XRT and *XMM-Newton*, a precise hard X-ray characterization was obtained by the two multi-hour *NuSTAR* exposures during both IXPE 2 and IXPE 3. In the third panel from the top of Figure 7.2, the *NuSTAR* fluxes are also shown in the 3-7 keV and 7-30 keV bands using 1 hour time bins. For IXPE 2, the observation by *NuSTAR* was simultaneous to MAGIC. The resulting intra-night VHE versus X-ray correlation is investigated in Section 7.3.5. During both

NuSTAR observations, a moderate flux change is observed on hour timescales (at the level of 30%). Nonetheless, a detailed study reveals spectral hysteresis patterns. This analysis is shown in Sect 7.3.6.

The *Fermi*-LAT data covering the MeV-GeV band shows a similar flux state as during IXPE 1 and is close to the average activity for Mrk 421 (Abdo et al., 2011). For the UV, optical, IR, and radio emission, the emission does not reveal significant evolution compared to IXPE 1 either.

The two bottom panels of Figure 7.2 display the evolution of the polarization degree and angle in the X-ray 2-8 keV band (pink markers; the data are taken from Di Gesu et al., 2023). The averaged degree is 10 ± 1 % during IXPE 2 and IXPE 3. While the polarization degree is compatible with a constant behavior (see also section 7.3.6), the polarization angle shows an evident rotation, which seems continuous between the two IXPE 2 and IXPE 3 epochs. The angle rotates at an average angular velocity of $80 \pm 9\,^{\circ}$/day amounting to a total rotation of $120\,^{\circ}$ during IXPE 2. The rotation continued at a similar rate of $91 \pm 8\,^{\circ}$/day during IXPE 3, for a total rotation of $140\,^{\circ}$. The previously described significant X-ray flux increase and spectral hardening measured by *Swift*-XRT is therefore accompanied by a rotation of the polarization angle. In Section 7.3.6, the short timescale spectral variability in the hard X-rays is investigated during the observed polarization angle rotation using simultaneous *NuSTAR* data.

Interestingly, at lower frequencies, in the radio, IR, and optical bands, neither the flux nor polarization properties show any prominent variability. The polarization degree in the optical and IR fluctuates only around 5% while the radio polarization is even lower, around 2%, both for the 86 GHz and 230 GHz bands.

7.3.3 Spectral evolution throughout the IXPE observing epochs

Figure 7.3 presents the broadband SEDs obtained during each of the IXPE periods from the IR up to VHE gamma rays. For comparison, the average state of Mrk 421 taken from Abdo et al. (2011) is plotted in light gray. The VHE flux level reported in Abdo et al. (2011) is close to the average state found by Whipple over a time span of 14 years (45% of the Crab Nebula flux, Acciari et al., 2014). The SED shown in Abdo et al. (2011) can therefore be considered an average activity state and is used as a reference for comparison. VHE flux points by MAGIC from IXPE 1 were obtained by averaging all data within the corresponding IXPE observation time frame, since there is no significant spectral flux variability. For IXPE 2, only a single MAGIC observation is available, and it took place at the beginning of the IXPE window, while IXPE 3 completely lacks VHE coverage (see Figure 7.2 and previous section). The *Fermi*-LAT SEDs were averaged over seven days, centered around the middle of the IXPE windows, to achieve sufficient statistics. The *Swift*-XRT SED on MJD 59704.02 (May 5, 2022) is used for IXPE 1, which is close to the center of the IXPE window and simultaneous to the *XMM-Newton* observation. For IXPE 2 and IXPE 3, the individual *Swift*-XRT SEDs, which were first recorded within the IXPE windows, are used. These SEDs are accompanied by simultaneous *XMM-Newton* (for IXPE 1 and IXPE 2) and *NuSTAR* data (for IXPE 2 and IXPE 3). The *Swift*-XRT SEDs corresponding to the subsequent pointing of IXPE 2 and IXPE 3 are shown with white centered markers in order to illustrate the daily timescale variability along the IXPE exposure. For the UV, optical and IR data, measurements that are the closest in time to each of the X-ray observations are displayed.

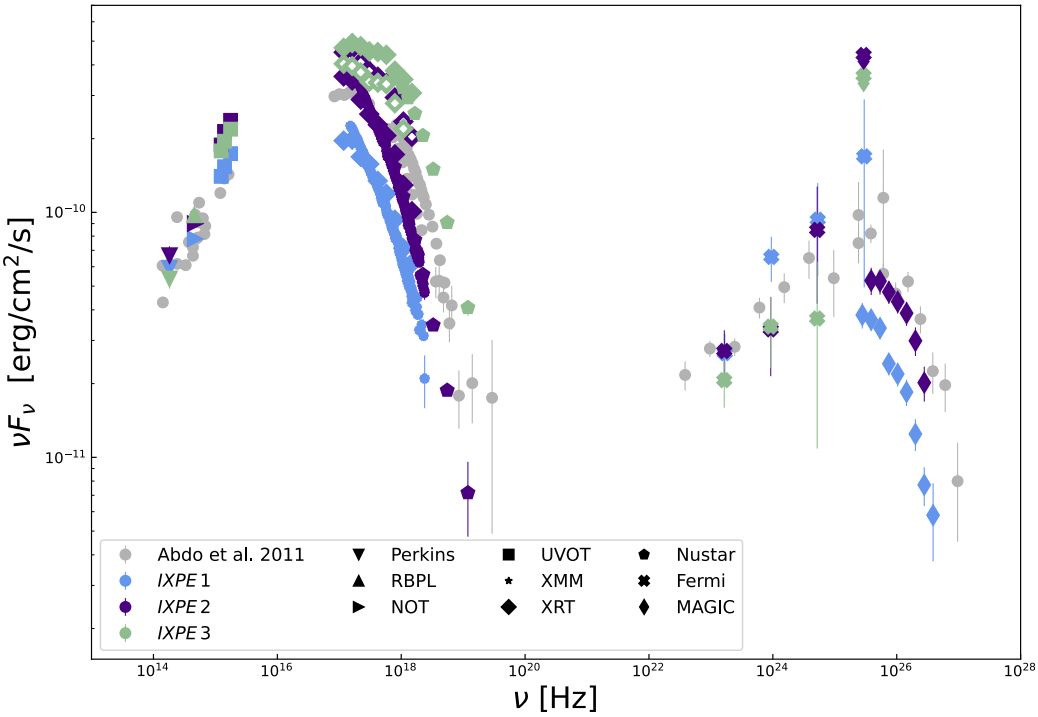

Figure 7.3: Broadband SED around the three IXPE observations. Data from MAGIC were corrected for the extragalactic background light absorption using the model outlined in Domínguez et al. (2011). In plain colored markers, the *Swift*-XRT data correspond to the pointing that happened first within the IXPE windows. The *Swift*-XRT data in diamond markers with a face color in white are from the subsequent observation. For comparison, the SED of an average emission state of Mrk 421 from Abdo et al. (2011) is shown in light gray.

Table 7.1: Spectral parameters from the VHE and X-ray observations around the three IXPE observing epochs. The table contains four primary rows corresponding to the different instruments. The first sub row for an individual instrument shows the MJD of the observations performed during the three IXPE observations given by the main columns. The second subrow contains the obtained fluxes in units of $10^{-10}\,\mathrm{erg\,cm^{-2}s^{-1}}$ (for MAGIC the integrated photon flux between 200 GeV and 1 TeV is used, for *Swift*-XRT and *XMM-Newton* the flux between 2-10 keV and for *NuSTAR* the 3-7 keV flux). The spectral index α, assuming a log-parabola for MAGIC (with β fixed to 0.50 and reference energy of 300 GeV) as well as for *Swift*-XRT (with β fixed to 0.29 and reference energy of 1 keV), *XMM-Newton* (with β fixed to 0.20 and reference energy of 1 keV), and *NuSTAR* (with β fixed to 0.45 and reference energy of 1 keV) is given in the third subrow. The last sub row gives the χ^2/d.o.f.. Regarding *XMM-Newton* and *NuSTAR*, the parameters were obtained by fitting jointly the data from the available cameras on board these observatories (i.e., EPIC-pn and EPIC-MOS2 for *XMM-Newton*, FPMA and FPMB for *NuSTAR*).

		IXPE 1			*IXPE 2*			*IXPE 3*	
MAGIC	MJD	59703.5 to 59705.5			59734.5 to 59735.5			–	
	Flux	0.34 ± 0.01			0.67 ± 0.03			–	
	α	-2.64 ± 0.06			-2.30 ± 0.08			–	
	χ^2/d.o.f.	25.0 / 13			2.5 / 9			–	
Swift-XRT	MJD	59703.55	59704.02	59704.62	59734.92	59735.00	59736.27	59737.58	59738.25
	Flux	$0.84^{+0.04}_{-0.03}$	$1.13^{+0.04}_{-0.04}$	$1.20^{+0.04}_{-0.04}$	$2.01^{+0.05}_{-0.05}$	$1.70^{+0.05}_{-0.05}$	$3.68^{+0.08}_{-0.08}$	$5.26^{+0.05}_{-0.06}$	$3.40^{+0.12}_{-0.12}$
	α	$-2.52^{+0.02}_{-0.02}$	$-2.38^{+0.02}_{-0.02}$	$-2.38^{+0.02}_{-0.02}$	$-2.40^{+0.01}_{-0.01}$	$-2.43^{+0.02}_{-0.02}$	$-2.22^{+0.01}_{-0.01}$	$-2.07^{+0.01}_{-0.01}$	$-2.19^{+0.02}_{-0.02}$
	χ^2/d.o.f.	223.5/197	236.1/216	225.4/220	261.5/266	241.9/223	346.3/309	549.0/481	218.6/199
XMM-Newton	MJD	59703.93 to 59704.13			59734.68 to 59735.11			–	
	Flux	$1.056^{+0.002}_{-0.002}$			$1.838^{+0.002}_{-0.002}$			–	
	α	$-2.541^{+0.001}_{-0.001}$			$-2.545^{+0.001}_{-0.001}$			–	
	χ^2/d.o.f.	814.8/329			2082.13/345			–	
NuSTAR	MJD	–			59734.65 to 59735.11			59737.53 to 59738.04	
	Flux	–			0.968 ± 0.004			2.693 ± 0.006	
	α	–			-2.309 ± 0.007			-1.913 ± 0.004	
	χ^2/d.o.f.	–			704.7/761			1143.8/1133	

Compared to the average state of Abdo et al. (2011), the IXPE 1 epoch (blue markers) show a significantly lower VHE and X-ray emission. The X-ray SED is also softer, meaning a steeper slope, indicating a shift of the synchrotron peak toward lower frequencies. Based on a log-parabola fit of the SED peak ($\nu F_\nu \propto 10^{-b(\log(\nu/\nu_p))^2}$), a peak frequency can be derived located at $\nu_p = (2.00 \pm 0.07) \times 10^{16}$ Hz, while the state from Abdo et al. (2011) suggests $\nu_p \approx 10^{17}$ Hz. Throughout the IXPE 2 and IXPE 3, Figure 7.3 highlights the spectral changes occurring during the polarization angle swing reported by IXPE. At the beginning of IXPE 2 (plain violet color markers), the emission is roughly similar to the average state at all frequencies. Compared to IXPE 1, the synchrotron peak frequency is marginally larger with $\nu_p = (2.27 \pm 0.09) \times 10^{16}$ Hz. The emission increases significantly with the subsequently observed X-ray SED, which shows a flux well above the typical state as well as a harder emission. The maximum observed brightness is reached at the beginning of IXPE 3 (green diamond markers), which coincides with the second *NuSTAR* observation and shows an enhanced emission state throughout the full synchrotron peak accompanied by a significant shift of the synchrotron peak toward a higher frequency ($\nu_p = (7.6 \pm 1.3) \times 10^{16}$ Hz). A decrease is observed the following day (shown with a white centered marker).

The spectral parameters of the X-rays and VHE gamma rays are listed in Table 7.1. As for Figure 7.3, the MAGIC spectral fits are performed after averaging all nights within the IXPE windows, analogous to the SED extrtaction. The MAGIC data show a preference for a log-parabola model (see Eq.7.1) over a simple power-law function for all IXPE epochs. This preference is above 3σ for IXPE 1 and at the level of around 2σ for IXPE 2. No significant variability of the curvature parameter β was found, which stays consistent at $\beta = 0.50$. The MAGIC spectra simultaneous to the IXPE observations were therefore fitted using a log-parabola model with a fixed curvature of $\beta = 0.50$. This choice removes any correlation between α and β (see Eq. 7.1), better assessing the hardness evolution during the different epochs. The normalization energy in the spectrum was fixed to 300 GeV. The resulting best-fit spectral indices of MAGIC are displayed in the first primary row of Table 7.1.

The *Swift*-XRT spectra show a significant preference for a log-parabola model over a power law as well. As in the MAGIC spectral study, the data were fitted using a log parabola with fixed curvature to better characterize the hardness evolution throughout the IXPE epochs. A curvature of $\beta = 0.29$ is used, which is the average curvature over the campaign. The second primary row of Table 7.1 contains the best-fit parameters for each exposure simultaneous to IXPE (the pivot energy of the log-parabola model is 1 keV).

For *XMM-Newton* and *NuSTAR*, the spectral parameters are derived in the 0.6-10 keV and 3-79 keV bands, respectively. Similarly to the fits for MAGIC and *Swift*-XRT, the curvature is fixed to a value of $\beta = 0.2$ for *XMM-Newton* and to $\beta = 0.45$ for *NuSTAR*. The pivot energy was set to 1 keV for both instruments.

The spectral evolution is consistent with the already mentioned harder-when-brighter trend found frequently in Mrk 421 (Acciari et al., 2021; MAGIC Collaboration et al., 2021). For VHE gamma rays, the spectral index α obtained during IXPE 2 is smaller compared to IXPE 1 ($\alpha = -2.30 \pm 0.08$ versus $\alpha = -2.64 \pm 0.06$ for IXPE 1), while the emitted flux doubled. A similar trend is found in X-rays with *Swift*-XRT, *XMM-Newton* and *NuSTAR* data and confirmed by the visual trend in Figure 7.3. The spectral hardening is especially evident between IXPE 2 and IXPE 3 when the X-ray polarization angle rotates. The spectral parameter α hardens by $\approx 0.3 - 0.4$ (see Table 7.1) for both in *Swift*-XRT and *NuSTAR* .

Most of the spectral variability in X-rays occurs on a close to daily timescale. Variability on shorter timescales can be probed thanks to the multi-hour exposures from *XMM-Newton* and *NuSTAR*. The reader is referred to the Figures in the Appendix of Abe et al. (2024), which show the 0.3-2 keV the 2-10 keV fluxes (binned in 500 s) as well as the hardness ratio obtained during the observations of *XMM-Newton*. The ratios do not reveal any particularly interesting spectral evolution over approximately hour timescales for either day. However, the *NuSTAR* analysis reveals a moderate spectral change on approximately hour timescales, including a spectral hysteresis behavior, which is reported in detail in section 7.3.6.

7.3.4 Broadband evolution of the polarization degree between the IXPE epochs

The polarization degree as a function of the frequency for all IXPE observing epochs is summarized in Figure 7.4. The panel on the bottom shows the ratio to the X-ray polarization degree. One can see an energy dependence of the polarization degree, with a clear increase in the X-ray

band, as already reported by Di Gesu et al. (2022) and Liodakis et al. (2022b), both in Mrk 421 and Mrk 501.

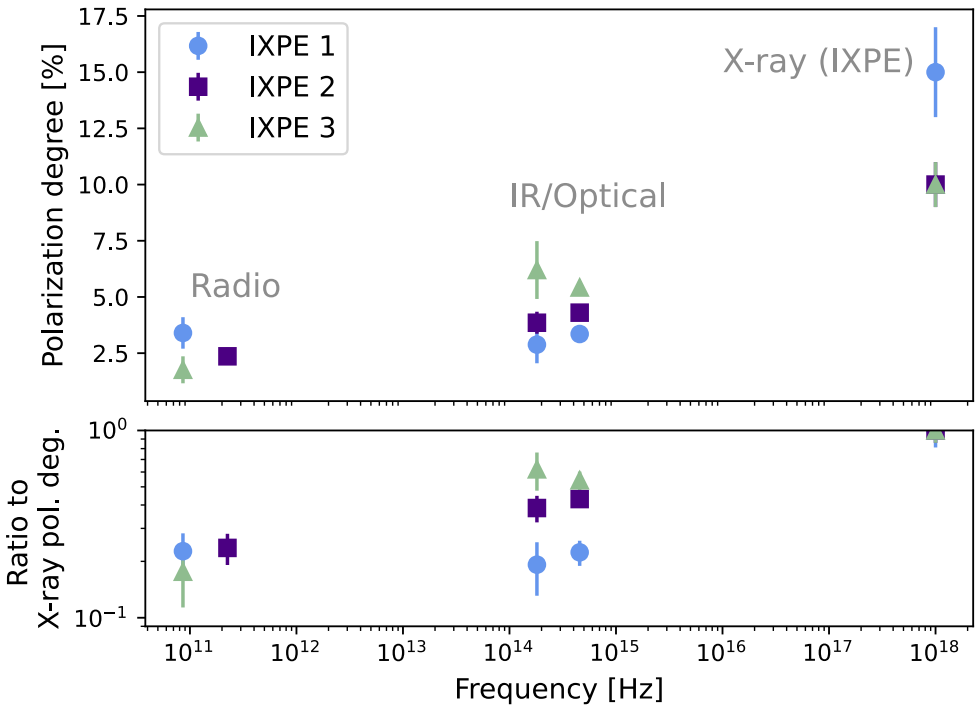

Figure 7.4: Frequency dependency of the polarization degree. Top: MWL polarization degree as a function of frequency during all three IXPE epochs. Bottom: The frequency-dependent polarization degree ratio to the corresponding X-ray polarization degree.

The trend of a significantly higher polarization in X-rays compared to lower frequencies can be seen for all IXPE epochs. This shows why the additional X-ray data is so valuable in combination to the optical and radio polarization data. The ratio between the optical and IR polarization degree and the one in the X-ray band is significantly lower during IXPE 1 than during IXPE 2 and IXPE 3. Besides, there was no correlation between the polarization degree and the flux or spectral hardness for the individual energy bands.

It is interesting to compare the polarization degree behavior with the fractional variability (see description in section 6.5.2). F_{var} is computed using all observations inside the IXPE windows. The results are shown in Figure 7.5. The simultaneity criteria used for Figure 7.4 in the radio are slightly relaxed and also include measurements taking place less than half a day before the start or after the end of the IXPE observing times to compute F_{var}. The F_{var} in the radio can only be computed with data from IRAM in the 86.24 GHz band since it is the only one that has more than one measurement. Results for *NuSTAR* and *XMM-Newton* are plotted in gray since neither of the two instruments has simultaneous data for all IXPE epochs (unlike *Swift*-XRT). The resulting bias created by the different temporal coverage explains the discrepancy to the *Swift*-XRT F_{var}.

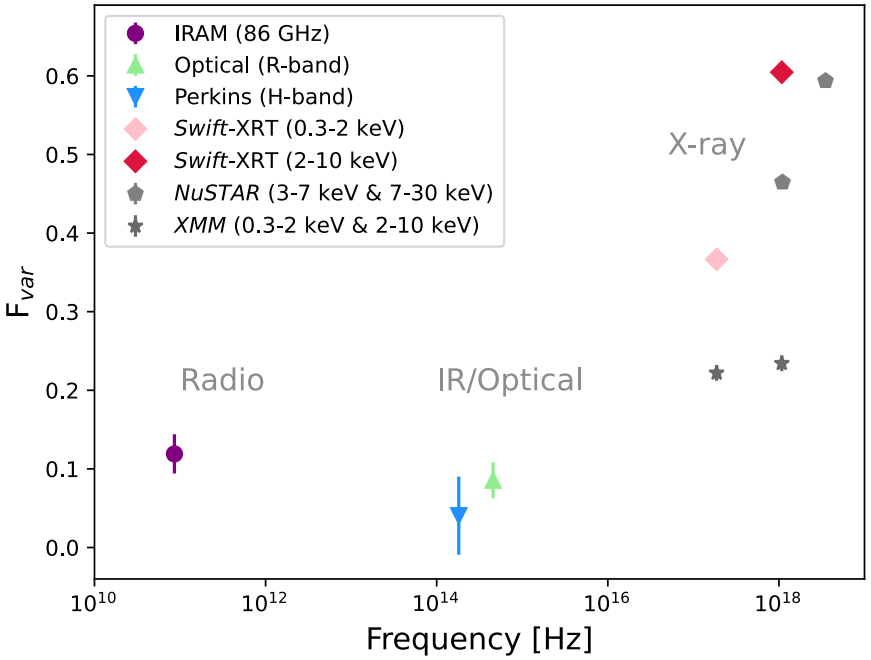

Figure 7.5: Fractional variability (F_{var}) as a function of the frequency during the IXPE epochs. F_{var} is computed using all data from Figure 7.2 that are within the IXPE time windows. In the radio, the simultaneity criteria are slightly relaxed and also include measurements that took place less than half a day before the start or after the end of the IXPE observing times (see the main text for more details). Radio, optical, IR, and *Swift* data are daily binned. The F_{var} from the *NuSTAR* and *XMM*-Newton multi-hour exposures is included using 1 h binning. These measurements are plotted in gray since the instrument did not gather data for all IXPE epochs, which biases the comparison with other wavebands.

Similarly to the polarization degree, F_{var} is high (>0.3) in the X-rays, while the optical and radio bands are low (<∼0.1) and compatible within 1σ. This trend is found routinely in Mrk 421 and other HSPs (also in the 2010 data set subject to Chapter 6 or other works, e.g., Aleksić et al., 2015a; Patel et al., 2018). The similarity potentially suggests a common underlying physical origin with the broadband behavior of the polarization degree.

7.3.5 Intra-night MAGIC and *NuSTAR* light curves

During the night of 5-6 June, 2022 (MJD 59734 to MJD 59735), MAGIC observations were strictly simultaneously with *NuSTAR*. The resulting light curves are shown in Figure 7.6. The data were binned by around 30 min. To avoid an otherwise limited exposure time by *NuSTAR*, the first bin was extended to ≈ 40 min. The upper panel shows the MAGIC fluxes above 400 GeV. This threshold is higher than in Figure 7.2 since some of the time bins contain observations taken under a zenith distance of up to 60°. This increases the energy threshold of the MAGIC telescopes to well above 200 GeV.

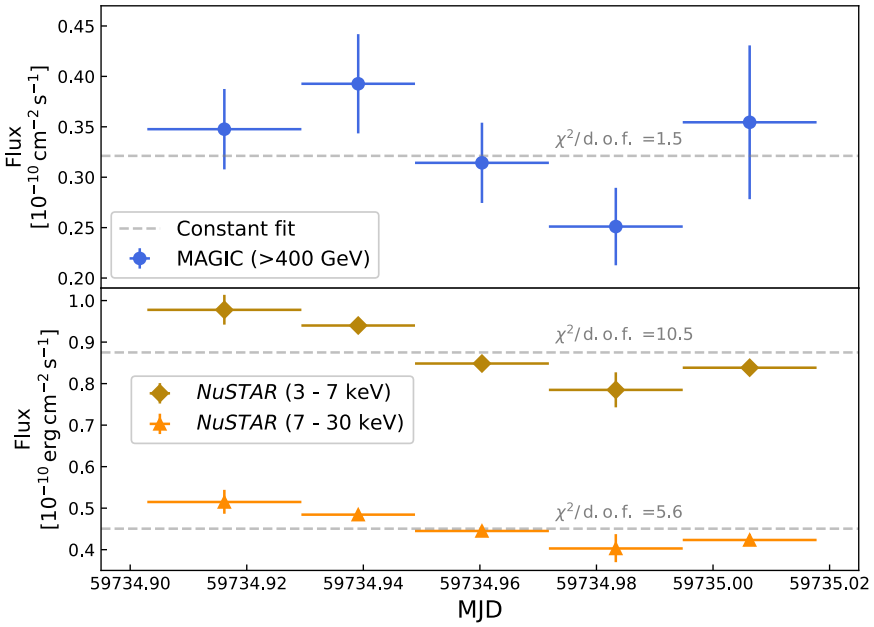

Figure 7.6: MAGIC and *NuSTAR* intra-night light curve between June 4, 2022 (MJD 59734) and June 5, 2022 (MJD 59735), corresponding to the IXPE 2 epoch. Upper panel: Light curve above 400 GeV obtained with MAGIC. A constant model fit is shown in dashed gray with the corresponding reduced χ^2. Lower panel: Light curves for the 3-7 keV and the 7-30 keV band taken by *NuSTAR*, and constant fits for both. Fluxes from both instruments are computed in ≈ 30 min time bins, except for the first bin that is ≈ 40 min long due to the limited exposure of *NuSTAR* around at the start of the MAGIC observation.

No significant intra-night variability could be found for the MAGIC observations, but *NuSTAR* detects significant variability in both energy bands. By fitting the data with a constant model, the hypothesis of a non-variable emission is rejected at a significance of above 5σ for the 3-7 keV band and above 3σ for the 7-30 keV band.

Figure 7.7 shows the flux measured by MAGIC plotted against the flux of both *NuSTAR* energy bands. For the correlation between the 3-7 keV and >400 GeV flux, I dervied a Pearson's r correlation coefficient of $r = 0.74$, and between 7-30 keV and >400 GeV of $r = 0.66$. Both cases suggest a slight positive correlation. To evaluate the significance of the correlation, Monte Carlo simulated light curves are generated. Each simulated flux point was produced by assuming a Gaussian distribution with the flux values of the actual data as a mean of the distribution and the uncertainty of the flux as the corresponding standard deviation. New light curves were then drawn, and the temporal information was shuffled in order to obtain pairs of "realistic" uncorrelated light curves with the same underlying PDFs. I simulated 10^6 pairs of light curves. Using the resulting distribution of the r coefficients, a p-value can be extracted by integrating the distribution above the observed value. This results in a p-value of 0.068 (equivalent to $\approx 1.8\sigma$) between the 3-7 keV and >400 GeV bands and a p-value of 0.102 (equivalent to $\approx 1.6\sigma$) for 7-30 keV and >400 GeV. Due to the relatively large statistical uncertainties in the VHE light

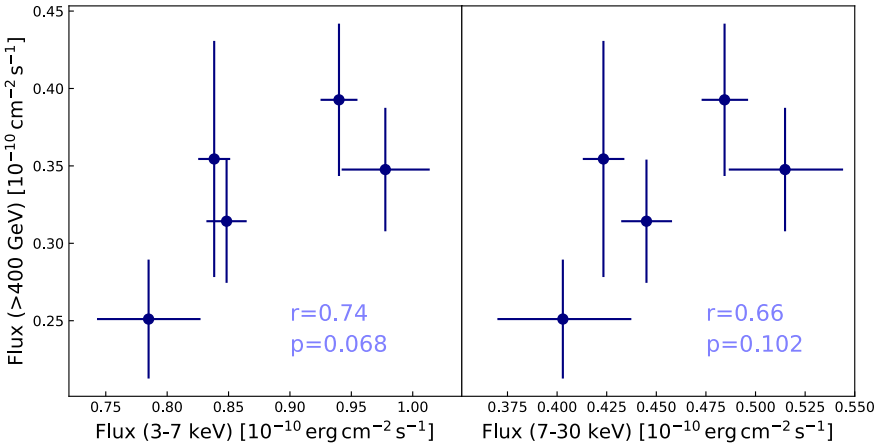

Figure 7.7: MAGIC flux versus *NuSTAR* flux and quantification of the correlation during the IXPE 2 epoch. The MAGIC flux is computed above 400 GeV while the X-ray flux is evaluated in two different energy bands: 3-7 keV for the left panel and 7-30 keV for the right panel. In each panel, the obtained Pearson's r coefficient is indicated. The p-value that describes the probability of obtaining the observed r coefficient for two uncorrelated light curves is given below. This p-value was estimated based on Monte Carlo toy simulations (see the main text for more details).

curve, no significant correlation can be claimed, and only an indication of a correlation can be proposed at best.

In section 7.4, the search for correlation is extended over longer timescale and larger binning by including data from the entire MWL campaign between April 2022 and June 2022.

7.3.6 Evidence of X-ray spectral hysteresis simultaneous to a polarization angle swing

The multi-hour exposure of *NuSTAR* allows a study of the X-ray spectral evolution during the period where a polarization angle swing is detected by IXPE. Figure 7.8 is a zoomed-in view of the LC during the polarization angle swing, showing the *NuSTAR* measurements together with the polarization degree and angle in the radio, optical, and IR. The IXPE polarization degree and angle were binned in ~ 3 hours. No significant variability is observed in the polarization degree. Using a constant fit model, the data are consistent with a stable X-ray polarization hypothesis within 3σ (both for IXPE 2 and IXPE 3 periods).

The top panel shows the fluxes in the 3-7 keV and 7-30 keV bands, in 1 hour time bins. Small variability in the form of a decrease is observed during the observation from June 5 to 6, 2022 (MJD 59734 to MJD 59735, simultaneous to IXPE 2). More structured variability patterns can be seen during the observation simultaneous to IXPE 3, between June 8 and 9, 2022 (MJD 59737 to MJD 59738). The light curve displays two "humps" caused by two consecutive flux rise and decay phases, which thus reveal variability on $\sim$1 hour timescale.

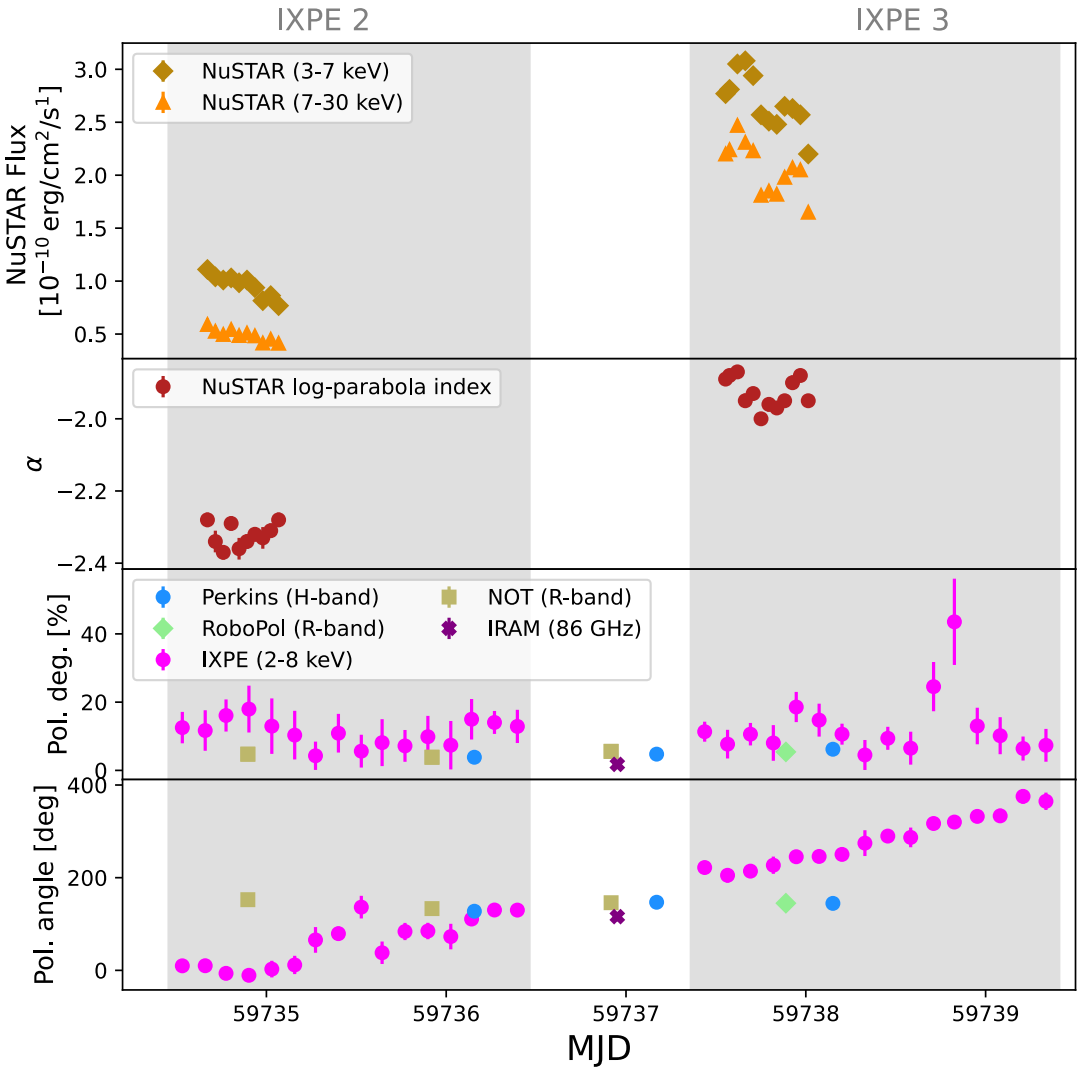

Figure 7.8: Zoomed-in view of the *NuSTAR* light curves in the 3-7 keV and 7-30 keV bands during the IXPE 2 and IXPE 3 epochs. The top panel reports the fluxes in 1 hour bins. The second panel from the top is the α index evolution derived from fits of the *NuSTAR* spectra. The last two panels show the simultaneous polarization degree and polarization angle in the X-ray band (IXPE), optical, and radio bands.

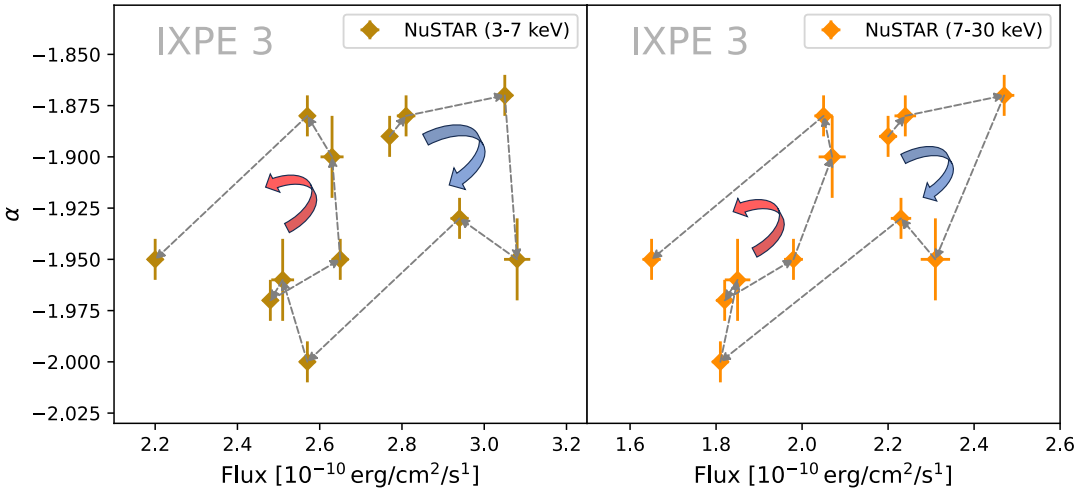

Figure 7.9: Log-parabola photon index, α, versus 3-7 keV and 7-30 keV flux as measured by *NuSTAR* during the third IXPE observation (IXPE 3 period). The data are 1 hour binned, and α is obtained by fitting a log-parabola function that has a fixed curvature parameter $\beta = 0.45$. The gray arrows show the direction of time, and the blue and red arrows in the middle of the panels depict the clockwise and counterclockwise directions observed in the data, respectively.

The *NuSTAR* spectra were fitted in the 3-30 keV band adopting a log-parabola model with the pivot energy fixed at 1 keV and the curvature fixed to $\beta = 0.45$ to remove any correlation between α and β in order to obtain a more straightforward assessment of the spectral hardness evolution. The resulting index α as a function of time in 1 hour bins is plotted in the second panel from the top in Figure 7.8.

For the observation simultaneous to the IXPE 2 p the sepctral index does not vary strongly. It varies by at most 5% around a value of ≈ -2.35, during a quasi-monotonic flux decay of $\approx 30\%$. There is no correlation between α and flux, nor any spectral hysteresis pattern.

The *NuSTAR* observations taken during IXPE 3, show a hysteresis patterns when α is reported as a function of the flux. Hysteresis in general describes a phenomenon where the response of a system depends not only on its current state but also on past conditions, such as changes in input. In the context of blazar emission, this dependency can create loop-like diagrams when drawing spectral slope against the integrated flux. Figure 7.9 shows the value of α versus the 3-7 keV and 7-30 keV fluxes during IXPE 3. The gray arrows indicate the flow of time in 1 h bins. During the first part of the observation, the data points (both in the 3-7 keV and 7-30 keV bands) display a loop in a clockwise direction. This means that the during the flux decay the spectrum is softer than during the rising of the flux. The second part of the observations exhibits a loop in counterclockwise direction, meaning the decay phase has a harder spectrum than the rising phase. Spectral hysteresis in the form of clockwise and counterclockwise directions has been previously detected in Mrk 421 (Brinkmann et al., 2003; Ravasio et al., 2004). Nevertheless, this is the first time that two continuous clockwise and counterclockwise rotations are detected over an hour timescale.

7.4 MWL evolution and correlation throughout the observing campaign

7.4.1 VHE–X-ray correlation over the entire campaign

The flux in the X-ray and VHE regimes (as shown in Figure 7.2) displays the strongest variability, which is typical for HSPs. The MAGIC light curves show a noticeable enhanced state of activity between MJD 59719 (May 20, 2022) and MJD 59723 (May 24, 2022). A peak flux of ~ 1.4 C.U. is measured in both the 0.2-1 TeV and >1 TeV bands which is around ≈ 3 times the typical state. The *Swift*-XRT light curves also display this flux increase. Both energy bands also show their strongest hardening during this state.

The results in Section 7.3.5 indicate a hint of a positive correlation between the MAGIC and *NuSTAR* fluxes during the IXPE 2 observations on a sub-daily timescale. In this section, the study of the VHE versus X-ray correlation is extended over the entire campaign by making use of the MAGIC and *Swift*-XRT measurements to fully exploit the available satistics. The daily binned MAGIC fluxes (in the 0.2-1 TeV and >1 TeV bands) are correlated with the *Swift*-XRT fluxes (0.3-2 keV and 2-10 keV bands) using a DCF based analysis, similar to the one shown in section 6.6. The DCF is applied with a 2-day binning. Again, the significance of the DCF was estimated based on Monte Carlo simulations as described in section 6.6. Since the light curves are much shorter in this data sample, the PSD indices were not estimated from the data. They were taken directly from MAGIC Collaboration et al. (2021) for the X-rays and are -1.45 for the 0.3-2 keV band and -1.3 for the 2-10 keV band. These slopes, derived with *Swift*-XRT data in 2016-2017 that cover a longer time span than the one considered in this work, were found to be in agreement with the 2022 observations and represent a good proxy to estimate the significance. For the MAGIC data, a PSD slope of -1.3 is used, which was reported by (Aleksić et al., 2015a) using Whipple observations during a campaign organized in 2009.

Figure 7.10 shows the DCF obtained from MAGIC 0.2-1 TeV versus *Swift*-XRT 2-10 keV in dark blue. The fine lines depict the 2σ (red), 3σ (green), and 4σ (purple) confidence bands. A positive correlation is found at zero time lag with a significance of 4σ. This provides a significant confirmation for the hinted trend in Section 7.3.5. The resulting DCF for the MAGIC >1 TeV band versus *Swift*-XRT 2-10 keV also shows a 4σ correlation at zero time lag and can be found in Abe et al. (2024). The correlation of the MAGIC fluxes with the 0.3-2 keV band yields a slightly lower significance of around 3σ. The results can also be found in Abe et al. (2024). These results suggest that the 2-10 keV flux is more closely related to the VHE flux compared to the 0.3-2 keV band during this period.

7.4.2 Investigation of the UV and optical versus X-ray anticorrelation

The *Swift*-UVOT fluxes in the UV band display an interesting quasi-monotonic increase starting from MJD ~59710 (May 11, 2022) to MJD ~59760 (June 30, 2022). The highest UV state is reached on MJD 59753 (June 23, 2022), and slightly more than twice the minimum flux. Over the same period, the X-ray band shows the opposite evolution with an overall decay of the 0.3-2 keV and 2-10 keV fluxes. This behavior might point towards an anticorrelation between the

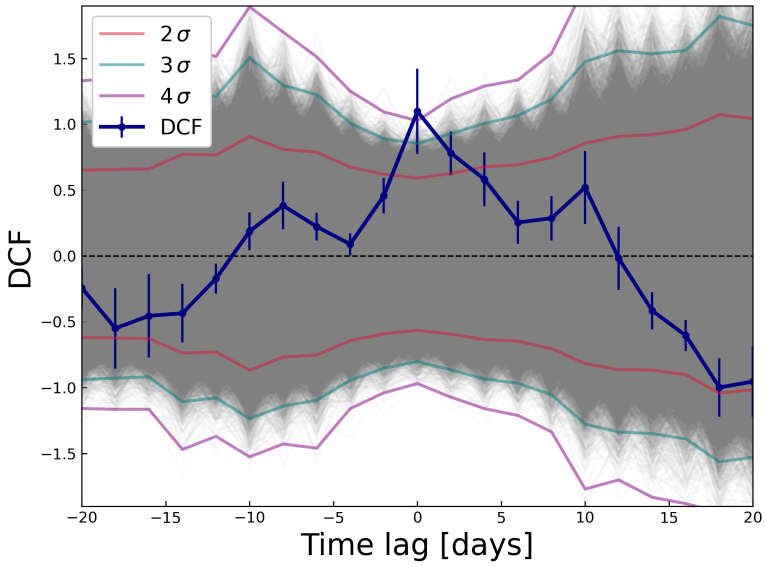

Figure 7.10: DCF computed for the MAGIC 0.2 − 1 TeV and *Swift*-XRT 2-10 keV light curves between MJD 59700 (May 1, 2022) and MJD 59740 (June 10, 2022) with a time-lag binning of 2 days. It is computed for a range of time lags between -20 to +20 days. The 2 σ, 3 σ and 4 σ confidence levels obtained by simulations are shown by the red, green, and purple lines, respectively.

X-ray and UV bands. Such trend can be caused by a shift of the entire synchrotron component to lower frequencies.

The anticorrelation is investigated using the DCF between both *Swift*-XRT bands and the *Swift*-UVOT W1 filter. Only the W1 data is used for simplicity. The fluxes in the M2 and W2 filters give very similar results, which is expected given their proximity in frequency with W1. The PSD slopes for the W1 band was taken from MAGIC Collaboration et al. (2021), which is −1.45. Figure 7.11 shows the correlation between the W1 and the 2-10 keV band. The significance of the anticorrelation reaches a level of around 2.5σ and can therefore only be considered marginal evidence. The highest significance for the W1 and the 0.3-2 keV band is around 2σ, which can be seen in the corresponding DCF plot shown in Abe et al. (2024).

To also have an unbiased result, the same method is applied to the entire MWL campaign (i.e., from MJD 59695 to MJD 59760; April 26, 2022, to June 30, 2022). The results reveal significance below 2σ. The corresponding plots can be also found in Abe et al. (2024). The marginal evidence of anticorrelation is therefore only observed over a 1.5-month period between MJD ∼59710 (May 1, 2022) and MJD ∼59760 (June 30, 2022).

This marks the third time that an indication of anticorrelation between UV and X-ray fluxes is found in Mrk 421. The first two hints were observed during MWL campaigns organized during 2009 (Aleksić et al., 2015a) and 2017 (MAGIC Collaboration et al., 2021). Similarily, they were also happening over an approximately monthly timescale. This reoccurring behavior might point toward some physical connection between the UV and X-ray emitting regions, which

is particularly relevant in the context of the recent IXPE results suggesting energy-stratified emitting regions.

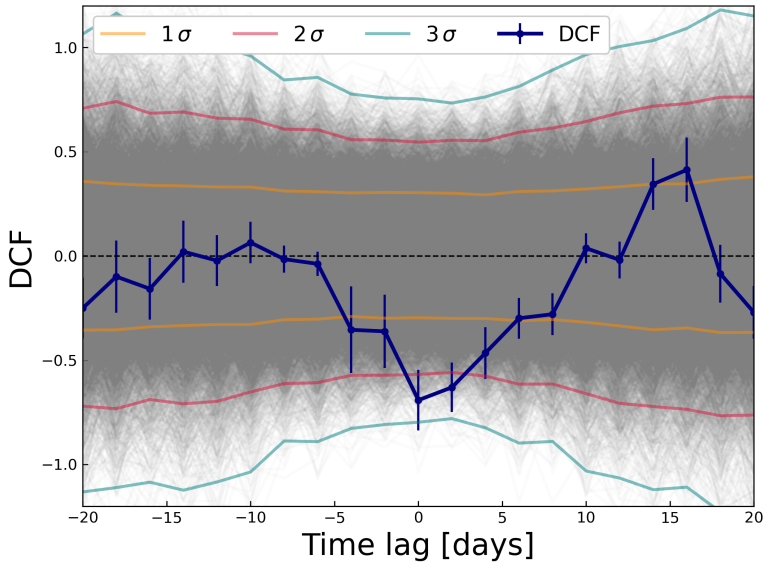

Figure 7.11: DCF computed for the *Swift*-UVOT W1 and *Swift*-XRT 2-10 keV light curves between MJD 59710 (May 11, 2022) and MJD 59760 (June 30, 2022), with a time-lag binning of 2 days. It is computed for a range of time lags between -20 to +20 days. The 1 σ, 2 σ and 3 σ confidence levels obtained by simulations are shown by the yellow, red, and green lines, respectively.

7.4.3 Optical polarization evolution throughout the entire campaign

Similar to the UV, the flux in the R-band also displays an increase throughout the campaign, in particular during the second part (between MJD 59710 and MJD 59760; May 11, 2022, to June 30, 2022). The R-band is unfortunately not well sampled enough to properly quantify the trend in that waveband in great detail. Nevertheless, the increase of the optical flux seems to be accompanied by an increase in the polarization degree in the optical. Figure 7.12 shows the polarization degree as a function of flux using strictly simultaneous R-band measurements. The data mostly cover the time from MJD 59710 to MJD 59760, which is the period when UV and X-rays show a hint of anti-correlation. Only a single NOT measurement took place before that, on MJD 59703. Using a Pearson's r, a positive correlation is found with r of $r = 0.8$. The same method as in section 7.3.5 is used to estimate an associated p-value of $p_{value} \approx 1 \times 10^{-5}$. This corresponds to a correlation significance of $\approx 4\sigma$. The slope of the correlation is $a = 0.52 \pm 0.09$.

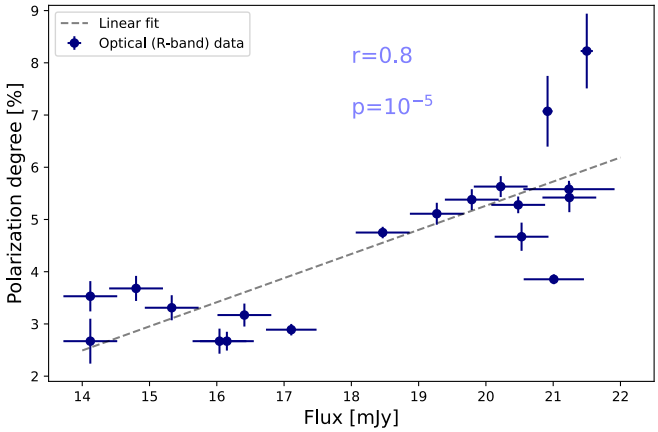

Figure 7.12: Correlation between the polarization degree and flux in the R band over the entire campaign. The dotted black line is a linear fit, yielding a best-fit slope of $a = 0.52 \pm 0.09$. The Pearson's r and the associated p-value is given in light blue.

7.5 Discussion

7.5.1 Polarization and variability behavior

During the first IXPE observation, IXPE 1 (in May 2022), the polarization degree is significantly stronger in X-rays than at lower frequencies. As was discussed in Di Gesu et al. (2022) and Liodakis et al. (2022b), these results point towards an energy-stratified jet, where the most energetic particles, emitting X-ray photons, are located in a smaller region with a more ordered magnetic field, close to the acceleration site. This energy dependency and the slow variability of the polarization degree strongly point toward a shock acceleration scenario. The accelerated electrons subsequently cool and diffuse into larger regions, where the field is more turbulent. They continue to emit from optical to radio frequencies. During IXPE 1, there is no variation in the polarization angle (Di Gesu et al., 2022) in any energy band. In particular, the X-ray polarization angle is compatible with that in the optical and radio.

The second and third IXPE observations, IXPE 2 and 3 (in June 2022), also show a constant X-ray polarization degree that is significantly higher compared to lower frequencies. This behavior of the polarization degree shares some similarities with the variability strength, which was quantified by the fractional variability, F_{var}, which also shows an increase with energy. This commonality may be explained by a single or a few compact regions dominating the X-ray emission and whose temporary appearance within the jet drives the observed variability. The emission at lower frequencies receives simultaneous contributions from several broader regions, which decreases the overall variability and degree of polarization. Such a scenario is in line with the energy stratification of the jet.

While the IXPE 2 and 3 epochs show a constant polarization degree, the polarization angle exhibits an evident rotation in X-rays. The rotation occurs at a constant angular velocity between the two epochs, which is highly suggestive of a single rotation event observed during the two

consecutive IXPE 2 and 3 observations. The optical and radio observations do not show any simultaneous angle rotation.

The VHE emission could only be characterized at the beginning of the polarization angle rotation. During that time period, the VHE emission state is higher, and the spectrum is harder than during IXPE 1, but still similar to the average for the source. Starting from the second half of the IXPE 2 epoch and during IXPE 3, the activity in X-rays increases, and the spectrum hardens simultaneously with the rotation. The emission peaks well above the typical state. The VHE usually shows a strong correlation with X-rays, especially during X-ray flaring activities, such as the activity during IXPE 3 (see, e.g., Acciari et al., 2020). Unfortunately, the lack of simultaneous observations with MAGIC prevents an evaluation of this characteristic during this specific flaring activity in June 2022.

Previous works on LSP and ISP objects have shown that rotations of the polarization angle in the optical can be associated with flares (Ahnen et al., 2017a; MAGIC Collaboration et al., 2018; Abdo et al., 2010c; Gupta et al., 2019; Chandra et al., 2015; Marscher et al., 2008). In LSPs and ISPs, the synchrotron peak is located around the optical band, while in HSPs, it is in the X-ray regime. One could naively extrapolate that X-ray flares in HSPs can similarly be associated with X-ray polarization angle swings. Even if the enhanced X-ray state during IXPE 2 and 3 remains below that of previous notable outbursts of Mrk 421, the strong X-ray flux rise and hardening, temporally coincident with a polarization angle swing, may be due to a similar physical mechanism as the angular swings observed in lower synchrotron peaked blazars.

The absence of a simultaneous polarization angle swing in the optical, IR, and radio could be explained by the following scenario: the smaller region emitting the X-ray photons, where the B field is more ordered, is streaming down the jet, following helical field lines, leading to an apparent rotation of the polarization angle. The emitting regions are larger at lower frequencies and do not closely follow a helical path, unlike the X-ray region.

The movement of a compact region through a helical path inside the jet induces changes in the Doppler factor since the angle between the region's movement and the observer's line of sight is slightly modified with the rotation. This leads to a significant flux variability caused by the changing Doppler boosting. The discussion in Abe et al. (2024) contains a short estimation of the impact of this effect using a rotation rate derived from the polarization angle swing and an assumed Lorentz factor of 20. This strongly modulates the flux amplitude depending on the rotation phase of the helical movement. The effect is stronger for larger viewing angles and zero in case one views the helical movement on axis. The resulting flux variability is compatible with the one observed in the 3-7 keV band under a viewing angle of $\sim 0.5°$. The flux variability is, however, also likely affected by acceleration and cooling processes, as suggested by the spectral changes observed on approximately day-to-hour timescales in *NuSTAR* data during IXPE 2 and 3. Hence, the MWL data tell us that the changes in the δ cannot be the only reason for the observed flux variability.

7.5.2 Spectral hysteresis

The observations by *NuSTAR* simultaneous to the polarization angle swing during IXPE 3 reveal two spectral hysteresis loops in opposite directions during a single exposure. In a clockwise direction, the first loop is likely the signature of strong synchrotron cooling, causing a delay of

the low-energy X-ray photons with respect to the high-energy ones, also called a soft lag. The subsequent counterclockwise loop indicates a delay of the high-energy X-ray photons compared to the lower-energy ones, a so-called hard lag. This points to a system that is observed at energies for which the acceleration timescale is comparable to the cooling timescale, $t'_{acc} \approx t'_{cool,synch}$ Kirk et al. (1998). The discussion in (Abe et al., 2024) contains a derivation of the gyro-factor, ξ, which is related to the efficiency in the acceleration of the high-energy particle population and is always ≥ 1. Assuming a typical value of $\delta = 30$ for Mrk 421, one can derive $\xi \approx 8 \times 10^4$ for the second part of the *NuSTAR* observation during the IXPE 3 epoch. The first part of the observation, where a clockwise loop is observed, suggests a regime in which $t_{acc}/t_{cool,synch} << 1$ since synchrotron cooling is most likely the driver of a soft lag. Due to the much shorter acceleration time, the acceleration must occur more effectively. During this part of the observation, ξ must be at least an order of magnitude smaller, i.e., $\xi \lesssim 8 \times 10^3$. The consecutive clockwise and counterclockwise loops during IXPE 3 imply an increase of ξ of at least one order of magnitude, indicating a large decrease of the acceleration efficiency over approximately hour timescales.

7.5.3 VHE vs X-ray correlation

After exploiting data from the entire MWL campaign, a positive correlation at the level of $4\,\sigma$ was found between X-rays and VHE gamma rays at zero time lag between the MAGIC energy bands and the 2-10 keV band of *Swift*-XRT and at the level of $3\,\sigma$ with the 0.3-2 keV band. This positive correlation supports leptonic scenarios in which the same electron population produces the X-ray and VHE emission via the SSC process. Positive correlations at zero time lags were previously reported in several studies (see, e.g., MAGIC Collaboration et al., 2021; Arbet-Engels et al., 2021; Acciari et al., 2021; Aleksić et al., 2015a) and were also found in the data set investigated in chapter 6. The trend suggests that VHE gamma rays are also emitted close to the shock front, cospatially to the X-rays. The higher significance obtained when using the X-ray 2-10 keV band suggests that the VHE emission has a tighter relation with the X-ray fluxes above a few keVs rather than below that. Looking at the SEDs in Figure 7.3, this implies that the falling edge of the high-energy SED component is mostly dominated by electrons that emit synchrotron photons well above ν_p. This is in agreement with the expectation of typical leptonic scenarios (Tavecchio et al., 1998).

7.5.4 UV vs X-ray anticorrelation

Looking at lower energies, there is marginal evidence of an anticorrelation at zero time lag between the X-ray and UV fluxes from May 2022 to June 2022. Although the peak significance is estimated to be only $\sim 2.5\sigma$, this suggestion is interesting in the context of previous results as well as the newly available X-ray polarization measurements. This is the third time that an indication of X-ray versus UV anticorrelation has been reported for Mrk 421 (Aleksić et al., 2015a; MAGIC Collaboration et al., 2021). Also, an anticorrelation directly implies a physical connection between the X-ray, UV, and optical emitting regions. While the IXPE results suggest that those regions are not co-spatial, the anticorrelation further supports a scenario in which particles are first accelerated close to a shock front and then diffuse toward a broader region in the jet, dominating the observed UV and optical emission after losing energy.

In principle, one would expect a positive correlation because the increase in electrons that emit in X-rays would later emit UV. However, a long-term evolution of the acceleration efficiency might be a possible scenario explaining the anticorrelation. If the electron injection luminosity stays roughly constant while the acceleration efficiency decreases, the relative proportion of lower-energy electrons will increase since fewer higher-energy electrons are accelerated and shift the synchrotron SED toward lower frequencies while keeping the amplitude of the SED peak at a roughly similar level. This scenario is expected to increase the UV and optical flux at the synchrotron component's rising edge and decrease the X-ray flux at the falling edge.

7.5.5 Optical polarization degree vs flux correlation

The optical range is farther from the synchrotron peak frequency, ν_p, in HSPs and, therefore, comprises emission radiated by electrons that already had time to advect away. Since further downstream from the shock, the level of magnetic field disorder increases, the observed optical polarization degree decreases. If the anticorrelation between the UV and X-rays discussed above is caused by a shift of ν_p toward lower frequencies, one would expect a simultaneous rise in the optical polarization degree over time as it is observed. The resulting higher optical polarization degree could also produce a higher ratio between the optical/IR and X-ray polarization degree throughout the IXPE 2 and IXPE 3 epochs, which are within the time range where a hint of UV versus X-ray anticorrelation is reported. For other samples of BL Lac objects, an indication of anticorrelation between the optical polarization degree and the synchrotron peak frequencies, ν_p, was already reported in Angelakis et al. (2016), supporting the above scenario. This behavior was qualitatively explained by the fact that in the case of BL Lac objects with lower ν_p (such as LSPs), the synchrotron peak is close to the optical band, which is emitted by freshly accelerated electrons near the shock.

In an alternative scenario, the rise in the degree of optical polarization during the UV versus X-ray anticorrelation time range might be caused by an increase in the relative dominance of a few emitting zones radiating in the optical and UV flux. In the case where the optical flux receives contributions from many regions over a larger distance with different magnetic field configurations, the resulting overall polarization degree would decrease.

Chapter 8

Summary and conclusion

Observing gamma rays has been an essential part of high-energy astrophysics for decades. With energies of over 100 GeV, also known as very high energy (VHE) gamma rays, these photons are produced in the most extreme environments in the universe, e.g., in the remnants of supernovae, gamma-ray bursts, or active galactic nuclei (AGN). All these phenomena act as cosmic particle accelerators that can take particles to energies far beyond the TeV scale and exhibit high levels of non-thermal electromagnetic emission. Unlike charged particles, gamma rays are ideally suited as direct probes for these environments as they travel through the cosmos undisturbed by magnetic fields. They can provide direct information from these cosmic accelerators and thus help us to answer the most critical questions in astroparticle physics.

Since gamma rays are absorbed by the Earth's atmosphere upon impact, two main strategies for the detection emerged: Direct detection with space-born instruments and indirect detection with ground-based instruments. In the former case, the gamma rays interact directly with the detector, and hence they have a high accuracy in the reconstruction of the event (direction, energy), as well as in the signal-background separation. However, these instruments have a limited spatial extent, resulting in effective detection areas of $\sim 1\text{m}^2$. Gamma-ray fluxes decrease with higher energies to a point where such instruments cannot detect significant signal events (typically at around 100 GeV), making them no longer suitable to study individual sources. The second form of detection uses indirect detection and works particularly well for high energies (typically larger than 100 GeV). Upon impact, VHE gamma rays produce atmospheric air showers of charged particles, which themselves induce the emission of Cherenkov light in the atmosphere. Imaging Atmospheric Cherenkov Telescopes (IACTs) collect the light with large mirror surfaces onto a light-sensitive and fast camera to reconstruct the properties of the primary gamma rays. Since the cone of Cherenkov light covers a large area on the ground, the effective area of IACTs reaches the $\sim\text{km}^2$ scale, which enables the measurement of very low photon fluxes. However, using the atmosphere as a calorimeter comes at the price of being exposed to changing atmospheric conditions at all times. Higher aerosol concentrations, primarily caused by clouds and dust, lead to increased absorption and scattering of Cherenkov light. The reconstructed data is then impaired or, in extreme cases, unusable. In order to assess the quality of the atmospheric conditions and to correct affected data, the MAGIC collaboration has built and operated a LIDAR system continuously since 2013. MAGIC is the only IACT in the world that has continuously used a LIDAR for atmospheric monitoring over many years and has pioneered its application for VHE astronomy. The correction of atmospherically impaired data had been validated on small observations and had been used in several publications since then. Even though the LIDAR has been operating for a decade, no systematic evaluation of its correction capabilities over a multi-

year timescale and under different conditions had been performed before my PhD work. The presented study provides the most detailed investigation of the effects of applying LIDAR-based corrections to IACT data. I used nearly seven years of data from the Crab Nebula to study the performance of two different correction methods under different zenith angles and aerosol transmission at 9 km, including data affected by dust intrusions and clouds. The key findings relevant for future analyzers of MAGIC data can be summarized as follows: For transmissions above 0.9, the data quality is excellent and the LIDAR corrections are unnecessary. Under transmission levels between 0.65 and 0.9, the reconstructed fluxes and spectra of the Crab Nebula (and therefore any other gamma-ray source) are substantially degraded and should not be used under standard assumptions. The LIDAR corrections, as applied through the two available methods, lead to a compatible result (within uncertainties) with the actual emission of the Crab Nebula that is obtained during optimal atmospheric conditions. The data is therefore fully recovered in this range, extending the telescopes' duty cycle over times with sub-optimal conditions. For data taken under very low transmission (0.5-0.65), the results differ depending on the correction method used. The two methods, i.e. Method I and Method II, are distinguished by their averaging of the effective area. Method I shows a bias-free reconstruction, whereas Method II shows a remaining bias of 10%–15% for the correction. Depending on the scientific objective of the analysis, data with such low transmission may still be useable under the assumption of increased systematic uncertainties. Lastly, one must note that systematic uncertainties are higher for clouds than for stable aerosol layers due to their movement in and out of the LIDAR's and MAGIC's FoV and their higher altitudes, leading to Cherenkov light being emitted within the aerosol layers. Wider and lower aerosol distributions, as is the case with Calima, lead to a more stable layer below the emission of the Cherenkov light, resulting in a more accurate correction. Due to these challenges, past works have focused on the correction of the latter effect. This work is the first time that IACT data corrections for the case of clouds have been assessed using real data in a systematic manner. The knowledge gained from this study will be of great value for future observations with MAGIC and for the next generation of IACTs, namely the Cherenkov Telescope Array (CTA). CTA will continue to rely on LIDAR systems to monitor and characterize atmospheric conditions at its observation sites. Therefore, the use of LIDAR systems will be further developed and will remain an important element of ground-based gamma-ray astronomy in the future. My PhD thesis work will be a useful reference for these future activities.

In the later part of the thesis, I shifted the focus from technical aspects to astrophysical ones by presenting new insights into the emission of the AGN Mrk 421. AGN are among the most studied objects in the high-energy universe. They appear in the center of some galaxies as the result of a supermassive black hole surrounded by an accretion disk of matter. Accretion onto the central black hole provides vast amounts of energy, making AGN the most luminous long-lived (i.e., emitting well beyond 10^5 years) sources known. Despite their immense brightness, they can show rapid variability in their emission down to a time scale of minutes. Some AGN have a pair of jets, i.e., highly collimated and fast outflows that emerge orthogonal to the accretion disk. A particular subclass of AGN, known as blazars, occurs if the object is viewed at an angle closely aligned ($<10^\circ$) with the jet direction. Relativistic effects can then amplify the observed luminosity by factors of 10^4 and beyond, producing exceptionally bright emission across the entire electromagnetic spectrum. Despite extensive research over half a century, several fundamental issues remain unresolved. This includes the question of whether the emission is mainly produced

in a single region or whether it occurs simultaneously in several regions within the jets, as well as the acceleration and contributions of the different particle populations (leptonic vs. hadronic) to the broadband emission. Mrk 421 is one of the brightest TeV-emitting blazars, which is primarily caused by its closeness of around 135 Mpc. It is one of the best-studied sources in the VHE sky and is regularly observed with a variety of instruments covering the entire electromagnetic spectrum. The source has been the subject of an extended MWL campaign since 2009, in which the period from November 2009 to June 2010 stands out, as it shows the most violent behavior of the source measured to date. The source changes from an already enhanced activity state to producing the brightest flare ever observed from an AGN in VHE, and then it dies down to an extremely low emission state. The data set provides excellent coverage in VHE and HE gamma rays, X-rays, UV, and optical. In addition, interferometric observations by the VLBA connect multiple radio telescopes to achieve an extremely high angular resolution in the order of ~ 0.1 mas. At the distance of Mrk 421, this corresponds to a resolution of ~ 0.05 pc, enabling us to obtain images of the substructure of the jet. As with all blazars, a bright core is visible in the center. In addition, the ejection of two plasma blobs from this core was observed for the first time around the time of the observations in 2010. Due to the considerable uncertainty regarding the emission times of the blobs (> 50 days), a significant correlation of the ejection with any of the observed gamma-ray flares is not feasible. It is nevertheless interesting to see such a unique phenomenon during a period of such strong activity, which has never been detected in other observing periods. The extensive MWL coverage of the data set allowed me to investigate the variability behavior in great detail, showing the strongest variability in the X-ray and VHE. For the latter, even intra-night variability on sub-hour time scales was observed on three nights. The variability was also analyzed by fitting the power spectral density with a power-law model. This characterizes the power of variability at different frequencies and is also a crucial feature for the simulation of realistic light curves, which are needed to assess the significance of correlations. I investigated the correlation behavior between different energy bands with great detail, revealing a pattern that is difficult to explain within widely used models, such as a single particle population responsible for the broadband emission. In particular, the large flare in February 2010, which is the largest to date, shows different characteristics compared to the activity of the source during the rest of the campaign. Due to this flare, significant correlations are observed between VHE and HE gamma rays as well as between X-rays and HE gamma rays. In addition, a clear decrease of certain correlations is seen depending on whether the flare is included or not, such as the unprecedented correlation between HE gamma rays and the UV. A plausible explanation for these observations is obtained using two spatially separated but possibly interacting emission zones dominating the emission in different energy ranges. This scenario is a simplified model of an energy-stratified jet, which is also favored by my other research activity, which used the first observations of the Imaging X-ray Polarimeter Explorer (IXPE) satellite in 2022.

IXPE was launched in December 2021, and provides unprecedented X-ray polarization measurements for all types of astrophysical sources. Among other things, this opened a completely new window to the study of blazars. The first IXPE observation campaign of Mrk 421 took place in May and June 2022. IXPE found a much higher polarization degree in X-rays than other instruments in the optical and radio, indicating that the magnetic field in the X-ray-emitting region must be more ordered than in the radio- and optical-emitting regions. This polarization signature suggests a shock within an energy-stratified jet as the most plausible acceleration mechanism.

I analyzed the data from the MAGIC observations around and during the IXPE observations, resulting in the first combined observations of Mrk 421 with VHE gamma rays and X-ray polarization. Beyond that, extensive MWL observations from radio to HE gamma rays complement the data set. Especially in the X-rays, the continuous observations from *Swift*-XRT and dedicated long exposures from *NuSTAR* allow a precise characterization of the variability pattern throughout the campaign and down to hourly timescales. The source showed a wide variety of activity with a rather low emission state at the beginning and an enhanced state in the second half of the observations. In the latter observations, a rotation of the X-ray polarization angle was observed over multiple days, during which the source showed strong activity in the X-ray. The association of polarization angle swings in the optical with flaring activities had been observed frequently for low-synchrotron-peaked blazars. In these blazars, the optical emission is produced by the electrons of the highest energy. In high-synchrotron peaked blazars such as Mrk 421, on the other hand, the high-energy electrons emit predominantly in the X-ray. Therefore, a similar physical origin might be responsible for the swing in X-rays in combination with the flux rise and spectral hardening observed in Mrk 421. The X-ray spectra taken during the half-day-long observation on June 8/9, when the rotation of the IXPE polarization angle occurred, revealed a spectral hysteresis pattern showing clockwise and counter-clockwise loops in the plane of spectral index vs flux. Depending on the direction, these loops indicate a time delay between particles with higher and lower energy, pointing towards changes in the particle acceleration efficiency on hourly timescales. There is no direct evidence of a TeV flare during the rotation of the polarization angle because observations by MAGIC had to stop with the rise of the full moon during those days. However, the data from the 2-month-long observation campaign show a significant correlation between the X-ray and VHE gamma-ray emissions, which makes an unobserved enhanced VHE state very likely. This direct correlation means that all findings on the geometry and magnetic field structure of the emission region of X-rays also hold for the VHE emission site. The study is the first step towards a new way of investigating blazars. The combination of MWL observations over the entire electromagnetic spectrum with detailed polarization measurements have provided valuable insights into particle acceleration mechanisms and efficiency within jets. Still, they also show that further observations are necessary to characterize the behavior of the source in different emission and polarization states. New joint observations with MAGIC and IXPE have already been carried out in December 2023 and April 2024, which will continue to expand our understanding of Mrk 421, and blazars in general.

Only the brightest blazars, such as Mrk 421, can be studied with such great detail and precision with the current generation of instruments. This high brightness allows the reconstruction of fluxes and spectra on daily and sub-daily timescales, making Mrk 421 a perfect cosmic laboratory for studying TeV blazars. For the majority of sources, such studies are simply impossible, as their fainter emission requires integration over many days or even weeks to obtain significant signals. Only with the sensitivity of the next generation of telescopes, like CTA, can these studies be repeated and extended to many more sources to improve and complete our understanding of blazars. Because of that, the current work on Mrk 421 is a pioneering effort that paves the way for studies in the decades to come.

To conclude, the findings of this thesis contribute to the field of VHE gamma-ray astronomy from a technical and an astrophysical point of view. I conducted the first systematic evaluation

of the atmospheric correction capabilities of a LIDAR system for IACT data. I led the most comprehensive study on Mrk 421 in the time from November 2009 to June 2010, which is the source's most active year to date. Lastly, I was one of the main authors and analyzers of the first combined VHE and X-ray polarization observations of Mrk 421, opening new possibilities to study blazars. All projects of my doctoral research have resulted in published or recently submitted publications (Schmuckermaier et al., 2023; Abe et al., 2024; Abe et al., 2024), demonstrating their novelty and large scientific value to the astrophysical community.

List of Figures

List of Tables

Bibliography

A. Ångström. On the Atmospheric Transmission of Sun Radiation and on Dust in the Air. *Geografiska Annaler*, 11(10.2307/519399):156–166., 1929.

A. A. Abdo et al. The Spectral Energy Distribution of Fermi Bright Blazars. *ApJ*, 716(1):30–70, June 2010a. doi: 10.1088/0004-637X/716/1/30.

A. A. Abdo et al. Gamma-ray Light Curves and Variability of Bright Fermi-detected Blazars. *ApJ*, 722(1):520–542, Oct. 2010b. doi: 10.1088/0004-637X/722/1/520.

A. A. Abdo et al. A change in the optical polarization associated with a γ-ray flare in the blazar 3C279. *Nature*, 463(7283):919–923, Feb. 2010c. doi: 10.1038/nature08841.

A. A. Abdo et al. Fermi Large Area Telescope Observations of the Crab Pulsar And Nebula. *ApJ*, 708:1254–1267, Jan. 2010d. doi: 10.1088/0004-637X/708/2/1254.

A. A. Abdo et al. Fermi Large Area Telescope Observations of Markarian 421: The Missing Piece of its Spectral Energy Distribution. *ApJ*, 736(2):131, Aug. 2011. doi: 10.1088/0004-637X/736/2/131.

S. Abdollahi et al. Fermi Large Area Telescope Fourth Source Catalog. *ApJS*, 247(1):33, Mar. 2020. doi: 10.3847/1538-4365/ab6bcb.

S. Abe et al. Characterization of Markarian 421 during its most violent year: Multiwavelength variability and correlations. Submitted to *Astronomy & Astrophysics* on July 23, 2024.

S. Abe et al. First characterization of the emission behavior of Mrk 421 from radio to very high-energy gamma rays with simultaneous X-ray polarization measurements. *A&A*, 684:A127, Apr. 2024. doi: 10.1051/0004-6361/202347988.

A. U. Abeysekara et al. The Great Markarian 421 Flare of 2010 February: Multiwavelength Variability and Correlation Studies. *ApJ*, 890(2):97, Feb. 2020. doi: 10.3847/1538-4357/ab6612.

V. A. Acciari et al. TeV and Multi-wavelength Observations of Mrk 421 in 2006-2008. *ApJ*, 738 (1):25, Sept. 2011. doi: 10.1088/0004-637X/738/1/25.

V. A. Acciari et al. Observation of Markarian 421 in TeV gamma rays over a 14-year time span. *Astroparticle Physics*, 54:1–10, Feb. 2014. doi: 10.1016/j.astropartphys.2013.10.004.

V. A. Acciari et al. Unraveling the Complex Behavior of Mrk 421 with Simultaneous X-Ray and VHE Observations during an Extreme Flaring Activity in 2013 April. *ApJS*, 248(2):29, June 2020. doi: 10.3847/1538-4365/ab89b5.

V. A. Acciari et al. Multiwavelength variability and correlation studies of Mrk 421 during historically low X-ray and γ-ray activity in 2015-2016. *MNRAS*, 504(1):1427–1451, June 2021. doi: 10.1093/mnras/staa3727.

M. Ackermann et al. The Fermi Large Area Telescope on Orbit: Event Classification, Instrument Response Functions, and Calibration. *ApJS*, 203(1):4, Nov 2012. doi: 10.1088/0067-0049/203/1/4.

F. Aharonian et al. Variations of the TeV energy spectrum at different flux levels of Mkn 421 observed with the HEGRA system of Cherenkov telescopes. *A&A*, 393:89–99, Oct. 2002. doi: 10.1051/0004-6361:20021005.

M. L. Ahnen et al. Long-term multi-wavelength variability and correlation study of Markarian 421 from 2007 to 2009. *A&A*, 593:A91, Sept. 2016. doi: 10.1051/0004-6361/201628447.

M. L. Ahnen et al. Multiwavelength observations of a VHE gamma-ray flare from PKS 1510-089 in 2015. *A&A*, 603:A29, July 2017a. doi: 10.1051/0004-6361/201629960.

M. L. Ahnen et al. Multiband variability studies and novel broadband SED modeling of Mrk 501 in 2009. *A&A*, 603:A31, July 2017b. doi: 10.1051/0004-6361/201629540.

M. L. Ahnen et al. Performance of the MAGIC telescopes under moonlight. *Astroparticle Physics*, 94:29–41, Sept. 2017c. doi: 10.1016/j.astropartphys.2017.08.001.

M. Ajello et al. The Fourth Catalog of Active Galactic Nuclei Detected by the Fermi Large Area Telescope: Data Release 3. *ApJS*, 263(2):24, Dec. 2022. doi: 10.3847/1538-4365/ac9523.

J. Albert et al. Observations of Markarian 421 with the MAGIC Telescope. *ApJ*, 663(1):125–138, July 2007a. doi: 10.1086/518221.

J. Albert et al. Variable Very High Energy γ-Ray Emission from Markarian 501. *ApJ*, 669(2):862–883, Nov. 2007b. doi: 10.1086/521382.

J. Albert et al. Unfolding of differential energy spectra in the MAGIC experiment. *Nuclear Instruments and Methods in Physics Research A*, 583:494–506, 2007c. doi: 10.1016/j.nima.2007.09.048.

J. Albert et al. FADC signal reconstruction for the MAGIC telescope. *Nuclear Instruments and Methods in Physics Research A*, 594(3):407–419, Sept. 2008. doi: 10.1016/j.nima.2008.06.043.

J. Aleksić et al. Performance of the MAGIC stereo system obtained with Crab Nebula data. *Astroparticle Physics*, 35(7):435–448, Feb. 2012. doi: 10.1016/j.astropartphys.2011.11.007.

J. Aleksić et al. The 2009 multiwavelength campaign on Mrk 421: Variability and correlation studies. *A&A*, 576:A126, Apr. 2015a. doi: 10.1051/0004-6361/201424216.

J. Aleksić et al. Unprecedented study of the broadband emission of Mrk 421 during flaring activity in March 2010. *A&A*, 578:A22, June 2015b. doi: 10.1051/0004-6361/201424811.

J. Aleksić et al. Measurement of the Crab Nebula spectrum over three decades in energy with the MAGIC telescopes. *Journal of High Energy Astrophysics*, 5:30–38, Mar. 2015c. doi: 10.1016/j.jheap.2015.01.002.

J. Aleksić et al. The major upgrade of the MAGIC telescopes, Part II: A performance study using observations of the Crab Nebula. *Astroparticle Physics*, 72:76–94, Jan. 2016a. doi: 10.1016/j.astropartphys.2015.02.005.

J. Aleksić et al. The major upgrade of the MAGIC telescopes, Part I: The hardware improvements and the commissioning of the system. *Astroparticle Physics*, 72:61–75, Jan. 2016b.

J. Aleksić et al. The major upgrade of the MAGIC telescopes, Part II: A performance study using observations of the Crab Nebula. *Astroparticle Physics*, 72:76–94, Jan. 2016c. doi: 10.1016/j.astropartphys.2015.02.005.

E. Angelakis et al. RoboPol: the optical polarization of gamma-ray-loud and gamma-ray-quiet blazars. *MNRAS*, 463(3):3365–3380, Dec. 2016. doi: 10.1093/mnras/stw2217.

M. Arakawa, M. Hayashida, D. Khangulyan, and Y. Uchiyama. Detection of Small Flares from the Crab Nebula with Fermi-LAT. *ApJ*, 897(1):33, July 2020. doi: 10.3847/1538-4357/ab9368.

A. Arbet Engels. *The Broadband Behaviour of Bright TeV Gamma-Ray Emitting Blazars*. Doctoral thesis, ETH Zurich, Zurich, 2021.

A. Arbet-Engels et al. The relentless variability of Mrk 421 from the TeV to the radio. *A&A*, 647:A88, Mar. 2021. doi: 10.1051/0004-6361/201935557.

W. B. Atwood et al. The Large Area Telescope on the Fermi Gamma-Ray Space Telescope Mission. *ApJ*, 697(2):1071–1102, Jun 2009. doi: 10.1088/0004-637X/697/2/1071.

M. Baloković et al. Multiwavelength Study of Quiescent States of Mrk 421 with Unprecedented Hard X-Ray Coverage Provided by NuSTAR in 2013. *ApJ*, 819(2):156, Mar. 2016. doi: 10.3847/0004-637X/819/2/156.

V. Beckmann and C. R. Shrader. *Active Galactic Nuclei*. 2012.

K. Bernlöhr. Impact of atmospheric parameters on the atmospheric Cherenkov technique. *Astroparticle Physics*, 12:255–268, Jan. 2000. doi: 10.1016/S0927-6505(99)00093-6.

J. Betorz. Search for correlations of atmospheric transmission obtained from the magic lidar and the pyrometer and characterization of asics for the cta. Bachelor's thesis, Universitat Autònoma de Barcelona, June 2015.

A. Biland, M. Garczarczyk, H. Anderhub, V. Danielyan, D. Hakobyan, E. Lorenz, and R. Mirzoyan. The Active Mirror Control of the MAGIC Telescopes. In *International Cosmic Ray Conference*, volume 3 of *International Cosmic Ray Conference*, pages 1353–1356, Jan. 2008. doi: 10.48550/arXiv.0709.1574.

R. Blandford, D. Meier, and A. Readhead. Relativistic Jets from Active Galactic Nuclei. *Annu*, 57:467–509, Aug. 2019. doi: 10.1146/annurev-astro-081817-051948.

M. G. Blasi et al. The TeV blazar Markarian 421 at the highest spatial resolution. *A&A*, 559: A75, Nov. 2013. doi: 10.1051/0004-6361/201321858.

S. Bonometto and A. Saggion. Polarization in Inverse Compton Scattering of Synchrotron Radiation. *A&A*, 23:9, Feb. 1973.

D. Borla Tridon, F. Goebel, D. Fink, W. Haberer, J. Hose, C. C. Hsu, T. Jogler, R. Mirzoyan, R. Orito, O. Reimann, P. Sawallisch, J. Schlammer, T. Schweizer, B. Steinke, and M. Teshima. Performance of the Camera of the MAGIC II Telescope. In *31st International Cosmic Ray Conference, Lodz*, page arXiv:0906.5448, June 2009.

M. Böttcher, A. Reimer, K. Sweeney, and A. Prakash. Leptonic and Hadronic Modeling of Fermi-detected Blazars. *ApJ*, 768(1):54, May 2013. doi: 10.1088/0004-637X/768/1/54.

H. V. Bradt, R. E. Rothschild, and J. H. Swank. X-ray timing explorer mission. *A&A, Supplement*, 97(1):355–360, Jan. 1993.

W. Brinkmann, I. E. Papadakis, J. W. A. den Herder, and F. Haberl. Temporal variability of Mrk 421 from XMM-Newton observations. *A&A*, 402:929–947, May 2003. doi: 10.1051/0004-6361:20030264.

D. N. Burrows et al. The Swift X-Ray Telescope. *SSR*, 120(3-4):165–195, Oct. 2005. doi: 10.1007/s11214-005-5097-2.

M. I. Carnerero et al. Dissecting the long-term emission behaviour of the BL Lac object Mrk 421. *MNRAS*, 472(4):3789–3804, Dec. 2017. doi: 10.1093/mnras/stx2185.

M. Cerruti. Leptonic and Hadronic Radiative Processes in Supermassive-Black-Hole Jets. *Galaxies*, 8(4):72, Oct. 2020. doi: 10.3390/galaxies8040072.

S. Chandra, H. Zhang, P. Kushwaha, K. P. Singh, M. Bottcher, N. Kaur, and K. S. Baliyan. Multi-wavelength Study of Flaring Activity in BL Lac Object S5 0716+714 during the 2015 Outburst. *ApJ*, 809(2):130, Aug. 2015. doi: 10.1088/0004-637X/809/2/130.

R. Chatterjee et al. Correlated Multi-Wave Band Variability in the Blazar 3C 279 from 1996 to 2007. *ApJ*, 689(1):79–94, Dec. 2008. doi: 10.1086/592598.

P. A. Cherenkov. Visible luminescence of pure liquids under the influence of γ-radiation. *Dokl. Akad. Nauk SSSR*, 2(8):451–454, 1934. doi: 10.3367/UFNr.0093.196710n.0385.

G. W. Clark, G. P. Garmire, and W. L. Kraushaar. Observation of High-Energy Cosmic Gamma Rays. *ApJL*, 153:L203, Sept. 1968. doi: 10.1086/180252.

G. de Vaucouleurs, A. de Vaucouleurs, J. Corwin, Herold G., R. J. Buta, G. Paturel, and P. Fouque. *Third Reference Catalogue of Bright Galaxies*. 1991.

L. Di Gesu et al. The X-Ray Polarization View of Mrk 421 in an Average Flux State as Observed by the Imaging X-Ray Polarimetry Explorer. *ApJL*, 938(1):L7, Oct. 2022. doi: 10.3847/2041-8213/ac913a.

L. Di Gesu et al. Discovery of X-ray polarization angle rotation in the jet from blazar Mrk 421. *Nature Astronomy*, 7:1245–1258, Oct. 2023. doi: 10.1038/s41550-023-02032-7.

A. Domínguez et al. Extragalactic background light inferred from AEGIS galaxy-SED-type fractions. *MNRAS*, 410(4):2556–2578, Feb. 2011. doi: 10.1111/j.1365-2966.2010.17631.x.

I. Donnarumma et al. The June 2008 Flare of Markarian 421 from Optical to TeV Energies. *ApJL*, 691(1):L13–L19, Jan. 2009. doi: 10.1088/0004-637X/691/1/L13.

M. Doro, M. Gaug, J. Pallotta, G. Vasileiadis, O. Blanch, F. Chouza, R. D'Elia, A. Etchegoyen, L. Font, D. Garrido, F. Gonzales, A. López-Oramas, M. Martínez, L. Otero, E. Quel, P. Ristori, and for the CTA consortium. Status and motivation of Raman LIDARs development for the CTA Observatory. In *Proceedings of the First AtmoHEAD Conference, Saclay*, 2014.

J. Ebr, S. Karpov, J. Eliášek, J. Blažek, R. Cunniffe, I. Ebrová, P. Janeček, M. Jelínek, J. Juryšek, D. Mandát, M. Mašek, M. Pech, M. Prouza, and P. Trávníček. A New Method for Aerosol Measurement Using Wide-field Photometry. *Astronomical Journal*, 162(1):6, July 2021. doi: 10.3847/1538-3881/abf7b1.

A. S. Eddington. On the radiative equilibrium of the stars. *MNRAS*, 77:596–612, June 1917. doi: 10.1093/mnras/77.8.596.

R. A. Edelson and J. H. Krolik. The Discrete Correlation Function: A New Method for Analyzing Unevenly Sampled Variability Data. *ApJ*, 333:646, Oct 1988. doi: 10.1086/166773.

D. Emmanoulopoulos, I. M. McHardy, and I. E. Papadakis. Generating artificial light curves: revisited and updated. *MNRAS*, 433(2):907–927, Aug. 2013. doi: 10.1093/mnras/stt764.

B. L. Fanaroff and J. M. Riley. The morphology of extragalactic radio sources of high and low luminosity. *MNRAS*, 167:31P–36P, May 1974. doi: 10.1093/mnras/167.1.31P.

E. A. Fath. The spectra of some spiral nebulae and globular star clusters. *Lick Observatory Bulletin*, 149:71–77, Jan. 1909. doi: 10.5479/ADS/bib/1909LicOB.5.71F.

D. J. Fegan. γ/hadron separation at TeV energies. *Journal of Physics G: Nuclear and Particle Physics*, 23(9):1013–1060, sep 1997. doi: 10.1088/0954-3899/23/9/004. URL https://doi.org/10.1088/0954-3899/23/9/004.

E. Fermi. On the Origin of the Cosmic Radiation. *Physical Review*, 75(8):1169–1174, Apr. 1949. doi: 10.1103/PhysRev.75.1169.

C. E. Fichtel, R. C. Hartman, D. A. Kniffen, D. J. Thompson, G. F. Bignami, H. Ögelman, M. E. Özel, and T. Tümer. High-energy gamma-ray results from the second Small Astronomy Satellite. *ApJ*, 198:163–182, May 1975. doi: 10.1086/153590.

V. P. Fomin, A. A. Stepanian, R. C. Lamb, D. A. Lewis, M. Punch, and T. C. Weekes. New methods of atmospheric Cherenkov imaging for gamma-ray astronomy. I. The false source method. *Astroparticle Physics*, 2(2):137–150, May 1994. doi: 10.1016/0927-6505(94)90036-1.

I. M. Frank and I. E. Tamm. Coherent visible radiation of fast electrons passing through matter. *Compt. Rend. Acad. Sci. URSS*, 14(3):109–114, 1937. doi: 10.3367/UFNr.0093.196710o.0388.

C. Fruck. *The Galactic Center resolved with MAGIC and a new technique for Atmospheric Calibration*. PhD thesis, Technische Unversität München, Germany, Arcisstr. 21, 80333 München, Germany, jan 2015. available at https://mediatum.ub.tum.de/doc/1237928/document.pdf.

C. Fruck, M. Gaug, R. Zanin, D. Dorner, D. Garrido, R. Mirzoyan, and L. Font. A novel LIDAR-based Atmospheric Calibration Method for Improving the Data Analysis of MAGIC. In *Proceedings of the 33rd ICRC, Rio de Janeiro*, July 2013. arXiv:1403.3591.

C. Fruck, M. Gaug, A. Hahn, V. Acciari, J. Besenrieder, D. Dominis Prester, D. Dorner, D. Fink, L. Font, S. Mićanović, R. Mirzoyan, L. Müller, D. Pavletić, F. Schmuckermaier, and M. Will. Characterizing the aerosol atmosphere above the observatorio del roque de los muchachos by analyzing seven years of data taken with an gaasp hpd-readout, absolutely calibrated elastic lidar. *MNRAS*, June 2022a. doi: 10.1093/mnras/stac1563.

C. Fruck, M. Gaug, A. Hahn, V. Acciari, J. Besernrieder, D. Dominis Prester, D. Dorner, D. Fink, L. Font, S. Mićanović, R. Mirzoyan, D. Müller, L. Pavletić, F. Schmuckermaier, and M. Will. Characterizing the atmosphere above the magic site by analyzing seven years of lidar data with an hpd-readout, absolutely calibrated elastic lidar. *MNRAS*, page 4520–4550, 2022b. doi: 10.1093/mnras/stac1563.

T. K. Gaisser, R. Engel, and E. Resconi. *Cosmic Rays and Particle Physics*. 2016.

D. Garrido, M. Gaug, M. Doro, L. Font, A. López-Oramas, and A. Moralejo. Atmospheric Aerosols at the MAGIC Site. In *Proceedings of the 33rd ICRC, Rio de Janeiro*, July 2013. arXiv:1308.0473.

M. Gaug. CTA Atmospheric Calibration. In *European Physical Journal Web of Conferences*, volume 144 of *European Physical Journal Web of Conferences*, page 01003, 2017. doi: 10.1051/epjconf/201714401003.

M. Gaug, O. Blanch, M. S. Çolak, M. Doro, L. Font, S. Griffths, C. Maggio, M. Martinez, Ò. Martinez, P. Munar-Adrover, and V. Da Deppo. The IFAE/UAB Raman LIDAR for the CTA-North. In *European Physical Journal Web of Conferences*, volume 197 of *European Physical Journal Web of Conferences*, page 02005, Sept. 2019. doi: 10.1051/epjconf/201919702005.

M. Gaug, A. Hahn, V. Acciari, J. Besenrieder, D. Dominis Prester, D. Dorner, D. Fink, L. Font, C. Fruck, S. Mićanović, R. Mirzoyan, L. Pavletić, F. Schmuckermaier, and M. Will. Seven

years of quasi-continuous LIDAR data. *Journal of Physics: Conference Series*, 2398(1): 012010, dec 2022. doi: 10.1088/1742-6596/2398/1/012010.

M. Georganopoulos and D. Kazanas. Decelerating Flows in TeV Blazars: A Resolution to the BL Lacertae-FR I Unification Problem. *ApJL*, 594(1):L27–L30, Sept. 2003. doi: 10.1086/378557.

G. Ghisellini, F. Tavecchio, and M. Chiaberge. Structured jets in TeV BL Lac objects and radiogalaxies. Implications for the observed properties. *A&A*, 432(2):401–410, Mar. 2005. doi: 10.1051/0004-6361:20041404.

G. Ghisellini, F. Tavecchio, L. Foschini, and G. Ghirlanda. The transition between BL Lac objects and flat spectrum radio quasars. *MNRAS*, 414(3):2674–2689, July 2011. doi: 10.1111/j.1365-2966.2011.18578.x.

D. Giannios, D. A. Uzdensky, and M. C. Begelman. Fast TeV variability in blazars: jets in a jet. *MNRAS*, 395(1):L29–L33, May 2009. doi: 10.1111/j.1745-3933.2009.00635.x.

P. Giommi, P. Padovani, G. Polenta, S. Turriziani, V. D'Elia, and S. Piranomonte. A simplified view of blazars: clearing the fog around long-standing selection effects. *MNRAS*, 420(4): 2899–2911, Mar. 2012. doi: 10.1111/j.1365-2966.2011.20044.x.

A. C. Gupta et al. Characterizing Optical Variability of OJ 287 in 2016-2017. *Astronomical Journal*, 157(3):95, Mar. 2019. doi: 10.3847/1538-3881/aafe7d.

H. E. S. S. Collaboration. H.E.S.S. observations of the Crab during its March 2013 GeV gamma-ray flare. *A&A*, 562:L4, Feb. 2014. doi: 10.1051/0004-6361/201323013.

J. Hahn et al. Impact of aerosols and adverse atmospheric conditions on the data quality for spectral analysis of the H.E.S.S. telescopes. *Astroparticle Physics*, 54:25–32, 2014.

F. A. Harrison et al. The Nuclear Spectroscopic Telescope Array (NuSTAR) High-energy X-Ray Mission. *ApJ*, 770(2):103, June 2013. doi: 10.1088/0004-637X/770/2/103.

D. Heck, J. Knapp, J. N. Capdevielle, G. Schatz, and T. Thouw. *CORSIKA: a Monte Carlo code to simulate extensive air showers.* 1998.

V. F. Hess. Über Beobachtungen der durchdringenden Strahlung bei sieben Freiballonfahrten. *Phys. Z.*, 13:1084–1091, 1912.

A. M. Hillas. The Origin of Ultra-High-Energy Cosmic Rays. *Annu*, 22:425–444, Jan. 1984. doi: 10.1146/annurev.aa.22.090184.002233.

A. M. Hillas. Cerenkov Light Images of EAS Produced by Primary Gamma Rays and by Nuclei. In *19th International Cosmic Ray Conference (ICRC19), Volume 3*, volume 3 of *International Cosmic Ray Conference*, page 445, Aug. 1985a.

A. M. Hillas. Cherenkov light images of eas produced by primary gamma showers. In *Proc. of the* 19$^{\text{th}}$ *International Cosmic Ray Conference, La Jolla*, pages 445–448, Aug. 1985b.

P. T. P. Ho, J. M. Moran, and K. Y. Lo. The Submillimeter Array. *ApJL*, 616(1):L1–L6, Nov. 2004. doi: 10.1086/423245.

T. L. Holch, F. Leuschner, J. Schäfer, and S. Steinmassl. Assessing aerosol induced errors in Monte Carlo based air-shower reconstruction for atmospheric Cherenkov detectors. *Journal of Physics: Conference Series*, 2398(1):012017, dec 2022. doi: 10.1088/1742-6596/2398/1/012017.

T. Hovatta, M. Petropoulou, J. L. Richards, D. Giannios, K. Wiik, M. Baloković, A. Lähteenmäki, B. Lott, W. Max-Moerbeck, V. Ramakrishnan, and A. C. S. Readhead. A combined radio and GeV γ-ray view of the 2012 and 2013 flares of Mrk 421. *MNRAS*, 448(4):3121–3131, Apr. 2015. doi: 10.1093/mnras/stv220.

IceCube Collaboration. Evidence for High-Energy Extraterrestrial Neutrinos at the IceCube Detector. *Science*, 342(6161):1242856, Nov. 2013. doi: 10.1126/science.1242856.

IceCube Collaboration. Evidence for neutrino emission from the nearby active galaxy NGC 1068. *Science*, 378(6619):538–543, Nov. 2022. doi: 10.1126/science.abg3395.

IceCube Collaboration et al. Neutrino emission from the direction of the blazar TXS 0506+056 prior to the IceCube-170922A alert. *Science*, 361(6398):147–151, July 2018. doi: 10.1126/science.aat2890.

K. Ishio and D. Paneque. A novel energy reconstruction method for the MAGIC stereoscopic observation. *Astroparticle Physics*, 158:102937, June 2024. doi: 10.1016/j.astropartphys.2024.102937.

F. Jansen, D. Lumb, B. Altieri, J. Clavel, M. Ehle, C. Erd, C. Gabriel, M. Guainazzi, P. Gondoin, R. Much, R. Munoz, M. Santos, N. Schartel, D. Texier, and G. Vacanti. XMM-Newton observatory. I. The spacecraft and operations. *A&A*, 365:L1–L6, Jan. 2001. doi: 10.1051/0004-6361:20000036.

K. G. Jansky. Radio Waves from Outside the Solar System. *Nature*, 132(3323):66, July 1933. doi: 10.1038/132066a0.

J. Jormanainen, T. Hovatta, I. M. Christie, E. Lindfors, M. Petropoulou, and I. Liodakis. Quantitative comparisons of very-high-energy gamma-ray blazar flares with relativistic reconnection models. *A&A*, 678:A140, Oct. 2023. doi: 10.1051/0004-6361/202346286.

S. G. Jorstad, A. P. Marscher, J. R. Mattox, M. F. Aller, H. D. Aller, A. E. Wehrle, and S. D. Bloom. Multiepoch Very Long Baseline Array Observations of EGRET-detected Quasars and BL Lacertae Objects: Connection between Superluminal Ejections and Gamma-Ray Flares in Blazars. *ApJ*, 556(2):738–748, Aug. 2001. doi: 10.1086/321605.

S. G. Jorstad et al. Kinematics of Parsec-scale Jets of Gamma-Ray Blazars at 43 GHz within the VLBA-BU-BLAZAR Program. *ApJ*, 846(2):98, Sept. 2017. doi: 10.3847/1538-4357/aa8407.

E. Jourdain and J. P. Roques. 2003-2019 Monitoring of the Crab Emission through INTEGRAL SPI, or Vice Versa. *ApJ*, 899(2):131, Aug. 2020. doi: 10.3847/1538-4357/aba8a4.

M. A. Kastendieck, M. C. B. Ashley, and D. Horns. Long-term optical variability of PKS 2155-304. *A&A*, 531:A123, July 2011. doi: 10.1051/0004-6361/201015918.

K. Katarzyński, G. Ghisellini, F. Tavecchio, L. Maraschi, G. Fossati, and A. Mastichiadis. Correlation between the TeV and X-ray emission in high-energy peaked BL Lac objects. *A&A*, 433(2):479–496, Apr. 2005. doi: 10.1051/0004-6361:20041556.

K. I. Kellermann, R. Sramek, M. Schmidt, D. B. Shaffer, and R. Green. VLA Observations of Objects in the Palomar Bright Quasar Survey. *Astronomical Journal*, 98:1195, Oct. 1989. doi: 10.1086/115207.

O. G. King et al. The RoboPol pipeline and control system. *MNRAS*, 442(2):1706–1717, Aug. 2014. doi: 10.1093/mnras/stu176.

J. G. Kirk, F. M. Rieger, and A. Mastichiadis. Particle acceleration and synchrotron emission in blazar jets. *A&A*, 333:452–458, May 1998. doi: 10.48550/arXiv.astro-ph/9801265.

T. P. Li and Y. Q. Ma. Analysis methods for results in gamma-ray astronomy. *ApJ*, 272:317–324, Sept. 1983. doi: 10.1086/161295.

R. Lico et al. VLBA monitoring of Mrk 421 at 15 GHz and 24 GHz during 2011. *A&A*, 545: A117, Sept. 2012. doi: 10.1051/0004-6361/201219870.

I. Liodakis et al. Polarized blazar X-rays imply particle acceleration in shocks. *Nature*, 611 (7937):677–681, Nov. 2022a. doi: 10.1038/s41586-022-05338-0.

I. Liodakis et al. Polarized blazar X-rays imply particle acceleration in shocks. *Nature*, 611 (7937):677–681, Nov. 2022b. doi: 10.1038/s41586-022-05338-0.

N. R. Lomb. Least-Squares Frequency Analysis of Unequally Spaced Data. *Ap&SS*, 39(2): 447–462, Feb. 1976. doi: 10.1007/BF00648343.

M. S. Longair. *High Energy Astrophysics*. 2011.

G. M. Madejski, M. Sikora, T. Jaffe, M. BŁażejowski, K. Jahoda, and R. Moderski. X-Ray Observations of BL Lacertae during the 1997 Outburst and Association with Quasar-like Characteristics. *ApJ*, 521(1):145–154, Aug. 1999. doi: 10.1086/307524.

MAGIC Collaboration. Teraelectronvolt emission from the γ-ray burst GRB 190114C. *Nature*, 575(7783):455–458, Nov. 2019. doi: 10.1038/s41586-019-1750-x.

MAGIC Collaboration et al. Multi-wavelength characterization of the blazar S5 0716+714 during an unprecedented outburst phase. *A&A*, 619:A45, Nov. 2018. doi: 10.1051/0004-6361/201832677.

MAGIC Collaboration et al. Investigation of the correlation patterns and the Compton dominance variability of Mrk 421 in 2017. *A&A*, 655:A89, Nov. 2021. doi: 10.1051/0004-6361/202141004.

MAGIC Collaboration et al. Insights into the broadband emission of the TeV blazar Mrk 501 during the first X-ray polarization measurements. *A&A*, 685:A117, May 2024. doi: 10.1051/0004-6361/202348709.

P. Majumdar, A. Moralejo, C. Bigongiari, O. Blanch, and D. Sobczynska. Monte Carlo simulation for the MAGIC telescope. In *29th International Cosmic Ray Conference (ICRC29), Volume 5*, volume 5 of *International Cosmic Ray Conference*, page 203, Jan. 2005.

L. Maraschi, G. Ghisellini, and A. Celotti. A Jet Model for the Gamma-Ray–emitting Blazar 3C 279. *ApJL*, 397:L5, Sept. 1992. doi: 10.1086/186531.

B. E. Markarian and V. A. Lipovetskij. Galaxies with ultraviolet continuum. V. *Astrofizika*, 8: 155–164, Jan. 1972.

A. P. Marscher and W. K. Gear. Models for high-frequency radio outbursts in extragalactic sources, with application to the early 1983 millimeter-to-infrared flare of 3C 273. *ApJ*, 298: 114–127, Nov. 1985. doi: 10.1086/163592.

A. P. Marscher et al. The inner jet of an active galactic nucleus as revealed by a radio-to-γ-ray outburst. *Nature*, 452(7190):966–969, Apr. 2008. doi: 10.1038/nature06895.

P. J. Napier, D. S. Bagri, B. G. Clark, A. E. E. Rogers, J. D. Romney, A. R. Thompson, and R. C. Walker. The Very Long Baseline Array. *IEEE Proceedings*, 82(5):658–672, May 1994. doi: 10.1109/5.284733.

K. Nilsson, M. Pasanen, L. O. Takalo, E. Lindfors, A. Berdyugin, S. Ciprini, and J. Pforr. Host galaxy subtraction of TeV candidate BL Lacertae objects. *A&A*, 475(1):199–207, Nov. 2007. doi: 10.1051/0004-6361:20077624.

R. Orito et al. Development of HPD Clusters for MAGIC-II. *arXiv e-prints*, art. arXiv:0907.0865, July 2009.

A. N. Otte. *Observation of VHE γ-Rays from the Vicinity of magnetized Neutron Stars and Development of new Photon-Detectors for Future Ground based γ-Ray Detectors*. PhD thesis, Munich, Tech. U., 2007.

P. Padovani. The microjansky and nanojansky radio sky: source population and multiwavelength properties. *MNRAS*, 411(3):1547–1561, Mar. 2011. doi: 10.1111/j.1365-2966.2010.17789.x.

P. Padovani. The faint radio sky: radio astronomy becomes mainstream. *A&A Reviews*, 24(1): 13, Sept. 2016. doi: 10.1007/s00159-016-0098-6.

P. Padovani, D. M. Alexander, R. J. Assef, B. De Marco, P. Giommi, R. C. Hickox, G. T. Richards, V. Smolčić, E. Hatziminaoglou, V. Mainieri, and M. Salvato. Active galactic nuclei: what's in a name? *A&A Reviews*, 25(1):2, Aug. 2017. doi: 10.1007/s00159-017-0102-9.

S. Paltani and M. Türler. The mass of the black hole in 3C 273. *A&A*, 435(3):811–820, June 2005. doi: 10.1051/0004-6361:20041206.

S. R. Patel, A. Shukla, V. R. Chitnis, D. Dorner, K. Mannheim, B. S. Acharya, and B. J. Nagare. Broadband study of blazar 1ES 1959+650 during flaring state in 2016. *A&A*, 611:A44, Mar. 2018. doi: 10.1051/0004-6361/201731987.

K. Pearson. Note on regression and inheritance in the case of two parents. *Proceedings of the Royal Society of London*, 58:240–242, 1895. ISSN 03701662. URL http://www.jstor.org/stable/115794.

B. M. Peterson, I. Wanders, K. Horne, S. Collier, T. Alexander, S. Kaspi, and D. Maoz. On Uncertainties in Cross-Correlation Lags and the Reality of Wavelength-dependent Continuum Lags in Active Galactic Nuclei. *PASP*, 110(748):660–670, June 1998. doi: 10.1086/316177.

D. Petry et al. Detection of VHE γ-rays from MKN 421 with the HEGRA Cherenkov Telescopes. *A&A*, 311:L13–L16, July 1996. doi: 10.48550/arXiv.astro-ph/9606159.

B. G. Piner and P. G. Edwards. VLBA Polarization Observations of Markarian 421 after a Gamma-Ray High State. *ApJ*, 622(1):168–177, Mar. 2005. doi: 10.1086/428039.

J. Poutanen, A. A. Zdziarski, and A. Ibragimov. Superorbital variability of X-ray and radio emission of Cyg X-1 - II. Dependence of the orbital modulation and spectral hardness on the superorbital phase. *MNRAS*, 389(3):1427–1438, Sept. 2008. doi: 10.1111/j.1365-2966.2008.13666.x.

I. Puerto-Giménez, M. Gaug, R. Barrena, J. Castro, M. Doro, L. Font, M. Nievas Rosillo, J. Zamorano, and C. Consortium. Characterization of the candidate site for the Cherenkov Telescope Array at the Observatorio del Teide. In *International Cosmic Ray Conference*, volume 33 of *International Cosmic Ray Conference*, page 2976, Jan. 2013. doi: 10.48550/arXiv.1307.4989.

G. Pühlhofer et al. The technical performance of the HEGRA system of imaging air Cherenkov telescopes. *Astroparticle Physics*, 20(3):267–291, Dec. 2003. doi: 10.1016/j.astropartphys.2003.06.001.

M. Punch et al. Detection of TeV photons from the active galaxy Markarian 421. *Nature*, 358 (6386):477–478, Aug. 1992a. doi: 10.1038/358477a0.

M. Punch et al. Detection of TeV photons from the active galaxy Markarian 421. *Nature*, 358 (6386):477–478, Aug. 1992b. doi: 10.1038/358477a0.

A. N. Ramaprakash et al. RoboPol: a four-channel optical imaging polarimeter. *MNRAS*, 485 (2):2355–2366, May 2019. doi: 10.1093/mnras/stz557.

M. Ravasio, G. Tagliaferri, G. Ghisellini, and F. Tavecchio. Observing Mkn 421 with XMM-Newton: The EPIC-PN point of view. *A&A*, 424:841–855, Sept. 2004. doi: 10.1051/0004-6361:20034545.

J. L. Richards et al. An Exceptional Radio Flare in Markarian 421. In *European Physical Journal Web of Conferences*, volume 61 of *European Physical Journal Web of Conferences*, page 04010, Dec. 2013. doi: 10.1051/epjconf/20136104010.

G. D. Rochester and C. C. Butler. Evidence for the Existence of New Unstable Elementary Particles. *Nature*, 160(4077):855–857, Dec. 1947. doi: 10.1038/160855a0.

P. W. A. Roming et al. The Swift Ultra-Violet/Optical Telescope. *SSR*, 120(3-4):95–142, Oct. 2005. doi: 10.1007/s11214-005-5095-4.

A. Rudy et al. Characterization of the Inner Knot of the Crab: the Site of the Gamma-ray Flares? *The Astrophysical Journal*, 811(1):24, sep 2015. doi: 10.1088/0004-637x/811/1/24. URL https://doi.org/10.1088/0004-637x/811/1/24.

J. D. Scargle. Studies in astronomical time series analysis. II. Statistical aspects of spectral analysis of unevenly spaced data. *ApJ*, 263:835–853, Dec. 1982. doi: 10.1086/160554.

F. Schmidt. CORSIKA shower images. https://www.iap.kit.edu/corsika/, 2005. [Online; accessed 1-July-2023].

F. Schmuckermaier. Detailed characterization of the performance of the magic lidar using a 7-year dataset. Master's thesis, Technische Universität München, October 2021. Available at https://magic.mpp.mpg.de/backend/publication/show/549.

F. Schmuckermaier, M. Gaug, C. Fruck, A. Hahn, V. Acciari, J. Besenrieder, D. Dominis Prester, D. Dorner, D. Fink, L. Font, , S. Mićanović, R. Mirzoyan, D. Müller, L. Pavletić, and M. Will. Correcting MAGIC Telescope Data taken under non-optimal atmospheric conditions with an elastic LIDAR. *Journal of Physics: Conference Series*, 2398(1):012011, dec 2022. doi: 10.1088/1742-6596/2398/1/012011.

F. Schmuckermaier, M. Gaug, C. Fruck, A. Moralejo, A. Hahn, D. Dominis Prester, D. Dorner, L. Font, S. Mićanović, R. Mirzoyan, D. Paneque, L. Pavletić, J. Sitarek, and M. Will. Correcting Imaging Atmospheric Cherenkov Telescope data with atmospheric profiles obtained with an elastic light detecting and ranging system. *A&A*, 673:A2, May 2023. doi: 10.1051/0004-6361/202245787.

K. Schwarzschild. Über das Gravitationsfeld eines Massenpunktes nach der Einsteinschen Theorie. *Sitzungsberichte der Königlich Preussischen Akademie der Wissenschaften*, pages 189–196, Jan. 1916.

C. K. Seyfert. No. 671. Nuclear emission in spiral nebulae. *Contributions from the Mount Wilson Observatory / Carnegie Institution of Washington*, 671:1–13, Jan. 1943.

D. Sobczyńska and W. Bednarek. Influence of clouds on the parameters of images measured by IACT at very high energies. *Journal of Physics G: Nuclear and Particle Physics*, 41 (12):125201, Oct. 2014. ISSN 0954-3899. doi: 10.1088/0954-3899/41/12/125201. URL https://doi.org/10.1088/0954-3899/41/12/125201.

M. Spurio. *Probes of Multimessenger Astrophysics*. 2018. doi: 10.1007/978-3-319-96854-4.

R. A. Sramek and D. W. Weedman. The radio properties of optically discovered quasars. *ApJ*, 238:435–444, June 1980. doi: 10.1086/158000.

S. Stefanik, D. Nosek, R. de los Reyes, M. Gaug, and P. Travnicek. Atmospheric monitoring and inter-calibration of the telescope optical throughput efficiencies using the trigger rates of the Cherenkov Telescope Array. *Astroparticle Physics*, 109:12 – 24, 2019. doi: 10.1016/j.astropartphys.2019.02.002. URL http://www.sciencedirect.com/science/article/pii/S0927650518302299.

B. Steinke. *First study of fast variability in Markarian 421 with the MAGIC stereoscopic system*. PhD thesis, Technische Unversität München, Germany, Arcisstr. 21, 80333 München, Germany, mar 2012. available at https://mediatum.ub.tum.de/doc/1097511/document.pd.

L. Strüder et al. The European Photon Imaging Camera on XMM-Newton: The pn-CCD camera. *A&A*, 365:L18–L26, Jan. 2001. doi: 10.1051/0004-6361:20000066.

B. N. Swanenburg, K. Bennett, G. F. Bignami, R. Buccheri, P. Caraveo, W. Hermsen, G. Kanbach, G. G. Lichti, J. L. Masnou, H. A. Mayer-Hasselwander, J. A. Paul, B. Sacco, L. Scarsi, and R. D. Wills. Second COS-B catalogue of high-energy gamma-ray sources. *ApJL*, 243:L69–L73, Jan. 1981. doi: 10.1086/183445.

M. Tavani et al. Discovery of Powerful Gamma-Ray Flares from the Crab Nebula. *Science*, 331 (6018):736, Feb. 2011. doi: 10.1126/science.1200083.

F. Tavecchio, L. Maraschi, and G. Ghisellini. Constraints on the Physical Parameters of TeV Blazars. *ApJ*, 509(2):608–619, Dec. 1998. doi: 10.1086/306526.

F. Tavecchio, M. Landoni, L. Sironi, and P. Coppi. Probing dissipation mechanisms in BL Lac jets through X-ray polarimetry. *MNRAS*, 480(3):2872–2880, Nov. 2018. doi: 10.1093/mnras/sty1491.

M. J. L. Turner et al. The European Photon Imaging Camera on XMM-Newton: The MOS cameras. *A&A*, 365:L27–L35, Jan. 2001. doi: 10.1051/0004-6361:20000087.

C. M. Urry and P. Padovani. Unified Schemes for Radio-Loud Active Galactic Nuclei. *PASP*, 107:803, Sept. 1995. doi: 10.1086/133630.

P. Uttley, I. M. McHardy, and I. E. Papadakis. Measuring the broad-band power spectra of active galactic nuclei with RXTE. *MNRAS*, 332(1):231–250, May 2002. doi: 10.1046/j.1365-8711.2002.05298.x.

J. van Scherpenberg, R. Mirzoyan, I. Vovk, M. Peresano, D. Zaric, P. Temnikov, N. Godinović, and J. Besenrieder. Searching for Variability of the Crab Nebula Flux at TeV Energies using MAGIC Very Large Zenith Angle Observations. In *36th International Cosmic Ray Conference (ICRC2019)*, volume 36 of *International Cosmic Ray Conference*, page 812, July 2019.

S. Vaughan, R. Edelson, R. S. Warwick, and P. Uttley. On characterizing the variability properties of X-ray light curves from active galaxies. *MNRAS*, 345(4):1271–1284, Nov. 2003. doi: 10.1046/j.1365-2966.2003.07042.x.

M. Villata et al. Multifrequency monitoring of the blazar <ASTROBJ>0716+714</ASTROBJ> during the GASP-WEBT-AGILE campaign of 2007. *A&A*, 481(2):L79–L82, Apr. 2008. doi: 10.1051/0004-6361:200809552.

M. Villata et al. The GASP-WEBT monitoring of <ASTROBJ>3C 454.3</ASTROBJ> during the 2008 optical-to-radio and γ-ray outburst. *A&A*, 504(3):L9–L12, Sept. 2009. doi: 10.1051/0004-6361/200912732.

S. Wakely and D. Horan. Tev cat. http://tevcat.uchicago.edu/, 2023. Accessed: 2024-02-15.

Z. R. Weaver et al. Kinematics of Parsec-scale Jets of Gamma-Ray Blazars at 43 GHz during 10 yr of the VLBA-BU-BLAZAR Program. *ApJS*, 260(1):12, May 2022. doi: 10.3847/1538-4365/ac589c.

T. C. Weekes, M. F. Cawley, D. J. Fegan, K. G. Gibbs, A. M. Hillas, P. W. Kowk, R. C. Lamb, D. A. Lewis, D. Macomb, N. A. Porter, P. T. Reynolds, and G. Vacanti. Observation of TeV Gamma Rays from the Crab Nebula Using the Atmospheric Cerenkov Imaging Technique. *ApJ*, 342:379, July 1989. doi: 10.1086/167599.

M. Weisskopf. The Imaging X-ray Polarimetry Explorer (IXPE) Mission Overview. In *AAS/High Energy Astrophysics Division*, volume 54 of *AAS/High Energy Astrophysics Division*, page 301.01, Apr. 2022.

R. Zanin, E. Carmona, J. Sitarek, P. Colin, K. Frantzen, M. Gaug, S. Lombardi, M. Lopez, A. Moralejo, K. Satalecka, V. Scapin, and V. Stamatescu. MARS, The MAGIC Analysis and Reconstruction Software. In *International Cosmic Ray Conference*, volume 33 of *International Cosmic Ray Conference*, page 2937, Jan. 2013a.

R. Zanin, E. Carmona, J. Sitarek, P. Colin, K. Frantzen, M. Gaug, S. Lombardi, M. Lopez, A. Moralejo, K. Satalecka, V. Scapin, and V. Stamatescu. MARS, The MAGIC Analysis and Reconstruction Software. In *International Cosmic Ray Conference*, volume 33 of *International Cosmic Ray Conference*, page 2937, Jan. 2013b.

H. Zhang and M. Böttcher. X-Ray and Gamma-Ray Polarization in Leptonic and Hadronic Jet Models of Blazars. *ApJ*, 774(1):18, Sept. 2013. doi: 10.1088/0004-637X/774/1/18.

Appendix A

Hardware upgrades to the MAGIC LIDAR

A.1 A new mirror

The construction and first tests of the LIDAR started before 2010. The old mirror was purchased in 2008 when the first tests began. It was a 60 cm solid aluminum mirror produced by *LT Ultra* in Germany. Since 2013, the LIDAR has been fully operating at the MAGIC site. The LIDAR works under open sky and, during standby, is covered by a protective dome, which is not perfectly sealed. Humidity and dust can easily enter the dome and deposit on the mirror. The mirror had a protective coating of quartz (SiO_2) to protect the Al-surface from corrosion. Over the years, this layer is diminished, and the moisture can lead to corrosion at the surface, leading to a loss of reflectivity.

A good mirror reflectivity is imperative for operating the MAGIC LIDAR. One needs to gather high photon statistics to achieve a good return signal. This can be achieved by several means: First, the photon number at the source can be increased, i.e., using a more powerful laser. Increasing the laser power too much can cause interference with the observation of MAGIC and other telescopes at the ORM. Thus, a laser with a power of only 25 μJ was chosen for the MAGIC LIDAR. This way, the LIDAR can be operated at night and gather concurrent data without obstructing the regular observations. As previously described, the detector used by the LIDAR is an HPD. It reaches a quantum efficiency of around 50% at 532 nm with single photo-electron resolution and a very low after pulsing. The detector element is also well-optimized for the intended purpose, leaving the mirror as the final component that can be optimized to achieve good photon statistics.

A.1.1 Characteristics of the new LIDAR mirror

The old mirror was made from solid aluminum since it was cheaper than the usually used glass mirrors in optical astronomy. All options were explored for the new mirror, and several manufacturers were contacted. Ultimately, a mirror made by *Media Lario* from Milan, Italy, was purchased. The mirror is made from solid Borofloat, a borosilicate glass. The mirror shape is highly stable with a deviation of only $\sim$2 μm PV (peak to valley). Also, the surface roughness showed an excellent accuracy of 2-3 nm. The mirror has a slighter larger diameter than the previous one, 61 cm vs 60 cm. The curvature must be 300 cm to achieve a focal point at 150 cm. Ideally, a parabolic shape is desired, but the manufacturing process is more complex, so the cost becomes significantly higher. Since the difference between spherical and parabolic is almost negligible for the intended purpose, the mirror shape is selected as spherical. The standard alu-

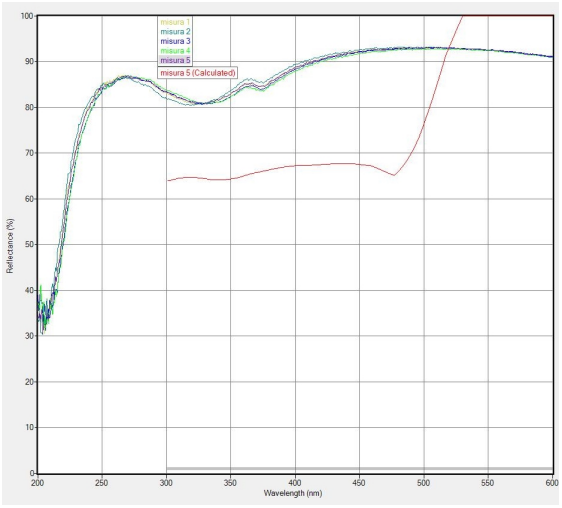

Figure A.1: Reflectance of the new mirror as a function of the wavelength obtained by five measurements. The reflectance peaks around 500 nm, close to the frequency of the used laser of 532 nm. All five measurements agree well, except for an additional one which does not show an actual measurement (in red).

minum coating with SiO_2 coating provides a reflectivity of 93% at 532 nm. The reflectivity curve provided by the manufacturer can be seen in figure A.1. The reflectivity peaks around 500 nm. Hence, the choice of material is very well suited for the intended purpose.

The mirror was ordered in June 2021 and was delivered to the MPP in October 2021. Due to the volcanic eruption on La Palma, the mirror was not mounted until the volcanic activity calmed down. Mounting the mirror during the activity would have risked the contamination of the mirror surface with heavy volcanic ash. The new mirror was shipped to La Palma on 13 April 2022 and exchanged in the following week. The new mirror can be seen in figure A.2. It was mounted flat on the inside of the telescope frame. Since the new mirror setup is thicker than the old one, the focal point had to be adjusted by moving the detector back. This was done by covering the detector and pointing at a bright star. The detector can then be adjusted until the

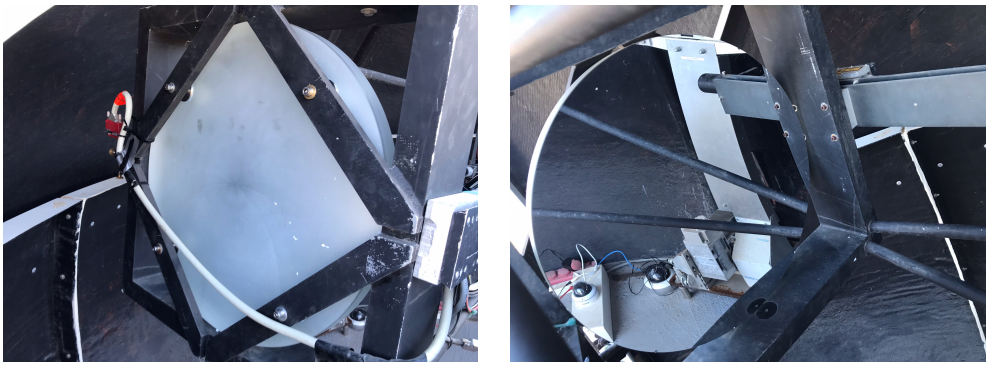

Figure A.2: Images of the new LIDAR mirror. Viewed from the back (left) and front (right).

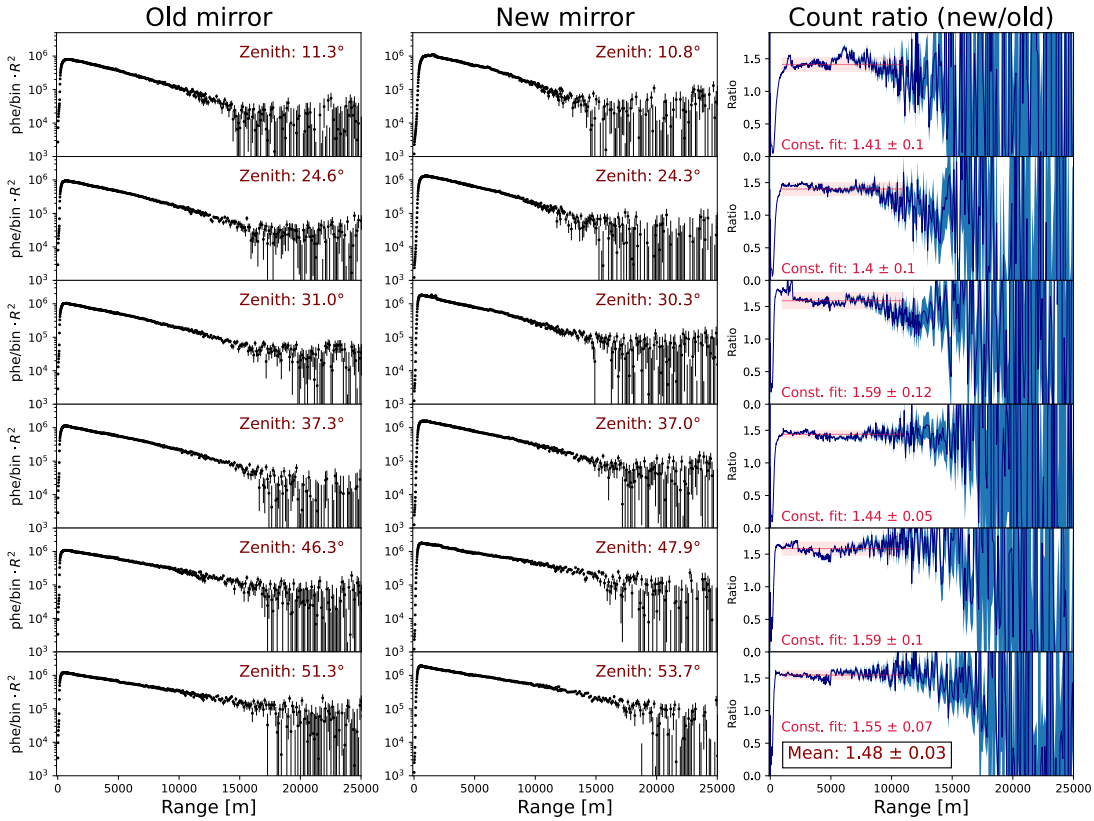

Figure A.3: Comparison of the mirror performance during optimal weather conditions. First column: six different LIDAR profiles taken under different zenith angles with the old mirror. Middle column: six LIDAR profiles taken under comparable zenith angles with the new mirror. Right column: Ratio of photoelectron counts as a function of distance. The ratios up to 12 km are fitted with a constant model in red.

projected light spot reaches a minimal size. Finally, the laser needs to be aligned regarding the mirror. More details on the alignment procedure can be found in the following section of the Appendix.

A.1.2 Comparison of the mirror performance

To compare the performance of the new mirror, LIDAR profiles taken during a wide range of zenith angles, and optimal weather conditions were used. Each profile shows the number of photoelectrons (weighted with the range squared) as a function of distance from the LIDAR. These were taken during regular observation before and after the installation of the mirror. The profiles were selected so that the zenith angle matched closely. Figure A.3 shows the profiles obtained with the old mirror in the left column for six zenith angles. The second column shows profiles obtained with the new mirror. The third column on the right displays the ratio of detected

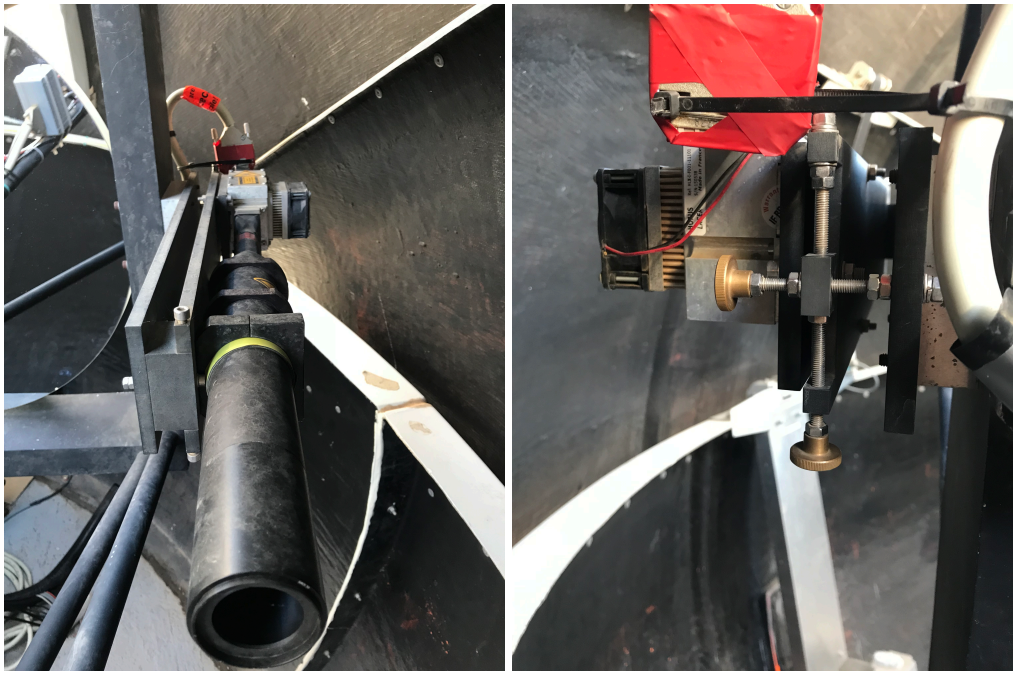

Figure A.4: Images of the old laser mount. The full setup from the front (left) and the screws used for the alignment of the plates (right).

photoelectrons as a function of range. Up to a distance of around 12 km, the signal-to-noise ratio is still stable, and a constant line can fit the ratio. The ratio was fit for every zenith; the average is shown in the bottom row. On average, the new mirror collects more photons by a factor of 1.48 ± 0.03. Roughly speaking, the new mirror achieved an increase of photon yield by 50%. The increase in photon counts helps achieve a good signal-to-noise ratio for larger distances, and when suboptimal atmospheric conditions cause more photon absorption due to the higher aerosol presence.

A.2 A new motorized laser mount

For all optical components of the LIDAR to work together, they must be precisely aligned. The mirror and detector are fixed to the telescope frame, which leaves the laser as the adjustable component. The laser is mounted on the side of the telescope frame on an aluminum plate with a beam expander and a baffle tube to reduce stray light. Previously, a laser mount that consisted of two aluminum plates was used, and the upper plate angles were freely movable in two directions. For the adjustment, two regular screws were used that had to be turned by hand and could be fixed by two nuts. Two images of the old setup are shown in Figure A.4. The old laser mount was a simple and effective solution requiring only a few components. However, it suffered from two main downsides: First, for the alignment procedure, it is almost mandatory that two people work simultaneously. One person has to be up in the LIDAR dome on site and turn the screws, whereas the other one is repeatedly firing the laser to see if the return signal improves.

The second person could also be controlling the laser remotely. Second, the screws made it challenging to reach a precise alignment. The size and angle of the thread caused considerable movement of the plates, even with a slight rotation by hand. Additionally, the screws started to gather some flash rust over the years and also became slightly bent, which impaired the accuracy with which the screws could be adjusted.

For these reasons, a new laser mount with motorized axes that allows precise alignment by a single person on-site or remotely had to be developed at the MPP.

A.2.1 Design of the new laser mount

The design and construction of the new mount described in the following section were performed by Georg Obermüller (an engineer from the MPP). The MPP workshops manufactured all milled parts.

The new design consists of three aluminum plates connected by two components composed of a stepper motor and a spindle. The bottom plate provides the connection to the telescope frame. The bottom and the middle plate are connected on one end by a bearing, providing the pivot point, and by a motor plus spindle component controlling the rotation of the middle plate concerning the bottom plate. The upper plate is then connected to the middle plate by a similar setup, allowing to tilt the plates towards each other. The laser and tube system is then mounted on the upper plate analogous to the old setup. CAD models of the new laser mount from two different angles are given in Figure A.5.

The stepper motors[1] are IP 67 certified. This ensures protection against any dust intrusion and even brief immersion in water. Additionally, the motors are enclosed in an aluminum housing, and plastic bellows cover the spindles. The stepper motors have a step angle of 1.8°, and the spindles have a thread angle of 2 mm per full rotation. This results in an axial motion of 0.01 mm per step, allowing an excellent laser adjustment. To limit the movement of the motors at the maximal or minimal length of the spindle, two sensors act as end switches to prevent further movement of the plates. Two inductive sensors[2], which are also IP 67 certified, register thin metal plates defining the end positions and trigger a stop of the motors. This way, any usage damaging the mount is excluded.

A.2.2 Installation of the new laser mount

The new mount was installed in June 2023 by a team from MPP coasting on myself, Georg Obermüller, and Jens Schlammer. The front view of the mount with the attached laser is shown in the right image of Figure A.6. The left image shows the back view with the motors and cabling. In addition to the mount, an electronic box was installed to control the motors and sensors. The setup is connected to the LIDAR PC via a USB interface. From the main box, the cables follow along the LIDAR telescope frame. Furthermore, two small electronic boxes were attached to the back of the telescope frame, connecting the motors and sensors with the main electronic box. A simple user interface from the LIDAR PC can then control the mount, allowing movement in all four directions with various step sizes. The interface is shown in Figure A.7.

[1] https://www.jvl.dk/913/stepper-motors (MSW231A254W1AA3.0)
[2] https://de.rs-online.com/web/p/naherungsschalter/1646093?gb=s

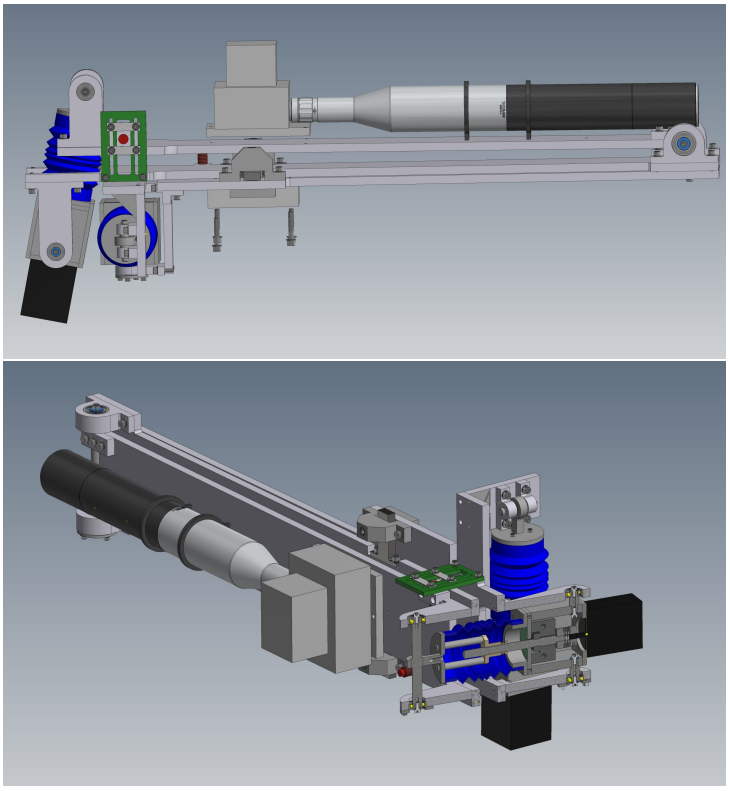

Figure A.5: CAD model of the new laser mount. Side view (top) and inclined view with cross-section (bottom)

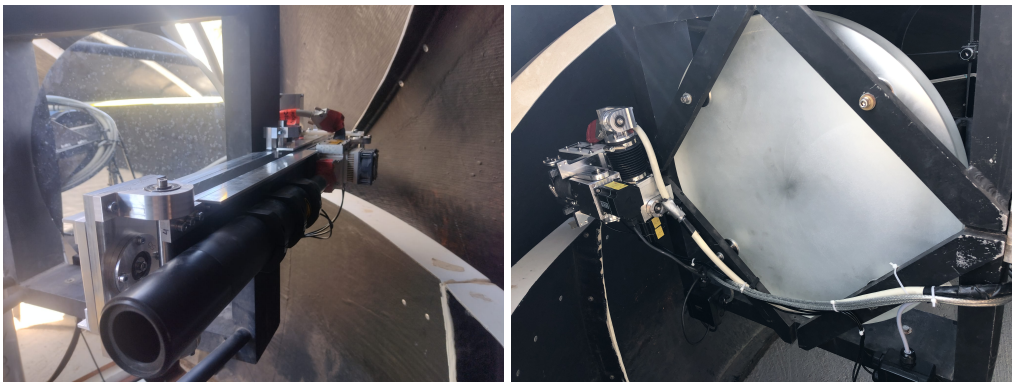

Figure A.6: The newly installed laser mount. The full setup from the front (left) and the motors used to align the plates (right).

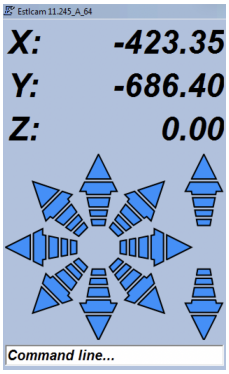

Figure A.7: User interface to control the motorized laser mount.

The new system allows an exact laser alignment by a single person, remote or on-site. This reduces the workload of the local telescope staff and supports the long-term goal of automatizing the MAGIC telescopes and their subsystems.

Appendix B

Supplemental material of Chapter 6

B.1 Discrete correlation functions

This section presents the remaining results of the DCF analysis shown in section 6.6. It covers the remaining DCFs between VHE and HE gamma rays, and between HE and X-rays with and without the big flare in February 2010. Additionally, the DCF results between HE and the UV and optical without the flare are shown.

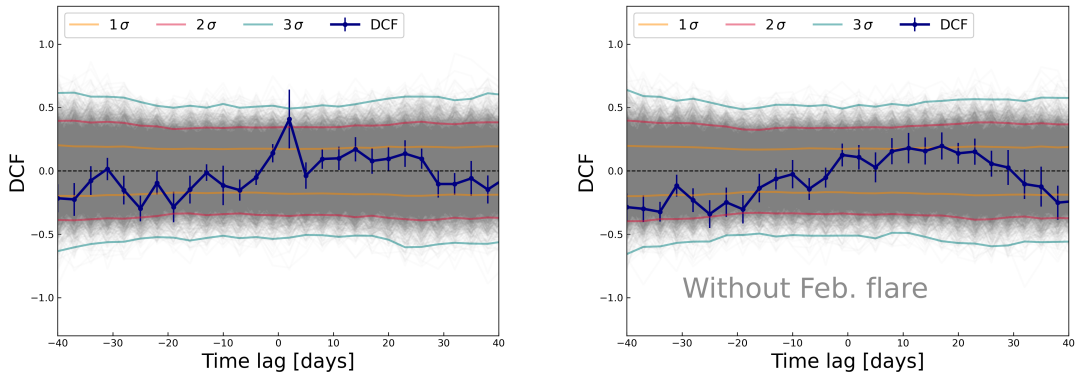

(a) >0.2 TeV vs 0.3-3 GeV

(b) >0.2 TeV vs 0.3-3 GeV without the flare in February 2010

Figure B.1: Discrete correlation function computed between the VHE gamma-ray fluxes above 0.2 TeV, as measured by MAGIC and VERITAS, and the HE gamma-ray fluxes in the 0.3-3 GeV energy range measured by *Fermi*-LAT. The left panel shows the results for the full dataset, and the right panel those obtained when excluding the large flare in February 2010. The DCF is computed using a time bin of 3-days for a range of time lags between -40 to +40 days. The 1 σ, 2 σ, and 3 σ confidence levels obtained by simulations are shown by the yellow, red, and green lines, respectively.

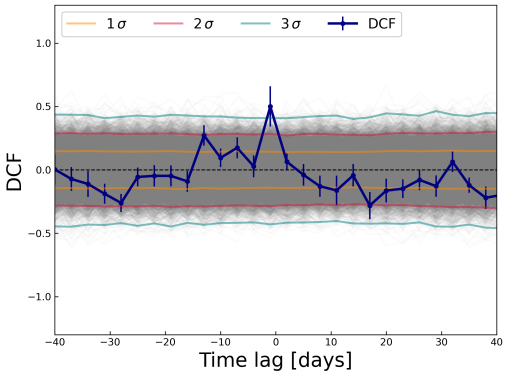

(a) 0.3-3 GeV vs 0.3-2 keV

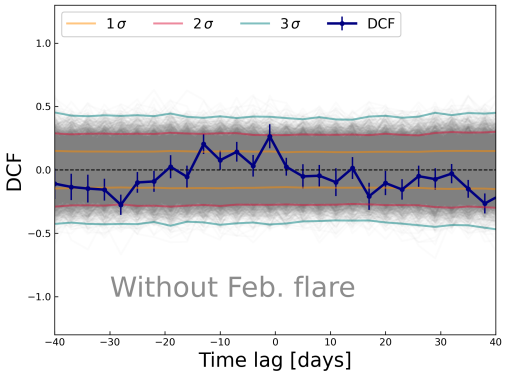

(b) 0.3-3 GeV vs 0.3-2 keV without the flare in February 2010

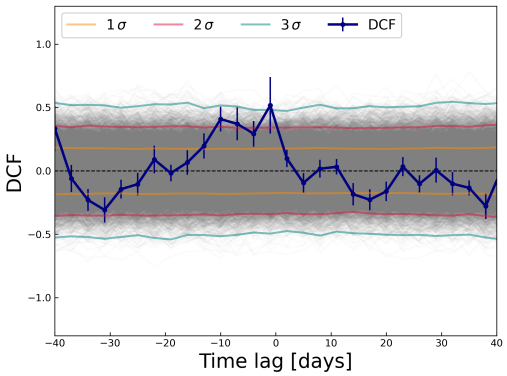

(c) 3-300 GeV vs 2-10 keV

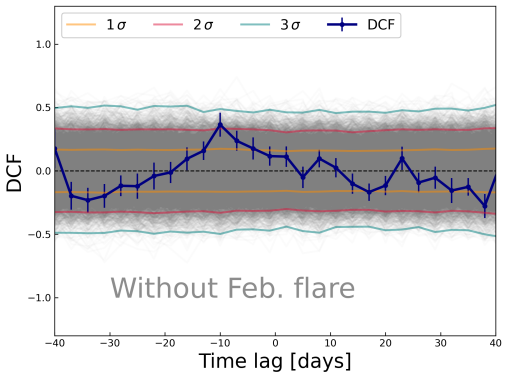

(d) 3-300 GeV vs 2-10 keV without the flare in February 2010

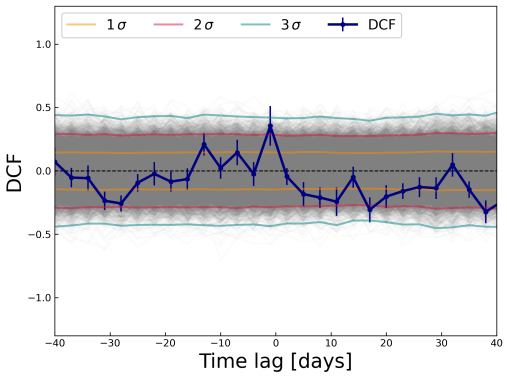

(e) 0.3-3 GeV vs 2-10 keV

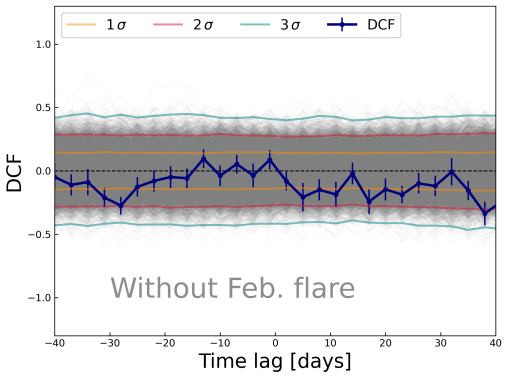

(f) 0.3-3 GeV vs 2-10 keV without the flare in February 2010

Figure B.2: Discrete correlation function computed between two energy ranges provided by *Fermi*-LAT and *Swift*-XRT with and without the big flare in February using a binning of 3 days. It is computed for a range of time lags between -40 to +40 days. The 1 σ, 2 σ, and 3 σ confidence levels obtained by simulations are shown by the yellow, red, and green lines, respectively.

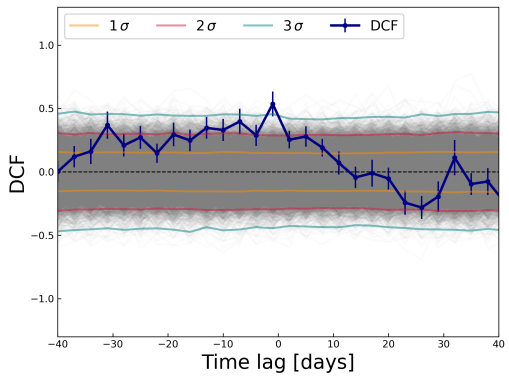

(a) 0.3-3 GeV vs UV-W1

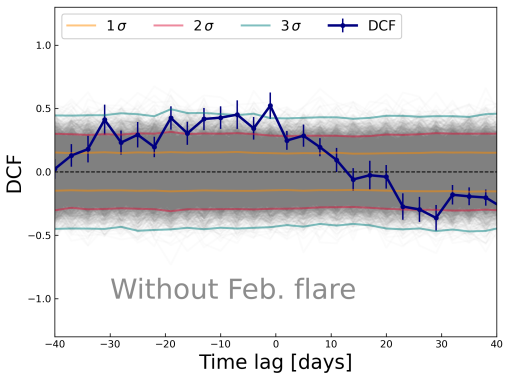

(b) 0.3-3 GeV vs UV-W1 without the flare in February 2010

Figure B.3: Discrete correlation function computed between the 0.3-3 GeV band and the W1 filter by *Swift*-UVOT with and without the big flare in February using a binning of 3 days. It is computed for a range of time lags between -40 to +40 days. The 1 σ, 2 σ, and 3 σ confidence levels obtained by simulations are shown by the yellow, red, and green lines, respectively.

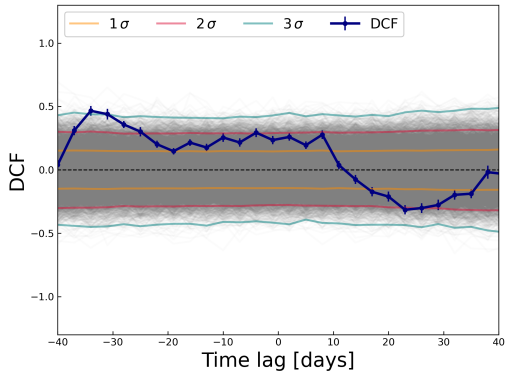

(a) 0.3-3 GeV vs R-band

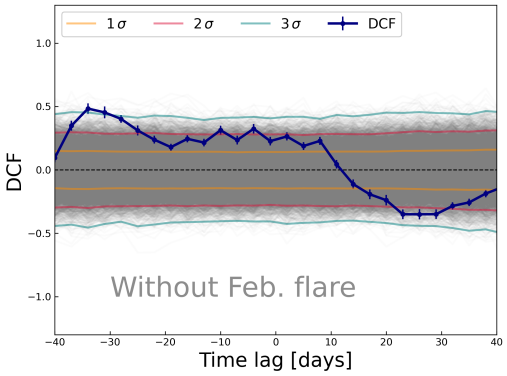

(b) 0.3-3 GeV vs R-band (GASP-WEBT) without the flare in February 2010

Figure B.4: Discrete correlation function computed between the 0.3-3 GeV band and the R-band by GASP-WEBT with and without the big flare in February using a binning of 3 days. It is computed for a range of time lags between -40 to +40 days. The 1 σ, 2 σ, and 3 σ confidence levels obtained by simulations are shown by the yellow, red, and green lines, respectively.

Acknowledgements

In this last chapter, I would like to thank everyone who has supported me throughout my journey and made this thesis possible.

My biggest gratitude goes to David Paneque. David invited me to join the group when I was looking for a topic for my Master's thesis. Since then, he supervised me all the way to the completion of my PhD. His support, the choice of projects we worked on, and his constant advice were among the most important factors in successfully completing this work.

I would also like to thank Béla Majorovits, who has agreed to act as my official supervisor and referee once again. He always made time when there was a need for advice and discussion. In this regard, I would also like to thank Elisa Resconi for acting as my second referee and also for inviting me to her group as a student employee many years ago, which is what got me interested in astroparticle physics in the first place.

Also, many thanks to Razmik Mirzoyan for welcoming me to the group and for the valuable discussions and advice on atmospheric science, engineering, and physics of all kinds. I also thank Masahiro Teshima for accepting me into the group and supporting my work.

A never-ending thank you goes to all members of the MPP MAGIC group. Each of you has made me enjoy going to the office and made this thesis possible by providing help, advice, or simply gossip during coffee breaks. Starting with Diana, who made everyday office life effortless by taking care of all organizational and administrative matters. Without Axel, my thesis would never have been completed in this form. Working with and learning from him during the second half of my PhD was incredibly valuable and absolutely crucial for the successful completion. The same goes for Alex, from whom I learned most of the technical things, be it my first MARS analysis or how to heat up every office on our floor. I also want to thank Lea a lot for answering all my questions and always having time to chat whenever I needed advice. I am incredibly grateful to be part of such an amazing group of PhD students. Juli, Jarred, Giorgio and all the others already mentioned, I couldn't have wished for better people around me. This also holds true for every other current and former member of the group: Martin, Giovanni, David, Alessio, Seiya, Michele, Irene, Lucas, Marine, and Yating. Thanks a lot to every one of you!

Being part of the MAGIC collaboration for many years has given me unforgettable memories. It was a lot of fun spending time with all of you at conferences, meetings, and trips to La Palma. In particular, I want to thank Markus Gaug for working with him on all my LIDAR-related projects, the Maestros Eduardo and Victor for their support on-site, and everyone I have been on shift with.

The last paragraph is for my closest friends and family, who made these years a wonderful time. Thank you to all my friends who are close to me, even though some of you are now scattered far and wide. My grandparents and parents have always helped me in every possible way and have given me unconditional support. I owe them endless gratitude. The same gratitude is due to my brother, the strongest person I know and whose support I can always count on.

My final page is dedicated solely to Alma. I can't put into words how much happiness and support you give me every day.